UNIVERSITY of CALIFORNIA

Santa Barbara

Phosphors for solid-state lighting: New systems, deeper understanding

A Dissertation submitted in partial satisfaction of the

requirements for the degree

Doctor of Philosophy

in

Materials

by

Kristin Ashley Denault

Committee in charge:

Professor Ram Seshadri, Chair
Professor Galen Stucky
Professor Michael Gordon
Professor Fred Wudl

March 2015

The dissertation of Kristin Ashley Denault is approved.

_____

Professor Galen Stucky

_____

Professor Michael Gordon

_____

Professor Fred Wudl

_____

Professor Ram Seshadri, Committee Chair

December 2014

Phosphors for solid-state lighting: New systems, deeper understanding

by

Kristin Ashley Denault

for my family

Acknowledgements

I would like to start by acknowledging my advisor, Professor Ram Seshadri. Over the past four years you have provided a rich and multifaceted environment for learning, and the knowledge and guidance I have received from you has allowed me to grow as a scientist and an individual. I would also like to thank my committee members and collaborators, especially Professors Steve DenBaars, Galen Stucky, Michael Gordon, and Fred Wudl for all of their expertise and insights throughout.

This experience was of course shaped by the many group members that I have had the opportunity and pleasure to work with, learn from, and enjoy the company of. During my work on phosphor materials, I collaborated closely on projects with Dr. Alex Birkel and Professor Jakoah Brgoch. Thank you both for insightful scientific conversations, help and training in the lab, and interesting dialogues that made every day more enjoyable. I would also like to thank the many interns over the years who have worked with me on projects including Sara Paden, Courtney Doll, Takia Wheat, and Zhiyuan Cheng.

Many of my important graduate school milestones were shared with Dr. Moureen Kemei, whose high spirits, love of science, and infectious laugh were a welcome reprieve between classes and exams. The amazing opportunity to

travel abroad for international conferences would not have been as enjoyable without the excellent travel partners that I had, Dr. Kim See and Jason Douglas. I would like to thank all of the other Seshadri group members for creating a great group dynamic and making this a truly memorable and positive experience. I would also like to thank the MRL and Materials department staff. The facilities would not be such a productive and welcoming environment without the skilled staff members that keep the labs, equipment, and administration running so smoothly.

I have also had the pleasure of meeting wonderful people on the UCSB campus and the Santa Barbara area, including friends, housemates, and officemates. You have all shaped my experience in graduate school for the better, and I am happy to know and have met each one of you.

Finally, I would like to thank my family. My mother and father have fostered and supported the decisions throughout my life that have led me to becoming the person I am today. Without them, none of this would have been possible. I am so grateful for everything they have done for me, allowing and encouraging me to pursue my dreams.

Curriculum Vitæ

Kristin Ashley Denault

Education

2010–2015   Ph.D. in Materials, University of California, Santa Barbara, CA, USA.

2013–2014   Certificate in the Graduate Program in Management Practice, Technology Management Program, University of California, Santa Barbara, CA, USA.

2006–2010   B.S. in Materials Science and Engineering (Summa cum laude), Rutgers, the State University of New Jersey, New Brunswick/Piscataway, NJ, USA.

Publications

16. K. A. Denault, J. Brgoch, S. D. Kloß, M. W. Gaultois, J. Siewenie, K. Page, and R. Seshadri, Average and local structure, Debye temperature, and structural rigidity in some oxide compounds related to phosphor hosts, *ACS*

Appl. Mater. Interfaces **accepted** (2015).

15. A. P. Black, K. A. Denault, J. Oró-Solé, A. R. Goñi, and A. Fuertes, Red luminescence and ferromagnetism in europium oxynitridosilicates with a β-K_2SO_4 structure, *Chem. Commun.* **51** 2166–2169 (2015). [doi]

14. J. Brgoch, K. Hasz, K. A. Denault, C. K. H. Borg, A. A. Mikhailovsky, and R. Seshadri, Data-driven discovery of energy materials: Efficient $BaM_2Si_3O_{10}$:Eu^{2+} (M = Sc, Lu) phosphors for application in solid state white lighting, *Faraday Discuss.* **176** 333–347 (2014). [doi]

13. J. Brgoch, S. D. Kloß, K. A. Denault, and R. Seshadri, Accessing $(Ba_{1-x}Sr_x)Al_2Si_2O_8$:$Eu^{2+}$ phosphors for solid state white lighting *via* microwave assisted preparation: Tuning emission color through coordination environment, *Z. Anorg. Allg. Chem.* (C. N. R. Rao FestSchrift) **640(6)** 1182–1189 (2014). [doi]

12. K. A. Denault, J. Brgoch, M. W. Gaultois, A. Mikhailovsky, R. Petry, H. Winkler, S. P. DenBaars, and R. Seshadri, Consequences of optimal bond valence on structural rigidity and improved luminescence properties in $Sr_xBa_{2-x}SiO_4$:Eu^{2+} orthosilicate phosphors, *Chem. Mater.* **26(7)** 2275–2282 (2014). [doi]

11. J. Brgoch, C. K. H. Borg, K. A. Denault, J. R. Douglas, T. A. Strom, S. P. Den-

Baars, and R. Seshadri, Rapid microwave preparation of cerium-substituted sodium yttrium silicate phosphors for solid state white lighting, *Solid State Sci.* **26** 115–120 (2013). [doi]

10. K. A. Denault, Z. Cheng, J. Brgoch, S. P. DenBaars, and R. Seshadri, Structure–composition relationships and optical properties in cerium-substituted $(Sr,Ba)_3(Y,La)(BO_3)_3$ borate phosphors, *J. Mater. Chem. C* **1(44)** 7339–7345 (2013). [doi]

9. K. A. Denault, M. Cantore, S. Nakamura, S. P. DenBaars, and R. Seshadri, Efficient and stable laser-driven white lighting, *AIP Advances* **3** 072107 (2013). [doi]

8. J. Brgoch, C. K. H. Borg, K. A. Denault, A. Mikhailovsky, S. P. DenBaars, and R. Seshadri, An efficient, thermally stable cerium-based silicate phosphor for solid state white lighting, *Inorg. Chem.* **52(14)** 8010–8016 (2013). [doi]

7. N. C. George, K. A. Denault, and R. Seshadri, Phosphors for solid-state white lighting, *Annu. Rev. Mater. Res.* **43** 481–501 (2013). [doi]

6. J. Brgoch, C. K. H. Borg, K. A. Denault, and R. Seshadri, Tuning luminescent properties via structure modification in the solid-solution $(Ba_{1-x}Sr_x)_9Sc_2Si_6O_{24}$:$Ce^{3+}$,$Li^+$, *Solid State Sci.* **18** 149–154 (2013). [doi]

5. K. A. Denault, A. A. Mikhailovsky, S. Brinkley, S. P. DenBaars, and R. Seshadri, Improving color rendition in solid state white lighting through the use of quantum dots, *J. Mater. Chem. C* **1** 1461 (2013). [doi]

4. K. A. Denault, N. C. George, S. R. Paden, S. Brinkley, A. A. Mikhailovsky, J. Neuefeind, S. P. DenBaars, and R. Seshadri, A green-yellow emitting oxyfluoride solid solution phosphor $Sr_2Ba(AlO_4F)_{1-x}(SiO_5)_x:Ce^{3+}$ for thermally stable, high color rendition solid state white lighting, *J. Mater. Chem.* **22** 18204–18213 (2012). [doi]

3. A. Birkel, K. A. Denault, N. C. George, and R. Seshadri, Advanced inorganic materials for solid state lighting, *Material Matters* **7(2)** 22–27 (2012). [link]

2. A. Birkel, K. A. Denault, N. C. George, C. E. Doll, B. Héry, A. A. Mikhailovsky, C. S. Birkel, B.-C. Hong, and R. Seshadri, Rapid microwave preparation of highly efficient Ce^{3+}-substituted garnet phosphors for solid state white lighting, *Chem. Mater.* **24** 1198–1204 (2012). [doi]

1. S. E. Brinkley, N. Pfaff, K. A. Denault, Z. Zhang, H. T. Hintzen, R. Seshadri, S. Nakamura, and S. P. DenBaars, Robust thermal performance of $Sr_2Si_5N_8:Eu^{2+}$: An efficient red emitting phosphor for light emitting diode based white lighting, *Appl. Phys. Lett.* **99** 241106 (2011). [doi]

Intellectual property

3. K. A. Denault, R. Seshadri and S. P. DenBaars, Phosphor compositions of the formula $A_3RE(BO_3)_3$:Ce^{3+} (A = alkaline earth ion; RE = rare earth ion) for solid state white lighting, US Patent Appl. No. 61/864355 (2013) *patent pending*.

2. K. A. Denault, S. P. DenBaars, and R. Seshadri, Laser-driven white lighting system for high-brightness applications, US Patent Appl. No. 61/860619 (2013) *patent pending*.

1. R. Seshadri, S. P. DenBaars, K. A. Denault, and M. Cantore, Efficient and stable, high-power, laser-driven white light source, PCT Patent Appl. No. PCT/US13/057538 (2012) *patent pending*.

Abstract

Phosphors for solid-state lighting: New systems, deeper understanding

by

Kristin Ashley Denault

Phosphor materials are a crucial component in energy efficient lighting with the ability to affect overall device performance. The structure and crystal chemistry of these materials greatly dictate the resulting optical properties. Understanding the relationship between structural and optical properties in phosphors allows for insights into the methods for developing materials with targeted properties. Here, we explore the structure–composition–property relationships in phosphor materials using a multitude of structural and optical characterization methods including high resolution synchrotron X-ray and neutron powder diffraction and total scattering, low-temperature heat capacity, temperature- and time-resolved photoluminescence, and density functional theory calculations. We describe the development of several new phosphor compositions and provide an in-depth description of the structural and optical properties. We show structural origins of improved thermal performance of photoluminescence

and methods for determining structural rigidity in phosphor hosts that may lead to improved luminescent properties. New white light generation strategies are also explored including quantum dots for improved color rendition and laser-based lighting for efficient and thermally stable high-power lighting.

We begin by presenting the development of a green-yellow emitting oxyfluoride solid-solution phosphor $Sr_2Ba(AlO_4F)_{1-x}(SiO_5)_x$:$Ce^{3+}$. An examination of the host lattice, and the local structure around the Ce^{3+} activator ions points to how chemical substitutions play a crucial role in tuning the optical properties of the phosphor. The emission wavelength can be tuned from green to yellow by tuning the composition, x. Photoluminescent quantum yield is determined to be 70±5% for some of the examples in the series with excellent thermal properties. Phosphor-converted LED devices are fabricated using an InGaN LED and are shown to exhibit high color rendering white light.

Next, we identify two new phosphor solid-solution systems, $(Ba_{1-x}Sr_x)_9Sc_2Si_6O_{24}$:$Ce^{3+}$,$Li^+$ and $Ba_9(Y_{1-y}Sc_y)_2Si_6O_{24}$:$Ce^{3+}$. The substitution of Sr for Ba in $(Ba_{1-x}Sr_x)_9Sc_2Si_6O_{24}$:$Ce^{3+}$,$Li^+$ results in a decrease of the alkaline earth–oxygen bond distances at all three crystallographic sites, leading to changes in optical properties. The room temperature photoluminescent measurements show the structure has three excitation peaks corresponding to Ce^{3+} occupying the three independent alkaline earth sites. The emission

of $(Ba_{1-x}Sr_x)_9Sc_2Si_6O_{24}:Ce^{3+},Li^+$ is red-shifted from the near-UV to blue with compositional changes. The red-shifted photoluminescent quantum yield also increases when Sr is substituted for Ba in these compounds. The end member $Ba_9Y_2Si_6O_{24}:Ce^{3+}$ was identified as an efficient blue-green phosphor with high thermal stability of the luminescence, viable for near-UV LED excitation. An efficient emission, with a quantum yield of $\approx$60%, covers a broad portion of the visible spectrum leading to the observed blue-green color. The emission of this compound can be red-shifted via the solid-solution $Ba_9(Y_{1-y}Sc_y)_2Si_6O_{24}:Ce^{3+}$ allowing for tunable color properties when device integration is considered.

We then explore the structure–composition relationships and optical properties in newly developed cerium-substituted $(Sr,Ba)_3(Y,La)(BO_3)_3$ borate phosphors. Examination of the coordination environment of the Ce^{3+} active site polyhedra coupled with low-temperature photoluminescence reveals three distinct excitation bands corresponding to Ce^{3+} located on three distinct crystallographic sites. Comparing the position of these excitation bands with crystal field splitting effects due to changes in polyhedral volumes and distortions suggests an assignment of the three excitation bands. These compounds are efficiently excited by UV light with blue emission, the most efficient compound determined to be $Sr_3La(BO_3)_3:Ce^{3+},Na^+$ with a quantum yield of 50%.

A data-driven discovery of energy materials then reveals the efficient

BaM_2Si$_3$O$_{10}$:Eu^{2+} (M = Sc, Lu) phosphors with UV-to-blue and UV-to-blue-green phosphors. Interestingly, substituting Eu^{2+} in the Lu^{3+} containing material produces two emission peaks, at low temperature, as allowed by two substitution sites. The photoluminescence of the Sc^{3+} compound is robust at high temperature, while the Lu-analogue has a large decrease of its room temperature intensity. The decrease in emission intensity is explained as stemming from charge transfer quenching due to the short distances separating the luminescent centers on the Lu^{3+} substitution site. The correlation between structure and optical response in these two compounds indicates that even though the structures are three-dimensionally connected, high symmetry is required to prevent structural distortions that could impact photoluminescence.

Next, the consequences of optimal bond valence on structural rigidity are explored and linked to the improved luminescence properties in Sr$_x$Ba$_{2-x}$SiO$_4$:Eu^{2+} orthosilicate phosphors. We observe that in the intermediate compositions, the two cation sites in the crystal structure are optimally bonded as determined from bond valence sum calculations. Optimal bonding results in a more rigid crystal, as established by the intermediate compositions possessing the highest Debye temperature, determined experimentally from low-temperature heat capacity measurements. Greater rigidity, in turn, results in high luminescence efficiency for intermediate compositions at elevated temper-

atures.

We then conduct an in-depth analysis of the average and local structure, Debye temperature, and structural rigidity in oxide phosphor host materials. The average and local structure of the oxides Ba_2SiO_4, $BaAl_2O_4$, $SrAl_2O_4$, and Y_2SiO_5 are examined in order to evaluate crystal rigidity in light of recent studies suggesting that highly connected and rigid structures yield the best phosphor hosts. Simultaneous momentum-space refinements of synchrotron X-ray and neutron scattering yield accurate average crystal structures, with reliable atomic displacement parameters. The Debye temperature Θ_D, which has proven to be a useful proxy for structural rigidity, is extracted from the experimental atomic displacement parameters and compared with predictions from density functional theory calculations and experimental low-temperature heat capacity measurements. The role of static disorder on the measured displacement parameters, and the resulting Debye temperatures, are also analyzed using pair distribution function analysis of total neutron scattering, as refined over varying distance ranges of the pair distribution function. The interplay between optimal bonding in the structure, structural rigidity, and correlated motion in these structures is examined, and the different contributions are delineated.

Finally, new light generation strategies including quantum dots and laser-based lighting are explored.

Contents

List of Figures

List of Tables

Chapter 1

Introduction: Phosphor considerations for high-performance solid-state white lighting

Advancements in the field of energy efficient lighting have since led to the emergence of solid-state light sources. Light-emitting diodes (LEDs) were introduced as a means of white light generation following the groundbreaking

---

[1] The contents of this chapter have substantially appeared in reference [1]: N. C. George, K. A. Denault, and R. Seshadri, Phosphors for solid-state white lighting, *Annu. Rev. Mater. Res.* **43** 481–501 (2013) ©2013 Annual Reviews.

achievements of Nakamura and co-workers facilitating high brightness blue-emitting (In,Ga)N LEDs.[2] The use of these solid-state devices for lighting in place of traditional light sources has become quite appealing for a wide range of applications with advantages including higher efficiency and reduced energy consumption, longer lifetimes, and devices that avoid the use of toxic elements such as mercury.[3, 4] Such white lighting devices are proliferating all over the world, and are increasingly replacing incandescent, halogen, xenon, and fluorescent light sources.

Generation of white light using an LED source can be accomplished by combining several different wavelengths of LEDs, for example red-, green-, and blue-emitting LEDs, or by using a down-converting phosphor material in conjunction with a single LED. Down-converting phosphors are used to make white light with highly efficient (In,Ga)N blue or near-UV LEDs. Such a device uses a thin coating of phosphor material on top of an LED, as depicted in Figure 1.1. The phosphor layer down-converts LED light to light in the visible region ranging from blue to red, and the combination of radiations mix to produce white light. Phosphor-converted white LEDs offer advantages over all-LED devices including easy tunability of a wide range of color temperatures with a high color rendering index.[5, 6]

Phosphor materials have thus emerged as a crucial research area due to their

(a) LED + yellow phosphor
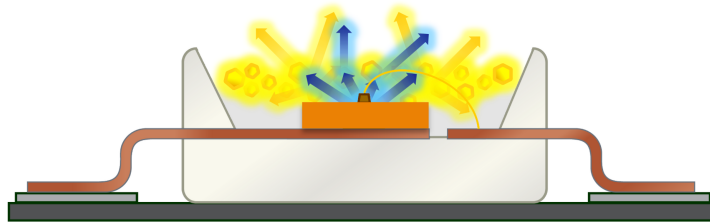
(b) Emission characteristics

λ (nm)
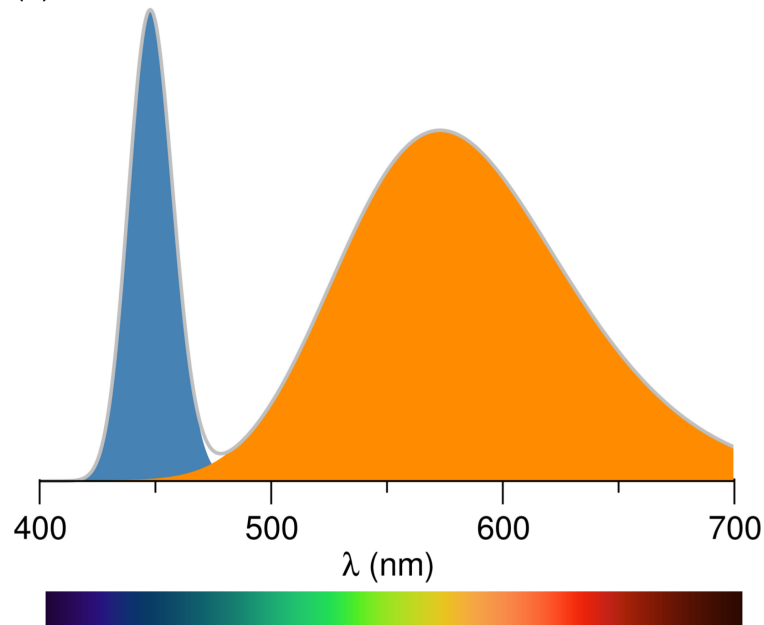
Figure 1.1: (a) Scheme showing a typical phosphor-converted white LED device. Some of the blue light from the LED chip is allowed to combine with the phosphor-converted yellow light. (b) Representative emission spectrum from such a device, showing the exciting blue radiation from the semiconducting component, and the yellow phosphor-converted radiation combining to give white light. Reproduced with permission from reference [1], ©2013 Annual Reviews.

widespread use in energy efficient lighting and ability to affect overall device performance. Phosphor properties such as excitation and emission spectra, photoluminescent quantum yield (PLQY), and resistance to thermal quenching of the luminescence will dictate the device luminous efficacy, color temperature, color rendition, and thermal stability. The structure and crystal chemistry of these materials greatly dictate the resulting optical properties. As a result, understanding the relationship between structural and optical properties of phosphor materials allows for insight as to the methods for developing phosphors with targeted properties.

1.1   Some general aspects of color in lighting

The human eye response to light spans a region from about 400 nm to 750 nm. Standardization of colorimetry for photopic (bright-light) vision was carried out in 1931 by the Commission Internationale de l'Éclairage (The International Commission for Illumination, CIE) and is represented by the 1931 CIE diagram as shown in Figure 1.2. Monochromatic wavelengths form the locus outlining the colored area in Figure 1.2, and any color in the visible spectrum can be represented by x and y coordinates. Some common LEDs and phosphors are indicated as examples. White light is in the center of the diagram,
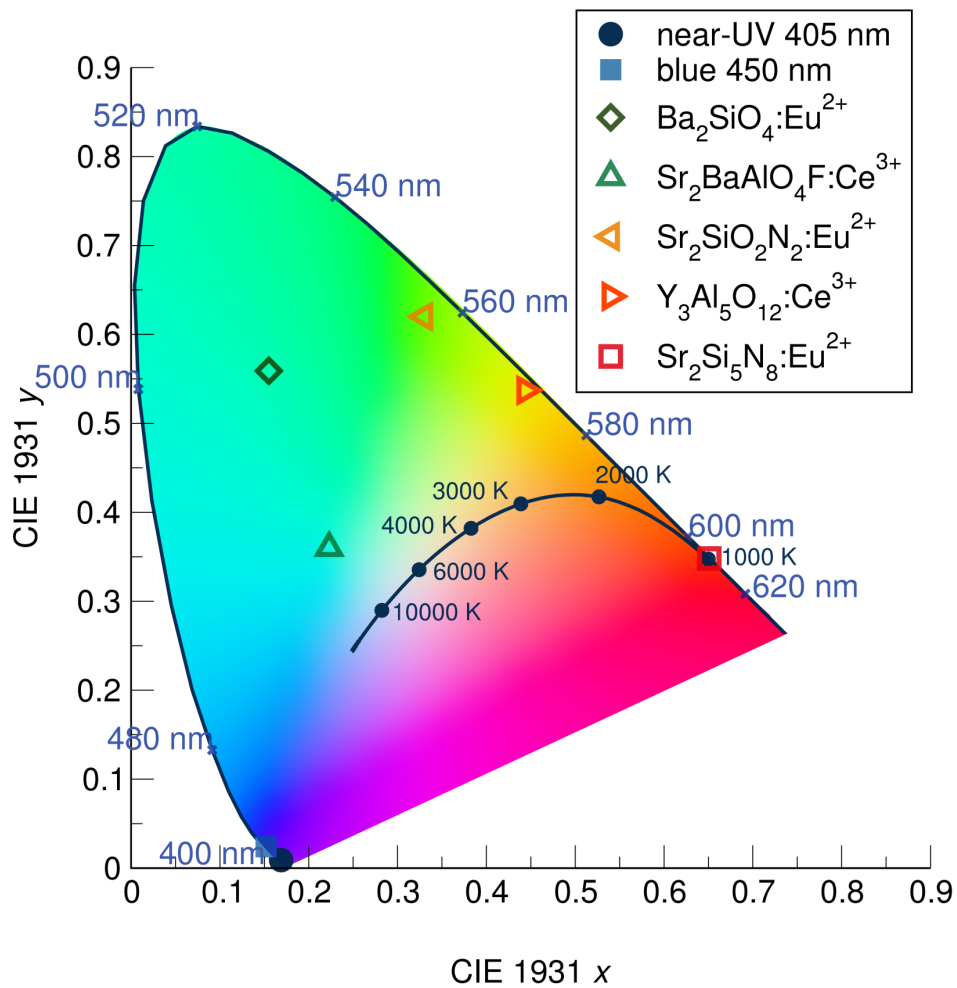
Figure 1.2: The 1931 CIE diagram, showing the Planckian locus in black, with the color coordinates of some common phosphors and LEDs plotted. Reproduced with permission from reference [1], ©2013 Annual Reviews.

with the equal energy point at the coordinates $(\frac{1}{3}, \frac{1}{3})$. To find the color of a combination of two color coordinates, a straight line can be drawn between the two points, and the final color point will depend on the relative intensity of the two sources. For example, the emission from a 450 nm LED and yellow-emitting cerium-substituted yttrium aluminum garnet phosphor ($Y_3Al_5O_{12}$:Ce^{3+} or YAG:Ce), as depicted in Figure 1.1, produces white light because the point between the 450 nm LED and YAG:Ce on the CIE diagram in Figure 1.2 lies in the white portion of the spectrum.

The Planckian locus shown as the trace in the middle of Figure 1.2, represents the emission color of black-body radiators at different color temperatures as labeled in the figure. The color of a black-body radiator is characterized by only the temperature, with higher color temperatures corresponding to a more blue color and lower temperatures a more red color. For example, diffuse sunlight has a color temperature of between 5700 K and 6500 K, while the CIE standard candle flame has a color temperature of around 2000 K.[7] Any light source can be assigned a correlated color temperature (CCT), which is the temperature of an ideal black-body that is closest in hue to the light source. The common blue LED and YAG:Ce phosphor typically has a CCT between 4000 K to 8000 K.[8]

The standard method of characterizing the quality of light is to use the color-

rendering index (CRI), which specifies how well a light source can illuminate, or render, the true color of an object. By definition, any black-body radiator has a CRI of 100 (the maximum value). The CRI is found by comparing the difference in the color coordinates in the CIE of an object illuminated with the test source, and a black-body with the same CCT as the test source. Typically, eight different standard test samples are used. A blue LED and YAG:Ce phosphor device has a CRI ranging from 70 to 80.[8]

1.2   Strategies for solid-state white lighting

Generation of white light using an LED source can be accomplished by combining several different wavelengths of LEDs, for example red-, green-, and blue-emitting LEDs, or by using a down-converting phosphor material in conjunction with a single LED. At this point, III-V semiconducting materials have been developed to cover the entire visible spectrum. However, while efficient blue and red emitters are available today, bright green emitters remain an challenge, making efficient white light production only using LEDs difficult. To overcome this limitation, down-converting phosphors are used.

The three principle strategies for creating white light with a solid-state device are illustrated in Figure 1.3: (a) multiple LED chips emitting at different
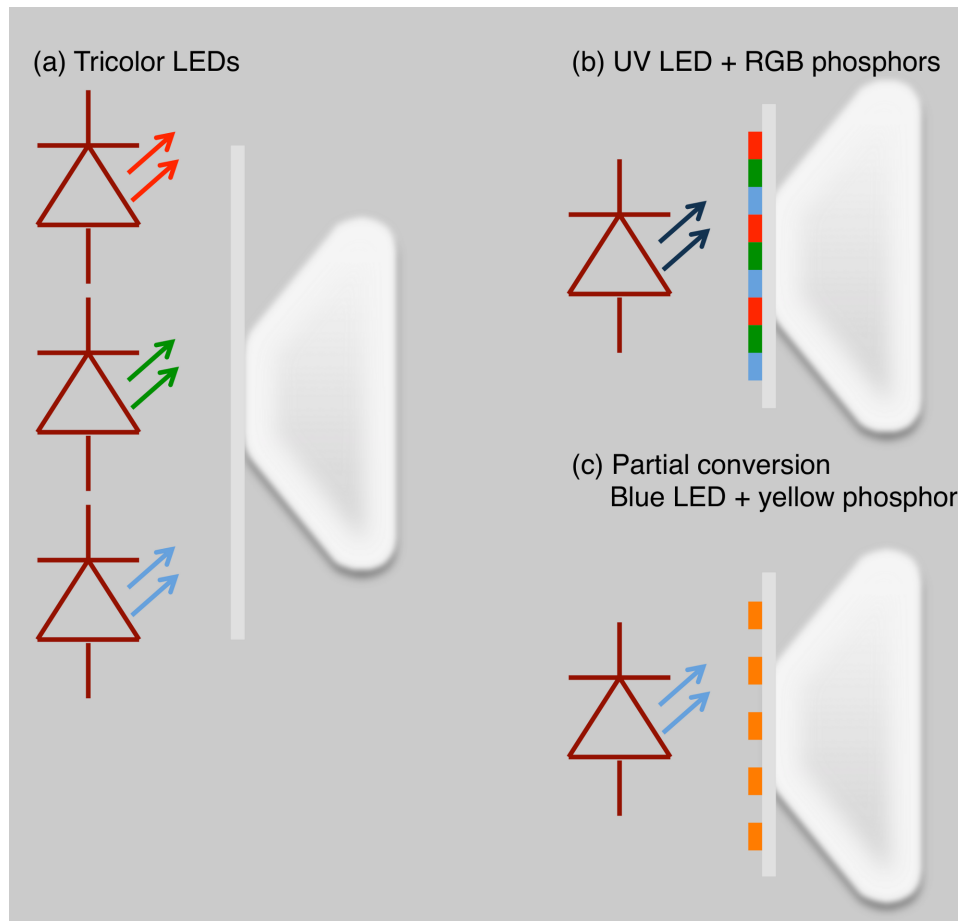
Figure 1.3: Schematics of the three principal white lighting strategies are shown. (a) A 3-LED strategy with red, green, and blue LED chips, (b) a 3-phosphor strategy with a UV LED and red, green, and blue phosphors, and (c) a blue LED with a yellow down-converting phosphor. Reproduced with permission from reference [1], ©2013 Annual Reviews.

wavelengths in a single device, (b) a UV LED chip and a combination of red, green, and blue (RGB) down-converting phosphors, and (c) a blue LED chip with a yellow down-converting phosphor that allows some of the exciting blue radiation to bleed through (*i.e.* partial down-conversion)[9]. In principle, the best strategy is the use of three LEDs, since energy is lost in phosphor-converted devices due to the Stokes shift. However, the current low efficiency of yellow and green LEDs prevents multi-LED devices from achieving high efficiencies. The color temperature of a multi-LED device is tunable by varying the power of the individual LED components, although this necessitates additional circuitry, adding cost and complexity. Another drawback of the multi-LED strategy is poor color rendering, associated with the white light comprising relatively narrow radiation components; such a device would have a low CRI value, potentially in the mid 70s [9]. Furthermore, dimming such a device proves to be very challenging, since LED chips that emit at different wavelengths have a different intensity response to changes in voltage. Differential aging and responses to temperature of the different colored diodes would also necessitate additional electronic circuitry.

Another strategy is to use an LED with down-converting phosphors, as shown in Figure 1.3(b) and (c). To minimize the energy lost due to the Stokes Shift, also deemed the "quantum deficit",[10] an LED with as long a wavelength as

possible should be used. This of course must be balanced with the desired color rendering of the device. If warm white light is desired, such as for residential applications, a blue LED and single yellow phosphor may not suffice. A device instead with a UV LED and multiple phosphors can cover a broad range of emission wavelengths, giving a good color rendering and stable emission color. This strategy of a UV LED combined with RGB phosphors becomes advantageous if the efficiency of UV LEDs exceeds that of blue LEDs. The UV LED strategy also has the advantage of stable color, since changes in the UV emission wavelength will not effect the color output of a device, whereas with a blue LED this is not true. However, multiple phosphors can reabsorb the emission of other phosphors, adding a loss mechanism and decreasing the efficiency of the system. The single-phosphor-converted blue LED device is currently the most common solid state white lighting device produced today, due to the high efficiency of blue LEDs and the yellow emitting YAG:Ce phosphor, despite the limitation of relatively poor color rendering (CRI <80) high color temperatures (>4000 K).

1.3   Structure–property relationships in phosphors

Phosphor materials absorb light of a certain energy or wavelength and emit light at a different energy or wavelength. Phosphors typically used in lighting

applications are down-conversion phosphors, meaning that the absorbed light is down-converted to longer wavelength, lower energy light. For example, a widely used phosphor composition for solid-state lighting is YAG:Ce due to its high absorption of blue light from (In,Ga)N LEDs, which is efficiently down-converted to yellow light (PLQY $\approx$ 90%).[11–14] The most commonly used activator ions for solid-state lighting applications are Ce^{3+} and Eu^{2+}.

In addition to high absorption of LED light and efficient PLQY, a number of other phosphor optical properties affect the overall device performance and light output. Color rendering index (CRI), discussed above, is a measure of how well the light source can portray the true color of an object illuminated by the light source. For example, sunlight represents the highest possible CRI of 100. Under sunlight, or any form of black-body radiation such as an incandescent light bulb, all wavelengths of the visible spectrum are represented and so all colors of an object may be perceived. As shown in the LED lamp spectra above in Figure 1.1, different wavelengths of the visible spectrum are represented based on the light source and phosphor materials used. Sharp emission lines, common in fluorescent lighting, will lead to poor color rendering, whereas in phosphor-converted LED lamps, the broad emission spectrum covers a wider region of the visible spectrum and leads to improved color rendering.

Phosphor materials also dictate the color point of the white light produced,

described by the color coordinates of a CIE diagram shown in Figure 1.2. The emission wavelengths and FWHM of the emission spectra, combined with the LED emission, produces the desired color point and CCT, which can be tuned by the choice of phosphor material and the use of multiple phosphor compositions. Finally, the resistance to thermal quenching and resistance to flux saturation of the photoluminescence are important properties of phosphors, especially with the advent of high-power devices.[8, 15]

The excitation and emission energies of a phosphor are dictated by both the activator ion and the host structure. The $5d$ levels of the activator ion are greatly affected by the surrounding environment and therefore can be tuned through host structure interactions. The host structure may consist of several elements from the alkali and alkaline earth metals, rare earth elements, and actinides composing oxides, aluminates, silicates, borates, phosphates, nitrides, fluorides, chlorides, and combinations thereof. The varying degrees of covalency, connectivity, and local coordination environment of activator ion substitution sites all affect the energetics of the associated activator ion and determine phosphor properties such as excitation and emission wavelengths, PLQY, and resistance to thermal quenching of the luminescence. As a result, the host structure and coordination environment around the activator ion play a large role in determining the optical characteristics of phosphor materials.

1.3.1 Energetics of Ce^{3+} and Eu^{2+} activator ions

The energy levels of the activator ions in the phosphor determines the excitation and emission properties of phosphors, and is directly related to the $4f$ and $5d$ energy levels. Among the rare earths, there are essentially two types of optical transitions: those between different $4f$ levels, and those between $4f^{n-1}5d^1$ and $4f^n5d^0$ levels. In the case of transitions between two $4f^n$ levels, the excitation and emission energies are unaffected by the host crystal into which the activator is substituted, and the Dieke diagram[16] can be used to predict these energies. This is due to the buried, non-interacting nature of $4f$ orbitals, which also results in spectra with narrow line-widths. The $4f$ energies of rare earth ions vary systematically, depending on the number of electrons in the atom. Systematic variation of the $4f$ levels is understood in terms of the binding energy of the $4f$ electrons through the spin pairing theory of Jørgenson.[17] This energy effectively determines the excitation and emission energies of the transitions between $4f^{n-1}5d^1$ and $4f^n5d^0$, since the energy of the lowest of the $5d$ levels does not vary much compared to the change in $4f$ energy levels with the number of electrons in the atom. The energetic position of the $4f$ level then dictates the excitation and emission energies for transitions between $4f$ and $5d$ levels.

As a free ion, Ce^{3+} or Eu^{2+} has a large gap between the $4f$ ground state and

$5d$ excited state; for Ce^{3+} this is around $6.2\,eV$ ($50{,}000\,cm^{-1}$).[18] This gap is decreased substantially by crystal field splitting and a downward shift of the $5d$ centroid, leading to a $4f$ to $5d$ separation around $4{,}000\,cm^{-1}$, which enables absorption of blue light and emission of yellow light. Since the $5d$ orbitals are strongly effected by the surrounding crystal field and the polarizability of the host crystal,[19, 20] the excitation and emission energies can be tuned through the host crystal composition and structure.

The transitions between $4f^{n-1}5d^1$ and $4f^n$ levels give rise to a broad range of excitation and emission wavelengths, compared with the very narrow peaks from transitions between $4f^n$ levels. The broad range of emission and excitation energies for transitions between $4f^{n-1}5d^1$ and $4f^n$ levels is the result of two effects: the Franck-Condon principle, and breaking the degeneracy of the $4f$ ground state. The first effect, the Franck-Condon principle, results in transitions with many different energies due to different vibrational states of the $4f$ and $5d$ levels involved in the transitions. This wide range of transition energies is smeared by inhomogeneous broadening in solids. The second effect, breaking of the $4f$ degeneracy, is the result of a few effects. One is the spin-orbit coupling of the $4f$ ground state into multiple levels; for Ce^{3+} these are the $^2F_{5/2}$ and $^2F_{7/2}$ levels, and for Eu^{2+} there are 8 distinct levels ranging from $^8S_{7/2}$ to $^8S_{-7/2}$. For Ce^{3+} in solids, the splitting between the two ^2F states is typically around

14

$2000\,\mathrm{cm}^{-1}$,[21] so that the state with higher energy ($^2F_{7/2}$) is only accessed from relaxation from the excited $5d$ state at reasonable temperatures. The emission from the lowest energy $5d$ state ($^2D_{3/2}$) to the two ^2F levels produces an emission spectra that can be represented by two Gaussian curves.[14] These ground state ^2F levels are further split on the order of $100\,\mathrm{cm}^{-1}$ by the local crystal field splitting,[22] increasing the broad range of excitation and emission energies.

1.3.2   Crystal fields and nephelauxetic effect

The optical properties of phosphors with the activators Ce^{3+} and Eu^{2+} depend both on the activator ion and on the host crystal structure, which influences the $5d$ levels. The electronic energy levels of an activator ion in a crystal differ greatly from those of a free ion. For example, the difference in energy between the $5d$ and $4f$ levels of gaseous Ce^{3+} ions is in the ultraviolet region, whereas if Ce^{3+} ions are in a crystal this energy difference can range from ultraviolet across visible wavelengths, depending on the host crystal. When an activator ion is placed in a host crystal, there are two major effects that will dictate the photoluminescent properties: the centroid shift and the crystal field splitting. Overall these effects lead to a decrease in the energy difference be-
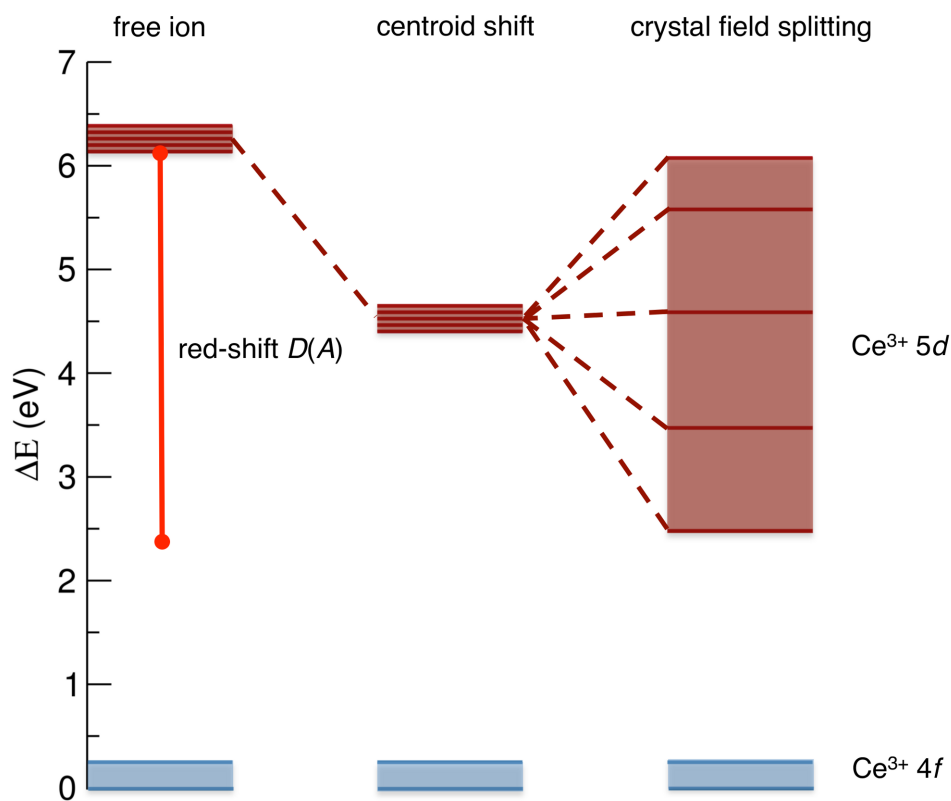
Figure 1.4: A schematic energy level diagram for Ce^{3+} shows the effects of the host crystal A, including the centroid shift and crystal field splitting, that lead to the overall decrease in the energy difference between the $5d$ and $4f$ levels, known as the red-shift, $D(A)$. Reproduced with permission from reference [1], ©2013 Annual Reviews.

tween the $5d$ and $4f$ energy levels, referred to as the red-shift. This effect is illustrated for Ce^{3+} in Figure 1.4 with the total red-shift labeled $D(A)$, where A is the host crystal. Both of these processes affect the $5d$ electrons of the activator ion to a great extent, whereas the well shielded $4f$ electrons are not strongly affected. The position of the $5d$ levels can change by tens of thousands of wavenumbers from one compound to another. The centroid shift is a lowering in energy of the $5d$ levels of the activator ion due to a decrease of the inter-electron repulsion. This stabilization has been linked to the polarizability of the surrounding anion ligands and covalency of the crystal. The centroid shift will increase with increasing anion polarizability and decreasing average cation electronegativity[19]. As the degree of covalency between the activator ion and surrounding anions increases, the stronger interaction causes the d-orbitals of the activator ions to shift to be stabilized. This process is similar to the nephelauxetic effect described by Jørgenson[23]. Nitride compounds in particular, produce a larger centroid shift than corresponding oxide compounds, and oxide compounds a larger shift than fluoride compounds.

The second effect, crystal field splitting, refers to the difference in energy between the highest and lowest $5d$ levels, and is again an effect of the host crystal. The magnitude of the crystal field splitting depends on the bond lengths from the activator ion to the coordinating anions, molecular orbital overlap or

17

degree of covalency between the activator ion and its ligands, the coordination environment, and the symmetry of the activator site. Equation 1.1 relates the effect of bond length on the energy level separation[24], Dq

$$Dq = \frac{Ze^2r^4}{6R^5} \qquad (1.1)$$

where Z is the charge or valence of the anion, e is the charge of an electron, r is the radius of the d-wavefunction, and R is the bond length. As the bond lengths, or polyhedral volume, of the activator ion decreases, the crystal field splitting increases.

The interaction between molecular orbitals of neighboring anions causes the d-orbitals of the activator ion to hybridize, creating bonding orbitals at lower energies and antibonding orbitals at higher energies. As the degree of covalency increases, as in the nephelauxetic effect described above, both the bonding and antibonding orbitals are displaced to lower energies, but not necessarily by the same amount. This may cause the crystal field splitting to either increase or decrease. The coordination geometry also affects the crystal field splitting of the $5d$ levels. Comparing five different coordination geometries, Dorenbos has determined that the crystal field splitting tends to be largest for octahedral coordination, followed by cubic, and dodecahedral coordinations. The smallest

crystal field splittings are found for tri-capped trigonal prisms and cuboctahedral coordinations.[25]

Furthermore, it has been shown by Wu, Gundiah, and Cheetham, that distortion of the activator ion site may also affect the crystal field splitting.[21] In this work, optical and structural data for solid solutions of the regular garnet $Y_3Al_{5-x}Ga_xO_{12}$:Ce ($0 \leq x \leq 5$) and the inverse garnet $Mg_3Y_{2-y}Gd_yGe_{3-z}Si_zO_{12}$:Ce ($0 \leq y \leq 2$, $z = 0$, 1) were compared. The regular garnet solid solution showed a decrease in the maximum excitation and emission wavelength when the lattice parameter increased, as expected from Equation 1.1. Conversely, the inverse garnets showed a relatively constant maximum excitation wavelength and a large increase in the maximum emission wavelength when the lattice parameter increased. The coordination of the activator ion site in garnets can be described as a distorted cube with four longer and four shorter Ce$-$O distances. Examining this coordination environment, the ratio d_{88}/d_{81} can be used to characterize the degree of distortion from the cubic symmetry of the lanthanide ion site, where d_{88} is defined as the O$-$O distance shared between two adjacent lanthanide sites and d_{81} is defined as the edge of a lanthanide site that connects a tetrahedral vertex to an octahedral vertex. Analyzing the relationship between this distortion and the shift in maximum excitation and emission wavelength, the unexpected increase of the maximum

emission wavelength in the inverse garnets can be attributed to the increasing distortion of the activator ion site.

Another effect of the host crystal on the energetics of the activator ion can be seen in the Stokes shift. The energy required to excite an electron from the $4f$ level to the $5d$ level in an activator ion is greater than the energy emitted during the transition from the excited state to the ground state. This difference in energy is known as the Stokes shift. Once an electron is excited to the $5d$ level, the surrounding lattice relaxes to new equilibrium positions due to coupling of the $5d$ electron with phonons. This creates an effective lowering of the energy difference between the $5d$ and $4f$ levels in the excited state. Since the Stokes shift requires interactions with phonons, this is again a property that is dictated by the host crystal.

1.3.3 Thermal and lifetime effects

Although nearly all rare-earth ions can be used as activators in phosphors, the relative position of their energies with respect to the host crystal bandgap will determine whether the activator can down-convert light or if emission is quenched by transfer to the host crystal conduction band. If the excited state energy of the rare-earth is near the conduction band of the host material, the

probability of photoionization or charge transfer becomes high, greatly diminishing the quantum efficiency. This can be avoided by choosing a host material that has a bandgap in the UV, far from the activator absorption energy, or by localizing the excited state charge. This can be done with Ce^{3+}, for example, by stabilizing the $+3$ state, or effectively giving Ce a positive charge.[26] Although the energy of the $5d$ band does not vary as widely with the number of electrons belonging to the rare earth ion, the $5d$ energy level changes enough to significantly alter the probability of non-radiative transitions. One primary mechanism for non-radiative transitions is thought to be thermal promotion of the $5d$ electron to the conduction band of the host crystal,[27] others purport $5d-4f$ crossover as another mechanism.[28] Regardless of the mechanism, phonons are needed to bring the excited activator to a point where non-radiative processes can happen. In most hosts, the $5d$ levels from La to Gd lie at nearly the same energy, regardless of the rare earth ion. As the rare earth ion changes along the Lanthanide series from Gd to Yb, the $5d$ level increases in energy by about 0.5 eV,[29] decreasing the required energy to promote an excited electron in the $5d$ state to the conduction band. This decreases the probability of radiative transitions greatly, and is likely a reason why Eu^{2+} is used more frequently than Yb^{2+} in phosphor compounds, in addition to the difficulty of stabilizing the divalent state Yb^{2+}.

The human eye can detect temporal changes in light down to about 0.1 s.[30] Anything longer than 0.1 s is typically deemed phosphorescence, whereas decay constants shorter than 0.1 s are called luminescence. For general lighting applications, a short decay time is desirable. Activator ions decay according to an exponential function, and the number of characteristic decay times that are needed to model the data typically indicates the number of emitting sites. Transitions between $4f$ levels have long decay times, on the order of μs to ms, because they are electric dipole forbidden. Transitions between $4f$ and $5d$ levels are on the order of 10 ns, due to the dipolar allowed (spin and parity allowed, since both states are doublets)[31] nature of the transition. The decay from higher-level $5d$ sites to the lowest-energy $5d$ site is on the order of 1 ns,[32] much faster than the $5d$ to $4f$ relaxation. The fast decay of $5d$ to $5d$ relaxation is due to the strong lattice coupling of the electron, and means that the emission will always come from relaxation of the lowest $5d$ state to the $4f$ ground state. Of all the rare earth activators, Ce^{3+} has the fastest radiative recombination, typically on the order of 10 ns. Eu^{2+} has decay times that are $20-30$ times slower than Ce^{3+}, due to the much larger degeneracy of the excited $4f^6\,5d^1$ state of Eu^{3+} compared with the $4f^0\,5d^1$ excited state of Ce^{3+}.[33] Allowed transitions such as these typically do not have a temperature dependence. However, as temperature is increased and non-radiative mechanisms increase in

frequency, the measured decay time shortens. Measurement of the decay time with temperature is in fact a better way to estimate the intrinsic temperature quenching of a phosphor than emission intensity, since the emission intensity is also affected by lower absorption at increased temperatures.[34]

1.3.4 Structural rigidity of phosphor hosts

Efficient phosphor performance, meaning a high photoluminescence quantum yield (Φ), requires the Ce^{3+} ion to be hosted in a rigid crystal structure. This is particularly important when the phosphor is operated at slightly elevated temperatures, as is becoming conventional in high brightness, phosphor-converted white solid-state light-emitting diodes. In the solid-state, it is often difficult to identify which compounds are more rigid than others by simply comparing their crystal structures. For example, the YAG crystal structure contains two sublattices, one composed of AlO_4 tetrahedra and AlO_6 octahedra, and a second of Y^{3+} ions. These networks lead to interpenetrating, three-dimensionally connectivity that will no doubt make YAG very rigid. However, the connectivity of other known oxide phosphor hosts such as the yttrium silicates, Y_2SiO_5 and β-$Y_2Si_2O_7$, (apart from the SiO_4 tetrahedra) are not self-evident, making a comparison of the structures difficult. A more tractable method for determining rigidity, and in

turn the degree of connectivity, is through the Debye temperature (Θ_D) of the host crystal. A larger value indicates a structure is not only (vibrationally) rigid but also likely highly connected.

The Debye temperature has recently been introduced as a measure of structural rigidity in phosphor hosts.[35] The higher the Debye temperature of a material, more energy is needed to activate the highest energy phonon mode, and the more rigid a structure is. It was found that he Debye temperature (Θ_D) of the un-doped host crystal structure, which is readily calculated using *ab-initio* methods within the quasi-harmonic approximation, is a useful proxy for structural rigidity. Θ_D is found here to correlate well with the experimentally measured Φ for a number of Ce^{3+} phosphors.[35] The Debye temperature may also used as a proxy to rapidly screen for new potential phosphor host materials using density functional theory (DFT) to estimate the Debye temperature. It is also important to consider the band gap of the host compound, which must be large enough to accommodate the Ce^{3+} $4f$ to $5d$ transition. Highly rigid structures typically have strong orbital overlap, leading to large band dispersion and small band gaps. When considering phosphor materials, band gaps must be large enough to accommodate the electronic transitions of the activator ions to prevent excitation into the conduction, which will decrease PLQY and promote thermal quenching mechanisms.

Bond valence sum (BVS) analysis can be used as another measure of structural rigidity in phosphor hosts. Bond valence is a measure of the strength of a bond and when summed over all bonds to a cation should equal the valence of the cation. BVS is therefore a measure of the over- or under-bonded nature of a structure. We have found that structures with more ideal bonding networks with BVS closer to the ideal value create a more rigid structure which may affect optical properties of phosphors. One such study has found that for the orthosilicate solid-solution phosphor $Sr_xBa_{2-x}SiO_4$:Eu^{2+}, intermediate compositions possess higher resistance to thermal quenching of the photoluminescence due a more optimized bonding network caused by site mixing of the Sr^{2+} ions and Ba^{2+} ions leading to higher structural rigidity to prevent non-radiative recombination.[36]

1.4 Environmental life cycle assessment and resource considerations

As new technologies emerge new areas of research are pursued, we must also begin to take into account environmental impacts of such. Along with in-depth life cycle analyses of materials and products, rapid assessment of the environmental impacts can be a useful tool for guiding early stage research and the

choice of materials to be used. The early assessment of the environmental and resource impacts of novel chemicals and materials requires new methods of predicting environmental impacts of those materials in products based on limited information. We have begun to explore, develop, and implement proxies that can be used in this manner. The Herfindahl-Hirschman Index (HHI) has previously been used as a metric for understanding the supply risk of elements. The supply risk is determined by factors including crustal abundance of elements, global production, reserves, and use. HHI takes into account geopolitical influence over materials supply and price, which is evidenced in the market concentration. It has been shown previously for several metals, and more recently for thermoelectric materials, that the HHI can be used to evaluate the practicality of certain material combinations.[37] Considering HHI and elemental scarcity values can allow for evaluation of the supply risk of different materials and help guide research and product development in an environmentally conscious manner.

1.5 Overview

As new lighting technologies emerge, the materials used must also evolve. With solid-state lighting devices moving into the high-power regime, choice of

phosphor materials may change and the importance of certain properties become intensified.[8, 15] Material selection therefore depends on a number of different phosphor properties, some of which are known and understood, some of which have been reported in the literature, and others which have yet to be thoroughly explored. This thesis will examine the structure–composition–property relationships in a number of known and newly developed phosphor materials for solid-state white lighting applications, gaining a deeper understanding of the underlying features that lead to observed optical properties in an effort to guide the search for improved materials that meet the demands of current and future technologies and allow for the emergence of new research pathways.

The present work will address the following objectives:

1. Development of a green-yellow emitting oxyfluoride solid-solution phosphor $Sr_2Ba(AlO_4F)_{1-x}(SiO_5)_x$:$Ce^{3+}$ for thermally stable, high color rendition solid-state white lighting.

2. Identification and tuning of luminescent properties through solid-solution in $(Ba_{1-x}Sr_x)_9Sc_2Si_6O_{24}$:$Ce^{3+}$,$Li^+$. Additionally, an efficient, thermally stable blue-green phosphor, $Ba_9Y_2Si_6O_{24}$:Ce^{3+}, is identified and color tuning explored through the solid-solution $Ba_9(Y_{1-y}Sc_y)_{1.94}Ce_{0.06}Si_6O_{24}$.

3. Structure–composition relationships and optical properties are explored in the newly developed cerium-substituted $(Sr,Ba)_3(Y,La)(BO_3)_3$ borate phosphors.

4. A data-driven discovery of energy materials reveals the efficient $BaM_2Si_3O_{10}:Eu^{2+}$ (M = Sc, Lu) phosphors for application in solid-state white lighting.

5. Consequences of optimal bond valence on structural rigidity are explored and linked to the improved luminescence properties in $Sr_xBa_{2-x}SiO_4:Eu^{2+}$ orthosilicate phosphors.

6. An in-depth analysis of the average and local structure, Debye temperature, and structural rigidity in some oxide compounds related to phosphor hosts is performed.

7. Improved color rendition in solid-state white lighting is realized through the use of quantum dots.

8. Efficient and stable laser-driven white lighting is identified as a viable option for high-power solid-state white light sources.

Impact: The in-depth understanding of the structure–composition–property relationships in phosphor materials will guide the development of new, improved

materials for energy efficient solid-state white lighting. Our studies of the optical and structural properties provide insight into the mechanisms leading to high efficiency, color tunability, thermally stable luminescence, and highly rigid structures. New phosphor systems have been developed and new light generation strategies including quantum dots and laser-based lighting have been explored.

Chapter 2

A green-yellow emitting oxyfluoride solid-solution phosphor $Sr_2Ba(AlO_4F)_{1-x}(SiO_5)_x$:$Ce^{3+}$ for thermally stable, high color rendition solid-state white lighting

A near-UV excited, oxyfluoride phosphor solid solution $Sr_{1.975}Ce_{0.025}Ba(AlO_4F)_{1-x}(SiO_5)_x$ has been developed for solid state white lighting applications. An examination of the host lattice, and the local structure around the Ce^{3+} activator ions through a combination of density functional theory, synchrotron X-ray and neutron powder diffraction and total scattering, and electron paramagnetic resonance, points to how chemical substitutions play a crucial role in tuning the optical properties of the phosphor. The maximum emission wavelength can be tuned from green (λ_{em} = 523 nm) to yellow (λ_{em} = 552 nm) by tuning the composition, x. Photoluminescent quantum yield is determined to be 70±5% for some of the examples in the series. Excellent thermal properties were found for the x = 0.5 sample, with the photoluminescence intensity at 160 °C only decreased to 82% of its room temperature value. Phosphor-converted LED devices fabricated using an InGaN LED (λ_{max} = 400 nm) exhibit high color rendering white light with R_a = 70 and a correlated color temperature near 7000 K. The value of R_a could be raised to 90 by the addition of a red component, and the correlated color temperature lowered to near 4000 K.

2.1 Introduction

The phosphor material used in solid state white lighting devices greatly affects the overall device, including the luminous efficacy, color rendition, thermal and chemical stability, and the color quality of the white light.[5, 6] Highly efficient phosphors are needed to convert the LED emission with little or no energy loss, apart from what is inevitably lost to the Stokes shift. Specific luminescence properties are needed to produce an optimal white light with a high color rendering index (R_a). These properties include strong absorption in the region of the LED emission and a broad emission profile across all regions of the visible spectrum. The thermal stability of the phosphor is also important, since thermal quenching of phosphor luminescence can lead to decreased efficiency and color instability at the operating temperatures of modern devices.

The most commonly used phosphor for solid state white lighting, is cerium-doped yttrium aluminum garnet $Y_3Al_5O_{12}$ (YAG:Ce^{3+}), developed by Blasse and coworkers in 1967.[11, 12] Its widespread use stems from its strong absorption of blue light, ideal for use with an InGaN LED, and its very efficient yellow emission (QY $\approx$ 85% or greater) in addition to excellent chemical stability. Yet YAG:Ce^{3+} is not ideal as it suffers from low color rendition due to weak luminescence in the red spectral region, and from thermal quenching[34]

at elevated temperatures. A variety of other phosphors have been developed including oxides,[39–41] oxyfluorides,[42, 43] oxynitrides[13, 44, 45] and nitrides.[46–49] Some promising phosphor candidates include $LaSr_2AlO_5:Ce^{3+}$ ($LSA:Ce^{3+}$)[39] and the isostructural $Sr_2BaAlO_4F:Ce^{3+}$ ($SBAF:Ce^{3+}$)[42] recently developed by our group. $SBAF:Ce^{3+}$ is a highly efficient phosphor with a quantum yield approaching 100% and good thermal properties. However, the emission from $SBAF:Ce^{3+}$ is too blue to create a suitable white light. Furthermore, it degrades upon contact with moisture. It was shown by Im *et al.*[43] that the oxyfluoride $Sr_3AlO_4F:Ce^{3+}$ compound (isostructural with $SBAF:Ce^{3+}$) exhibited increased moisture stability, and a red shift in emission when introduced into a solid solution with the nearly isostructural oxide compound, $Sr_3SiO_5:Ce^{3+}$.

In this contribution, we report the green-to-yellow emitting phosphor solid solution, $Sr_2Ba(AlO_4F)_{1-x}(SiO_5)_x:Ce^{3+}$ comprising Sr_2BaAlO_4F as the oxyfluoride end-member and the nearly isostructural Sr_3SiO_5 as the oxide end member. The structural, optical, and thermal properties have been examined, along with the quality of white LEDs fabricated using the solid solution phosphor in conjunction with a near-UV InGaN LED chip. The solid solution strategy suggested here greatly improves certain key properties of these promising oxyfluoride phosphors.

2.2 Experimental

Samples of $Sr_{1.975}Ce_{0.025}Ba(AlO_4F)_{1-x}(SiO_5)_x$ ($x = 0.1, 0.2, \ldots 0.9$) were prepared by mixing stoichiometric amounts of $SrCO_3$ (99.5% purity, Materion), CeO_2 (99.9% purity, Cerac), $BaCO_3$ (99.9% purity, Cerac), BaF_2 (99% purity, Cerac), Al_2O_3 (high purity, sub-micron SM8, Baikowski) and SiO_2 (amorphous fumed, Degussa Aerosil TT600). Powders were intimately mixed by grinding in an agate mortar with acetone for approximately 30 min., then pressed into pellets. Pellets were placed on sacrificial powder in alumina crucibles and heated at 1350 °C for 4 h in a reducing atmosphere of $5\%H_2/95\%N_2$ with heating and cooling ramps of 10 h.

Density functional theory (DFT) calculations were performed using the Vienna *ab initio* Simulation Package (VASP)[50–53] in order to predict site preferences for the Ce^{3+} ion in the host oxyfluoride compound. Projector augmented waves (PAW)[54, 55] were employed to describe the atomic cores and the valence electrons were described using plane-waves. The exchange-correlation energy was calculated using the generalized gradient approximation (GGA) functional within the Perdew-Burke-Ernzerhof (PBE) formulation.[56, 57] Calculations for bulk Sr_2BaAlO_4F and for the substitutions were performed on the conventional unit cell, using a 4×4×4 Monkhorst-Pack **k**-point sampling. A cutoff

energy of 550 eV was used in all calculations. Relaxations were deemed to have converged when the forces on all the atoms were less than $0.01\,\mathrm{eV\,\mathring{A}^{-1}}$.

Synchrotron X-ray diffraction data were collected at the 11-BM instrument at the Advanced Photon Source (APS), Argonne National Laboratory using a wavelength of $\lambda = 0.424629\,\mathring{A}$. Rietveld analysis was carried out using the XND Rietveld code.[58]. Time-of-flight neutron powder diffraction data was collected on the Nanoscale Ordered Materials Diffractometer (NOMAD) at the Spallation Neutron Source (SNS), Oak Ridge National Laboratory. Least-squares refinement was performed on the pair-distribution function (PDF) to obtain average structure information. Electron paramagnetic resonance (EPR) spectra were collected on powder samples using a Bruker X-Band EPR spectrometer (ν = 9.486 GHz), equipped with a Helium flow cryostat. Samples were placed in quartz tubes and data was acquired at 10 K.

Photoluminescence (PL) spectra were obtained on a Perkin Elmer LS55 spectrophotometer equipped with a xenon lamp. Spectra were measured by mixing the sample with KBr ($\geq$99% purity, FT-IR grade, Sigma-Aldrich) in a 1:10 ratio of sample to KBr and pressing into a pellet. Photoluminescence quantum yield (PLQY) was measured using phosphor powders encapsulated in silicone resin (GE Silicones, RTV-615) and deposited on transparent quartz substrates (Chemglass). The samples were placed inside a Spectralon™-coated integrating

sphere (6 inch diameter, Labsphere) and excited using 405 nm light generated by a solid-state laser (Crystalaser DL-405-40-S) operated at a power between 1 mW and 2 mW. The light was collected by a quartz lens and directed onto a calibrated Si photodiode (Newport 818-UV) using filters (Omega Filters) to collect respective wavelengths. Data collection and processing procedures were conducted similar to those described by Greenham *et al.*[59] Temperature dependence of the photoluminescence was measured in the temperature range from 77 K to 493 K using a home-built fluorimeter and incorporating a cryostat for low temperature measurements and a heating stage for high temperature data collection.

Electroluminescence spectra, (CIE) chromaticity coordinates, and color rendering index (R_a) were collected by incorporating the samples into a device. A "capping" strategy was used, described previously by our group,[43, 60] in which the phosphor powder (5 wt% to 6 wt%) was mixed into silicon resin (GE Silicones, RTV-615) and molded into a cap that was then placed over a silicone encapsulated InGaN LED chip (λ_{max} = 400 nm, 8 mm, FrozenCPU). A commercially available red phosphor (1 wt%) from Mitsubishi Chemical Corporation was also added for select measurements. The measurements were conducted in an integrating sphere using a forward bias current of 20 mA.
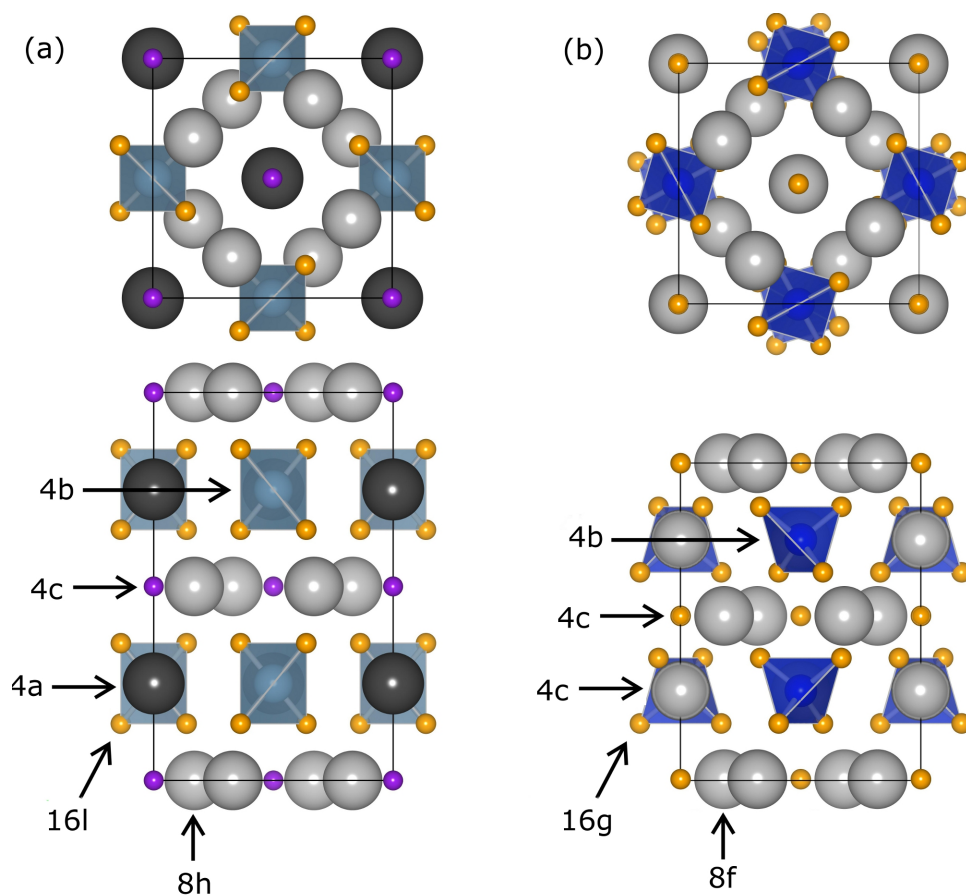
Figure 2.1: Crystal structures of (a) Sr_2BaAlO_4F and (b) Sr_3SiO_5 viewed along the c-axis (top) and the a-axis (bottom) with labeled Wyckoff positions. Sr^{2+}/Ba^{2+} (grey, black) and Al^{3+}/Si^{4+} (blue) ions occupy similar sites in both end members, while the O^{2-} (orange) and F^- (purple) ions have slightly different positions leading to a lower symmetry structure for Sr_3SiO_5. Reproduced with permission from reference [38], ©2012 Royal Society of Chemistry.

Table 2.1: Comparison of effective ionic radii shows that Ce^{3+} can potentially be substituted into two different crystallographic sites in both the SBAF and SSO structures, replacing Sr^{2+} and/or Ba^{2+} ions.

structure	site	CN	effective ionic radii (Å)		
			Sr^{2+}	Ba^{2+}	Ce^{3+}
SBAF	$8h$	8	1.26	1.42	1.143
SSO	$8f$				
SBAF	$4a$	10	1.36	1.52	1.25
SSO	$4c$				

2.3 Results and Discussion

Sr_2BaAlO_4F (SBAF) crystallizes in the tetragonal space group $I4/mcm$ (No. 140) while the nearly isostructural Sr_3SiO_5 (SSO) crystallizes in the tetragonal space group $P4/ncc$ (No. 130). In the SBAF structure, Sr^{2+} ions reside in the $8h$ site, Ba^{2+} ions the $4a$ site, Al^{3+} ions the $4b$ site, O^{2-} ions the $16l$ site and F^- ions the $4c$ site.[61] In the SSO structure, Sr^{2+} ions reside in the $8f$ and $4c$ sites, Si^{4+} ions the $4b$ site and O^{2-} ions the $16g$ and $4c$ sites.[62] Figure 2.1 portrays the structural differences between the two end members, highlighted by the tilted SiO_4 tetrahedra in the SSO structure which lends this compound to the lower symmetry space group. In both structures, there are two sites that Ce^{3+} can be substituted into based on ionic size and coordination number,[63, 64] summarized in Table 2.1. The first is the $8h$ site in the SBAF structure and the $8f$ site in the SSO structure, which is coordinated with six oxygen and two

fluorine atoms, in which the slightly smaller Ce^{3+} ion can reside. The second is the $4a$ site in the SBAF structure and the $4c$ site in the SSO structure, which is coordinated with eight oxygen and two fluorine atoms, in which the smaller Ce^{3+} ion can also reside.

DFT was used to calculate site preference for substituting La^{3+} into the SBAF lattice. La^{3+} substitution was chosen to model Ce^{3+} substitution, since they are similar in ionic size and charge, (CN = 8, $r_{eff,Ce^{3+}} = 1.143$ Å, $r_{eff,La^{3+}} = 1.160$ Å; CN =10, $r_{eff,Ce^{3+}} = 1.25$ Å, $r_{eff,La^{3+}} = 1.27$ Å) and La^{3+} does not require calculations of f-electrons, as Ce^{3+} would. Two types of substitutions were examined: La^{3+} substituting into the $8h$ site in place of Sr^{2+} and La^{3+} substituting into the $4a$ site in place of Ba^{2+}. Charge compensation for replacing a 2+ species with La^{3+} was taken into consideration and balanced, through F^-/O^{2-} ratios, as we would expect to occur. Total ground state energy calculations were performed for bulk SBAF, and the two substitution cases. The conventional unit cell was used, corresponding to 4 formula units and a total of 36 atoms. The first substitution renders the formula $Sr_{1.75}BaLa_{0.25}AlO_{4.25}F_{0.75}$ and the second $Sr_2Ba_{0.75}La_{0.25}AlO_{4.25}F_{0.75}$. To determine the lowest energy ground state for the unit cells with substitutions, ionic positions, unit cell volume and shape were relaxed.

Total energies for bulk SBAF and substitutions are presented in Table 2.2.

Table 2.2: Ground state energies *per* conventional unit cell for the SBAF structure without substitution, and with one La^{3+} ion per unit cell substituted into various crystallographic sites, calculated using density functional theory.

Wyckoff position	substitution	total energy per unit cell (eV)
bulk SBAF		-233.37
$8h$	La_{Sr}	-239.17
$4a$	La_{Ba}	-239.03
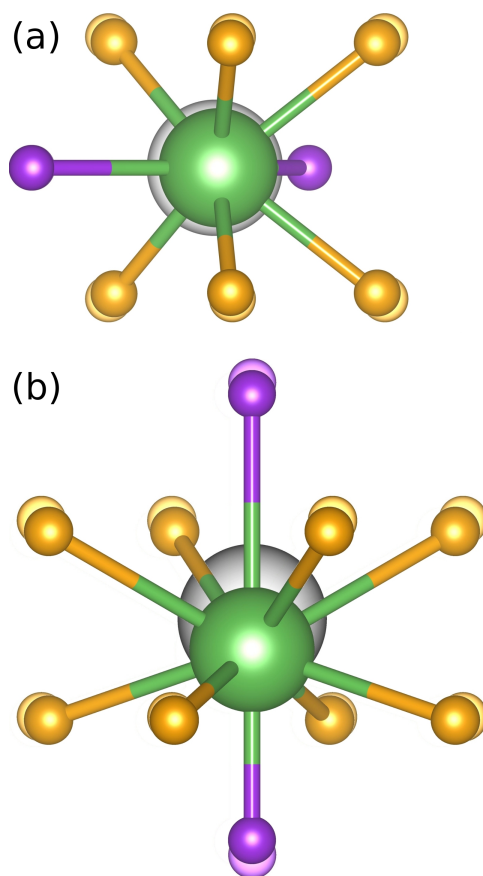
Figure 2.2: Ionic displacements of the coordinating ions when La^{3+} substitutions are made in place of (a) Sr^{2+} in the $8h$ site and (b) Ba^{2+} in the $4a$ site, where the substituted La^{3+} ions are represented by green spheres and the translucent ions represent the ions in the bulk structure prior to substitutions. Reproduced with permission from reference [38], ©2012 Royal Society of Chemistry.

Both types of substitutions result in a larger negative total energy, indicating the substitution is favorable and will occur. Figure 2.2 shows the ionic displacements of the coordinating ions that take place when La substitutions are made. The substitution of La^{3+} in the $8h$ site in place of Sr^{2+} is slightly more energetically favorable than La^{3+} in the $4a$ site in place of Ba^{2+}, but only by $0.14\,eV$. From this, we can expect Ce^{3+} substitution in SBAF to occur on both sites, with a slightly higher preference for the Sr^{2+} $8h$ site. This agrees well with experimental data obtained by Im $et\ al.$[42] of the emission spectrum $Sr_{1.975}BaCe_{0.025}AlO_4F$ at $77\,K$ deconvoluted into four Gaussian curves, corresponding to Ce^{3+} occupying two distinct sites and a slightly higher preference for Ce_{Sr} substitution considering the Ce^{3+} ion is closer in size to the Sr^{2+} ion than the Ba^{2+} ion.

Synchrotron X-ray diffraction patterns of prepared samples show all are nearly single phase compounds similar to both the SBAF and SSO compounds. The small amount of impurities are likely $(Sr,Ba)F_2$ and $(Sr,Ba)_2SiO_4$ and do not appear to contribute to the luminescence. Ce^{3+}-substituted $(Sr,Ba)_2SiO_4$ results in weak blue emission, which we have not observed.[65] For all compositions, the amount of substituted Ce^{3+} was held constant corresponding to the optimal amount found for $SBAF:Ce^{3+}$,[42] rendering the formula $Sr_{1.975}Ce_{0.025}Ba(AlO_4F)_{1-x}(SiO_5)_x$. Across the solid solution series, increasing values of x correspond to Si^{4+} ions (CN = 4, $r_{eff,Si^{4+}} = 0.26\,Å$) replacing Al^{3+}
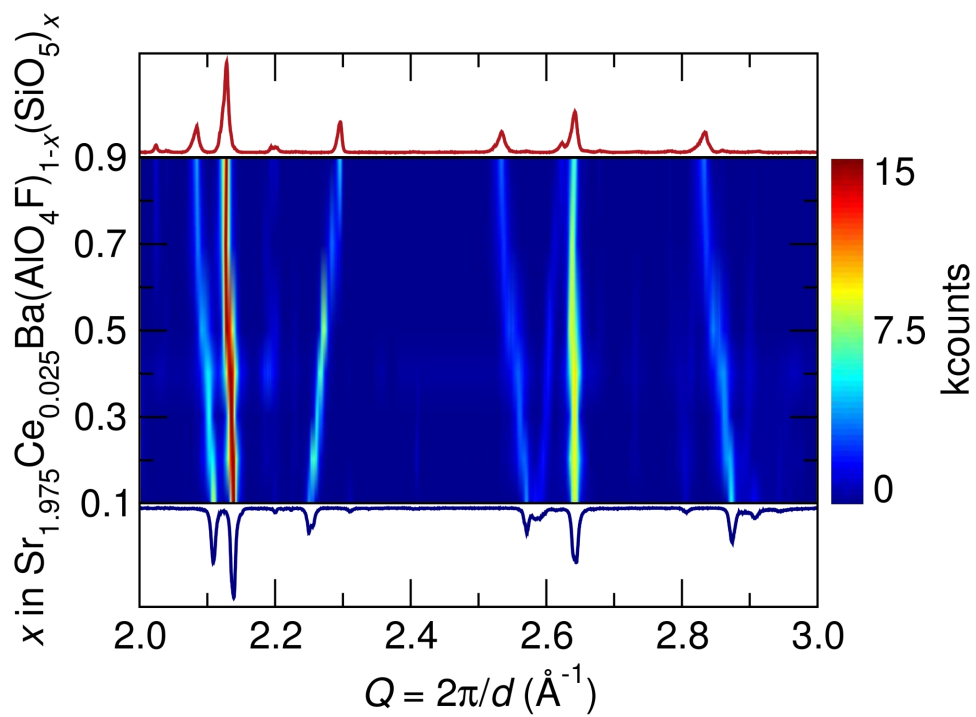
Figure 2.3: Portion of the synchrotron X-ray diffraction patterns, collected at room temperature, for the $Sr_{1.975}Ce_{0.025}Ba(AlO_4F)_{1-x}(SiO_5)_x$ series as a function of x clearly illustrates the structural evolution across the solid solution as demonstrated by the shifts in diffraction peak positions. Reproduced with permission from reference [38], ©2012 Royal Society of Chemistry.
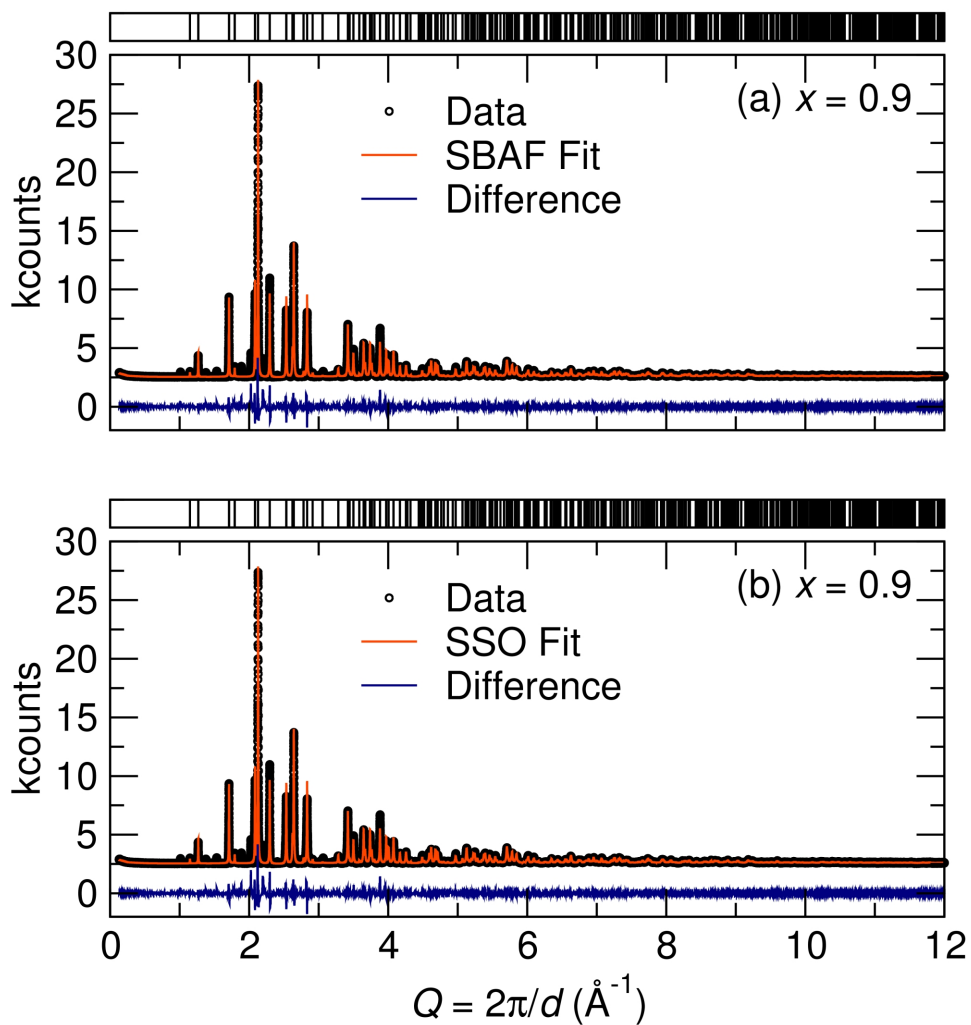
Figure 2.4: Rietveld refinements of synchrotron X-ray diffraction data collected at room temperature for the $x = 0.9$ sample show good fits to both (a) the SBAF structure and (b) the SSO structure. This inability to distinguish the space group is likely due to the fact that the differences arise from displaced O^{2-} and F^- ions, neither of which influence X-ray scattering greatly. Reproduced with permission from reference [38], ©2012 Royal Society of Chemistry.
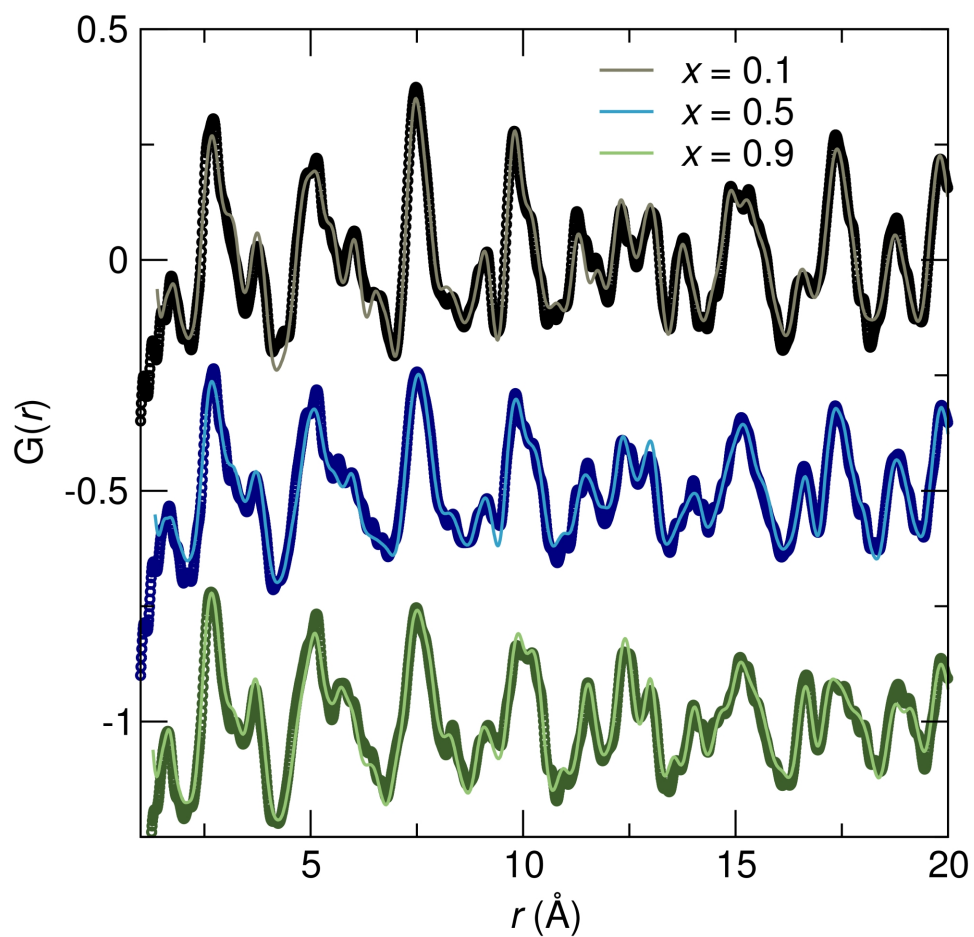
Figure 2.5: Refinements of neutron scattering PDF data collected at room temperature for the $x = 0.1$, $x = 0.5$, and $x = 0.9$ samples show changes in peak intensities across the solid-solution series, corresponding to changes in the average structure, as also seen in synchrotron X-ray diffraction data. Reproduced with permission from reference [38], ©2012 Royal Society of Chemistry.

ions (CN = 4, $r_{eff,Al^{3+}}$ = 0.39 Å) and simultaneously O^{2-} ions (CN = 6, $r_{eff,O^{2-}}$ = 1.40 Å) replacing F^- ions (CN = 6, r_{eff,F^-} = 1.33 Å). The diffraction patterns in Figure 2.3 illuminate the structural evolution as x increases. Rietveld refinements were conducted using both the SBAF structure and the SSO structure as models. Disorder between Sr^{2+} and Ba^{2+} in the $8h$ and $4a$ sites in the SBAF model and the $8f$ and $4c$ sites in the SSO model was considered due to similar ionic size and was included in refinements.[66] In further discussions, the Sr/Ba site with a multiplicity of 8 will be referred to as the Sr1/Ba1 site and the Sr/Ba site with a multiplicity of 4 the Sr2/Ba2 site in both structural models. Site disordering between O^{2-} and F^- was not considered since it has been found previously from NMR studies [43] that F^- resides in a single crystallographic site. Refinements yielded successful convergence with similar figures of merit for both the SBAF and the SSO structural models. Figure 2.4 shows the similarity in fit for the x = 0.9 sample using each model. This inability to distinguish the space group is most likely due to the fact that the differences arise from displaced O^{2-} and F^- ions, both are which are not sensitive to X-ray scattering techniques. Neutron scattering data was also collected for samples x = 0.1, x = 0.5, and x = 0.9, in an effort to enhance the structural model. Pair-distribution functions (PDF) were refined using a least-squares fitting method. Fits to the PDFs are shown in Figure 2.5, where the changing peak intensities

are indications of a change in the average structure as x increases. The PDFs fit well to both the SBAF and SSO structures, again arising from the similar neutron scattering lengths of oxygen (5.803 fm) and fluorine (5.654 fm). The structural parameters obtained from the PDF refinement agree well with the results from Rietveld refinement of the synchrotron X-ray diffraction data.

The shift in diffraction peaks in Figure 2.3 indicates changing lattice parameters, namely a linear increase in the a and b cell parameters and a decrease in the c cell parameter, shown in Figure 2.6. Lattice parameters for the $x = 0.1$ sample were determined to be $a = 6.9120(2)$ Å and $c = 11.1634(4)$ Å with $V = 533.31(2)$ Å^3 and for the $x = 0.9$ sample $a = 7.0127(1)$ Å and $c = 10.9486(3)$ Å with $V = 538.47(3)$ Å^3, and intermediate compounds varying linearly obeying the Végard law. Refined structural parameters for $x = 0.5$ fit to the SBAF structure and to the SSO structure are displayed in Table 2.3 and select interatomic distances in Table 2.4. The simultaneous expansion and contraction of the unit cell in different directions causes increased tilting of the $(Al,Si)O_4$ tetrahedra and greater distortion of the $(Sr,Ba)(O,F)_8$ and $(Sr,Ba)(O,F)_{10}$ polyhedra. A polyhedral distortion index,[67] D, can be defined as

$$D = \frac{1}{n} \sum_{i=1}^{n} \frac{\mid l_i - l_{av} \mid}{l_{av}} \tag{2.1}$$
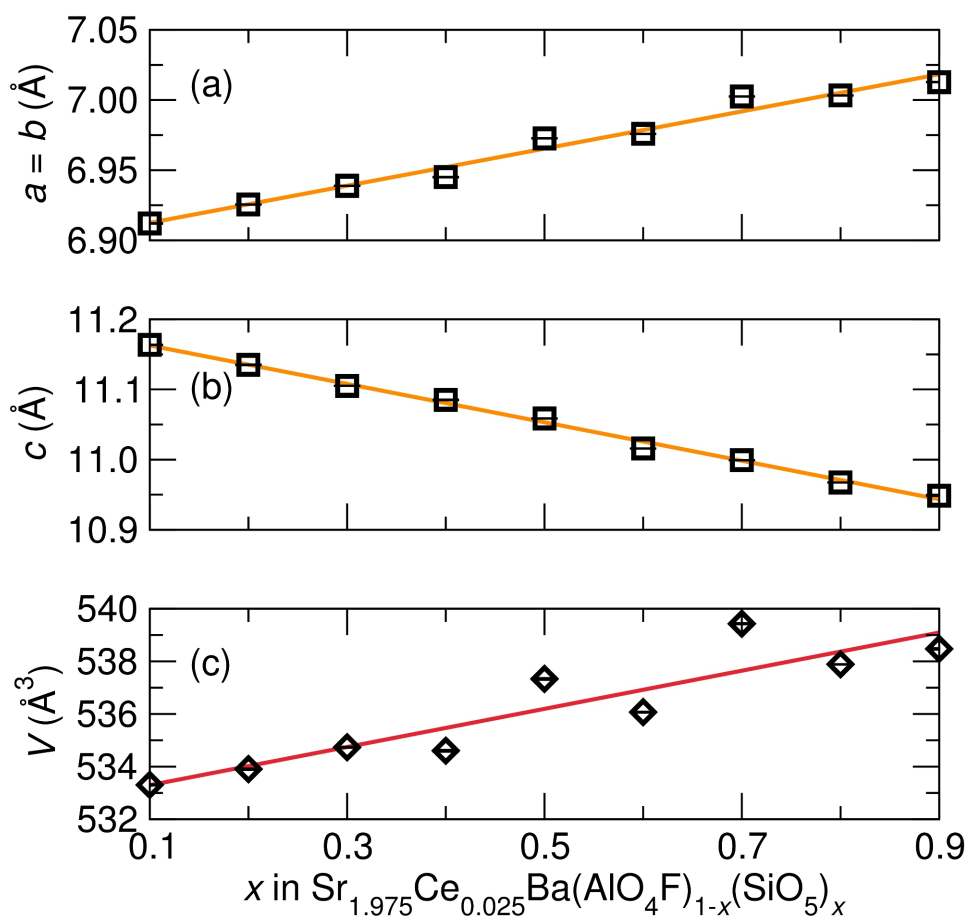
Figure 2.6: Unit cell parameters of $Sr_{1.975}Ce_{0.025}Ba(AlO_4F)_{1-x}(SiO_5)_x$ from Rietveld refinement of room temperature synchrotron X-ray diffraction data show (a) an expansion in the a lattice parameter and (b) a contraction in the c lattice parameter with (c) an overall increase in cell volume as x increases, reflecting the effects of the Al^{3+}/Si^{4+} and O^{2-}/F^- substitutions. Reproduced with permission from reference [38], ©2012 Royal Society of Chemistry.

Table 2.3: Refined atomic parameters for $Sr_{2.975}Ce_{0.025}BaAl_{0.5}Si_{0.5}O_{4.5}F_{0.5}$ ($x = 0.5$) determined by Rietveld refinement of powder synchrotron X-ray diffraction data collected at room temperature and using a fit to (a) the SBAF model and (b) the SSO model. The values in parentheses represent the average standard deviation.

atom	site	x	y	z	occupancy
		$Sr_{2.975}Ce_{0.025}BaAl_{0.5}Si_{0.5}O_{4.5}F_{0.5}{}^{a}$			
Sr1	$8h$	0.1758(1)	$x + \frac{1}{2}$	0	0.90(1)
Ba1	$8h$	0.1758	$x + \frac{1}{2}$	0	0.10
Sr2	$4a$	0	0	$\frac{1}{4}$	0.21(1)
Ba2	$4a$	0	0	$\frac{1}{4}$	0.79
Al	$4b$	0	$\frac{1}{2}$	$\frac{1}{4}$	0.5
Si	$4b$	0	$\frac{1}{2}$	$\frac{1}{4}$	0.5
O	$16l$	0.6324(4)	$x + \frac{1}{2}$	0.1494(4)	1
F	$4c$	0	0	0	1
		$Sr_{2.975}Ce_{0.025}BaAl_{0.5}Si_{0.5}O_{4.5}F_{0.5}{}^{b}$			
Sr1	$8f$	0.1750(1)	x	$\frac{1}{4}$	0.88(1)
Ba1	$8f$	0.1750	x	$\frac{1}{4}$	0.12
Sr2	$4c$	0	$\frac{1}{2}$	0.4992(7)	0.24(1)
Ba2	$4c$	0	$\frac{1}{2}$	0.4992(7)	0.76
Al	$4b$	0	0	0	0.5
Si	$4b$	0	0	0	0.5
O	$16g$	0.855(1)	0.121(1)	0.0985(4)	1
F	$4c$	0	$\frac{1}{2}$	0.250(5)	1

[a]Space group: $I4/mcm$ (No. 140), $Z = 4$, $a = 6.9726(2)$ Å, $c = 11.0586(4)$ Å,

$$V = 537.64(3) \, \text{Å}^3.$$

[b]Space group: $P4/ncc$ (No. 130), $Z = 4$, $a = 6.9698(2)$ Å, $c = 11.0611(4)$ Å,

$$V = 537.33(3) \, \text{Å}^3.$$

Table 2.4: Selected interatomic distances corresponding to active site polyhedra found in $Sr_{2.975}Ce_{0.025}BaAl_{0.5}Si_{0.5}O_{4.5}F_{0.5}$ ($x = 0.5$) using a fit to (a) the SBAF model and (b) the SSO model from Rietveld refinements of room temperature synchrotron X-ray diffraction data. The values in parentheses represent the average standard deviation.

atoms	distance (Å)
$Sr_{2.975}Ce_{0.025}BaAl_{0.5}Si_{0.5}O_{4.5}F_{0.5}{}^{a}$	
Sr1/Ba1–O	(×4) 2.728(3)
	(×2) 2.512(3)
Sr1/Ba1–F	(×2) 2.571(1)
Sr2/Ba2–O	(×8) 2.943(3)
Sr2/Ba2–F	(×2) 2.765(0)
$Sr_{2.975}Ce_{0.025}BaAl_{0.5}Si_{0.5}O_{4.5}F_{0.5}{}^{b}$	
Sr1/Ba1–O	(×2) 2.815(6)
	(×2) 2.666(6)
	(×2) 2.531(6)
Sr1/Ba1–F	(×2) 2.573(1)
Sr2/Ba2–O	(×4) 2.033(7)
	(×4) 2.829(7)
Sr2/Ba2–F	(×1) 2.78(6)
	(×1) 2.75(6)
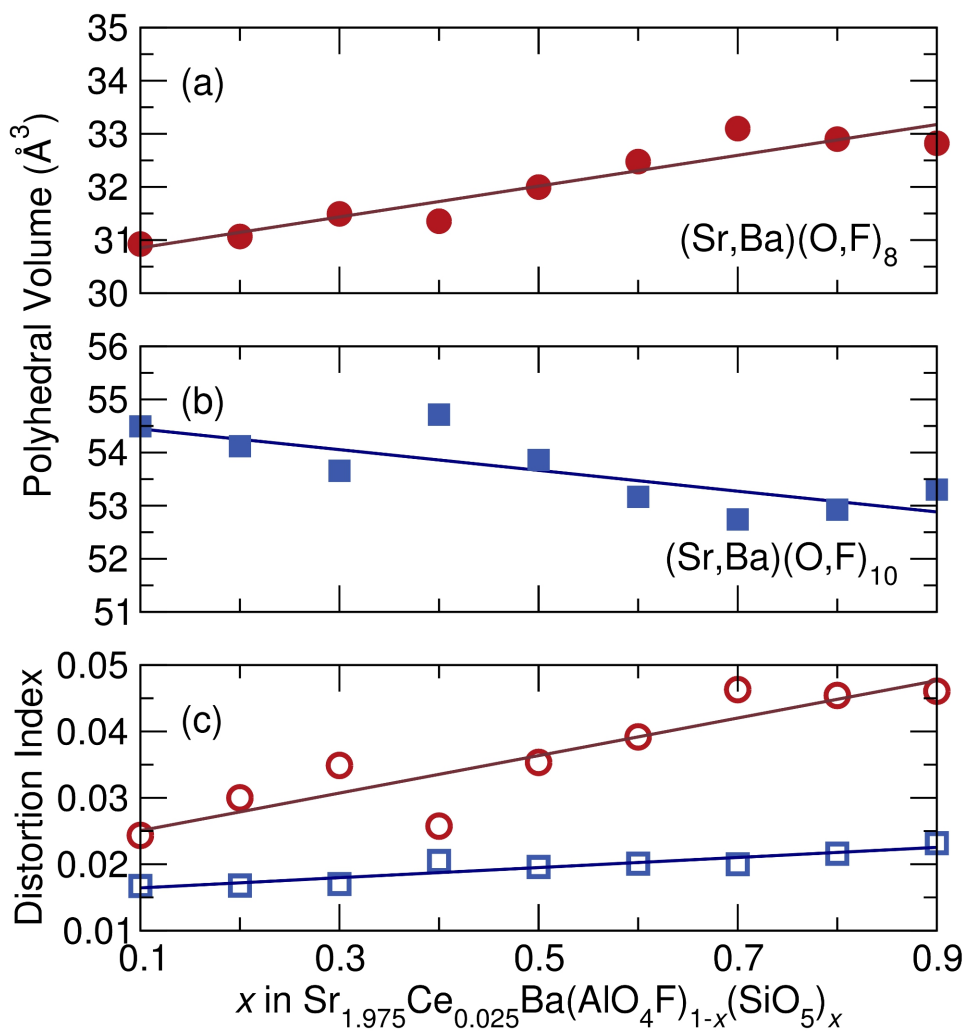
Figure 2.7: As x increases across the $Sr_{1.975}Ce_{0.025}Ba(AlO_4F)_{1-x}(SiO_5)_x$ solid solution series, the (a) $(Sr,Ba)(O,F)_8$ average polyhedral volume increases, the (b) $(Sr,Ba)(O,F)_{10}$ average polyhedral volume decreases, while the (c) polyhedral distortion of both sites increases as x increases, accounting for the experimentally seen red-shift in emission wavelength. Reproduced with permission from reference [38], ©2012 Royal Society of Chemistry.
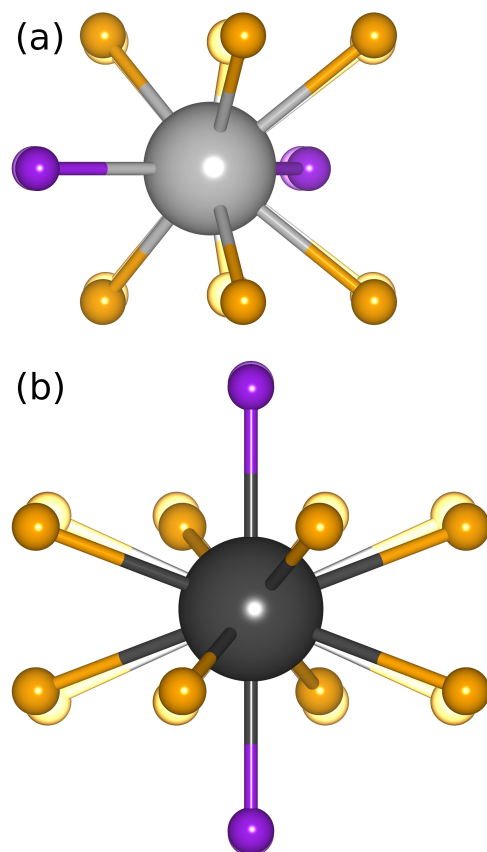
Figure 2.8: Increased distortion of the active site polyhedra, the origin of the red-shifted emission, as x increases across the $Sr_{1.975}Ce_{0.025}Ba(AlO_4F)_{1-x}(SiO_5)_x$ solid solution series can be seen by comparing (a) the Sr1/Ba1 site, viewed along the c-axis, and (b) the Sr2/Ba2 site, viewed along the a-axis, for compositions $x = 0.1$ (translucent spheres) and $x = 0.9$ (solid spheres). Reproduced with permission from reference [38], ©2012 Royal Society of Chemistry.

where l_i is the distance from the central atom to the ith coordinating atom and l_{av} is the average bond length. Figure 2.7 shows the changing polyhedral volume and distortion as x increases and Figure 2.8 depicts the distorted polyhedra for the $x = 0.1$ and $x = 0.9$ samples, obtained from fits to the SBAF structure model. Polyhedral volumes were calculated through the method outlined by Swanson and Peterson.[68] This distortion of the active sites where Ce^{3+} resides greatly affects the optical properties of the solid-solution phosphor, as discussed later in this paper.

Bond valence sums (BVS),[69] displayed in Figure 2.9, were calculated from refinements of synchrotron X-ray diffraction data using the SBAF model to again help determine the most favorable site for Ce^{3+}. The shorter bonds of the Sr1/Ba1 site result in a BVS of around 2 for Sr and Ce on the Sr1/Ba1 site, but a BVS of around 3 for Ba. This shows the valence state of $+2$ for Sr is satisfied on the Sr1/Ba1 site, but Ba is very over-bonded. This agrees with the refined occupancies for site mixing between Sr and Ba, with more Sr residing in the Sr1/Ba1 site (75%–80%) than in the Sr2/Ba2 site. Conversely, the BVS of Ba on the Sr2/Ba2 site is around 2, while that of Sr and Ce is closer to 1.25. This further supports Ba residing on the Sr2/Ba2 site and Sr on the Sr1/Ba1 site, since Sr would be very under-bonded on the Sr2/Ba2 site. Using the average structure Sr/Ba$-$O/F bond lengths from Rietveld refinement, Ce appears under-
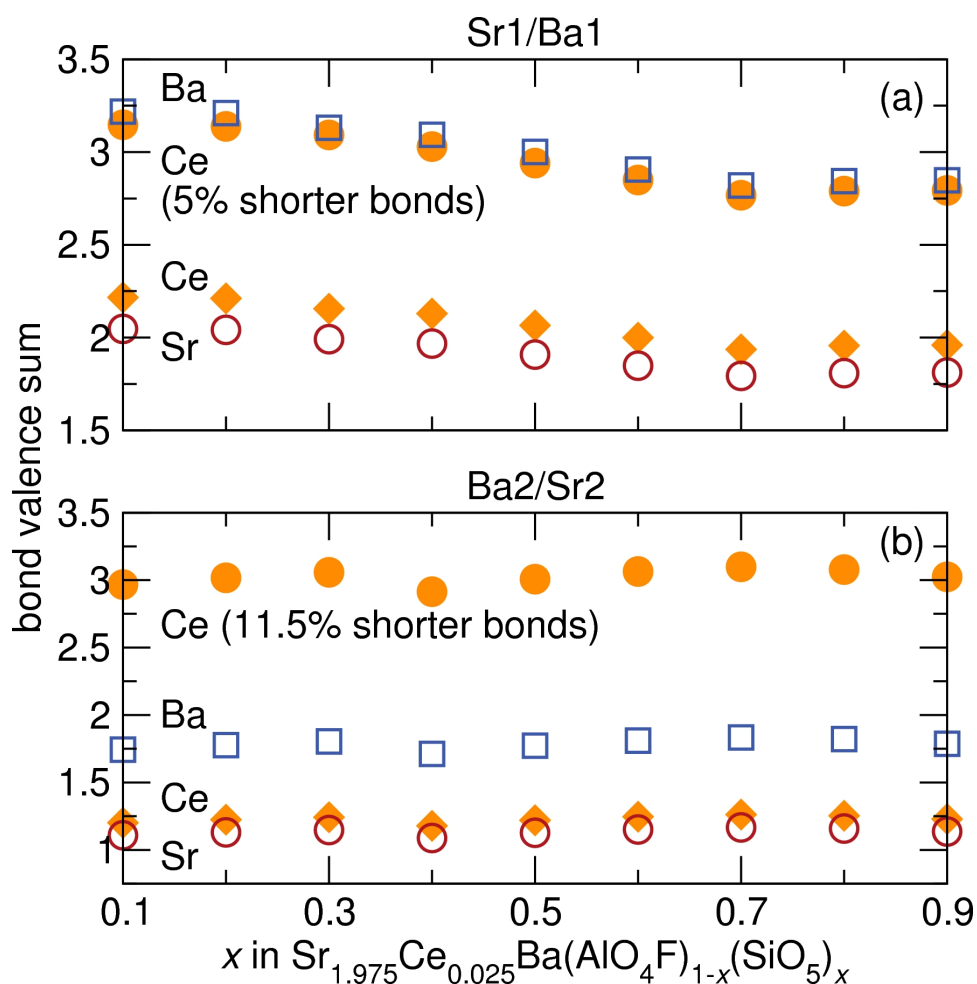
Figure 2.9: Bond valence sums of Ba, Sr, and Ce on (a) the Sr1/Ba1 site and (b) the Sr2/Ba2 site in $Sr_{1.975}Ce_{0.025}Ba(AlO_4F)_{1-x}(SiO_5)_x$, calculated using refined bond distances from synchrotron X-ray diffraction data, show Sr preferentially resides in the Sr1/Ba1 site, while Ba prefers the Sr2/Ba2 site. The BVS of Ce on both sites with slightly shorter bonds are shown, indicating Ce^{3+} is more easily incorporated into the Sr1/Ba1 site due to the smaller contraction in bond length required. Reproduced with permission from reference [38], ©2012 Royal Society of Chemistry.

Table 2.5: Components of the g-tensor from $10\,\text{K}$ powder EPR measurements of $Sr_{1.975}Ce_{0.025}Ba(AlO_4F)_{1-x}(SiO_5)_x$ shown in Figure 2.10.

Sr1/Ba1 site ($8h$)			Sr2/Ba2 site ($4a$)		
sample	$g_{\parallel}$	$g_{\perp}$	sample	$g_{\parallel}$	$g_{\perp}$
$x = 0.1$	2.71	1.71	$x = 0.1$	2.69	1.66
$x = 0.3$	2.53	1.67	$x = 0.3$	3.12	1.56
$x = 0.5$	2.54	1.69	$x = 0.5$	3.22	1.71
$x = 0.7$	2.55	1.70	$x = 0.7$	3.24	1.70
$x = 0.9$	2.31	1.67	$x = 0.9$	3.09	1.58

bonded in both sites. On the Sr1/Ba1 site, Ce has a BVS of 2, slightly less than the BVS of Ce of 1.25 on the Sr2/Ba2 site. The under-bonding can be reduced by contraction of the Ce–O/F bond lengths, making the local environment of Ce more amenable to the optically-active charge state of $+3$. A contraction of the Sr1/Ba1 bond lengths of around 5% from the average structure facilitates an increase in the BVS of Ce on the Sr1/Ba1 site from around 2 to around 3, which is small compared to what is required on the Sr2/Ba2 site. An average bond length contraction of 11.5% on the Sr2/Ba2 site brings the Ce BVS near 3. The smaller contraction of Ce$-$O/F bonds of the Sr1/Ba1 site compared with Ce$-$O/F bonds of the Sr2/Ba2 site required to make the BVS of Ce $= +3$ indicates Ce should be more easily incorporated on the Sr1/Ba1 site.

The structural information gleaned from synchrotron X-ray diffraction is useful for analysis of the average structure of the $Sr_{1.975}Ce_{0.025}Ba(AlO_4F)_{1-x}(SiO_5)_x$ phosphors, but the small amount of Ce^{3+} substituted into the lattice prohibits
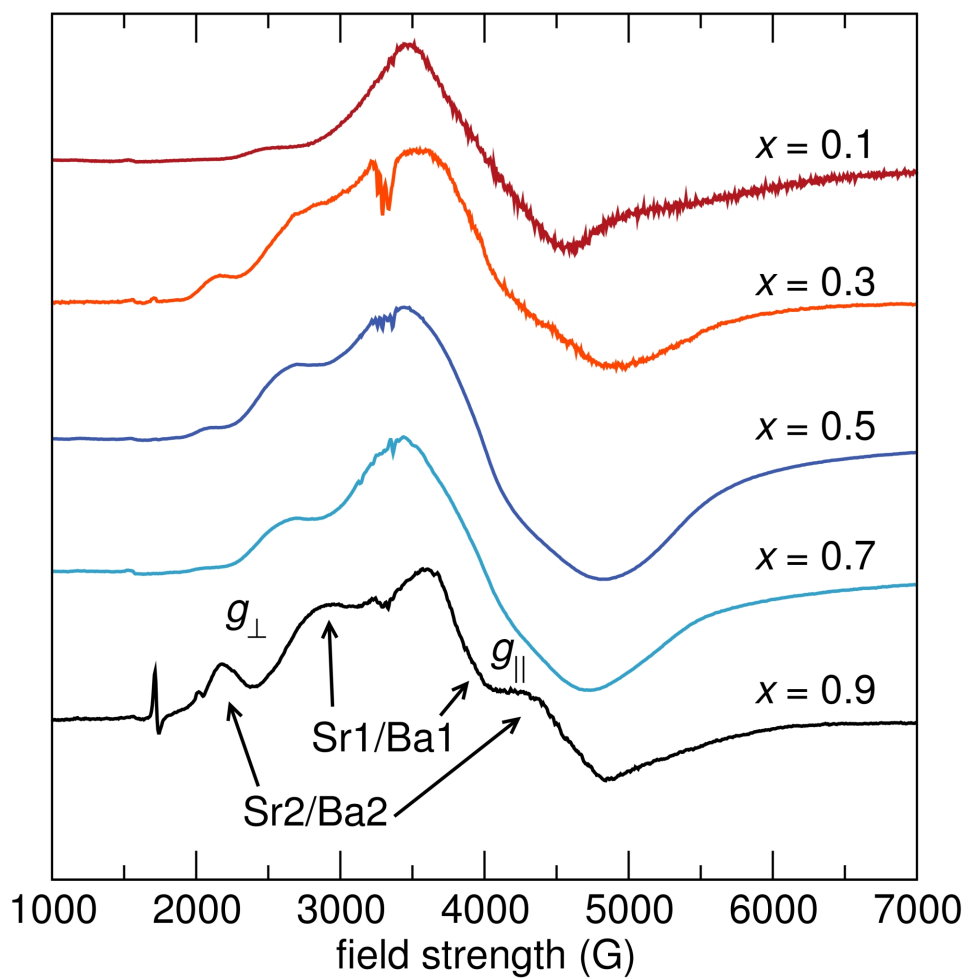
Figure 2.10: Powder EPR spectra of $Sr_{1.975}Ce_{0.025}Ba(AlO_4F)_{1-x}(SiO_5)_x$ taken at $10\,K$ on an X-band EPR spectrometer ($\nu = 9.4\,GHz$) indicate a large distribution of local Ce^{3+} environments, with a disproportionate amount of Ce^{3+} favoring the Sr1/Ba1 site over the Sr2/Ba2 site. Reproduced with permission from reference [38], ©2012 Royal Society of Chemistry.

using conventional scattering techniques to probe the structure of the lattice around Ce^{3+}. Electron paramagnetic resonance (EPR) spectroscopy provides a way to selectively probe unpaired spins in the system, such as Ce^{3+}, enabling a detailed examination of the local structure of Ce^{3+} in the lattice. In the $Sr_{1.975}Ce_{0.025}Ba(AlO_4F)_{1-x}(SiO_5)_x$ structure, the Sr1/Ba1 site has point-group symmetry of 2, while the Sr2/Ba2 site has point-group symmetry of $\bar{4}$. Both sites have axial symmetry, resulting in only two components of the g-tensor, $g_{\parallel}$ and $g_{\perp}$.[70, 71] The powder EPR spectra for the compositions $x = 0.1, 0.3, 0.5, 0.7,$ and 0.9, shown in Figure 2.10, display very wide lineshapes, indicative of a large distribution of local Ce^{3+} environments. This may be from the site mixing of Sr and Ba in the lattice as observed from the synchrotron X-ray analysis, or may be from the charge compensation mechanisms that are expected to be present due to the substitution of Ce^{3+} for Sr^{2+}/Ba^{2+}. The peak positions do not appear to move substantially with composition, likely due to the shielded nature of the $4f$ orbitals, which are not strongly affected by the local bonding environment. The small features near $1700\,G$ in the $x = 0.9$ spectra and near $3300\,G$ in the $x = 0.3$, $x = 0.5$, and $x = 0.7$ spectra are from Ce^{3+} in impurity phases. Table 2.5 lists the components of the g-tensors of both sites for all compositions.

The larger peaks have been attributed to the Sr1/Ba1 site since this site is twice as abundant in the crystal structure compared to the Sr2/Ba2 site and

analyses of bond valence sums and DFT calculations indicate that Ce^{3+} is more easily incorporated into the Sr1/Ba1 site. The other peaks, attributed to the Sr2/Ba2 site, are much smaller than the Sr1/Ba1 peaks, indicating much more Ce^{3+} resides on the Sr1/Ba1 site. The ratio of Ce^{3+} on the Sr1/Ba1:Sr2/Ba2 sites changes non-systematically with x, as exemplified by the changing intensity in the peak near $2200\,G$ from the Sr2/Ba2 site compared with the intensity of the peaks from the Sr1/Ba1 site. This peak at $2200\,G$ is the least prevalent in the $x = 0.7$ material, which also has the lowest quantum efficiency of all the compositions studied here. The intensity of this peak, and the inferred amount of Ce^{3+} substituted on the Sr2/Ba2 site, correlates well with the quantum efficiency reported later in this paper – high quantum efficiency correlates with a large Sr2/Ba2 substitution level. This seems counter-intuitive, since multiple substitution sites should increase excitation/emission overlap, thereby decreasing quantum efficiency. The correlation between high quantum efficiency and large relative Ce^{3+} substitution on the Sr2/Ba2 site may be due to a higher quantum efficiency of Ce^{3+} on this site compared to the Sr1/Ba1 site, or Ce^{3+} on the Sr2/Ba2 may sensitize Ce^{3+} emission on the Sr1/Ba1 site.

Excitation and emission spectra for all samples were collected using the relative maxima in emission/excitation intensity found for each sample. The resulting excitation and emission spectra are displayed in Figure 2.11, along with

57
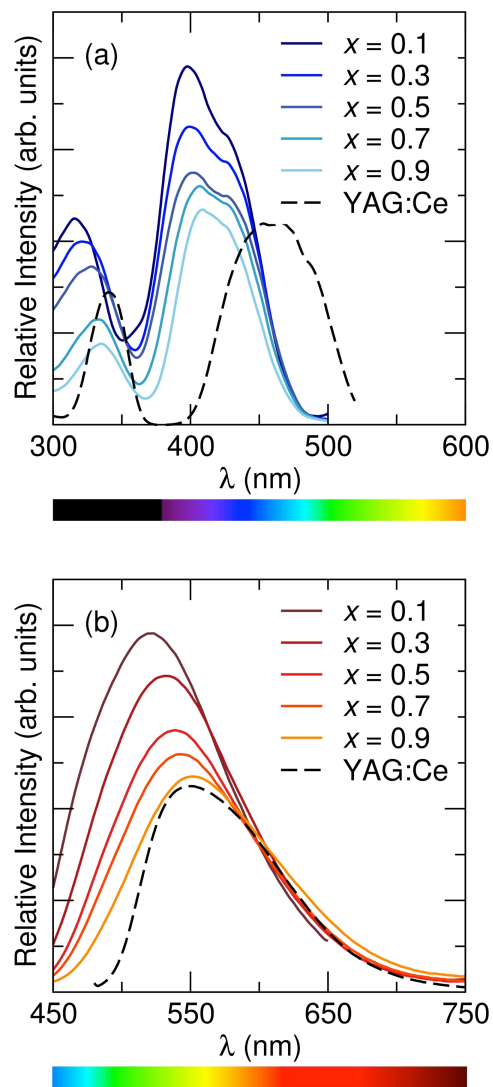
Figure 2.11: Photoluminescence (a) excitation spectra and (b) emission spectra of $Sr_{1.975}Ce_{0.025}Ba(AlO_4F)_{1-x}(SiO_5)_x$, collected at room temperature, show that the maximum excitation wavelength exhibits a slight red shift across the solid solution series as x increases, while the maximum emission wavelength shows an even greater shift to longer wavelengths. Excitation/emission spectra were recorded using the maximum emission/excitation wavelength. Reproduced with permission from reference [38], ©2012 Royal Society of Chemistry.
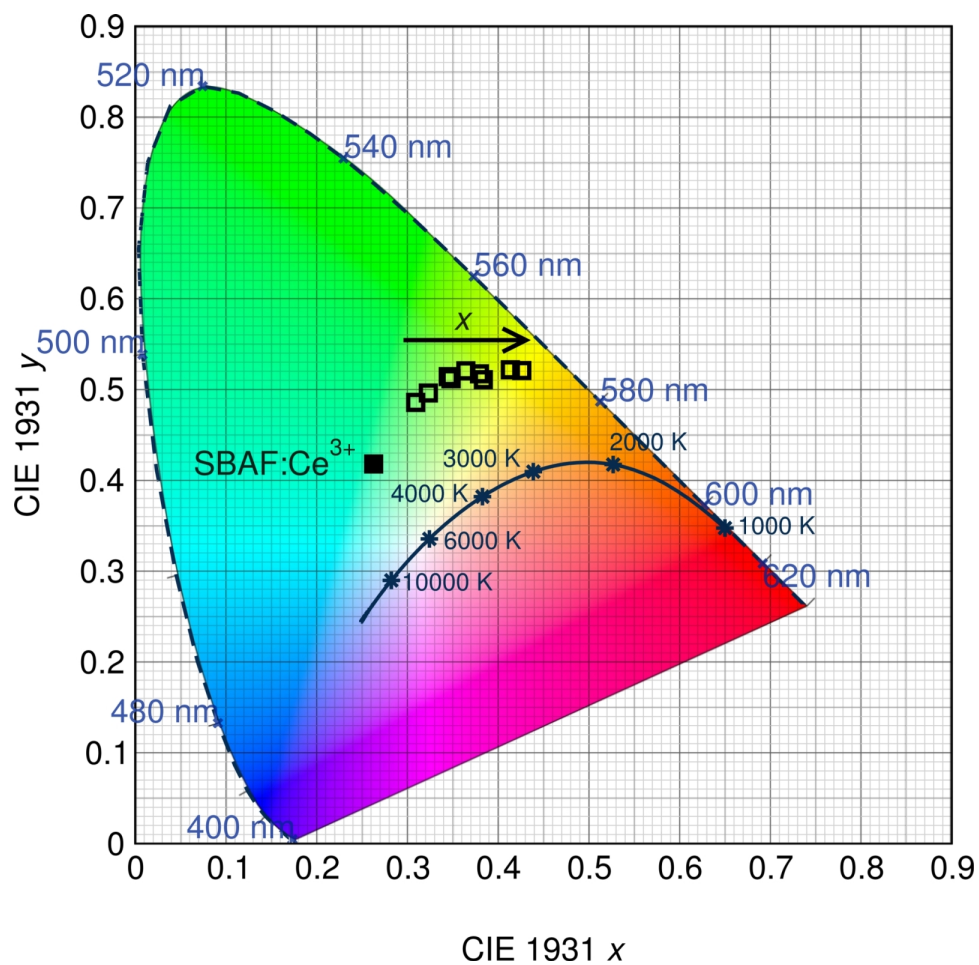
Figure 2.12: CIE color coordinates of the $Sr_{1.975}Ce_{0.025}Ba(AlO_4F)_{1-x}(SiO_5)_x$ phosphor series, along with the SBAF:Ce^{3+} end member, show the true color of the phosphor taking into account the broad emission spectra. Emission of the phosphor is tuned from green to yellow as x increases due to the increased distortion of the active site polyhedra. Reproduced with permission from reference [38], ©2012 Royal Society of Chemistry.

Table 2.6: Optical properties of the $Sr_{1.975}Ce_{0.025}Ba(AlO_4F)_{1-x}(SiO_5)_x$ solid solution phosphor at room temperature depict an easily tunable system that can vary emission color from green to yellow with a broad emission spectrum and high quantum yield.

sample	λ_{ex} (nm)	λ_{em} (nm)	FWHM (nm)	CIE (x, y)	PLQY (%)
$x = 0.1$	398	523	117	0.31, 0.49	70
$x = 0.3$	399	532	121	0.35, 0.51	70
$x = 0.5$	402	539	125	0.36, 0.52	63
$x = 0.7$	407	542	128	0.38, 0.52	54
$x = 0.9$	409	552	133	0.41, 0.52	67
YAG:Ce^{3+}	465	550	111	0.43, 0.55	87

that of YAG:Ce^{3+} for comparison, and photoluminescence data in Table 2.6. The maximum excitation wavelength exhibits a slight red-shift from 398 nm to 409 nm as x increases, while the maximum emission wavelength and the Commission Internationale de l'Eclairage (CIE) chromaticity coordinates, shown in Figure 2.12, exhibit a large red shift as x increases, from $\lambda_{em} = 523$ nm for $x = 0.1$ to $\lambda_{em} = 552$ nm for $x = 0.9$. This same trend in photoluminescent properties as x increases was also seen in the isostructural oxyfluoride solid solution developed by Im et $al.$[43]. Yet the introduction of Ba^{2+} into the host crystal results in a greater red shift in emission compared to the previous solid solution phosphor. The local environment around the Ce^{3+} activator ions is altered by the substitution of different cations and anions into the host lattice. In this compound, emission arises from electronic transitions in Ce^{3+} from the $5d$ ($^2D_{3/2}$, $^2D_{5/2}$) excited state to the $4f$ ($^2F_{5/2}$, $^2F_{7/2}$) ground state.[72] The

change in bond lengths from Ce^{3+} ions to their O^{2-} and F^- ligands, the degree of distortion of the $Ce(O,F)_8$ and $Ce(O,F)_{10}$ polyhedra, and the change in lattice covalency dictated by the relative change in charged species all result in changes in the crystal field splitting of the Ce^{3+} $5d$ levels. The crystal field splitting[24] can be modeled by

$$\Delta = Dq = \frac{Ze^2 r^4}{6R^5} \tag{2.2}$$

where Δ or Dq is the crystal field for octahedral symmetry, R is the distance between the central ion and its ligands, Z is the charge or valence of the anion, e is the charge of the electron, and r is the radius of the d wavefunction. Figure 2.7, discussed above, illustrates the changing polyhedral environments around the Ce^{3+} activator ions. The $(Sr,Ba)(O,F)_8$ average polyhedral volume increases by about $2.5\,\text{Å}^3$, which would indicate a blue-shift based on conventional crystal field splitting, while the $(Sr,Ba)(O,F)_{10}$ average polyhedral volume decreases, which would lead to a red-shift. Yet with twice as many $(Sr,Ba)(O,F)_8$ polyhedra than $(Sr,Ba)(O,F)_{10}$ in the unit cell and a greater change in volume, we would expect and overall blue-shift in emission wavelength. Yet, the experimentally seen red-shift contradicts this expected blue-shift.[24, 73] One explanation for this unconventional red-shift in emission, which has been seen in garnet systems,[21, 74–76] is the increased distortion of the active site polyhedra causing an increased crystal field splitting and red-shift. Although the $(Sr,Ba)(O,F)_8$

61

average polyhedral volume does increase, the coordination around the Sr1/Ba1 and Sr2/Ba2 sites becomes increasingly anisotropic as x increases due to alloying of Al^{3+}/Si^{4+}.[77–79] Figure 2.8 depicts this increased polyhedral distortion around the Sr1/Ba1 site and the Sr2/Ba2 site for the $x = 0.9$ composition compared to the $x = 0.1$ composition. Additionally, increased lattice covalency (nephelauxetic effect),[19, 20, 23, 80, 81] caused by replacing the more electronegative F^- with the less electronegative O^{2-}, contributes to a red-shift in both the excitation and emission. The slight change in excitation wavelength in the phosphor series and the drastic change in emission wavelength represent the changing crystal field around Ce^{3+} sites and the changing covalency of the lattice having different effects on the Ce^{3+} excited state and ground state energy levels.

The shift in emission wavelength with composition allows for the color properties of a solid state device to be easily tuned for different applications. The emission spectra of all compositions of the phosphor series are greatly red shifted from the green emission of the SBAF:Ce^{3+} end member, making these compositions promising candidates for white lighting. Additionally, the full-width at half-maximum (FWHM) of the emission profile is relatively broad for all samples, ranging from 117 nm to 133 nm as x increases, covering a wide range of the visible spectrum which will lead to high color rendering white LEDs. The

$x = 0.9$ composition in particular can be used to create high quality white light without the need for an additional red component. The moisture stability of the compounds was also increased from the SBAF end member. The compositions x = 0.5 and greater are stable under ambient laboratory storage conditions.

Photoluminescent quantum yield (PLQY) was measured to be 70% at room temperature for the most efficient samples, $x = 0.1$ and $x = 0.3$, with the lowest being 54% for $x = 0.7$. Thermal performance of the photoluminescence for $x = 0.5$ and $x = 0.9$ samples are shown in Figure 2.13. High temperature emission spectra were collected from room temperature to 220 °C to examine the thermal quenching of luminescence due to increased non-radiative transition probability in the configurational coordinate diagram[72] with increasing temperature. The maximum PL intensity at 160 °C decreased to 82% and 52% of their room temperature values for samples $x = 0.5$ and $x = 0.9$, respectively, while YAG:Ce^{3+} decreases to 64% of its room temperature value at 160 °C. The activation energy for thermal quenching can be calculated using the Arrhenius equation[82, 83] which obeys

$$I(T) = \frac{I_0}{1 + A \exp(\frac{-E}{kT})} \tag{2.3}$$

where I_0 is the initial intensity, $I(T)$ is the intensity at a given temperature T, A is a constant, E is the activation energy for thermal quenching and k is the Boltz-
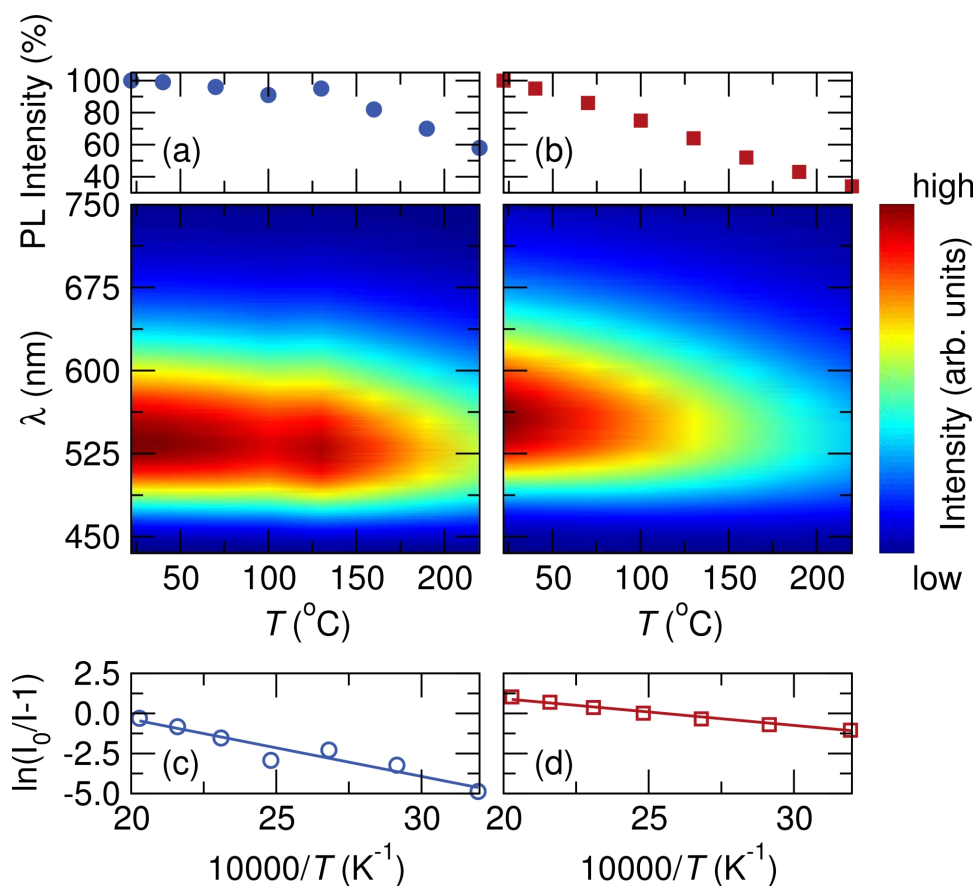
Figure 2.13: Temperature dependent PL data for $x = 0.5$ (circles) and $x = 0.9$ (squares) compositions of the $Sr_{1.975}Ce_{0.025}Ba(AlO_4F)_{1-x}(SiO_5)_x$ phosphor series show (a,b) weak thermal quenching from room temperature to $220\,^{\circ}C$ and (c,d) a large activation energy for thermal quenching. Reproduced with permission from reference [38], ©2012 Royal Society of Chemistry.
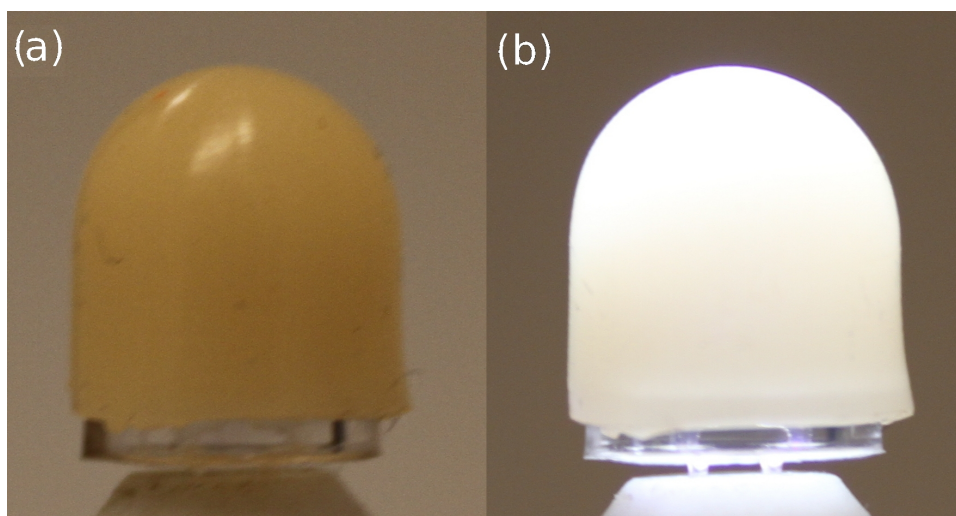
Figure 2.14: Photograph of the phosphor silicone 'cap' on a silicone-encapsulated LED chip when (a) the device is off and (b) illuminated, demonstrated using the $x = 0.9$ phosphor sample. Reproduced with permission from reference [38], ©2012 Royal Society of Chemistry.

mann constant. The activation energy for thermal quenching was determined to be 0.31 eV and 0.14 eV for $x = 0.5$ and $x = 0.9$, respectively. The $x = 0.5$ composition therefore exhibits impressive thermal stability, retaining more of its PL intensity at elevated temperatures than commercial YAG:Ce^{3+}. It has been suggested previously that in the fluoride compounds,[42] the high efficiency and low thermal quenching arise from the softer phonon modes associated with fluorine atoms in the host lattice.

The quality of the resulting white light produced by using this solid solution phosphor was examined by incorporating the phosphor into a device with an InGaN LED (λ_{max} = 400 nm). The "capping" strategy used here is depicted in

Table 2.7: Properties calculated from electroluminescence data collected at room temperature for the phosphor-converted white light using a InGaN LED chip (λ_{max} = 400 nm) operating under a forward bias current of 20 mA. Data for YAG:Ce^{3+} was collected using a blue InGaN LED (λ_{max} = 450 nm) also operating under a forward bias current of 20 mA.

sample	η (%)	efficacy (lm/W)	CIE (x, y)	CCT (K)	R_a
$x = 0.5$	40	19	0.31, 0.39	6264	68
$x = 0.9$	37	12	0.31, 0.32	6815	70
$x = 0.5 +$ red	43	16	0.37, 0.37	4113	90
YAG:Ce^{3+}	51	122	0.37, 0.42	4555	65

Figure 2.14. This phosphor deployment strategy allows for optimal light extraction in addition to reproducibility in measurements since the same LED can be used for all subsequent measurements. This strategy also allows us to calculate an energy efficiency of the phosphor when used with an LED. The energy efficiency[60] of the phosphor (η) can be calculated using

$$\eta = \frac{P_{phosphor}}{P_{LED} - P_{LED+phosphor}} \tag{2.4}$$

where $P_{phosphor}$ is the integrated radiometric power of the phosphor emission, and $P_{LED+phosphor}$ and P_{LED} are the integrated radiometric powers of the near-UV photon emission spectra with and without the phosphor cap, respectively. This energy efficiency includes the conversion and scattering efficiency of the phosphor as well as the extraction efficiency of the phosphor cap.

66
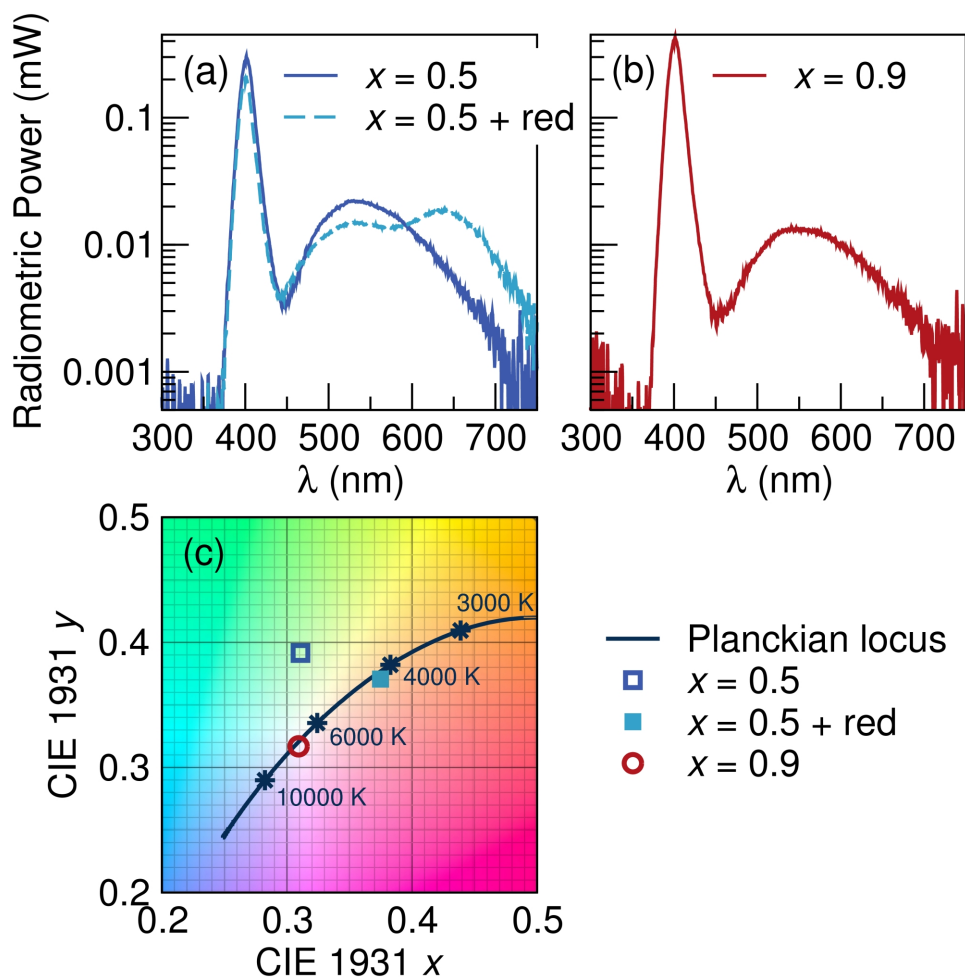
Figure 2.15: Electroluminescence data collected at room temperature for devices assembled using the phosphor compositions (a) $x = 0.5$ and (b) $x = 0.9$, in conjunction with a near-UV InGaN LED ($\lambda_{max} = 400\,\text{nm}$) operating under a forward bias current of $20\,\text{mA}$. The (c) CIE chromaticity coordinates are plotted for each device, showing the color quality of the white light produced. Reproduced with permission from reference [38], ©2012 Royal Society of Chemistry.

Figure 2.15 shows electroluminescence spectra and CIE chromaticity coordinates for devices made using samples $x = 0.5$ and $x = 0.9$. For $x = 0.5$, devices were also made by adding a commercially available red phosphor from Mitsubishi Chemical Corporation to obtain a white light closer to the Planckian locus of black body radiation. Table 2.7 lists the calculated values for phosphor energy efficiency, luminous efficacy, correlated color temperature (CCT) and color rendering (R_a). At room temperature, values for η ranged from 37% to 43% and values for the luminous efficacy ranged from 12 lm/W to 20 lm/W. The relatively low luminous efficacy numbers, compared to the blue-LED + YAG:Ce combination, is a consequence of the near-UV LEDs being not as bright, combined with the larger Stokes shift. High color rendering indices were obtained for all samples due to the broad nature of the emission profile, namely $x = 0.9$ with $R_a = 70$ and a CCT = 6815 K, with additional improvements through adding a red component to $x = 0.5$ for an $R_a = 90$ with CCT = 4113 K. The results indicate that this solid solution phosphor has strong potential applications in developing high-efficiency, thermally stable, warm-white LEDs.

68

2.4 Conclusions

In conclusion, a Ce^{3+}-doped oxyfluoride solid solution phosphor has been prepared from the Sr$_2$BaAlO$_4$F and Sr$_3$SiO$_5$ end members. Sr$_{1.975}$Ce$_{0.025}$Ba(AlO$_4$F)$_{1-x}$(SiO$_5$)$_x$ phosphors have easy color tunability, by changing the composition x, with near-UV excitation and green/yellow emission wavelengths optimal for solid state white lighting applications. With a highly efficient photoluminescent quantum yield of 70% at room temperature and photoluminescence intensity decreasing to only 82% of its room temperature value at 160 °C, this solid solution phosphor exhibits impressive thermal stability. Devices fabricated using InGaN LEDs with λ_{max} = 400 nm showed excellent white light characteristics, with a color rendering of R_a = 70 and CCT near 6815 K, eliminating the need for an additional red component. As such, this newly developed solid solution phosphor shows great potential for use in high efficiency, thermally stable white LEDs.

Chapter 3

Tuning luminescent properties through solid-solution in $(Ba_{1-x}Sr_x)_9Sc_2Si_6O_{24}:Ce^{3+},Li^+$ and an efficient, thermally stable cerium-based silicate phosphor for

solid-state white lighting

A solid-solution of cerium-substituted alkaline earth scandium silicate phosphors, $(Ba_{1-x}Sr_x)_9Sc_2Si_6O_{24}$:$Ce^{3+}$, Li^+ (x = 0, 0.25, 0.50, 0.75, 1), have been prepared by solid-state reaction. The structures, characterized using synchrotron X-ray powder diffraction, show the solid-solution closely follows Végard's law. The substitution of Sr for Ba results in decrease of the alkaline earth-oxygen bond distances by more than $0.1\,\text{Å}$ at all three crystallographic sites, leading to changes in optical properties. The room temperature photo-luminescent measurements show the structure has three excitation peaks corresponding to Ce^{3+} occupying the three independent alkaline earth sites. The emission of $(Ba_{1-x}Sr_x)_9Sc_2Si_6O_{24}$:$Ce^{3+}$, Li^+ is red-shifted from the near-UV (λ_{max} = 384 nm) for x = 0 to blue (λ_{max} = 402 nm) for x = 1. The red-shifted photo-luminescent quantum yield also increases when Sr is substituted for Ba in these compounds.

A novel cerium-substituted, barium yttrium silicate has been identified

---

[1]The contents of this chapter have substantially appeared in reference [84]: J. Brgoch, C. K. H. Borg, K. A. Denault, and R. Seshadri, Tuning luminescent properties via structure modification in the solid-solution $(Ba_{1-x}Sr_x)_9Sc_2Si_6O_{24}$:$Ce^{3+}$,$Li^+$, *Solid State Sci.* **18** 149–154 (2013) ©2013 Elsevier and reference [85]: J. Brgoch, C. K. H. Borg, K. A. Denault, A. Mikhailovsky, S. P. DenBaars, and R. Seshadri, An efficient, thermally stable cerium-based silicate phosphor for solid state white lighting, *Inorg. Chem.* **52(14)** 8010–8016 (2013) ©2013 American Chemical Society.

as an efficient blue-green phosphor for application in solid-state lighting. $Ba_9Y_2Si_6O_{24}$:Ce^{3+} was prepared and structurally characterized using synchrotron X-ray powder diffraction. The photoluminescent characterization identified a major peak at 394 nm in the excitation spectrum making this material viable for near-UV LED excitation. An efficient emission, with a quantum yield of $\approx$60%, covers a broad portion (430 nm to 675 nm) of the visible spectrum leading to the blue-green color. Concentration quenching occurs when the Ce^{3+} content exceeds $\approx$3 mole% while high temperature photoluminescent measurements show a 25% drop of the room temperature efficiency at 500 K. The emission of this compound can be red-shifted via the solid-solution, $Ba_9(Y_{1-y}Sc_y)_{1.94}Ce_{0.06}Si_6O_{24}$ ($x = 0.1, 0.2$) allowing for tunable color properties when device integration is considered.

3.1 Introduction

The search for new phosphors with remarkable optical properties has recently focused on silicate-based compounds. A few examples of rare-earth (RE) substituted silicate phosphors that show excellent emission properties include, M_2SiO_4:RE, [86–88] $MSiO_3$:RE, [89] Sr_3SiO_5:RE, [62] $Ba_3MgSi_2O_8$:RE, [90] and $M_2MgSi_2O_7$:Eu^{2+}[91]. Another silicate that has re-
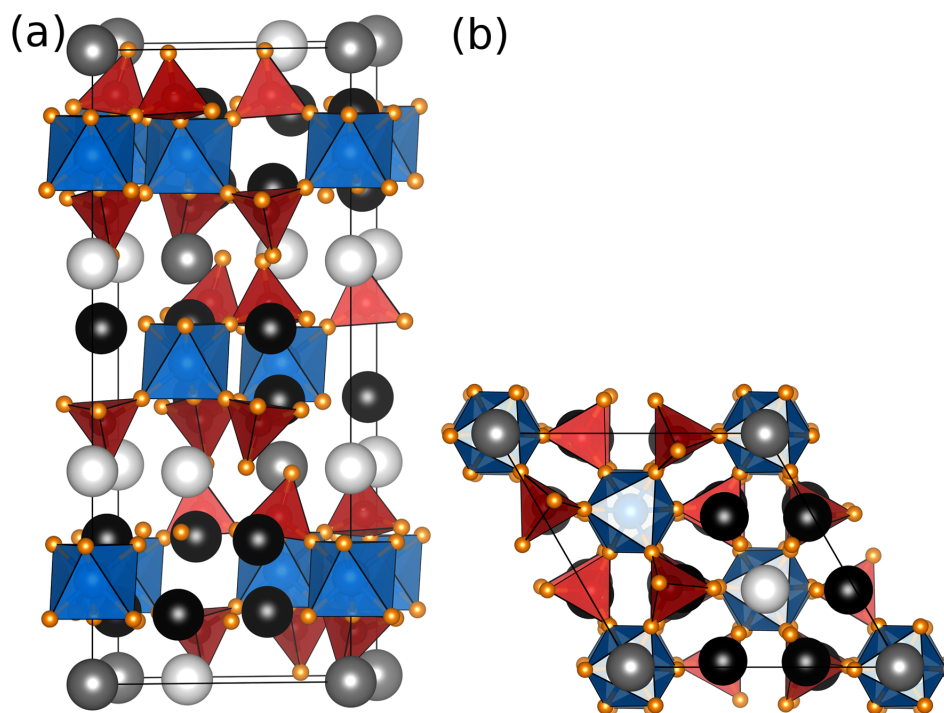
Figure 3.1: Crystal structure of $(Ba_{1-x}Sr_x)_9Sc_2Si_6O_{24}$ illustrated (a) close to the [100] direction and (b) along the [001] direction. Sc^{3+} and Si^{4+} polyhedra indicate the ScO_6 octahedra (blue) and SiO_4 octahedra (red), respectively. Ba/Sr(1) is gray, Ba/Sr(2) is white, Ba/Sr(1) is black, and Oxygen is illustrated by orange. Reproduced with permission from reference [84], ©2013 Elsevier.

cently been investigated is the compound $Ba_9Sc_2Si_6O_{24}$:RE, illustrated in Figure 3.1.

The structure was first determined using single crystal X-ray diffraction [92], and contains layers of ScO_6 octahedra that are corner-shared with SiO_4 tetrahedra. The compound is comprised of SiO_4–ScO_6–SiO_4 bilayers that stack along the [001] direction and are separated by Ba^{2+} ions. There are three independent

Ba^{2+} sites coordinated by 9-, 10-, and 12- oxygen atoms. Two of the Ba^{2+} ions (9- and 12-coordinate) occupy sites between the bilayers and the third Ba^{2+} ion (10-coordinate) is coordinated by the SiO$_6$ octahedra and SiO$_4$ tetrahedra.[92] Because of the three different Ba^{2+} coordination environments, the addition of a rare-earth luminescent center will likely have a broad emission covering a wide range of wavelengths making it a potentially interesting phosphor for light conversion. Initial investigations focused on Ba$_9$Sc$_2$Si$_6$O$_{24}$ substituted with Eu^{2+}[93]. In this case, the excitation spans between 350 to 450 nm while the emission λ_{max} is approximately 500 nm giving rise to a green phosphor.

Compounds that form complex solid solutions also provide a mechanism to tune the luminescent properties. The photoluminescent (PL) properties for the Eu^{2+}substituted silicate can also be moderately tuned via the solid solution (Ba$_{1-x}$Sr$_x$)$_9$Sc$_2$Si$_6$O$_{24}$ (x = 0–0.95) [94]. The excitation spectrum spans from between 300 nm to 500 nm while the emission spectra red-shifts by 20 nm as the solution is tuned from Ba- to Sr-rich. However, both reports contain discernible impurity peaks in the X-ray diffraction patterns potentially affecting the emission properties. Nevertheless, the reported PLQY for the Ba phase is ≈40%, making this structure worth further investigation.

Because Ce^{3+} is much smaller (r_{eff} = 1.196 Å; 9-coord.) than Ba^{2+} (1.47 Å; 9-coord.), there is a large potential for non-radiative relaxation. Substituting

the smaller Sr^{2+} (1.31 Å; 9-coord.) ion improves the emission slightly, though it is still rather low. Clearly, the alkaline earth site in this structure type is not ideal for the occupation of a luminescent center. The structure does contain a ScO_6 pseudo-octahedral site that would be ideal for rare-earth occupation, in particular Ce^{3+}. Unfortunately, the polyhedral volume is too small for substitution to occur.

Herein, we report the preparation and PL properties for the cerium substituted solid solution $(Ba_{1-x}Sr_x)_{8.46}(Ce_{0.27}Li_{0.27})Sc_2Si_6O_{24}$ (x = 0, 0.25, 0.50, 0.75, 1). The structural and optical properties have been examined for the entire series and show UV-excitation and a blue emission that can be tuned via the solid-solution. Additionally, we report the PLQY for $(Ba_{1-x}Sr_x)_{8.46}(Ce_{0.27}Li_{0.27})Sc_2Si_6O_{24}$ (x = 0, 0.25, 0.50). We also report the preparation of the yttrium analogue, $Ba_9Y_2Si_6O_{24}$, as an efficient near-UV to blue-green phosphor. The structure was determined using synchrotron X-ray diffraction and the Ce^{3+} content optimized. The optical properties examined include determining the photoluminescent quantum yield (PLQY), the Commission Internationale de l'Éclairage (CIE) color coordinates, and the critical distance for energy transfer are all reported. Additionally, the temperature dependence of the optical properties for $Ba_9Y_2Si_6O_{24}$ are investigated and show the efficiency is maintained even at high temperature (>500 K). Finally, a solid so-

lution of $Ba_9(Y_{1-y}Sc_y)_2Si_6O_{24}$:$Ce^{3+}$ ($y = 0.05, 0.1,\ldots0.25$) is employed to tune the emission color from blue-green to green based on changes in the polyhedral volume.

3.2 Experimental

Polycrystalline samples of $(Ba_{1-x}Sr_x)_{8.46}(Ce_{0.27}Li_{0.27})Sc_2Si_6O_{24}$ ($x = 0, 0.25$, 0.50, 0.75, 1.0) and $Ba_9(Y_{1-x}Ce_x)Si_6O_{24}$ ($x = 0, 0.01, 0.03,\ldots0.09, 0.12$) and $Ba_9(Y_{1-y}Sc_y)_{1.94}Ce_{0.06}Si_6O_{24}$ ($y = 0.05, 0.1,\ldots0.25$) were prepared by conventional high-temperature solid state reaction. The starting materials ($BaCO_3$, Cerac, 99.9%; $SrCO_3$, Aldrich, 99.995%; Sc_2O_3, Stanford Materials Corporation, 99.99%; Y_2O_3, Cerac, 99.99%; SiO_2, Johnson-Matthey, 99.9%; CeO_2, Cerac, 99.9%; Li_2CO_3, Cerac, 99.999%) were all weighed out in the desired stoichiometry and thoroughly mixed using an agate mortar and pestle for 30 minutes. Li^+ was used to compensate charge difference for substitution of Ce^{3+} at the Ba^{2+}/Sr^{2+} site. The mixed powders were pressed into a pellet and placed in an alumina crucible (CoorsTek) with sacrificial powder to prevent contact between the pellet and the crucible. The mixtures were fired in a tube furnace under reducing atmosphere (95% N_2/5% H_2) at 1350 $^\circ$ C for 3 h for $(Ba_{1-x}Sr_x)_{8.46}(Ce_{0.27}Li_{0.27})Sc_2Si_6O_{24}$ and 4 h for $Ba_9(Y_{1-x}Ce_x)Si_6O_{24}$ with heat-

76

ing and cooling rates of $3\,^\circ$ C/min. Additionally, a sample of $Ba_{1.94}Ce_{0.06}SiO_4$ was prepared using the same starting materials at $1400\,^\circ$ C for $8\,h$ to ensure the optical properties observed here are not from the impurity in the desired phase. The products are all colorless powders. Each composition was subsequently ground to a fine powder with an agate mortar and pestle for further analysis.

High resolution synchrotron X-ray powder diffraction data were collected at room temperature using beamline 11-BM at the Advanced Photon Source, Argonne National Laboratory. The average wavelength was $0.413949\,\text{Å}$. The diffraction data were fit by Rietveld refinements using the General Structure Analysis System (GSAS)[95, 96]. The background was handled using a shifted Chebyshev function while the peak shapes were handled using a pseudo-Voigt function with Finger-Cox-Jephcoat asymmetry to correct for axial divergence at low angle.

Scanning electron microscopy (SEM) images were collected using a FEI XL40 Sirion FEG Digital Scanning Microscope. Because the samples are highly insulating the surface was sputtered with gold to limit charging and a low ($5.00\,\text{kV}$) accelerating voltage was used. The images were collected using the resulting secondary electrons.

Room and low temperature photoluminescence spectra were obtained on a

Perkin-Elmer LS55 spectrophotometer. Each sample was mixed thoroughly with KBr ($\geq$99%, FT-IR grade, Sigma-Aldrich; $\approx$10:1 KBr to sample ratio by mass). The samples were pressed into a pellet (13 mm) for the room temperature measurements and used as a packed powder in a quartz tube for low temperature measurements. High temperature emission data were collected from room temperature to 503 K using a home-built fluorimeter incorporating a heating stage and an excitation wavelength of 407 nm. For the PLQY measurements, the phosphor powders were encapsulated in silicone resin (GE Silicones, RTV615) and deposited on a quartz substrate (Chemglass). The samples were then placed in a Spectralon$^{\text{TM}}$-coated integrating sphere (6 in. diameter, Lab-sphere) and excited using 405 nm light generated by a solid-state laser (Crystalaser DL-405-40-S) operated at a power between 1 mW and 2 mW. The light was collected by a quartz lens and directed onto a calibrated Si photodiode (Newport 818-UV) using filters (Omega Filters) to collect respective wavelengths. Additional experimental details have been described previously.[42, 59]

The CIE chromaticity coordinates were determined using an Instrument Systems integrating sphere (ISP-500) with a MAS-40 CCD array spectrometer and the SpecWin Lite software. The samples were excited using a commercially available laser diode (Pioneer, BDR-SO6J) with an emission $\lambda_{max} \approx 402$ nm and a forward bias current of 20 mA.

3.3 Results and Discussion

3.3.1 $(Ba_{1-x}Sr_x)_9Sc_2Si_6O_{24}$:$Ce^{3+}$,$Li^+$

The diffraction patterns collected using synchrotron X-ray powder diffraction are shown in Figure 3.2 for the entire solid-solution range. The major diffraction peaks in the $x = 0$ pattern correspond well to the standard pattern of $Ba_9Sc_2Si_6O_{24}$ (ICSD, 75175) [92]. The samples are nearly pure phase for $0 \leq x < 0.75$ with only minor additional peaks from an unidentified phase. The Sr-rich samples ($x \geq 0.75$) also contain the unidentified impurity as well as the silicate, $(Ba,Sr)_2SiO_4$. To determine changes in the structure as a function of composition, Rietveld refinements were performed for each composition employing the lattice parameters and atomic positions originally refined from single crystal X-ray diffraction as the starting point[92]. The resulting refinement for $x = 0$, presented in Figure 3.3, shows the pattern is well described by the model regardless of the minor impurity peaks. The refinement results for each composition are available in the Supporting Information.

The compounds crystallize in space group $R\bar{3}$ (No. 148) with refined lattice parameters of $a = 9.86288(1)$ Å and $c = 21.93734(4)$ Å for $Ba_9Sc_2Si_6O_{24}$, in agreement with previously published results [92–94]. The lattice parameters
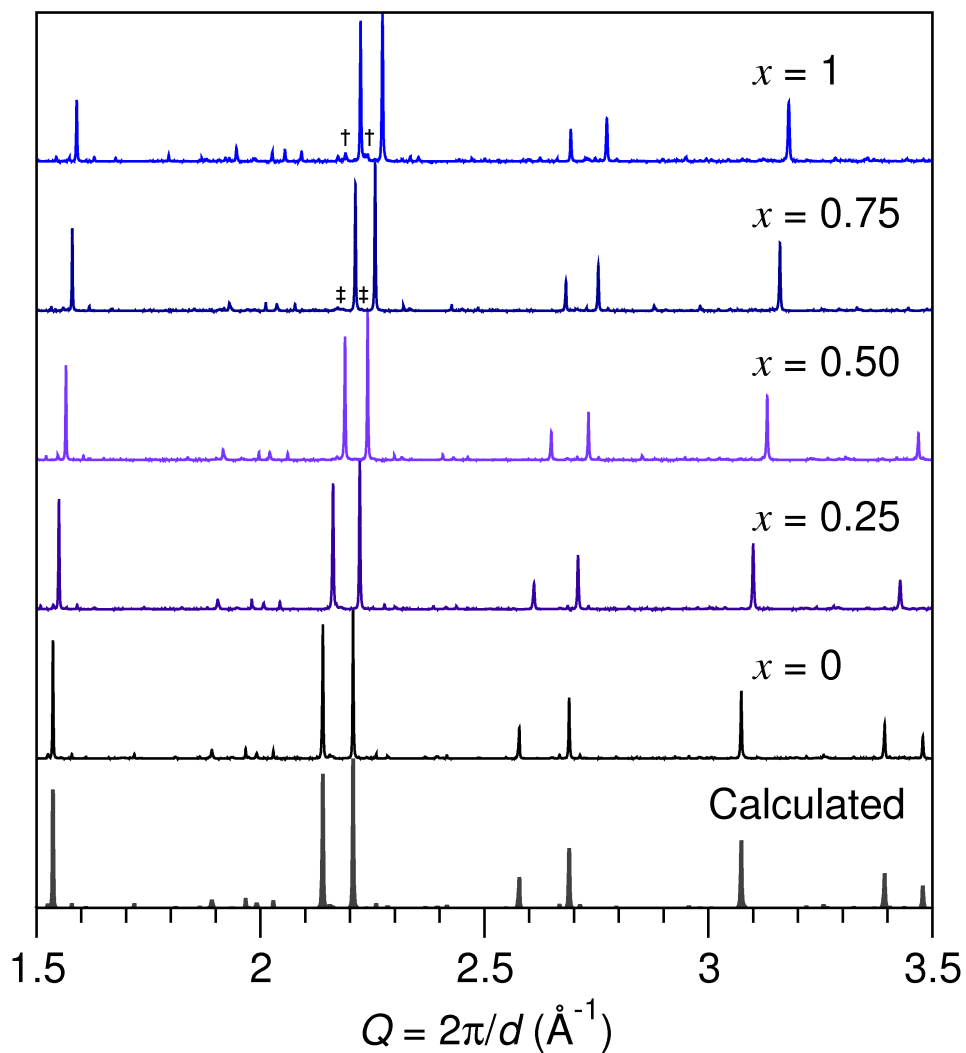
Figure 3.2: The synchrotron X-ray ($\lambda = 0.413949$) diffraction patterns for the solid-solution $(Ba_{1-x}Sr_x)_{8.46}(Ce_{0.27}Li_{0.27})Sc_2Si_6O_{24}$ ($x = 0$, 0.25, 0.50, 0.75, 1) indicates nearly pure phase samples across the entire substitution range. The double dagger ($\ddagger$) indicates a minor impurity of $(Ba,Sr)_2SiO_4$; the dagger ($\dagger$) indicates a minor impurity of Sr_2SiO_4. The bottom pattern is the calculated diffraction pattern for $Ba_9Sc_2Si_6O_{24}$. Reproduced with permission from reference [84], ©2013 Elsevier.
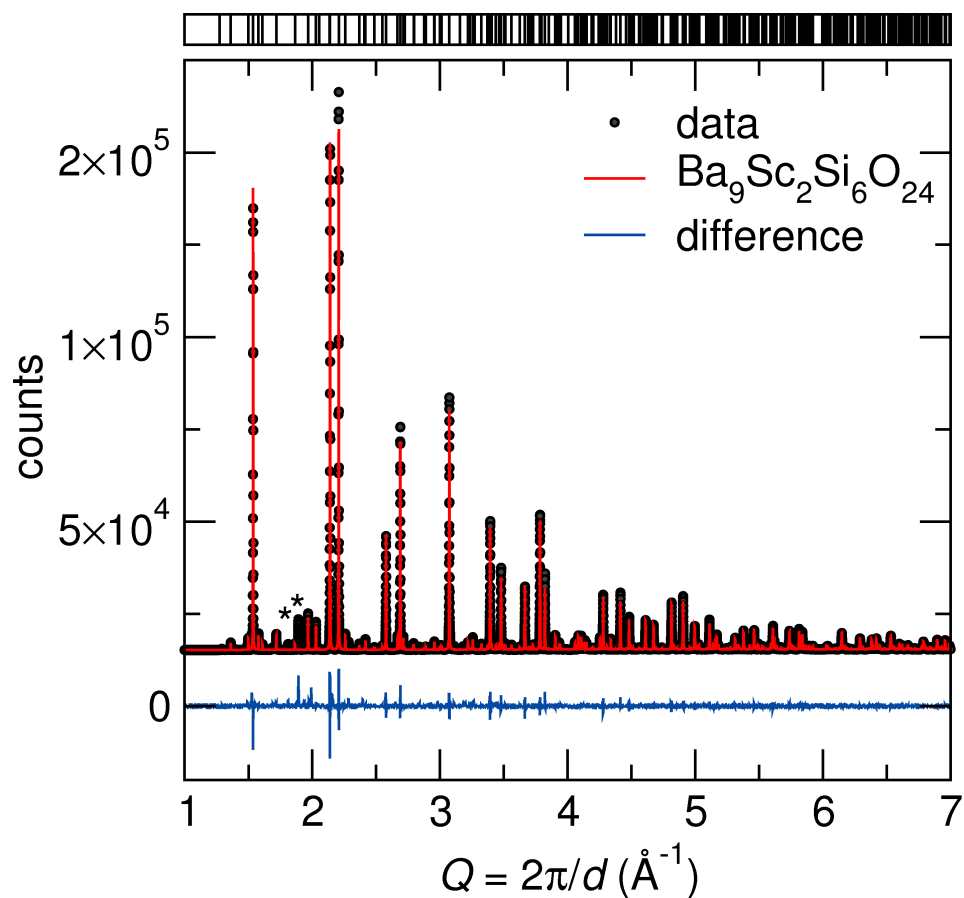
Figure 3.3: A Rietveld refinement was preformed on $Ba_9Sc_2Si_6O_{24}$ to determine the lattice parameters and atomic positions. The peaks marked with the asterisk (*) correspond to an unidentified phase. The refinements results for all compositions are presented in the Appendix. Reproduced with permission from reference [84], ©2013 Elsevier.
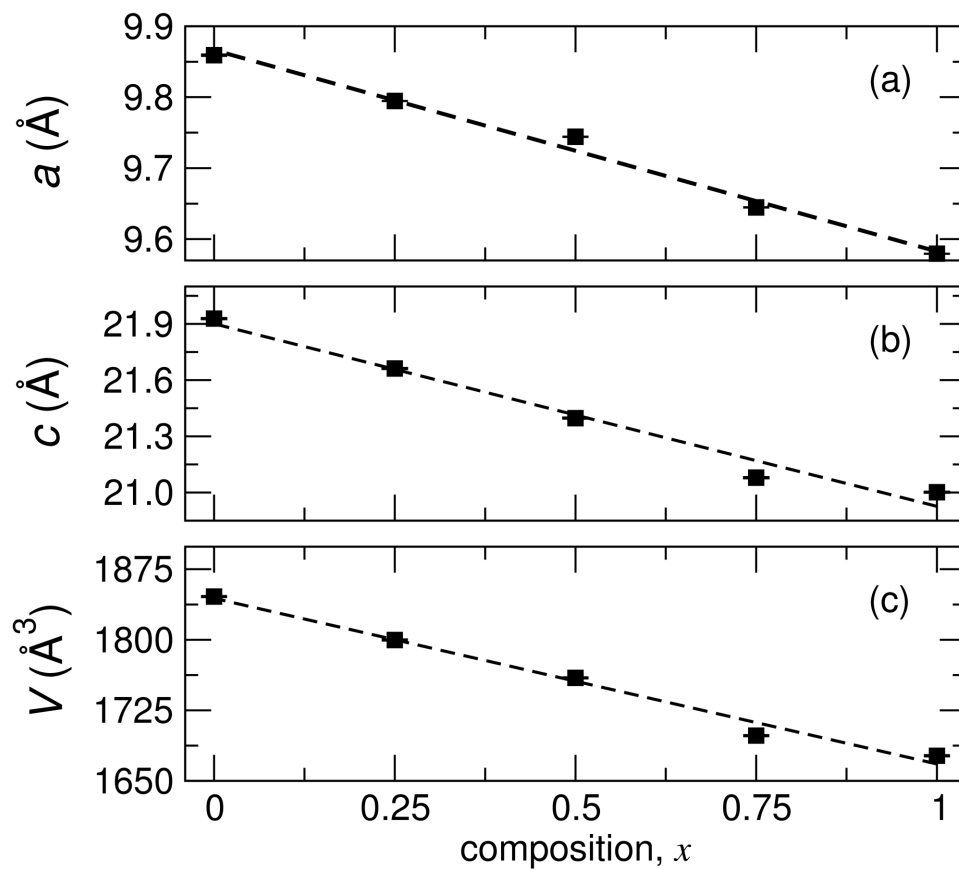
Figure 3.4: The refined lattice parameters (a, b) and unit cell volume (c) for the solid-solution of $(Ba_{1-x}Sr_x)_9Sc_2Si_6O_{24}$ ($x = 0$, 0.25, 0.50, 0.75, 1) show Végard's law is followed closely across the entire range. Reproduced with permission from reference [84], ©2013 Elsevier.

and cell volume, plotted in Figure 3.4, decrease as the smaller Sr^{2+} is substituted for Ba^{2+} indicating the solid-solution closely follows Végard's law.

Because the active luminescent centers, Ce^{3+}, occupy the Ba^{2+}/Sr^{2+} sites, careful analysis of these coordination environments was pursued. The structure contains three crystallographically independent Ba^{2+}/Sr^{2+} sites. Ba/Sr(1) sits at Wyckoff site 3*a* and is coordinated by 12 oxygen atoms (two crystallographic independent) forming a distorted cubeoctahedron; five oxygen atoms surround the waist in the *ab*-plane and the remaining six form a distorted Ba/Sr centered octahedron. Ba/Sr(2) sits at Wyckoff site 6*c* and is coordinated to 9 oxygen atoms (three crystallographic independent) and forms a distorted, tri-capped trigonal prism. Ba/Sr(3) sits at a general position, Wyckoff site 18*f*, and is connected to 10 oxygen atoms (three crystallographic independent). The Ba–O bond distances for these three sites have a significant variance in their bond lengths. For instance, the two Ba(1)–O distances are 3.253(6) Å and 2.933(6) Å, the Ba(2)–O distances range between 2.782(7) Å to 3.070(8) Å, and finally the Ba(3)–O distances range between 2.66(1) Å to 3.197(7) Å.

Substituting Sr following the solid solution leads to a decrease in the average metal–oxygen bond length as a function of the Ba/Sr content, shown in Figure 3.5a. The average bond distance for the Ba/Sr(1)–O site decreases linearly. Interestingly, the Ba/Sr(3)–O distance decreases rapidly with Sr addi-
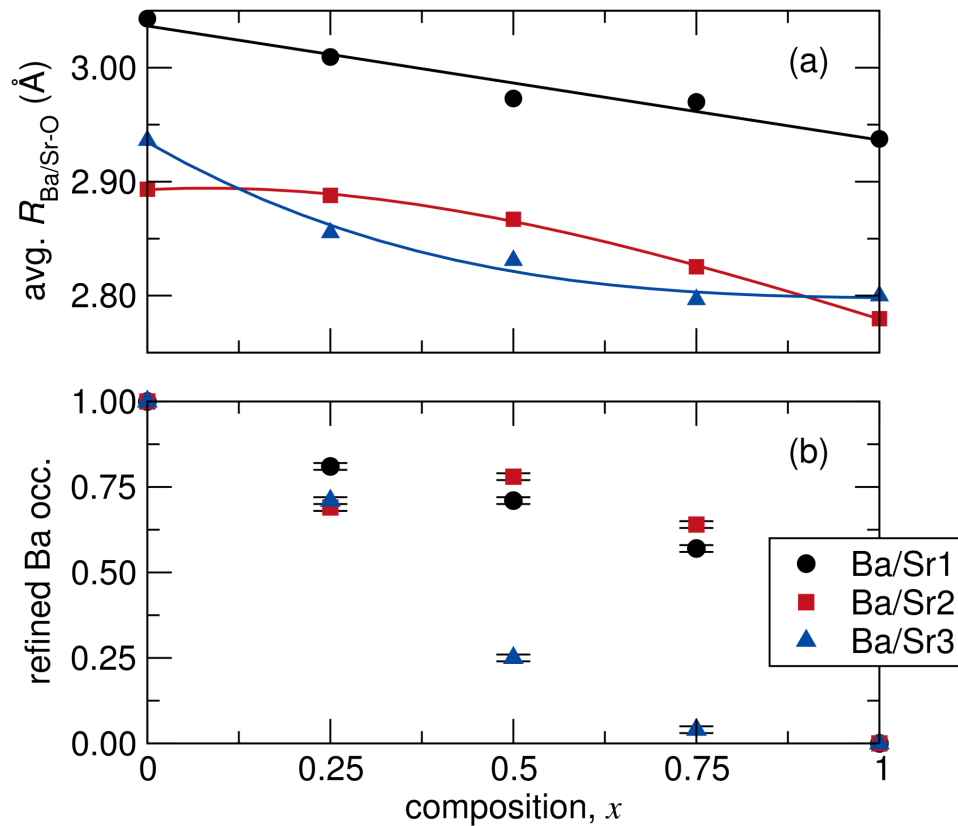
Figure 3.5: (a) The average (refined) metal–oxygen bond length for Ba/Sr1–O (black, circles), Ba/Sr2–O (red, squares), and Ba/Sr3–O (blue, triangles) show the changes in bond lengths. (b) The refined Ba occupancy at Ba/Sr1 (black, circles), Ba/Sr2 (red, squares), and Ba/Sr3 (blue, triangles). The composition, x, follows $(Ba_{1-x}Sr_x)_9Sc_2Si_6O_{24}$ ($x = 0$, 0.25, 0.50, 0.75, 1). Reproduced with permission from reference [84], ©2013 Elsevier.

tion and then levels out while the Ba/Sr(2)–O interaction decreases quicker at higher Sr loading. Additionally, the Ba^{2+}/Sr^{2+} occupancies were refined at all three sites, illustrated in Figure 3.5b. At low Sr concentrations ($x = 0.25$) a statistical distribution across all three divalent sites is observed, with approximately 25% Sr refined at all three sites. Increasing the concentration of Sr leads to a disproportionate amount of Sr occupying the 10-coordinate, Ba/Sr(3) site. In fact, the prepared $(Ba_{1-x}Sr_x)_9Sc_2Si_6O_{24}$ ($x = 0.50, 0.75$) has refined occupancies of 75(1)% Sr and 96(1)% Sr, respectively, at the Ba/Sr(3) site. These results, along with the changes in bond distances, there is a clear site preference for Sr to occupy the Ba/Sr(3) site.

The site preference is further evident by calculating the bond valence sums (BVS) for each site using the bond distances determined from refinements of the synchrotron X-ray diffraction data [69], Figure 3.6.

The long Ba/Sr–O bonds surrounding Ba/Sr(1) lead to an optimal BVS of 2 for Ba^{2+} across the entire range while Sr^{2+} on the same site is largely under-bonded (BVS = 1.1–1.6). This indicates a valence state of 2+ is satisfied for Ba but not necessarily for Sr. The same is true for the Ba/Sr(2) site, with Ba having a divalent BVS and Sr is, again, under-bonded. Although the Ba/Sr(2)–O bond is shorter than for Ba/Sr(1)–O, the BVS is nearly the same for both atoms. The difference likely arises from a modification of the coordination environment.
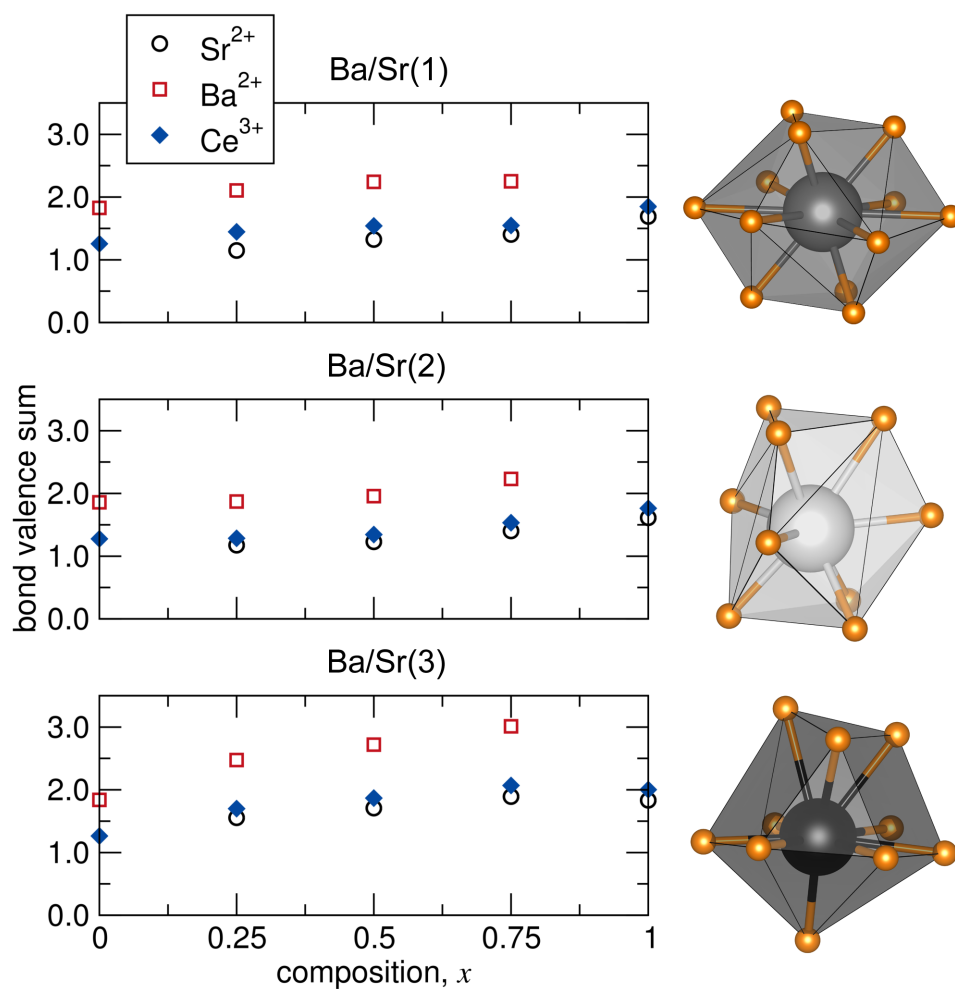
Figure 3.6: The bond valence sum (BVS) of Ba, Sr, and Ce on Ba/Sr(1) (top), Ba/Sr(2) (middle), and Ba/Sr(3) (bottom) calculated using the refined bond distances from synchrotron X-ray diffraction data for compositions $(Ba_{1-x}Sr_x)_9Sc_2Si_6O_{24}$ (x = 0, 0.25, 0.50, 0.75, 1). The corresponding coordination polyhedra for the three respective sites are shown on the right. Reproduced with permission from reference [84], ©2013 Elsevier.

For Ba/Sr(3), the divalent state for Sr^{2+} is achieved while Ba is over-bonded ranging between BVS = 2.5–3. This is in agreement with the refined occupancies indicating a larger portion of Sr at Ba/Sr(3) relative to the other two sites. Interestingly, Ce^{3+} is remarkably under-bonded at all three sites with a BVS ranging between 1 and 2 in all compositions. This likely leads to local distortions around the Ce^{3+}-site that are lost in the average crystal structure refined by powder X-ray diffraction. Regardless, based on the changes observed in the crystal structure that arise from the solid-solution, substituting Sr for Ba should undoubtedly affect the crystal field splitting of the atoms at these three sites and modify the luminescent properties.

The optical properties in previous reports indicate the optimum concentration of Eu^{2+} in these silicates is between 1 mole% and 3 mole% of alkaline earth, thus the PL properties were investigated for 3 mole% Ce^{3+}, *i.e.*, $(Ba_{1-x}Sr_x)_{8.46}(Ce_{0.27}Li_{0.27})Sc_2Si_6O_{24}$ ($x = 0$, 0.25, 0.50, 0.75, 1) [93, 94].

To ensure these compounds have a wide enough bandgap to accommodate the Ce^{3+} f-orbital to d-orbital transition, the diffuse reflectance was measured for the solid solution, shown in Figure 3.7. The (direct) bandgap of $Ba_{8.46}(Ce_{0.27}Li_{0.27})Sc_2Si_6O_{24}$ was determined using Tauc's plot to be 4.89 eV [97]. Upon Sr substitution the gap decreased by only 0.01 eV. In addition, the inset in Figure 3.7 shows the absorption bands from the Ce^{3+} confirming the desired
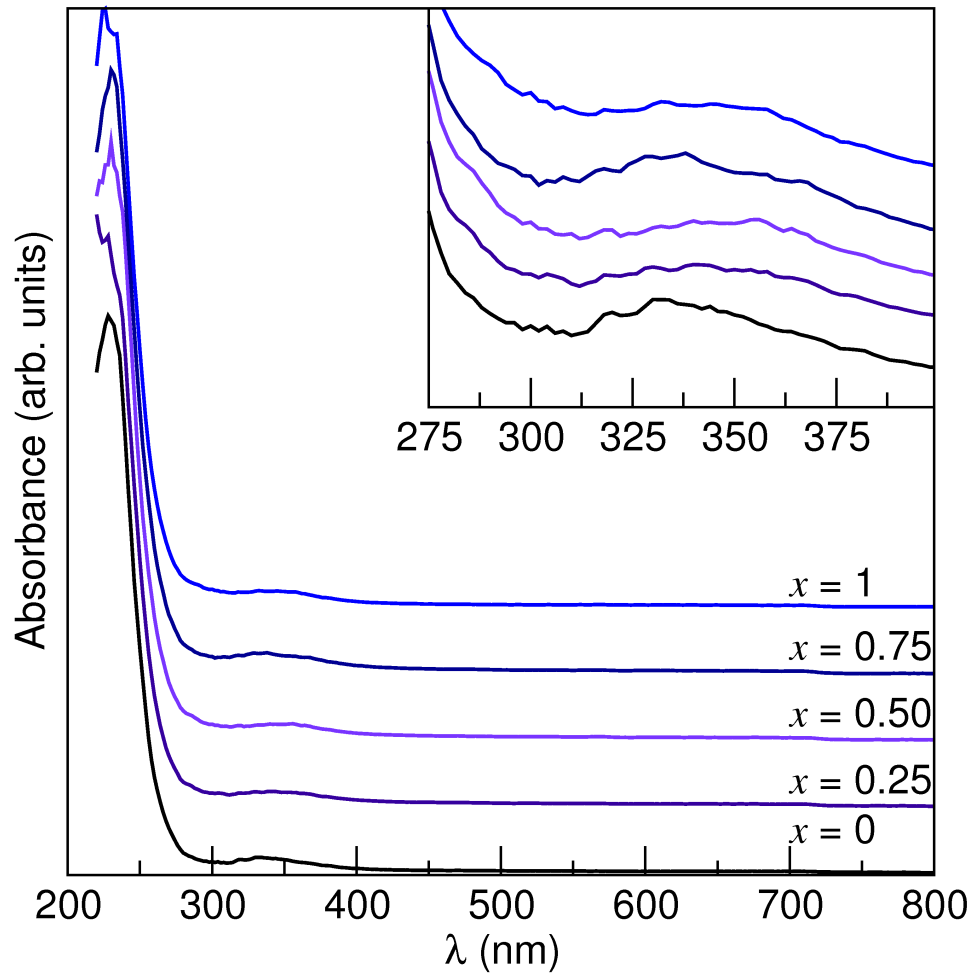
Figure 3.7: The diffuse reflectance of $(Ba_{1-x}Sr_x)_{8.46}(Ce_{0.27}Li_{0.27})Sc_2Si_6O_{24}$ ($x = 0$, 0.25, 0.50, 0.75, 1) is shown from 220 nm to 500 nm. Only minor changes in the calculated bandgap occur due to substitution. The inset shows the absorption bands for the $f \rightarrow d$ transition of Ce^{3+}. Reproduced with permission from reference [84], ©2013 Elsevier.
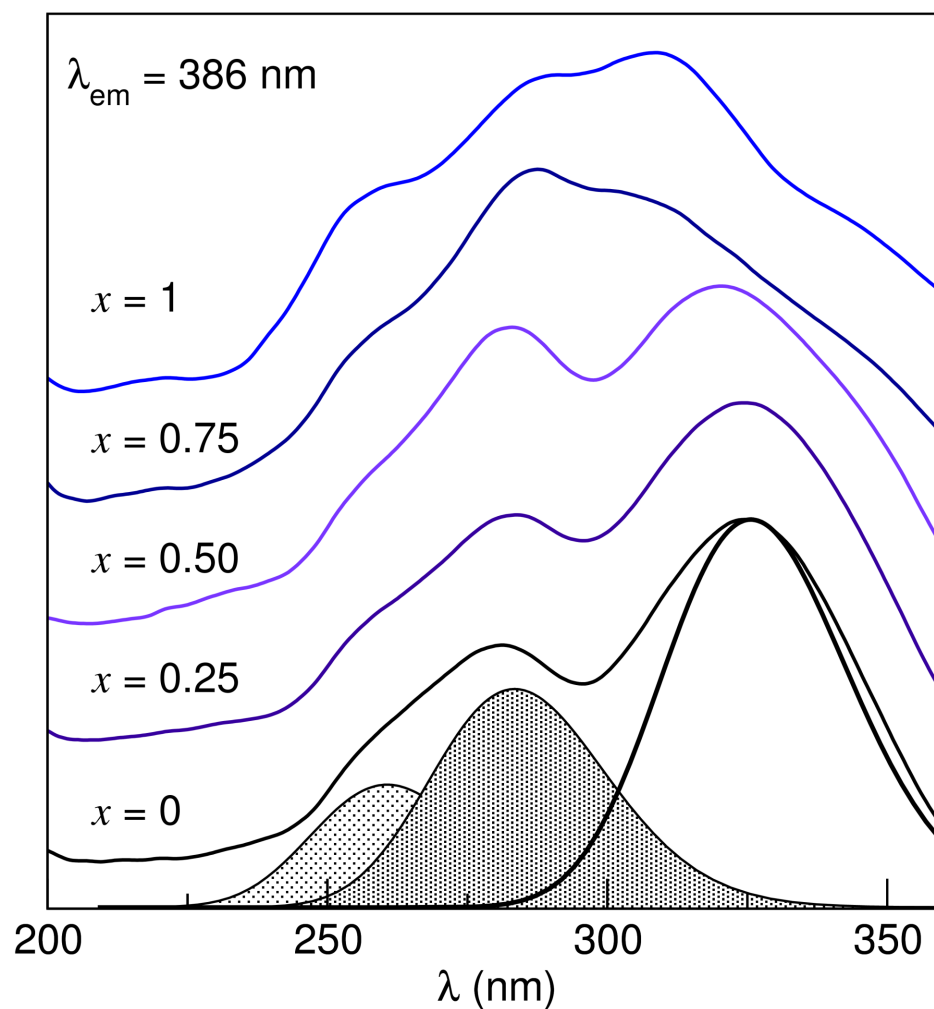
Figure 3.8: The excitation spectra of $(Ba_{1-x}Sr_x)_{8.46}(Ce_{0.27}Li_{0.27})Sc_2Si_6O_{24}$ ($x = 0$, 0.25, 0.50, 0.75, 1) collected using an emission wavelength of 386 nm is fit by three Gaussian curves corresponding to the three independent Ce^{3+} sites. The shoulder present in samples with $x > 0.75$ corresponds to the impurity $(Ba,Sr)_2SiO_4$. Reproduced with permission from reference [84], ©2013 Elsevier.

transition occurs within the wide bandgap of this host.

The excitation curves, Figure 3.8, confirms Ce occupies all three of the crystallographically independent Ba/Sr sites, as fit by three Gaussian curves. From the Rietveld refinements, the average Ba/Sr–O bond lengths (in $Ba_{8.46}(Ce_{0.27}Li_{0.27})Sc_2Si_6O_{24}$) are 3.043(1), 2.8933(8), and 2.936(1) Å for Ba sites (1), (2), and (3), respectively. Shorter bond lengths will give rise to a stronger crystal-field splitting of the $5d$-orbitals leading to a red-shift in the optical properties. As a result, the peak at 260 nm likely corresponds to the 12-coordinate Ba/Sr(1), with the longest average Ba–O bond length. Assigning excitation peaks for Ba(2) and (3) is difficult since their average Ba–O bond distances are similar. However, the intensity of the excitation spectra at 325 nm is approximately three times larger than at 283 nm; considering the Wyckoff multiplicities ($6c$ versus $18f$) of these two sites, and assuming statistical distribution of Ce^{3+} across all sites, the peak at 325 nm should correspond to the Ba/Sr(3) site ($18f$) while the peak at 283 nm arises from the Ba/Sr(2) site ($6c$). Furthermore, Ce^{3+} on the Ba/Sr(2) site has a greater degree of under-bonding relative to Ce^{3+} on Ba/Sr(3) which should lead to a blue-shift in the optical properties, further confirming the excitation peak assignments. As discussed above, when Sr is substituted for Ba in the structure there is a site preference for Sr to occupy Ba/Sr(3) (see Figure 5). Because Ce^{3+} (1.25 Å, 10 coord.) is

Table 3.1: Photoluminescent results for the solid-solution $(Ba_{1-x}Sr_x)_{8.46}(Ce_{0.27}Li_{0.27})Sc_2Si_6O_{24}$. The excitation peaks as fit by three Gaussian functions, the measured emission λ_{max}, and the PLQY excited at 351 nm are presented. Standard error for the PLQY measurements are $\pm5\%$.

x	ex. λ (nm) Ba/Sr(1), Ba/Sr(2), Ba/Sr(3)	em. λ_{max} (nm)	PLQY (at 351 nm)
$x = 0$	260, 283, 325	384	12%
$x = 0.25$	257, 283, 326	388	25%
$x = 0.50$	258, 283, 320	390	21%
$x = 0.75$	261, 284, 311	396	—
$x = 1$	256, 288, 313	402	—

closer in size to Sr^{2+} (1.36 Å, 10 coord.) than Ba^{2+} (1.52 Å, 10 coord.), there is likely a preference for Ce^{3+} to occupy the Ba/Sr(3) site in the solid solution [63]. Regardless, the general excitation spectrum is maintained when substituting Ba for Sr, namely containing three curves corresponding to the three co-ordination environments. Additionally, a shoulder in the excitation appears at high Sr substitution ($x > 0.75$), which can be attributed to an impurity phase, cerium substituted $(Ba,Sr)_2SiO_4$. For comparison, the excitation spectrum of the Sr_2SiO_4:Ce^{3+},Li^+ is presented in the Appendix.

The emission spectra of these compounds are presented in Figure 3.9. The peaks can be deconvoluted into two gaussian curves separated by approximately 2600 cm^{-1}, corresponding to the $^2F_{5/2}$ and $^2F_{7/2}$ states due to spin-orbit coupling [72]. Substituting Sr for Ba across the entire solid solution causes a decrease in the bond lengths and thus an increased crystal-field splitting. As illustrated in
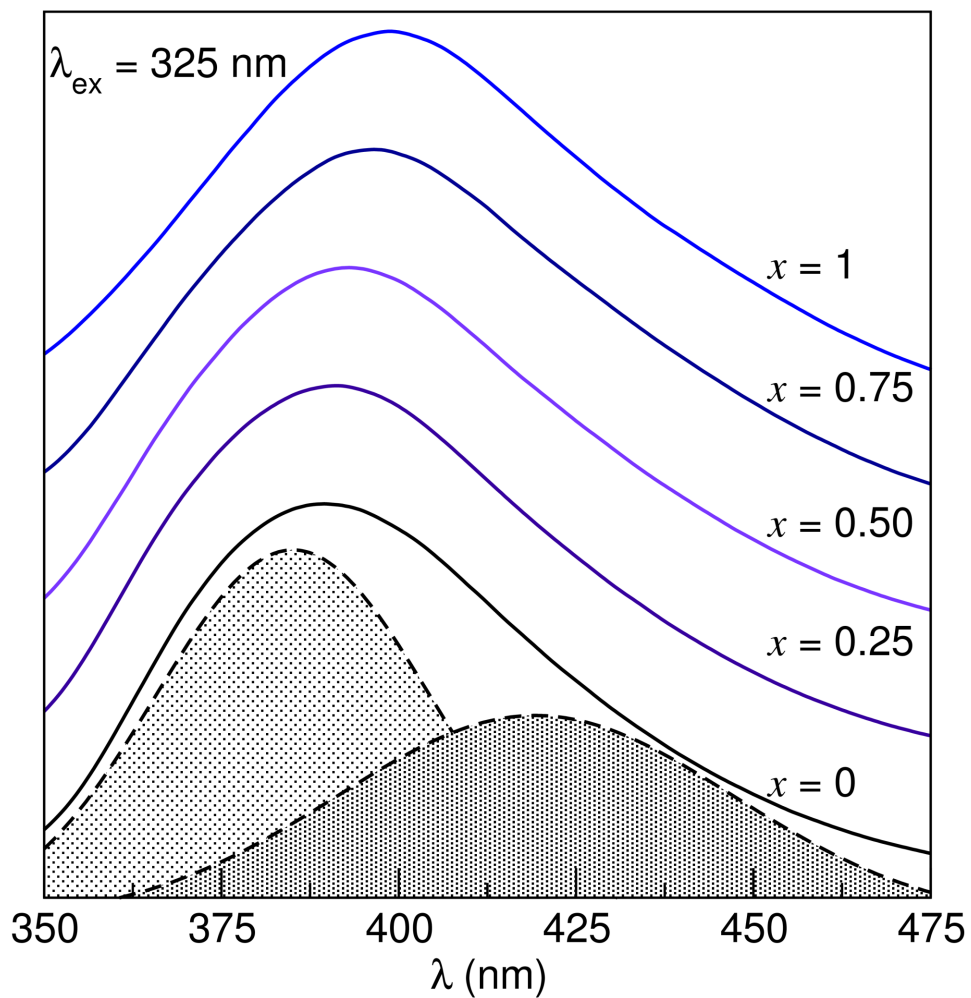
Figure 3.9: The emission spectra of $(Ba_{1-x}Sr_x)_{8.46}(Ce_{0.27}Li_{0.27})Sc_2Si_6O_{24}$ ($x = 0$, 0.25, 0.50, 0.75, 1) collected using an excitation wavelength of 325 nm. The spectra are fit by two Gaussian curves corresponding to the spin-orbit assisted $^2F_{5/2}$ and $^2F_{7/2}$ transitions. The emission red-shifts as the value of x increases. Reproduced with permission from reference [84], ©2013 Elsevier.

Equation 1, the crystal-field splitting, Δ, is inversely related to the bond length, R, where Z is the anionic charge, e is the charge of the electron, and r is the radius of the $5d$-wavefunctions [24].

$$\Delta = \frac{Ze^2r^4}{6R^5} \tag{3.1}$$

Considering the average bond length from $Ba_9Sc_2Si_6O_{24}$ to $Sr_9Sc_2Si_6O_{24}$ decreases by 11%, according to Equation 1 a significant increase in Δ should arise. Experimentally, the substitution of Sr for Ba leads to a red-shift of emission by approximately 20 nm. Exciting the Sr-rich compounds, $x = 0.75$ and 1, at longer wavelengths ($x > 360$ nm) result in an emission peak centered at 415 nm, which corresponds to the cerium-substituted $(Ba,Sr)_2SiO_4$ (for comparison the emission spectrum of Sr_2SiO_4:Ce^{3+},Li+ is presented in the Appendix).

PLQY measurements, presented in Table 3.1 along with additional PL data, were collected using an excitation wavelength of 351 nm. Due to the absorption of the $(Ba,Sr)_2SiO_4$ impurity in this region, the quantum yields are only reported for $(Ba_{1-x}Sr_x)_{8.46}(Ce_{0.27}Li_{0.27})Sc_2Si_6O_{24}$ ($x = 0$, 0.25, 0.50). The PLQY of the Eu^{2+} is reported as 47% for the pure Ba compound[94], whereas the PLQY for the Ce^{3+} phases presented here is $\approx$15%. The low quantum yield for the Ce^{3+} doping likely stems from placing a trivalent ion on a divalent site, which

is known to increase the probability of non-radiative relaxation [98, 99]. An increase in the radiationless process arises because the trivalent cation attracts the anion stronger than the divalent cation would resulting in shorter Ce^{3+}–O relative to Ba^{2+}/Sr^{2+}–O. In the excited state a larger expansion in the bonds is experienced, which favors the non-radiative process and leads to a low quantum efficiency [99, 100]. If the samples were not co-substituted with Li^+, it is expected that the PLQY would be even lower [100]. The addition of Sr to the structure increases the PLQY by approximately 5%. As the bond lengths, and in turn the site volume, decrease with Sr addition, the Ce^{3+} is squeezed by the host lattice limiting non-radiative relaxation pathways. Although this change is near the detection limit, excitation of a more intense band (*e.g.*, excitation at 330 nm) may resolve this issue. Nevertheless, the pure $Sr_{8.46}(Ce_{0.27}Li_{0.27})Sc_2Si_6O_{24}$ is predicted to have the highest PLQY of the series.

3.3.2 $Ba_9(Y_{1-x}Sc_y)_2Si_6O_{24}:Ce^{3+}$

$Ba_9Y_2Si_6O_{24}$, illustrated in Figure 3.10, is a novel silicate compound and was prepared as the majority phase (as indicated by powder X-ray diffraction) with only a minor impurity of Ba_2SiO_4. All attempts to remove the silicate impurity, including varying the loaded stoichiometry and reaction heating profile proved

94
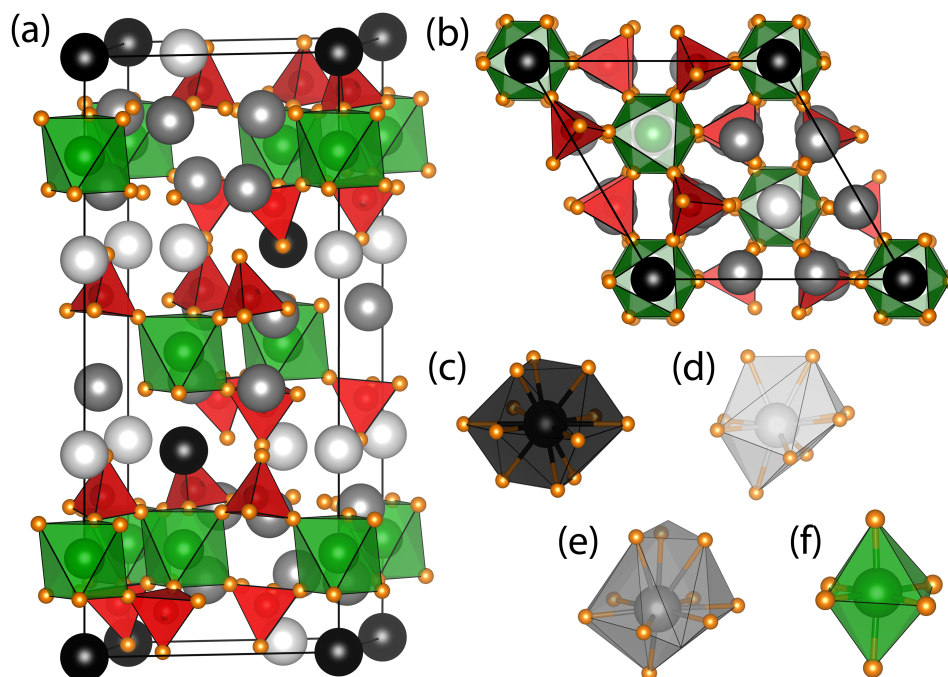
Figure 3.10: The structure of $Ba_9Y_2Si_6O_{24}$ (a) projected along near the [100] direction, (b) and the [001] direction. The oxygen polyhedra around (c) Ba1, (d) Ba2, (e) Ba3, and (f) Y. Reproduced with permission from reference [85], ©2013 American Chemical Society.

unsuccessful. The concentration of the impurity was limited by thoroughly mixing the starting materials using acetone as a grinding medium and following the heating profile described in the experimental section.

The as ground sample was imaged using the secondary electrons produced by a SEM, Figure 3.11, to determine the particle morphology, size, and size distribution. As is evident from the micrographs, the particles have a wide dispersion of sizes that are generally smaller than $\approx 10\,\mu$m, and various mor-
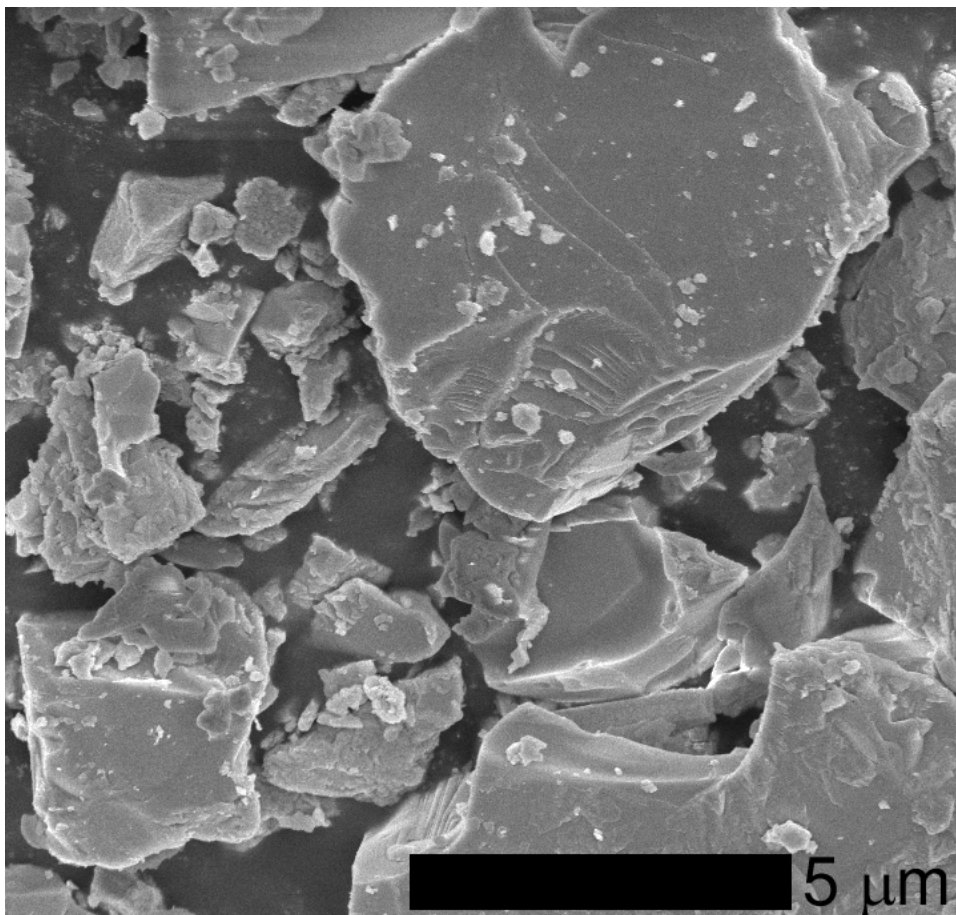
Figure 3.11: The sample imaged by the SEM secondary electrons shows a wide range of particle size including agglomerates of the smaller particles. Reproduced with permission from reference [85], ©2013 American Chemical Society.
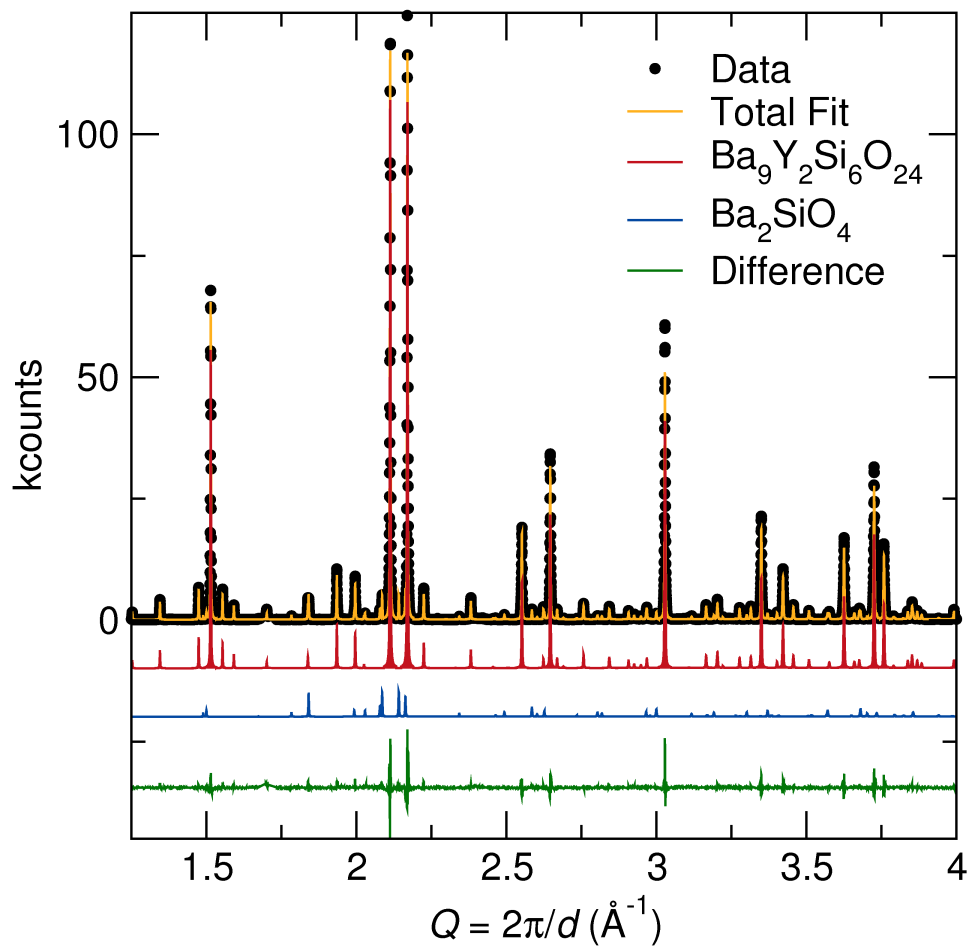
Figure 3.12: Synchrotron X-ray diffraction pattern of $Ba_9Y_2Si_6O_{24}$:Ce^{3+}. The pattern contains two phases, $Ba_9Y_2Si_6O_{24}$(red) and Ba_2SiO_4 (blue). Reproduced with permission from reference [85], ©2013 American Chemical Society.

Table 3.2: Rietveld refinement and crystal data for $Ba_9Y_2Si_6O_{24}$:Ce^{3+}.

refined formula	$Ba_9Y_2Si_6O_{24}$
radiation type	synchrotron X-ray (11-BM)
λ (Å)	0.413949
2θ range (degree)	0.5 to 49.995
temperature (K)	295
crystal system	trigonal
space group; Z	$R\bar{3}$ (No. 148); 3
lattice parameters (Å)	$a = 10.02892(1)$
	$c = 22.16790(4)$
volume (Å^3)	1930.92(1)
R_p (%)	10.3
R_{wp} (%)	12.9
$R_f{}^2$ (%)	7.4
χ^2	7.39

Table 3.3: Refined atomic coordinates and equivalent isotropic displacement parameters of $Ba_9Y_2Si_6O_{24}$:Ce^{3+} determined by Rietveld refinement of powder synchrotron X-ray diffraction data collected at room temperature. Atomic mixing of Ce^{3+} was not considered in the model due to its small concentration (3%). U_{eq} is defined as one-third of the trace of the orthogonalized U^{ij} tensor.

atom	site	x	y	z	U_{eq} ($\times 10^2$ Å^2)
Ba1	$3a$	0	0	0	2.18(4)
Ba2	$6c$	$\frac{1}{3}$	$\frac{2}{3}$	0.00394(5)	1.39(2)
Ba3	$18f$	0.02994(5)	0.66953(8)	0.10891(3)	0.99(1)
Y	$6c$	0	0	0.16481(6)	0.39(3)
Si	$18f$	0.3373(3)	0.01966(2)	0.07338(18)	0.28(4)
O1	$18f$	0.3592(5)	0.0664(5)	0.0042(2)	0.82(5)
O2	$18f$	0.4853(7)	0.1586(7)	0.1114(3)	0.82(5)
O3	$18f$	$-0.009(1)$	0.1702(7)	0.1011(2)	0.82(5)
O4	$18f$	0.1380(7)	0.4740(7)	0.0932(2)	0.82(5)

Table 3.4: Selected interatomic distances for $Ba_9Y_2Si_6O_{24}$:Ce^{3+}.

atoms	distance (Å)	atoms	distance (Å)
Ba1–O1 (6×)	3.321(6)	Ba1–O3 (6×)	2.849(6)
Ba2–O1 (3×)	2.907(5)	Ba2–O2 (3×)	3.119(8)
Ba2–O4 (3×)	2.774(6)	Ba3–O2	3.094(8)
Ba3–O1	2.535(5)	Ba3–O2	2.983(6)
Ba3–O2	3.107(6)	Ba3–O3	3.059(1)
Ba3–O4	2.710(6)	Ba3–O4	2.718(6)
Si–O1	1.586(5)	Ba3–O4	3.115(6)
Si–O2	1.669(5)	Y–O2 (3×)	2.190(7)
Si–O3	1.649(1)	Y–O3 (3×)	2.255(6)
Si–O4	1.634(8)		

phology. The $Ba_9Y_2Si_6O_{24}$ structure crystallizes in the $Ba_9Sc_2Si_6O_{24}$ structure-type[92] and was refined from this starting point using the Rietveld method with high-resolution, synchrotron X-ray powder diffraction data. Details of the refinement are presented in Table 3.2 and Table 3.3 while the refined X-ray pattern is presented in Figure 3.12. $Ba_9Y_2Si_6O_{24}$ crystallizes in rhombohedral space group $R\bar{3}$ (No. 148) with lattice parameters of $a = 10.02892(1)$ Å and $c = 22.16790(4)$ Å. It is composed of distorted, isolated SiO_4 tetrahedral units similar to the orthosilicates, *e.g.*, M_2SiO_4. However, in this structure the tetrahedra are corner-shared with YO_6 distorted octahedra (Figure 3.10f). Each YO_6 unit is connected *via* two tetrahedral units creating tetrahedra–octahedra–tetrahedra layers that stack along the [001] direction forming two-dimensional sheets. The SiO_4 tetrahedra are distorted with Si–O bond distances between 1.586(5) Å and 1.669(5) Å and O–Si–O angles ranging between 105.9(4)° and 117.9(3)°. Sim-

ilarly, the YO_6 octahedra has two different bond distance of $2.190(7)\,\text{Å}$ and $2.255(6)\,\text{Å}$ with O–Y–O bond angles distorted away from $90°$ ranging between $83.2(3)°$ and $97.1(3)°$. The structure also contains three independent Ba^{2+} sites. Ba1 occupies Wyckoff position $3a$ with three-fold inversion symmetry. It sits in-between the two-dimensional sheets and is coordinated by 12 oxygen atoms that form a distorted cubeoctahedron, as shown in Figure 3.10c. Six oxygen atoms surrounding the waist (Ba1–O1) have a bond distance of $3.321(6)\,\text{Å}$ while the remaining six oxygen atoms have shorter bond distances of $2.849(6)\,\text{Å}$. Ba2, Figure 3.10d, occupies Wyckoff site $6c$ and is coordinated to 9 oxygen atoms in a distorted, tri-capped trigonal prism. Ba3, Figure 3.10e, sits at a general position (Wyckoff site $18f$) and is connected to 10 oxygen atoms. The bond distances for additional selected interatomic bond distance are presented in Table 3.4.

To prepare the phosphor, Ce^{3+} (the luminescent center) is substituted for Y^{3+} following the composition $Ba_9(Y_{1-x}Ce_x)Si_6O_{24}$ ($x = 0$, 0.01, 0.03,$\ldots$0.09, 0.12). Because Ce^{3+} ($1.01\,\text{Å}$; 6-coord.) is larger than Y^{3+} ($0.900\,\text{Å}$; 6-coord.) the lattice parameters should increase with substitution[63]. As shown in Figure 3.13a, the lattice parameters actually decrease upon substitution. This discrepancy likely stems from Ce^{3+} occupying the Ba^{2+} sites as well as the Y^{3+} site. Because Ce^{3+} ($1.196\,\text{Å}$; 9-coord.) is much smaller than Ba^{2+} ($1.47\,\text{Å}$; 9-coord.), substitution at the Ba^{2+} and Y^{3+} sites could lead to the anomalous behavior observed here.
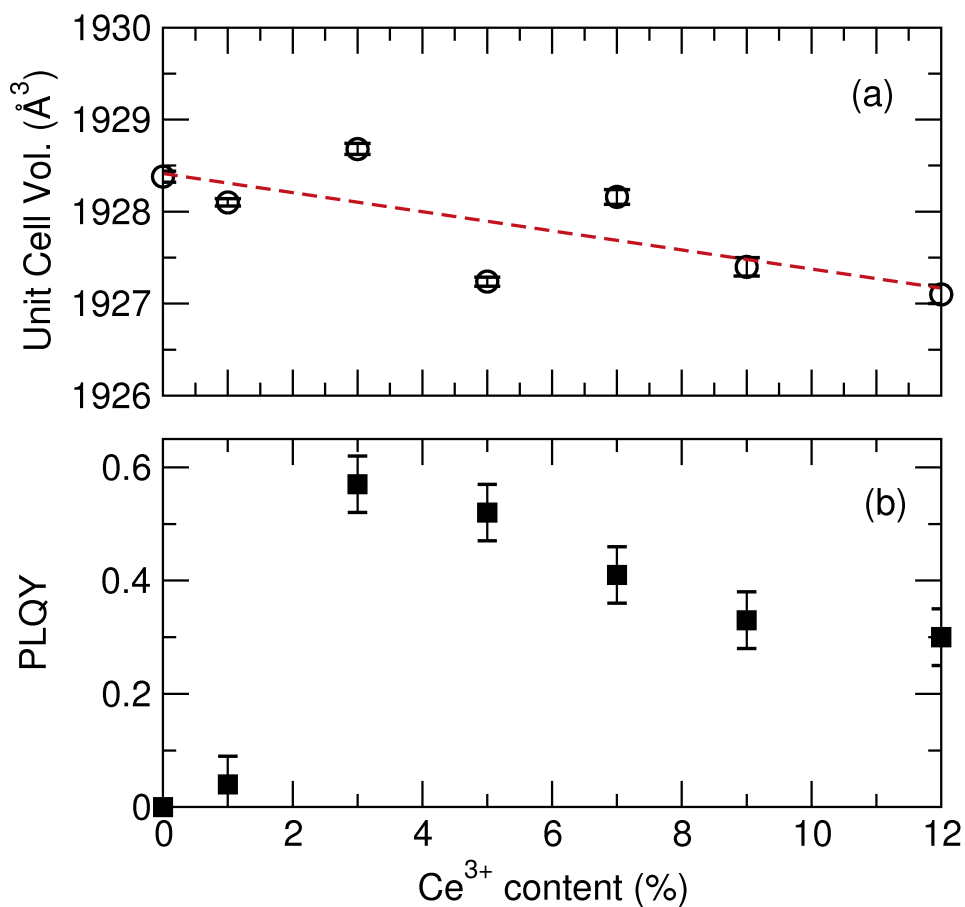
Figure 3.13: (a) The unit cell volume was determined for the compounds $Ba_9(Y_{1-x}Ce_x)Si_6O_{24}$ ($x = 0$, 0.01, 0.03, 0.05, 0.07, 0.09, 0.12) using a LeBail fit. (b) The optimum Ce^{3+} content was determined by varying the Ce content and measuring the PLQY excited at 405 nm. Standard error for the PLQY measurements are $\pm 5\%$. Reproduced with permission from reference [85], ©2013 American Chemical Society.

Attempts to refine the occupation of Ce^{3+} in the Rietveld refinement of the synchrotron X-ray powder diffraction data were unsuccessful. For instance, placing Ce^{3+} on the Y^{3+} site led to a non-physical, negative occupancy of Ce^{3+} at the site and therefore was not considered in the refinement. Nevertheless, the observed U_{eq} for Y^{3+} without Ce^{3+} is slightly smaller (presented in the Appendix) than expected indicating Ce^{3+} has likely substituted. Further analysis of the thermal parameters revealed a wide range of U_{eq} values for the Ba^{2+} sites ($8 \times 10^3 \, \text{Å}^2$ to $17 \times 10^3 \, \text{Å}^2$) further suggesting the possibility of Ba^{2+}/Ce^{3+} mixing. Although Ce^{3+}/Y^{3+} mixing could not be explicitly refined from the X-ray diffraction data, the optical properties confirm the presence of the substitution. Previously, the optical characterization of cerium-substituted $Ba_9Sc_2Si_6O_{24}{:}Ce^{3+}$ showed three excitation peaks from the presence of Ce^{3+} on the Ba^{2+} sites[84]. However, as discussed below, four peaks are present in $Ba_9Y_2Si_6O_{24}{:}Ce^{3+}$. The only structural difference between these two compounds is the presence of a ScO_6 versus YO_6 octahedral unit. Because Y^{3+} is closer in size to Ce^{3+} compared to Sc^{3+}, it follows that Ce^{3+} can substitute in the YO_6 but not the ScO_6 octahedra. The preparation of a Y–Sc solid solution, which is discussed in the final section of this paper, shows the evolution of the fourth peak as a function of the Y/Sc content further illustrating the dependence of the octahedral site composition.

As Figure 3.13b illustrates, the PLQY (excited at 405 nm) increases slightly with 1% Ce^{3+} substitution followed by a dramatic increase to maximum PLQY of 57% at 3% Ce^{3+} substitution. Additional Ce^{3+} decreases the quantum yield owing to concentration quenching affects arising from an energy transfer from one luminescent center to another. The critical distance of this energy transfer process (R_c) can be calculated using Equation 3.2 where V is the unit cell volume, x_c is the critical Ce^{3+} concentration, and N is the number of lattice sites in the unit cell that can be occupied by activator ions (the Wyckoff multiplicity of the activator sites).[101]

$$R_c \approx 2 \left[\frac{3V}{4\pi x_c N} \right]^{\frac{1}{3}} \tag{3.2}$$

In $Ba_9Y_2Si_6O_{24}$:Ce^{3+}, $x_c = 0.03$ and $V = 1928.68(6)\,Å^3$. The number of Ce^{3+} sites in the unit cell has a range between $N = 6$ and $N = 33$ depending on the substitution of Ce^{3+} on the Ba^{2+} sites. Using these values the resulting critical energy transfer distance ranges between 7.1 Å to 12.7 Å. These quenching distances are similar to those determined in other phosphors; $CaMgSi_2O_6$:Eu^{2+}[102] has a critical distance of 12 Å, $Ba_2ZnSi_2O_7$:Eu^{2+} has a R_c of 19 Å,[103] and the industry standard phosphor YAG:Ce^{3+} has a R_c of 16–18 Å.

The room temperature (298 K) and low temperature (77 K) excitation and emission spectra of $Ba_9Y_{1.94}Ce_{0.06}Si_6O_{24}$ are presented in Figure 3.14a and Fig-
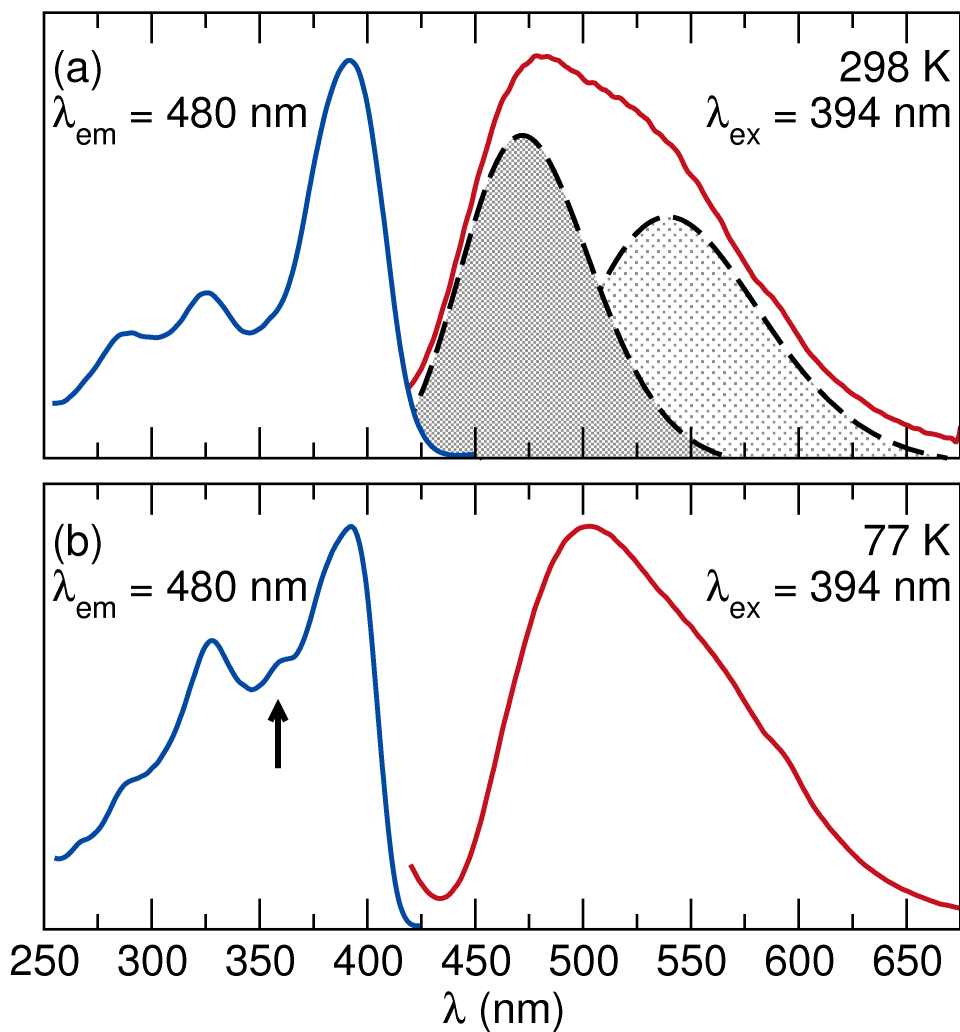
Figure 3.14: (a) Room temperature (298 K) and (b) low temperature (77 K) excitation (λ_{em} = 480 nm) and emission (λ_{ex} = 394 nm) spectra of $Ba_9Y_{1.94}Ce_{0.06}Si_6O_{24}$. The emission peak is fit by two Gaussian curves separated by $\approx$2600 cm^{-1}. Reproduced with permission from reference [85], ©2013 American Chemical Society.

ure 3.14b, respectively. The 298 K excitation spectra, collected using $\lambda_{em} =$ 480 nm, extends from 250 nm to 420 nm and contains three peaks. The two highest energy (shortest wavelength) peaks are attributed to Ce^{3+} occupying the Ba^{2+} site as these peaks occur in nearly the same energy range as in the scandium series, $Ba_9Sc_2Si_6O_{24}$:Ce^{3+}, Li^+.[84] Although the scandium series contains three peaks arising from the three independent Ba^{2+} sites, only two peaks are observed in the room temperature data. The low temperature excitation spectra reveals the third peak (highlighted by an arrow in Figure 3.14b) completing the three expected peaks from the Ba^{2+} sites. The main excitation peak occurs at $\lambda_{max} = 394$ nm from Ce^{3+} occupying the pseudo-octahedral coordination of the Y^{3+} site. This peak is not observed in $Ba_9Sc_2Si_6O_{24}$:Ce^{3+}, Li^+ because the ScO_6 octahedral volume (12.43 $Å^3$) is too small for the Ce^{3+} ion. Here, the YO_6 octahedral volume is 15% larger (14.66 $Å^3$) affording enough room for Ce^{3+} substitution. Despite the volume increase, Ce^{3+} is still too large for the YO_6 octahedra resulting in short Ce–O bonds. As illustrated in Equation 3.3, the crystal-field splitting, Δ, is inversely related to the bond distance, R, where Z is the anionic charge, e is the charge of the electron, and r is the radius of the $5d$-wavefunctions [24].

$$\Delta = \frac{Ze^2r^4}{6R^5} \tag{3.3}$$

This clearly illustrates the longer wavelength position of the excitation band

centered at 394 nm emerges from squeezing Ce^{3+} on the smaller yttrium site while the shorter wavelength peaks stem from Ce^{3+} sitting on the larger Ba^{2+} sites.

The emission spectra, collected using $\lambda_{ex} = 394$ nm, is broad extending from 400 nm to 675 nm. This data can be fit by two Gaussian curves separated by approximately 2600 cm^{-1} corresponding to the spin-orbit assisted $^2D_{3/2}$ to $^2F_{5/2}$ and $^2F_{7/2}$ transitions.[72] The position of the emission λ_{max} for this system does not appear to be dependent on the concentration of Ce^{3+} substitution. As a note, the excitation of $Ba_{1.94}Ce_{0.06}SiO_4$ at 394 nm did not yield an emission signal confirming the observed luminescent properties are from the desired phase. When $Ba_{1.94}Ce_{0.06}SiO_4$ was excited at 351 nm a PLQY $\approx$50% resulted. From the 298 K emission spectra, the CIE chromaticity coordinates, illustrated in Figure 3.15, are determined to be (0.241, 0.339) giving a blue-green emission.

The temperature dependence of the quantum yield was also determined for $Ba_9Y_2Si_6O_{24}$ and compared to the standard YAG:Ce^{3+}. In YAG:Ce^{3+}, the emission intensity approaches 100% below room temperature and is relatively constant. The room temperature PLQY is $\approx$90%, which is in agreement with the measurements taken from the integrating sphere. For $Ba_9Y_2Si_6O_{24}$, the relative PLQY as a function of temperature was determined by comparing the integrated intensities against the largest peak (at 295 K) and then scaled by the room tem-

perature PLQY determined from the integrating sphere (57%). Interestingly, the relative PLQY decreases with decreasing temperature dropping by nearly 20% by 77 K. Although this anomaly has been observed in systems that contain an energy-transfer process,[104] a mechanism in this system is unclear and requires further investigation. At 77 K emission spectra is red-shifted by approximately 20 nm from the room temperature data. This shift in emission wavelength causes the CIE coordinates to strongly red-shift, (0.285, 0.442), giving a more green emission. This change follows a contraction of the lattice parameters (and bond distances) at low temperature, again, leading to stronger crystal field splitting and the observed red-shift.

High temperature quenching studies of $Ba_9Y_{1.94}Ce_{0.06}Si_6O_{24}$ show the phosphor has excellent quenching characteristics. The relative PLQY, Figure 3.16a, decreases by only 25% of the room temperature efficiency at 500 K. This small drop indicates this phosphor host is more thermally robust than many other silicates. For example, M_2SiO_4:Eu^{2+} (M = Sr, Ba) decrease to 50% of room temperature efficiency around 400 K, much lower than the silicate presented here.[87] In fact, this phosphor has thermal quenching characteristics that approach the industry standard YAG:Ce^{3+}, which is also shown for comparison in Figure 3.16a.[14] The difference in thermal quenching properties likely arises from the connectivity of the compounds. For instance, the M_2SiO_4
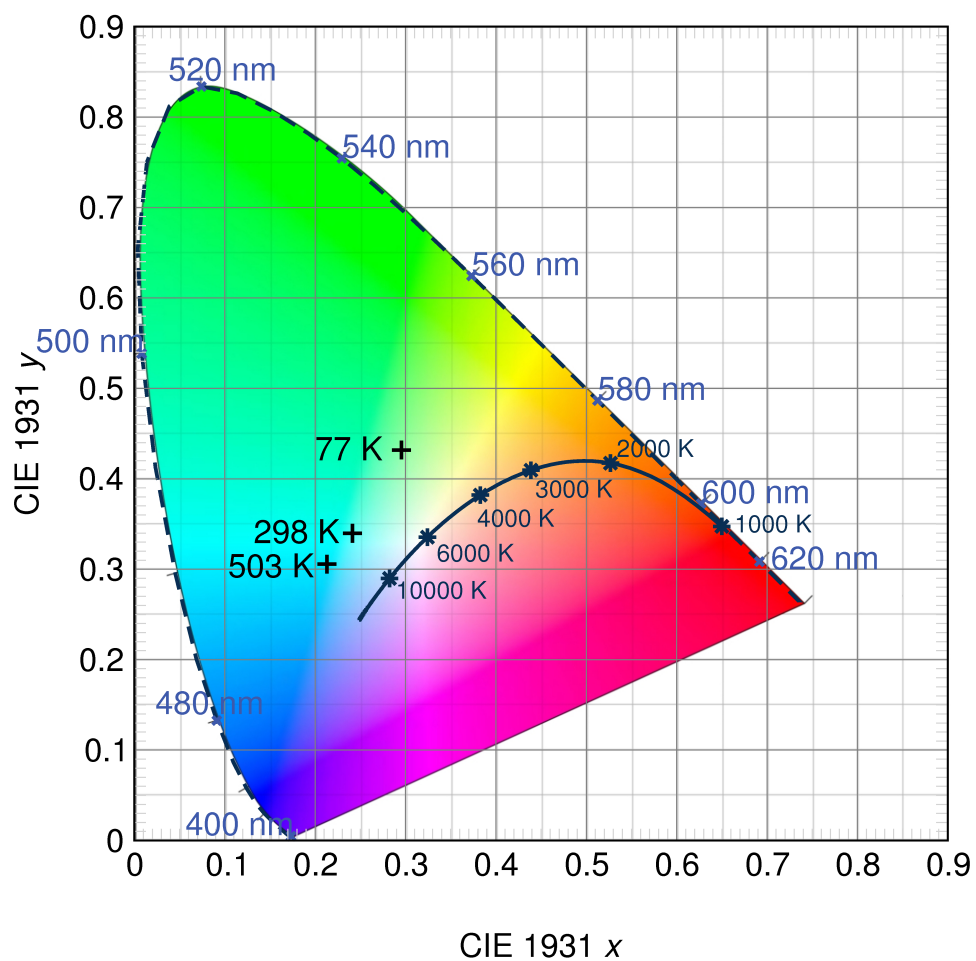
Figure 3.15: CIE color coordinates of $Ba_9Y_{1.94}Ce_{0.06}Si_6O_{24}$ at low temperature (77 K), room temperature (298 K), and high temperature (503 K) show the true color of the phosphor taking into account the broad emission spectra. Reproduced with permission from reference [85], ©2013 American Chemical Society.
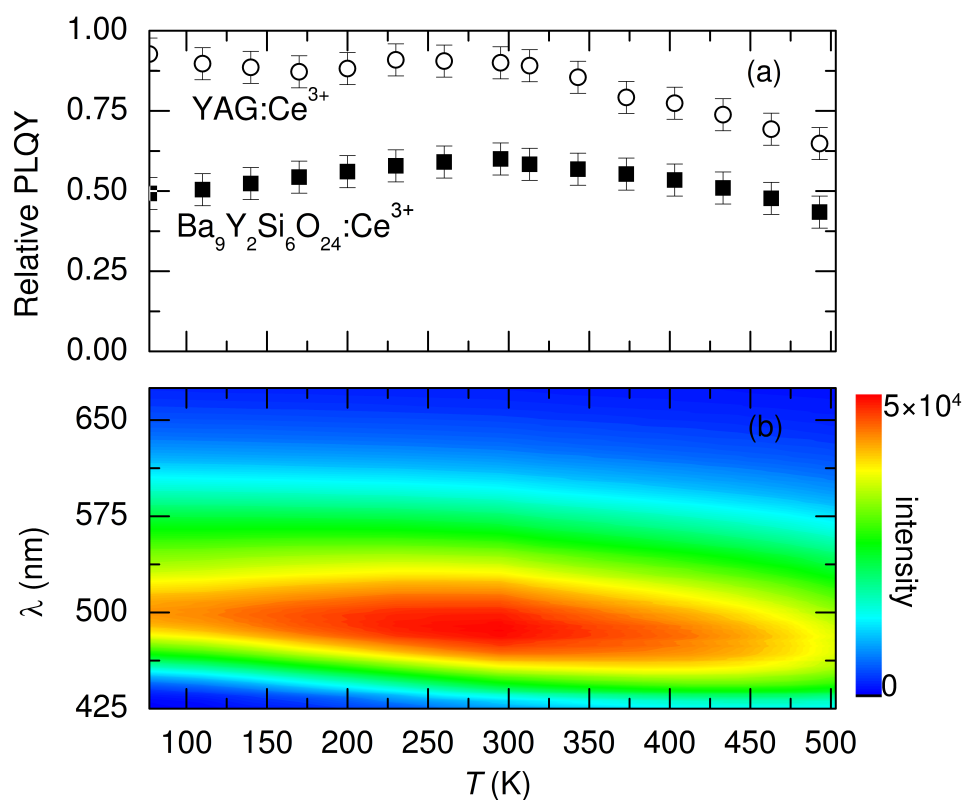
Figure 3.16: (a) The temperature dependence of the relative integrated PL intensity for $Ba_9Y_{1.94}Ce_{0.06}Si_6O_{24}$ (squares) shows a decrease of only 25% of room temperature quantum yield at 500 K, indicating this phosphor has thermal quenching properties on par with the industry standard, YAG:Ce^{3+} (circles)[14]. (b) A minimal red-shift and decrease in emission intensity are observed for $Ba_9Y_2Si_6O_{24}$ at temperatures below 295 K while blue shift of the emission intensity is observed for with increasing temperature. Reproduced with permission from reference [85], ©2013 American Chemical Society.

phosphors contain isolated SiO_4 tetrahedral units, that when excited have a greater degree of freedom allowing for an increase in non-radiative relaxation via active phonon pathways. YAG:Ce^{3+} is fully connected with corner-shared tetrahedra-octahedra units that limits the vibrational degrees of freedom, improving the quenching characteristics. The connectivity in $Ba_9Y_{1.94}Ce_{0.06}Si_6O_{24}$ is closer to YAG:Ce^{3+} containing corner-shared tetrahedra-octahedra. Even though $Ba_9Y_{1.94}Ce_{0.06}Si_6O_{24}$ only contains two-dimensional sheets rather than the three-dimensional connectivity of YAG:Ce^{3+}, it appears even the two-dimensional connections make the lattice rigid enough to limit quenching of the phosphor. Because of these excellent thermal quenching characteristics, optimizing this phosphor to increase the room temperature PLQY will yield an excellent, thermally stable blue-green phosphor. In addition to the decrease in PLQY there is a blue-shift of approximately 15 nm with increasing temperature, illustrated in Figure 3.16b. This leads to CIE coordinates of (0.213, 0.306). As with the red-shift in low temperature measurements, the higher temperatures cause an increase in the unit cell dimensions and corresponding Ce–O bond distances that decreases crystal field splitting.

Although $Ba_9Y_2Si_6O_{24}$:Ce^{3+} is an efficient blue-green phosphor, device integration would still require the addition of a red phosphor to improve color rendering. Alternatively, red-shifting $Ba_9Y_2Si_6O_{24}$:Ce^{3+} could alleviate the need

110

for an external red component. As was shown in $(Ba_{1-x}Sr_x)_9Sc_2Si_6O_{24}:Ce^{3+}, Li^+$,

substituting the smaller Sr^{2+} for the larger Ba^{2+} leads to a substantial decrease

in the lattice parameters causing an increase in the crystal field splitting of the

cerium ions red-shifting the emission spectra. Attempts to prepare a similar solid

solution with yttrium, *e.g.*, $(Ba_{1-x}Sr_x)_9Y_2Si_6O_{24}:Ce^{3+}$, did not lead to a forma-

tion of the desired phase and instead yielded a mix of Sr and Ba silicates. Thus,

to red-shift the spectra, a solid solution following $Ba_9(Y_{1-y}Sc_y)_2Si_6O_{24}:Ce^{3+}$ (y

= 0, 0.05, 0.1,...0.25) was prepared. The Sc content (y) was limited to less

than 25% because the absorption peak at 395 nm decreases beyond a point that

would make this compound a viable near-UV excited phosphor. Performing a

Rietveld refinement on these samples (y = 0.1 and 0.2; presented in the Ap-

pendix) indicates the expected decrease in lattice parameters as the smaller Sc^{3+}

is substituted for Y^{3+} [63] and only minor changes in the atomic positions. Sub-

stituting 10% and 20% of scandium to the structure leads to a respective unit cell

volume decrease of $\approx$7 $Å^3$ and 14 $Å^3$ compared to $Ba_9Y_2Si_6O_{24}$. Although this is

a minor change in the volume, because Ce^{3+} is already squeezed on the Y/Sc–O

site, this shortens the bonds Ce–O even more. As discussed in Equation 3.3, the

shorter bond distances lead to an increased crystal field splitting and a red-shift

in the emission spectra as is observed in Figure 3.17b and Figure 3.17d for y =

0.1 and 0.2.
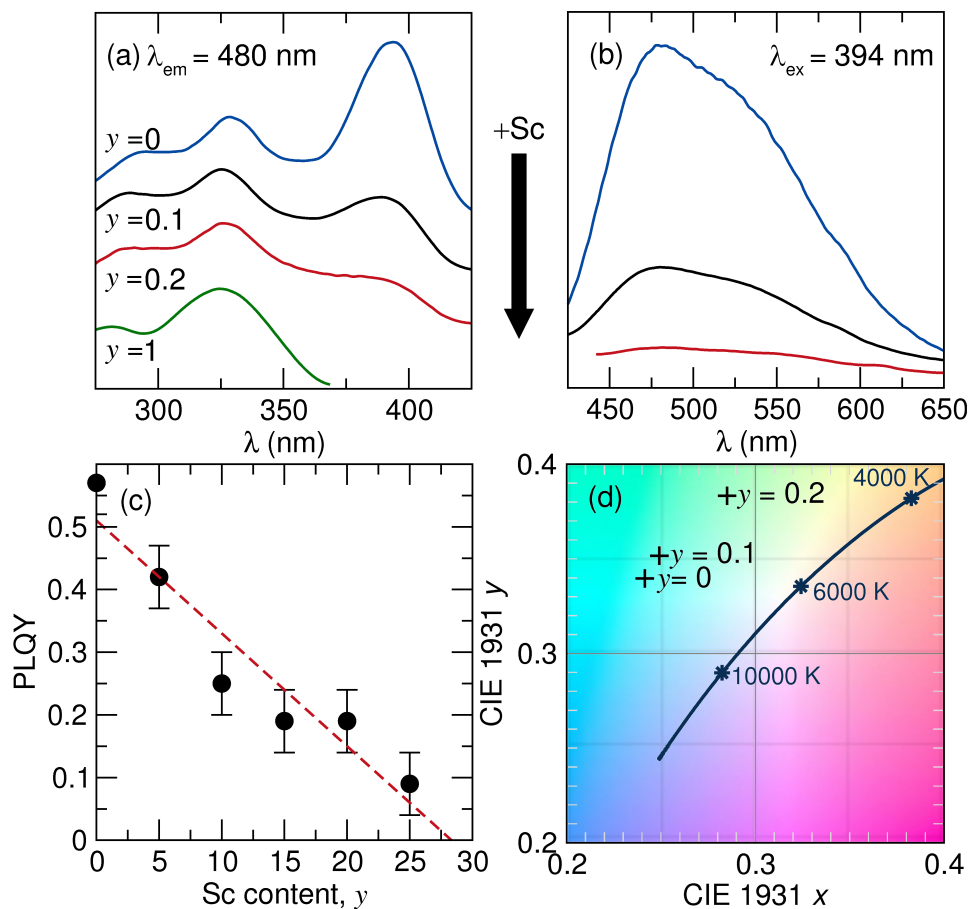
Figure 3.17: (a) The excitation spectra and (b) emission spectra for the solid solution of $Ba_9(Y_{1-y}Sc_y)_{1.94}Ce_{0.06}Si_6O_{24}$ show the changes associated with the peak at λ_{max} = 394 nm. For comparison $Ba_9Sc_2Si_6O_{24}$ is shown in green[84] (c) The PLQY decreases nearly linearly in the solid solution $Ba_9(Y_{1-y}Sc_y)_{1.94}Ce_{0.06}Si_6O_{24}$. (d) CIE color coordinates of $Ba_9(Y_{1-y}Sc_y)_{1.94}Ce_{0.06}Si_6O_{24}$ at room temperature show the red-shift of the emission peak with increasing Sc concentration. Reproduced with permission from reference [85], ©2013 American Chemical Society.

Although the desired red-shift can be achieved by substituting Sc in a solid solution, at relatively low substitution levels, $y > 0.25$, the (Y/Sc)O$_6$ pseudo-octahedral volume becomes too small for the larger Ce^{3+} limiting substitution at the site. This is reflected in the excitation spectra for Ba$_9$(Y$_{1-y}$Sc$_y$)$_{1.94}$Ce$_{0.06}$Si$_6$O$_{24}$ ($y = 0, 0.1, 0.2$), Figure 3.17a. A sharp decrease in the intensity of the peak at 394 nm is observed as the concentration of Ce^{3+} decreases due to the volume constraints. A corresponding decrease in the observed emission intensity when excited at 394 nm (Figure 3.17b) arises due to the limited absorption. With the decrease in excitation/emission intensity, the PLQY decreases nearly linear from PLQY = 57% for the $y = 0$ to PLQY = 10% for $y = 0.25$. Although the desired red-shift in the emission spectrum is achieved as indicated through CIE color coordinates, illustrated in Figure 3.17d, the substantial decrease in PLQY means careful optimization of the Ce^{3+} content and Sc^{3+} content will be required.

3.4   Conclusions

We have presented the preparation and characterization of a new near-UV to blue phosphors, cerium-substituted (Ba$_{1-x}$Sr$_x$)$_{8.46}$(Ce$_{0.27}$Li$_{0.27}$)Sc$_2$Si$_6$O$_{24}$ ($x = 0, 0.25, 0.50, 0.75, 1$). The compounds can be prepared nearly pure

phase across the entire range using traditional solid-state routes. The excitation spectra contains three peaks indicating cerium substitution on all three of the crystallographic independent alkaline earth sites. The emission of the pure $Ba_{8.46}(Ce_{0.27}Li_{0.27})Sc_2Si_6O_{24}$ occurs in the near-UV region while Sr substitution leads to a red-shift in the emission spectra resulting in blue emission from the pure $Sr_{8.46}(Ce_{0.27}Li_{0.27})Sc_2Si_6O_{24}$. The change in emission characteristic arises from a 5-10% decrease in the alkaline earth-oxygen bond length with Sr subtraction due to the smaller size of Sr^{2+} versus Ba^{2+}. Finally, the quantum yield for the pure Ba phase is 15% and increases to 20% with Sr substitution. Because of the broad excitation in the near-UV region and emission in the blue, these compounds are potentially useful as light conversion phosphors.

The identification of a novel barium yttrium silicate, $Ba_9Y_2Si_6O_{24}$, phase has provided a new host for a cerium-activated phosphor. The compound can be prepared nearly pure phase using conventional high temperature preparation methods and the structure solved using synchrotron X-ray powder diffraction. It is isostructural with $Ba_9Sc_2Si_6O_{24}$ and contains SiO_4–YO_6–SiO_4 layers that stack along the [001] direction forming infinite sheets. When Ce^{3+} is substituted in the structure, it occupies the Ba^{2+} and the Y^{3+} sites. The strong crystal field splitting of the pseudo-octahedral coordination environment leads to an excitation with a λ_{max} of 394 nm. When this peak is excited using near-UV light,

an efficient ($\approx$60%) blue-green emission is produced. Temperature-dependent measurements show a red-shift in the emission spectra at 77 K due to the contraction of the unit cell at low temperatures. At elevated temperatures the photoluminescence shows a decrease of only 25% at 500 K, outperforming many other Ce^{3+}-substituted silicate phosphors. Finally, a red-shift in the emission spectrum can be achieved by increasing the crystal field splitting of the pseudo-octahedral site by decreasing the polyhedral volume through the preparing the solid solution $Ba_9(Y_{1-y}Sc_y)_2Si_6O_{24}$:$Ce^{3+}$. Although a red-shift is obtained, a decrease in the PLQY accompanies the Y^{3+}/Sc^{3+} mixing. Nevertheless, careful optimization of the Ce^{3+} content and Sc^{3+} concentration can lead to an ideal blue-green phosphor. These photoluminescent characteristics make this new cerium-substituted phosphor a good candidate to cover the blue-green portion of the visible spectrum leading to a better white LED.

3.5   Appendix
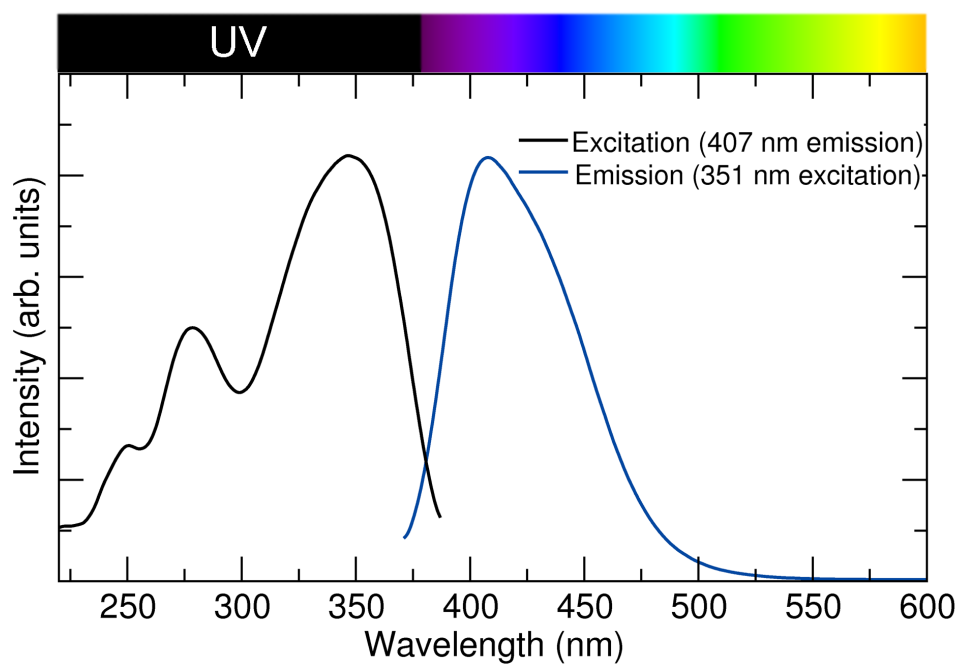
Figure 3.18: The excitation and emission spectra for Sr_2SiO_4:Ce^{3+}/Li^+ prepared at 1300 for 5 hours. This sample was prepared to compare the optical properties of the silicates. Reproduced with permission from reference [84], ©2013 Elsevier.
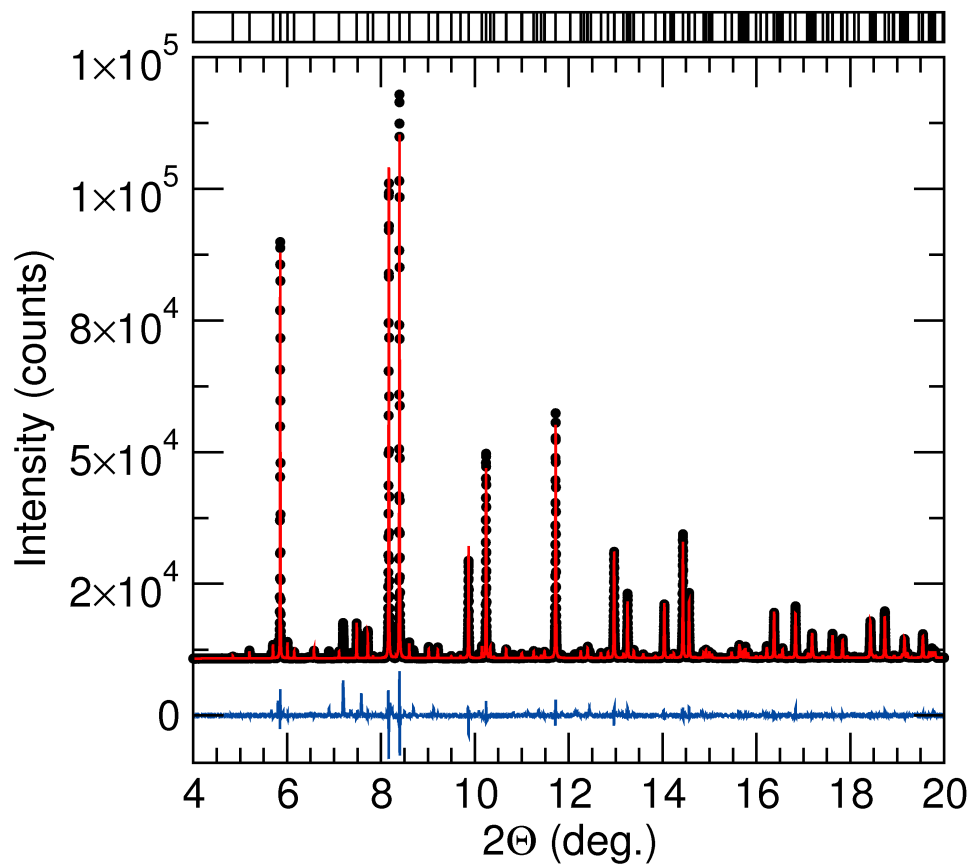
Figure 3.19: Rietveld refinement of $(Ba_{0.75}Sr_{0.25})_9Sc_2Si_6O_{24}$. The black circles are the data collected using synchrotron radiation ($\lambda = 0.413949$) at 11-BM, Advanced Photon Source; the red line is the Rietveld fit; blue is the difference line. Reproduced with permission from reference [84], ©2013 Elsevier.
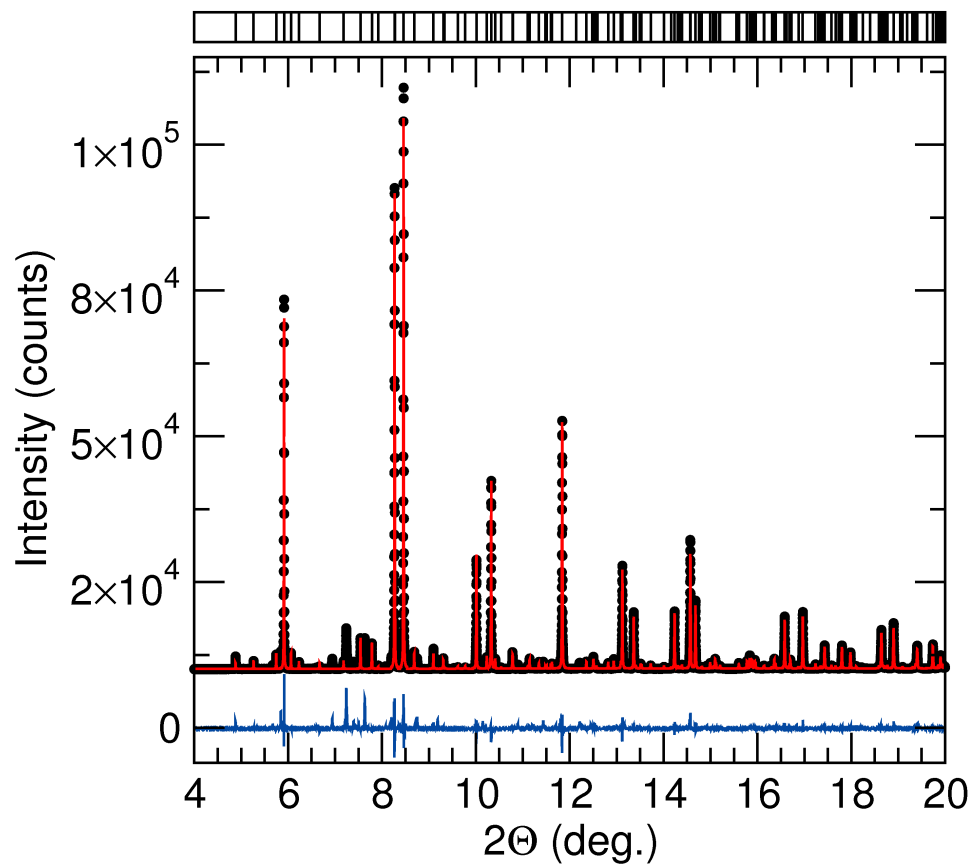
Figure 3.20: Rietveld refinement of $(Ba_{0.50}Sr_{0.50})_9Sc_2Si_6O_{24}$. The black circles are the data collected using synchrotron radiation ($\lambda = 0.413949$) at 11-BM, Advanced Photon Source; the red line is the Rietveld fit; blue is the difference line. Reproduced with permission from reference [84], ©2013 Elsevier.
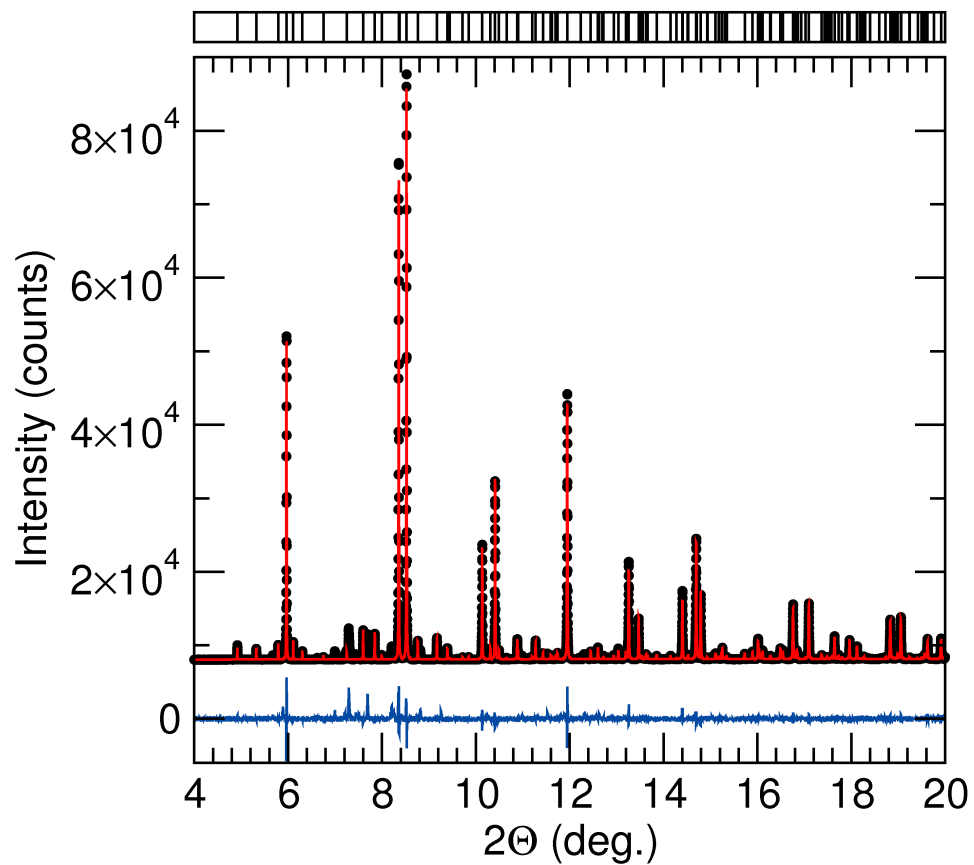
Figure 3.21: Rietveld refinement of $(Ba_{0.25}Sr_{0.75})_9Sc_2Si_6O_{24}$. The black circles are the data collected using synchrotron radiation ($\lambda = 0.413949$) at 11-BM, Advanced Photon Source; the red line is the Rietveld fit; blue is the difference line. Reproduced with permission from reference [84], ©2013 Elsevier.
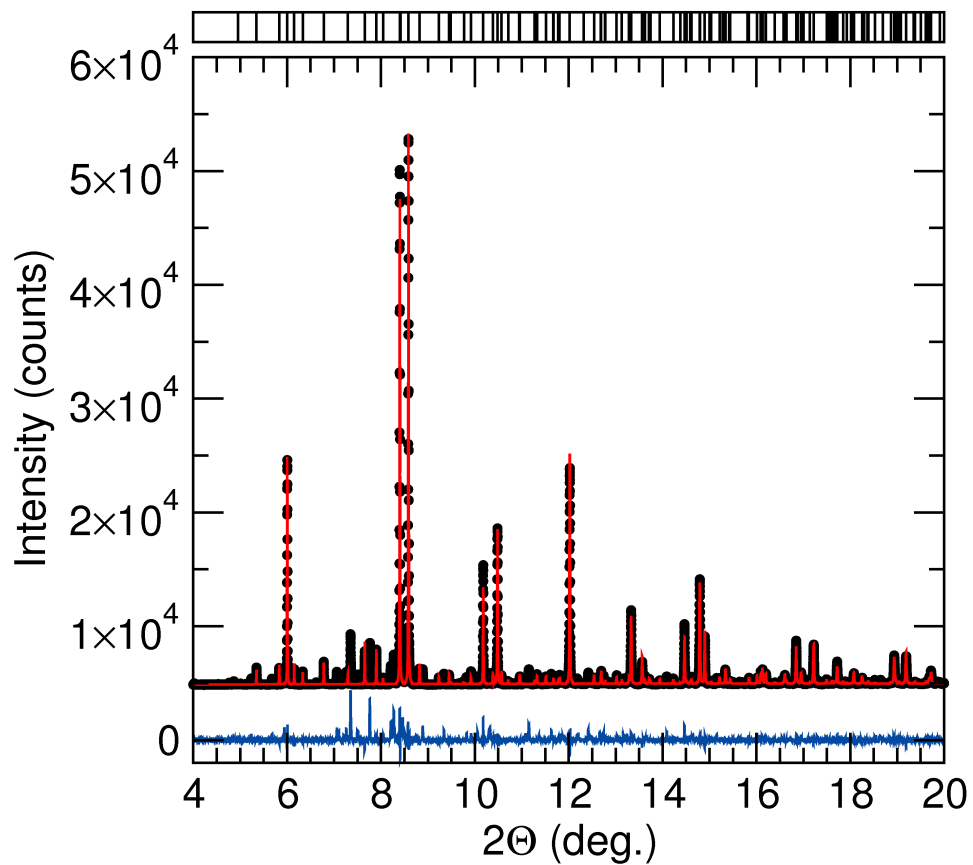
Figure 3.22: Rietveld refinement of $Sr_9Sc_2Si_6O_{24}$. The black circles are the data collected using synchrotron radiation ($\lambda = 0.413949$) at 11-BM, Advanced Photon Source; the red line is the Rietveld fit; blue is the difference line. Reproduced with permission from reference [84], ©2013 Elsevier.

Table 3.5: Rietveld refinement results for $(Ba_{1-x}Sr_x)_9Sc_2Si_6O_{24}$ $(x = 0\text{--}1)$ indicating the refined lattice parameters, atomic volume, and residuals

	$x = 0$	$x = 0.25$	$(Ba_{1-x}Sr_x)_9Sc_2Si_6O_{24}$ $(x = 0\text{--}1)$ $x = 0.50$	$x = 0.75$	$x = 1$
radiation type			synchrotron X-ray (11-BM)		
λ (Å)			0.413949		
2θ range (degree)			0.5 to 49.995		
temperature (K)			295		
crystal system			trigonal		
space group; Z			$R\bar{3}$ (No.148); 3		
lattice parameters (Å)	$a = 9.87063(3)$	$a = 9.79664(1)$	$a = 9.71876(1)$	$a = 9.64732(1)$	$a = 9.57778(2)$
	$c = 21.93601(1)$	$c = 21.66208(1)$	$c = 21.34605(5)$	$c = 21.08554(4)$	$c = 20.9986(7)$
volume (Å^3)	1850.88(1)	1801.174(2)	1746.466(4)	1699.530(4)	1668.246(6)
R_p (%)	12.2	10.7	14.0	12.6	16.3
R_{wp} (%)	19.4	17.9	21.0	19.8	25.1

Table 3.6: Atomic coordinates, occupancy, and equivalent isotropic displacement parameters (U_{iso}) for $Ba_9Sc_2Si_6O_{24}$ refined from synchrotron X-ray powder diffraction data.

atom	site	x	y	z	occupancy	U_{iso} ($\times 10^2$ Å^2)
Ba1	$3a$	0	0	0	1	0.0082(1)
Ba2	$6c$	$\frac{1}{3}$	$\frac{2}{3}$	0.00306(6)	1	0.82(1)
Ba3	$18f$	0.02605(7)	0.6702(1)	0.10833(4)	1	0.82(1)
Sc1	$6c$	0	0	0.1647(2)	1	0.81(7)
Si1	$18f$	0.3389(3)	0.0226(3)	0.0760(1)	1	0.60(6)
O1	$18f$	0.361(8)	0.0740(8)	0.0065(3)	1	1.74(8)
O2	$18f$	0.490(1)	0.166(1)	0.1135(3)	1	1.74(8)
O3	$18f$	−0.011(1)	0.163(1)	0.1042(3)	1	1.74(8)
O4	$18f$	0.140(1)	0.477(1)	0.0961(3)	1	1.74(8)

Table 3.7: Atomic coordinates, occupancy, and equivalent isotropic displacement parameters (U_{iso}) for $(Ba_{0.75}Sr_{0.25})_9Sc_2Si_6O_{24}$ refined from synchrotron X-ray powder diffraction data.

atom	site	x	y	z	occupancy	U_{iso} ($\times 10^2$ Å^2)
Ba/Sr1	$3a$	0	0	0	0.81(1)/0.19	1.50(5)
Ba/Sr2	$6c$	$\frac{1}{3}$	$\frac{2}{3}$	0.00350(6)	0.69(2)/0.31	1.24(4)
Ba/Sr3	$18f$	0.02711(8)	0.6702(1)	0.10971(4)	0.71(1)/0.29	0.89(2)
Sc1	$6c$	0	0	0.1660(2)	1	0.77(7)
Si1	$18f$	0.3388(1)	0.0214(3)	0.0757(1)	1	1.15(6)
O1	$18f$	0.3604(6)	0.0677(6)	0.0044(3)	1	1.34(9)
O2	$18f$	0.4937(8)	0.1576(8)	0.1131(3)	1	1.34(9)
O3	$18f$	−0.0204(9)	0.1610(8)	0.1014(3)	1	1.34(9)
O4	$18f$	0.1427(8)	0.4713(8)	0.0980(3)	1	1.34(9)

Table 3.8: Atomic coordinates, occupancy, and equivalent isotropic displacement parameters (U_{iso}) for $(Ba_{0.50}Sr_{0.50})_9Sc_2Si_6O_{24}$ refined from synchrotron X-ray powder diffraction data.

atom	site	x	y	z	occupancy	U_{iso} ($\times 10^2$ Å^2)
Ba/Sr1	$3a$	0	0	0	0.71(1)/0.29	1.19(5)
Ba/Sr2	$6c$	$\frac{1}{3}$	$\frac{2}{3}$	0.00417(7)	0.78(1)/0.22	1.18(3)
Ba/Sr3	$18f$	0.02805(9)	0.6702(1)	0.11150(4)	0.25(1)/0.75	1.53(2)
Sc1	$6c$	0	0	0.1646(2)	1	0.45(6)
Si1	$18f$	0.3389(4)	0.0178(4)	0.0745(1)	1	1.97(8)
O1	$18f$	0.3501(7)	0.0495(6)	0.0029(3)	1	0.77(8)
O2	$18f$	0.4875(8)	0.1771(8)	0.1101(3)	1	0.77(8)
O3	$18f$	−0.004(1)	0.1672(8)	0.1028(3)	1	0.77(8)
O4	$18f$	0.1363(8)	0.4820(9)	0.0992(3)	1	0.77(8)

Table 3.9: Atomic coordinates, occupancy, and equivalent isotropic displacement parameters (U_{iso}) for $(Ba_{0.25}Sr_{0.75})_9Sc_2Si_6O_{24}$ refined from synchrotron X-ray powder diffraction data.

atom	site	x	y	z	occupancy	U_{iso} ($\times 10^2$ Å^2)
Ba/Sr1	$3a$	0	0	0	0.57(1)/0.43	1.5(1)
Ba/Sr2	$6c$	$\frac{1}{3}$	$\frac{2}{3}$	0.00437(6)	0.64(1)/0.36	1.3(3)
Ba/Sr3	$18f$	0.02940(8)	0.6702(1)	0.11260(4)	0.04(1)/0.96	0.9(1)
Sc1	$6c$	0	0	0.1650(2)	1	0.2(1)
Si1	$18f$	0.3362(3)	0.0160(3)	0.0737(8)	1	0.34(5)
O1	$18f$	0.3514(6)	0.0470(5)	0.0007(2)	1	0.67(7)
O2	$18f$	0.4826(7)	0.1734(7)	0.1082(3)	1	0.67(7)
O3	$18f$	0.0098(7)	0.1764(6)	0.1042(3)	1	0.67(7)
O4	$18f$	0.1400(6)	0.4870(7)	0.0971(2)	1	0.67(7)

Table 3.10: Atomic coordinates, occupancy, and equivalent isotropic displacement parameters (U_{iso}) for $Sr_9Sc_2Si_6O_{24}$ refined from synchrotron X-ray powder diffraction data.

atom	site	x	y	z	occupancy	U_{iso} ($\times 10^2$ Å^2)
Sr1	$3a$	0	0	0	1	1.7(2)
Sr2	$6c$	$\frac{1}{3}$	$\frac{2}{3}$	0.0063(1)	1	1.7(2)
Sr3	$18f$	0.0303(1)	0.6704(2)	0.1100(1)	1	1.7(2)
Sc1	$6c$	0	0	0.1627(2)	1	1.0(7)
Si1	$18f$	0.3354(4)	0.0166(4)	0.07391(1)	1	1.0(7)
O1	$18f$	0.3607(9)	0.059(9)	0.0050(4)	1	3(1)
O2	$18f$	0.502(1)	0.173(1)	0.1121(4)	1	3(1)
O3	$18f$	−0.012(1)	0.168(1)	0.0986(4)	1	3(1)
O4	$18f$	0.145(1)	0.486(1)	0.0973(4)	1	3(1)

Table 3.11: Rietveld refinement and crystal data for $Ba_9(Y_{1-y}Sc_y)_2Si_6O_{24}$:$Ce^{3+}$ ($y =$ 0.1, 0.2).

refined formula	$Ba_9Y_{1.8}Sc_{0.2}Si_6O_{24}$	$Ba_9Y_{1.6}Sc_{0.4}Si_6O_{24}$
radiation type	synchrotron X-ray (11-BM)	
λ (Å)	0.413949	
2θ range (degree)	0.5 to 49.995	
temperature (K)	295	
crystal system	trigonal	
space group; Z	$R\bar{3}$ (No. 148); 3	
lattice parameters (Å)	$a = 10.01566(1)$	$a = 10.00249(3)$
	$c = 22.14108(4)$	$c = 22.1303(1)$
volume (Å^3)	1923.48(1)	1917.49(1)
R_p (%)	9.3	11.8
R_{wp} (%)	13.1	16.8
$R_f{}^2$ (%)	6.2	12.9
χ^2	10.3	16.0
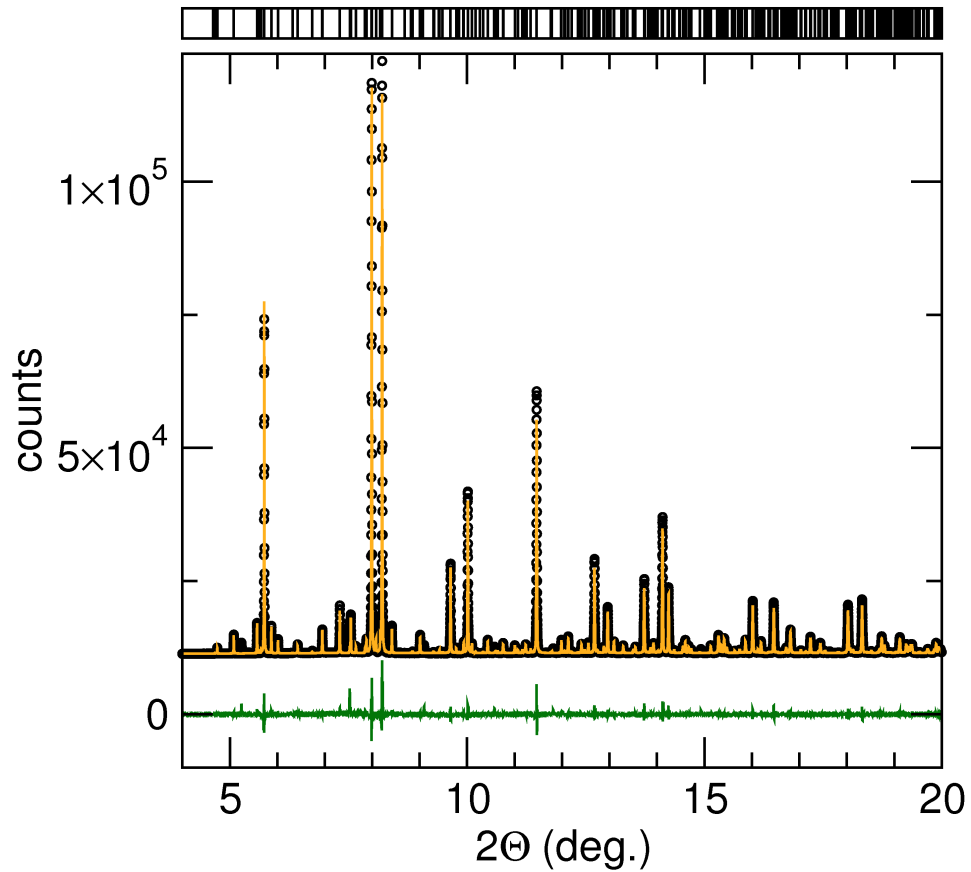
Figure 3.23: The diffraction pattern was collected for the loaded composition, $Ba_9(Y_{1-y}Sc_y)_{1.94}Ce_{0.06}Si_6O_{24}$ ($y = 0.1$). A Rietveld refinement (the total fit is orange, the difference line is green) was preformed to determine the lattice parameters and atomic positions. Reproduced with permission from reference [85], ©2013 American Chemical Society.

Table 3.12: Refined atomic coordinates and equivalent isotropic displacement parameters for a loaded composition of $Ba_9(Y_{1-y}Sc_y)_{1.94}Ce_{0.06}Si_6O_{24}$ ($y = 0.1$) determined by Rietveld refinement of powder synchrotron X-ray diffraction data collected at room temperature. Atomic mixing of Ce^{3+} was not considered in the refinement model due to its small concentration (3%). U_{eq} is defined as one-third of the trace of the orthogonalized U^{ij} tensor.

atom	site	x	y	z	occupancy	U_{eq} ($\times 10^2$ Å^2)
Ba1	$3a$	0	0	0	1	2.07(4)
Ba2	$6c$	$\frac{1}{3}$	$\frac{2}{3}$	0.00402(5)	1	1.41(2)
Ba3	$18f$	0.02954(6)	0.66929(8)	0.10895(3)	1	1.03(1)
Y/Sc	$6c$	0	0	0.16472(6)	0.9/0.1	0.41(3)
Si	$18f$	0.3376(6)	0.02053(3)	0.07338(8)	1	0.27(5)
O1	$18f$	0.3592(5)	0.0664(5)	0.0042(2)	1	1.34(6)
O2	$18f$	0.4848(8)	0.1620(8)	0.1110(3)	1	1.34(6)
O3	$18f$	−0.01097(1)	0.1710(8)	0.1007(3)	1	1.34(6)
O4	$18f$	0.1354(7)	0.4695(8)	0.0935(2)	1	1.34(6)

Table 3.13: Refined atomic coordinates and equivalent isotropic displacement parameters for the loaded composition $Ba_9(Y_{1-y}Sc_y)_{1.94}Ce_{0.06}Si_6O_{24}$ ($y = 0.2$) determined by Rietveld refinement of powder synchrotron X-ray diffraction data collected at room temperature. Atomic mixing of Ce^{3+} was not considered in the refinement model due to its small concentration (3%). U_{eq} is defined as one-third of the trace of the orthogonalized U^{ij} tensor.

atom	site	x	y	z	occupancy	U_{eq} ($\times 10^2$ Å^2)
Ba1	$3a$	0	0	0	1	2.07(6)
Ba2	$6c$	$\frac{1}{3}$	$\frac{2}{3}$	0.00404(8)	1	1.92(4)
Ba3	$18f$	0.02912(1)	0.6685(1)	0.10847(4)	1	1.15(2)
Y/Sc	$6c$	0	0	0.1648(1)	0.8/0.2	0.87(7)
Si	$18f$	0.3364(8)	0.01971(4)	0.07365(1)	1	0.75(7)
O1	$18f$	0.3554(8)	0.0611(8)	0.0044(3)	1	1.90(1)
O2	$18f$	0.4794(1)	0.1573(1)	0.1084(4)	1	1.90(1)
O3	$18f$	−0.006(1)	0.177(1)	0.1021(4)	1	1.90(1)
O4	$18f$	0.1359(9)	0.4699(1)	0.0937(1)	1	1.90(1))
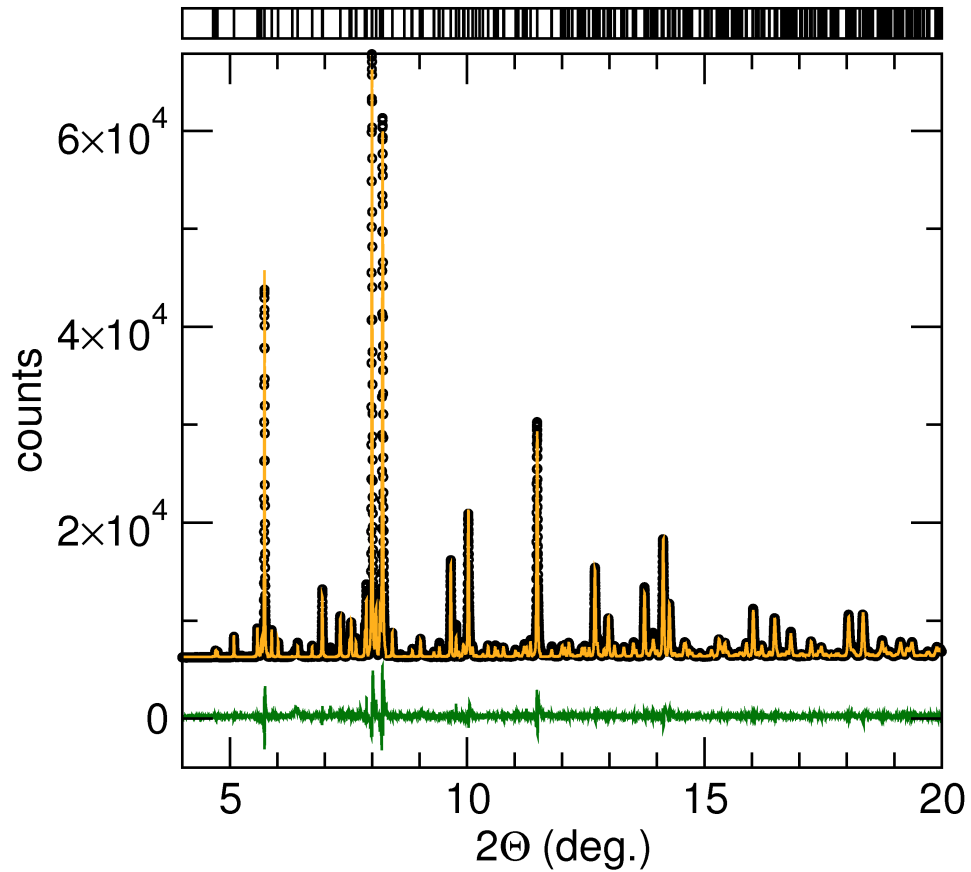
Figure 3.24: The diffraction pattern was collected for the loaded composition, $Ba_9(Y_{1-y}Sc_y)_{1.94}Ce_{0.06}Si_6O_{24}$ ($y = 0.2$). A Rietveld refinement (the total fit is orange, the difference line is green) was preformed to determine the lattice parameters and atomic positions. Reproduced with permission from reference [85], ©2013 American Chemical Society.

Chapter 4

Structure–composition relationships and optical properties in cerium-substituted $(Sr,Ba)_3(Y,La)(BO_3)_3$ borate phosphors

Relationships between the structure and composition, and their influence on the optical properties, of a family of cerium-substituted borate compounds with formula $A_3RE(BO_3)_3$ (A = Ba, Sr; RE = Y, La) are studied using a combination of high resolution synchrotron X-ray powder diffraction and photoluminescence. Examination of the coordination environment of the Ce^{3+} active site polyhedra coupled with photoluminescence at 77 K reveals three distinct excitation bands corresponding to Ce^{3+} located on three distinct crystallographic sites. Comparing the position of these excitation bands with crystal field splitting effects due to changes in polyhedral volumes and distortions suggest an assignment of the three excitation bands. These compounds are efficiently excited by UV light ($\approx$340 nm) with blue emission at a maximum wavelength of 413 nm for $Ba_3Y(BO_3)_3$:Ce^{3+},Na^+, 422 nm for $Sr_3Y(BO_3)_3$:Ce^{3+},Na^+, and 440 nm for $Sr_3La(BO_3)_3$:Ce^{3+},Na^+. The most efficient compound was determined to be $Sr_3La(BO_3)_3$:Ce^{3+},Na^+ with a quantum yield of 50%.

4.1 Introduction

Solid-state white lighting devices employing full conversion of the emission from a near-UV-emitting LED (λ_{max} = 405 nm) or a UV-emitting LED (λ_{max} = 350 nm) to longer wavelengths in the visible region of the spectrum often use

a combination of red-, green-, and blue-emitting phosphors. Fully phosphor-converted devices utilizing a blue-emitting phosphor instead of a blue-emitting LED may better represent wavelengths in the blue region, leading to higher color rendition devices, due to the broad nature of the Ce^{3+} or Eu^{2+} emission spectrum compared to the narrow emission spectrum of an LED. The current most widely used blue-emitting phosphor is $BaMgAl_{10}O_{17}:Eu^{2+}$, which is efficiently excited with UV to near-UV light, yet has poor temperature stability of the luminescence. Additionally, the use of laser diodes as the excitation source for high-power white lighting applications also requires broad blue-emitting phosphors to overcome the narrow emission spectrum of a blue- or UV-emitting laser diode.[15] There is therefore a need for chemically and thermally stable phosphors that are efficiently excited by UV light with tunable emission wavelength ranging across the visible spectrum from blue to red. Additionally, understanding the relationship between structural and optical properties of phosphor materials may help us gain insight as to the methods for developing phosphors with specific optical properties.

This work explores cerium-substituted borate compounds of the family $A_3RE(BO_3)_3$ (A = Ba, Sr; RE = Y, La). Some of these compounds have been studied primarily for solid-state laser host materials with other activator ions including Er^{3+}[106], Yb^{3+}[107–111], Er^{3+}/Yb^{3+} pairs[112], Nd^{3+}[113],

Pr^{3+}[114], and Ta^{3+}[115]. They have also been studied under vacuum-ultraviolet excitation for fluorescent lamps and plasma displays using Tb^{3+} as an activator ion[116] with Ce^{3+}-substituted $Sr_3Y(BO_3)_3$ reported as a scintillation material[117].

Here, we prepare and characterize the structural and optical properties of cerium-substituted $Ba_3Y(BO_3)_3$, $Sr_3Y(BO_3)_3$, and the new phase $Sr_3La(BO_3)_3$ for potential applications in solid-state white lighting as broad blue-emitting phosphors.

4.2 Experimental

Stoichiometric samples were prepared following the formula $A_{3-2x}RECe_xNa_x(BO_3)_3$. Na^+ was used to maintain charge neutrality when substituting trivalent cerium in place of the divalent cation. Cerium substitution in place of the trivalent cation resulted in formation of the hexagonal $A_3RE(BO_3)_3$ polymorph (space group $P6_3cm$ (No. 185)).[118] The optimum cerium concentration was determined to be $x = 0.06$ resulting in the formula $A_{2.88}RECe_{0.06}Na_{0.06}(BO_3)_3$. Samples of $Ba_{2.88}YCe_{0.06}Na_{0.06}(BO_3)_3$, $Sr_{2.88}LaCe_{0.06}Na_{0.06}(BO_3)_3$, and $Sr_{2.88}YCe_{0.06}Na_{0.06}(BO_3)_3$ were prepared by conventional high temperature solid-state reaction. The compound $Ba_3La(BO_3)_3$

was not able to be prepared due to formation of only the $Ba_3La_2(BO_3)_4$ phase.[119] Stoichiometric amounts of $BaCO_3$ (99.9% purity, Materion), $SrCO_3$ (99.5% purity, Materion), Y_2O_3 (99.9% purity, Materion), La_2O_3 (99.99% purity, Alfa Aesar), H_3BO_3 (99.99% purity, Sigma Aldrich), CeO_2 (99.99% purity, Alfa Aesar), and Na_2CO_3 (99.9999% purity, Sigma Aldrich) were intimately mixed using an agate mortar and pestle for approximately 30 min. Mixed powders were then pressed into pellets and placed in alumina crucibles (CoorsTek) on a bed of sacrificial powder to prevent contact with the crucible. The pellets were then heated for 5 h in a reducing atmosphere of $5\%H_2/95\%N_2$ at $1200\,^{\circ}$C for $Ba_{2.88}YCe_{0.06}Na_{0.06}(BO_3)_3$ and $1300\,^{\circ}$C for $Sr_{2.88}LaCe_{0.06}Na_{0.06}(BO_3)_3$ and $Sr_{2.88}YCe_{0.06}Na_{0.06}(BO_3)_3$ with heating and cooling ramps of $3\,^{\circ}$C/min.

Synchrotron X-ray powder diffraction data were collected at room temperature on the 11-BM instrument at the Advanced Photon Source (APS), Argonne National Laboratory using an average wavelength of $\lambda = 0.413845\,$Å. Rietveld analysis was carried out using the General Structure Analysis System (GSAS)[95, 96]. The background was handled using a shifted Chebyshev function, while the peak shapes were handled using a pseudo-Voigt function with Finger-Cox-Jephcoat asymmetry to correct for axial divergence at low angles.

Room temperature and $77\,$K photoluminescence spectra were obtained on a Perkin Elmer LS55 spectrophotometer equipped with a xenon lamp. Pho-

Table 4.1: Comparison of effective ionic radii shows that Ce^{3+} can potentially be substituted into three different crystallographic sites, replacing A^{2+} and/or RE^{3+} ions.

site	CN	effective ionic radii (Å)				
		Ba^{2+}	Sr^{2+}	Y^{3+}	La^{3+}	Ce^{3+}
$18f$	8	1.42	1.26	1.019	1.16	1.143
$3a$ and $3b$	6	1.35	1.18	0.9	1.032	1.01

toluminescence quantum yield (PLQY) was measured using phosphor powders encapsulated in silicone resin (GE Silicones, RTV-615) and deposited on transparent quartz substrates (Chemglass). The samples were placed inside a Spectralon™-coated integrating sphere (6 inch diameter, Labsphere) and excited using 351 nm light generated by an argon ion laser (Spectraphysics Beamlock 2065). The light was collected by a quartz lens and directed onto a calibrated Si photodiode (Newport 818-UV) using filters (Omega Filters) to collect respective wavelengths. Data collection and processing procedures were conducted similar to those described by Greenham *et al.*[59]

4.3   Results and Discussion

This family of borate compounds crystallizes in the rhombohedral space group $R\bar{3}$ (No. 148) with the $Sr_6HoSc(BO_3)_6$ structure type, as illustrated in Figure 4.1a.[118, 120–122] There are three crystallographically independent
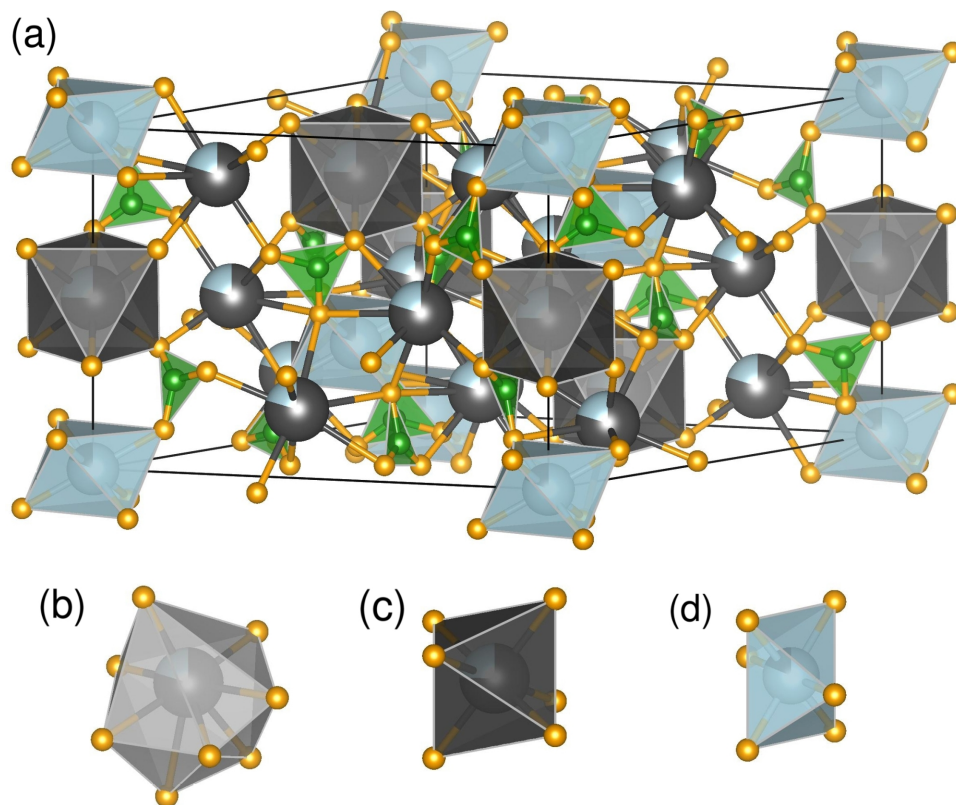
Figure 4.1: (a) Crystal structure of $Ba_3Y(BO_3)_3$ in the rhombohedral space group $R\bar{3}$ (No. 148) with coordination polyhedra of the three distinct crystallographic sites for which Ce^{3+} substitution may occur; (b) is Wyckoff position $18f$, (c) $3b$, and (d) $3a$. A^{2+} ions are depicted as gray, RE^{3+} as blue, B^{3+} as green, and O^{2-} as orange. Reproduced with permission from reference [105], ©2013 Royal Society of Chemistry.

Table 4.2: Rietveld refinement and crystal data.

refined formula	$Ba_{2.555}Y_{1.445}(BO_3)_3$	$Sr_{3.81}La_{0.19}(BO_3)_3$	$Sr_{3.25}Y_{0.75}(BO_3)_3$
radiation type		synchrotron X-ray (11-BM)	
λ (Å)		0.413845	
2θ range (degree)		0.5 to 49.995	
temperature (K)		295	
crystal system		trigonal	
space group; Z		$R\bar{3}$ (No. 148); 6	
lattice parameters (Å)	$a = 13.01931(2)$	$a = 12.58818(2)$	$a = 12.49257(1)$
	$c = 9.54839(3)$	$c = 9.33127(2)$	$c = 19.27592(2)$
volume (Å^3)	1401.641(4)	1280.553(3)	1253.693(2)
R_p (%)	9.9	17	12
R_{wp} (%)	13	22	14
$R_f{}^2$ (%)	13	48	26
χ^2	6.0	18	4.0

sites for the A^{2+} and RE^{3+} cations and therefore three potential sites for Ce^{3+} substitution. The first site is Wyckoff position $18f$ (Figure 4.1b) which is co-ordinated by 8 oxygen atoms, and the other two sites are Wyckoff positions $3b$ (Figure 4.1c) and $3a$ (Figure 4.1d) which form distorted octahedra coordinated by 6 oxygen atoms. Effective ionic radii for each of the cations in each of these coordination environments are listed in Table 4.1.[63, 64] Comparing the ionic radii, we expect Ce^{3+} to substitute on all three of these sites and that there may be site mixing between A^{2+} and RE^{3+} in the host structure.

Synchrotron X-ray powder diffraction data in Figure 4.2 show Ri-etveld analysis of samples $Ba_{2.88}YCe_{0.06}Na_{0.06}(BO_3)_3$, $Sr_{2.88}LaCe_{0.06}Na_{0.06}(BO_3)_3$, and $Sr_{2.88}YCe_{0.06}Na_{0.06}(BO_3)_3$ indicating samples are nearly pure phase.
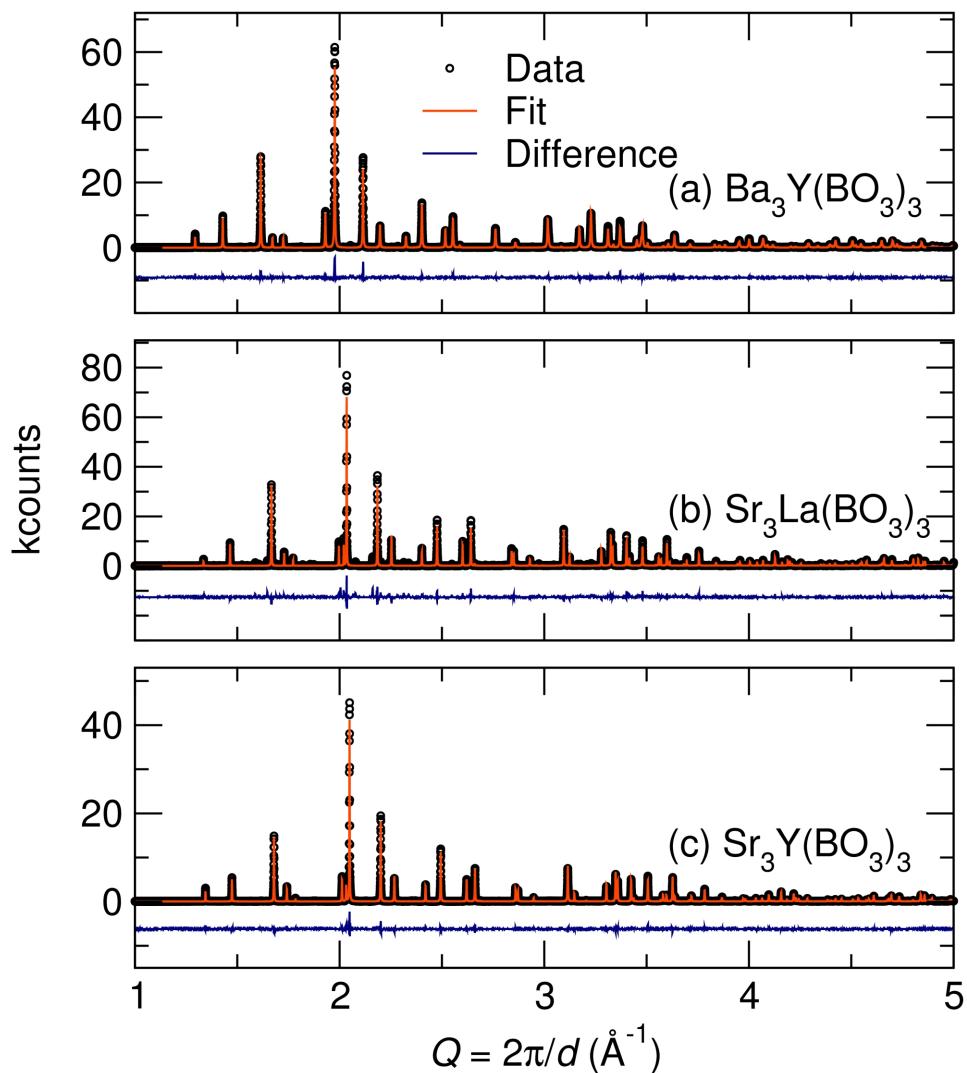
Figure 4.2: Rietveld refinements of synchrotron X-ray powder diffraction data collected at room temperature for (a) $Ba_{2.88}YCe_{0.06}Na_{0.06}(BO_3)_3$, (b) $Sr_{2.88}LaCe_{0.06}Na_{0.06}(BO_3)_3$, and (c) $Sr_{2.88}YCe_{0.06}Na_{0.06}(BO_3)_3$ show nearly phase pure materials with only a small impurity of $Sr_3La_2(BO_3)_4$ for $Sr_{2.88}LaCe_{0.06}Na_{0.06}(BO_3)_3$. Reproduced with permission from reference [105], ©2013 Royal Society of Chemistry.

Table 4.3: Refined atomic parameters as determined by Rietveld refinement. U_{eq} is defined as one-third of the trace of the orthogonalized U^{ij} tensor.

atom	site	x	y	z	occupancy	U_{eq} ($\times 10^2$ Å^2)
			$\mathrm{Ba}_{2.555}\mathrm{Y}_{1.445}(\mathrm{BO}_3)_3$			
Ba1	18f	0.37159(4)	0.24613(4)	0.47367(5)	0.72(2)	1.98(1)
Y1	18f	0.37159(4)	0.24613(4)	0.47367(5)	0.28(2)	1.98(1)
Ba2	3a	0	0	0	0.12(2)	1.85(6)
Y2	3a	0	0	0	0.88(2)	1.85(6)
Ba3	3b	0	0	$\frac{1}{2}$	0.67(2)	2.25(5)
Y3	3b	0	0	$\frac{1}{2}$	0.33(2)	2.25(5)
B1	18f	0.1371(8)	0.189(1)	0.7431(9)	1	2
O1	18f	0.1232(6)	0.1681(5)	0.8852(5)	1	2
O2	18f	0.2577(6)	0.2543(6)	0.6994(6)	1	2
O3	18f	0.0507(5)	0.1781(6)	0.6602(7)	1	2
			$\mathrm{Sr}_{3.81}\mathrm{La}_{0.19}(\mathrm{BO}_3)_3$			
Sr1	18f	0.37504(9)	0.25265(8)	0.47182(9)	0.95(1)	2.50(2)
La1	18f	0.37504(9)	0.25265(8)	0.47182(9)	0.05(1)	2.50(2)
Sr2	3a	0	0	0	1	10.4(2)
Sr3	3b	0	0	$\frac{1}{2}$	0.92(2)	2.75(9)
La3	3b	0	0	$\frac{1}{2}$	0.08(2)	2.75(9)
B1	18f	0.138(4)	0.158(3)	0.736(3)	1	2
O1	18f	0.1453(8)	0.1919(7)	0.8886(7)	1	2
O2	18f	0.255(1)	0.249(1)	0.7038(9)	1	2
O3	18f	0.0492(5)	0.1754(6)	0.6744(7)	1	2
			$\mathrm{Sr}_{3.25}\mathrm{Y}_{0.75}(\mathrm{BO}_3)_3$			
Sr1	18f	0.37252(5)	0.25063(5)	0.47707(6)	0.8(2)	2.70(2)
Y1	18f	0.37252(5)	0.25063(5)	0.47707(6)	0.2(2)	2.70(2)
Sr2	3a	0	0	0	0.9(3)	4.03(6)
Y2	3a	0	0	0	0.1(3)	4.03(6)
Sr3	3b	0	0	$\frac{1}{2}$	0.8(2)	2.09(5)
Y3	3b	0	0	$\frac{1}{2}$	0.2(2)	2.09(5)
B1	18f	0.152(1)	0.202(1)	0.7401(9)	1	2
O1	18f	0.1269(5)	0.1759(4)	0.8847(4)	1	2
O2	18f	0.2663(5)	0.2527(5)	0.7019(4)	1	2
O3	18f	0.0533(3)	0.1818(4)	0.6588(5)	1	2
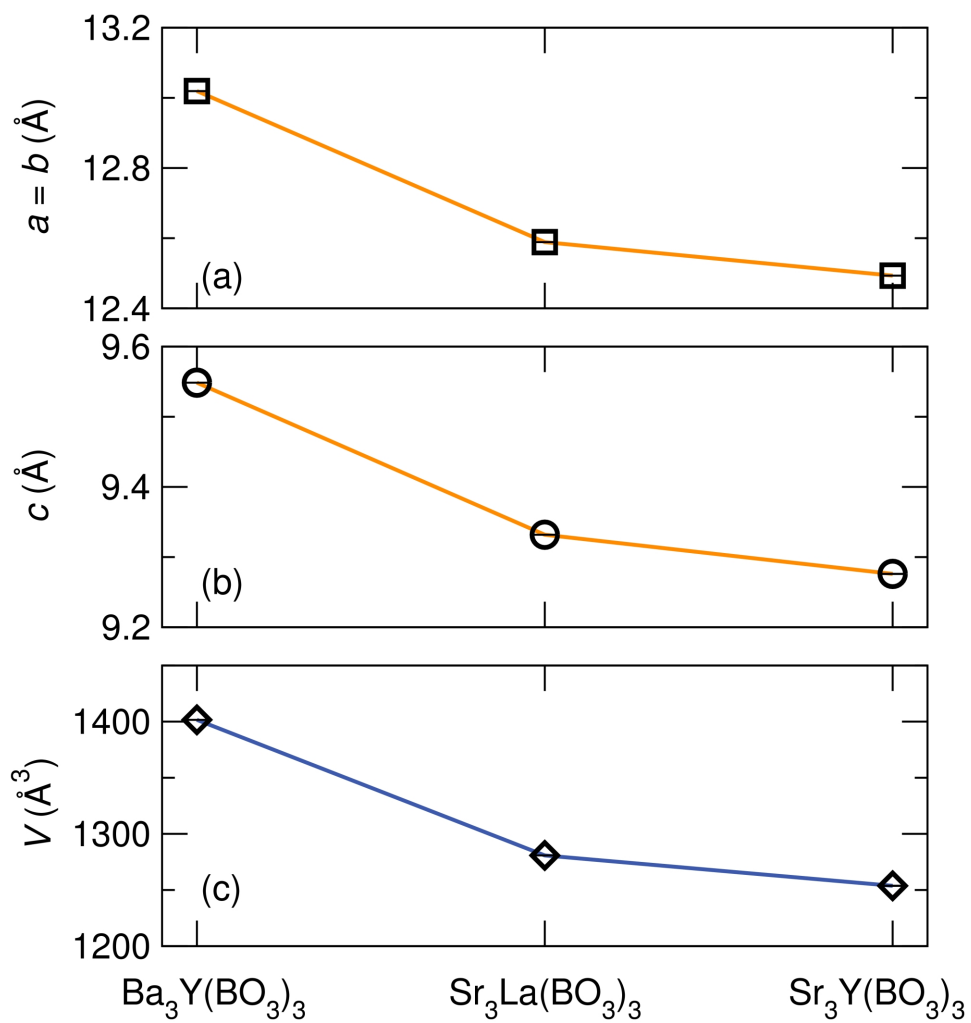
Figure 4.3: Unit cell parameters from Rietveld refinement of room temperature synchrotron X-ray powder diffraction data show (a) a decrease in the a lattice parameter and (b) a decrease in the c lattice parameter with (c) an overall decrease in cell volume from $Ba_{2.88}YCe_{0.06}Na_{0.06}(BO_3)_3$ to $Sr_{2.88}LaCe_{0.06}Na_{0.06}(BO_3)_3$ to $Sr_{2.88}YCe_{0.06}Na_{0.06}(BO_3)_3$. Error bars are indicated and are smaller than the symbols. Reproduced with permission from reference [105], ⓒ2013 Royal Society of Chemistry.

Table 4.4: Optical properties of $Ba_{2.88}YCe_{0.06}Na_{0.06}(BO_3)_3$, $Sr_{2.88}LaCe_{0.06}Na_{0.06}(BO_3)_3$, and $Sr_{2.88}YCe_{0.06}Na_{0.06}(BO_3)_3$ recorded at room temperature.

sample	λ_{ex} (nm)	λ_{em} (nm)	Stokes shift (nm)	FWHM (nm)	PLQY (%)
$Ba_{2.88}YCe_{0.06}Na_{0.06}(BO_3)_3$	337	413	76	92	16
$Sr_{2.88}LaCe_{0.06}Na_{0.06}(BO_3)_3$	342	440	98	87	50
$Sr_{2.88}YCe_{0.06}Na_{0.06}(BO_3)_3$	339	422	83	94	45

$Sr_{2.88}LaCe_{0.06}Na_{0.06}(BO_3)_3$ exhibits a small impurity of $Sr_3La_2(BO_3)_4$, leading to the poorer refinement. However, a visual inspection of the data shows a very good fit of the main phase. Details of the refinements are listed in Table 4.2 and Table 4.3. Ce^{3+} and Na^+ occupancies were not refined due to the small concentration. The change in lattice parameters and unit cell volume for the three compounds are shown in Figure 4.3. As expected based on ionic size (Table 4.1), the a and c lattice parameters and unit cell volume decrease going from $Ba_{2.88}YCe_{0.06}Na_{0.06}(BO_3)_3$ to $Sr_{2.88}LaCe_{0.06}Na_{0.06}(BO_3)_3$ to $Sr_{2.88}YCe_{0.06}Na_{0.06}(BO_3)_3$.

The photoluminescent excitation and emission curves of the three compounds are shown in Figure 4.4 and values are listed in Table 4.4. There is a red-shift in both the maximum excitation and emission wavelengths going from $Ba_3Y(BO_3)_3:Ce^{3+},Na^+$ to $Sr_3La(BO_3)_3:Ce^{3+},Na^+$, and then a blue-shift moving to $Sr_3Y(BO_3)_3:Ce^{3+},Na^+$. The FWHM of the emission spectra for these compounds is greater than that of $BaMgAl_{10}O_{17}:Eu^{2+}$ by a factor of about two, re-
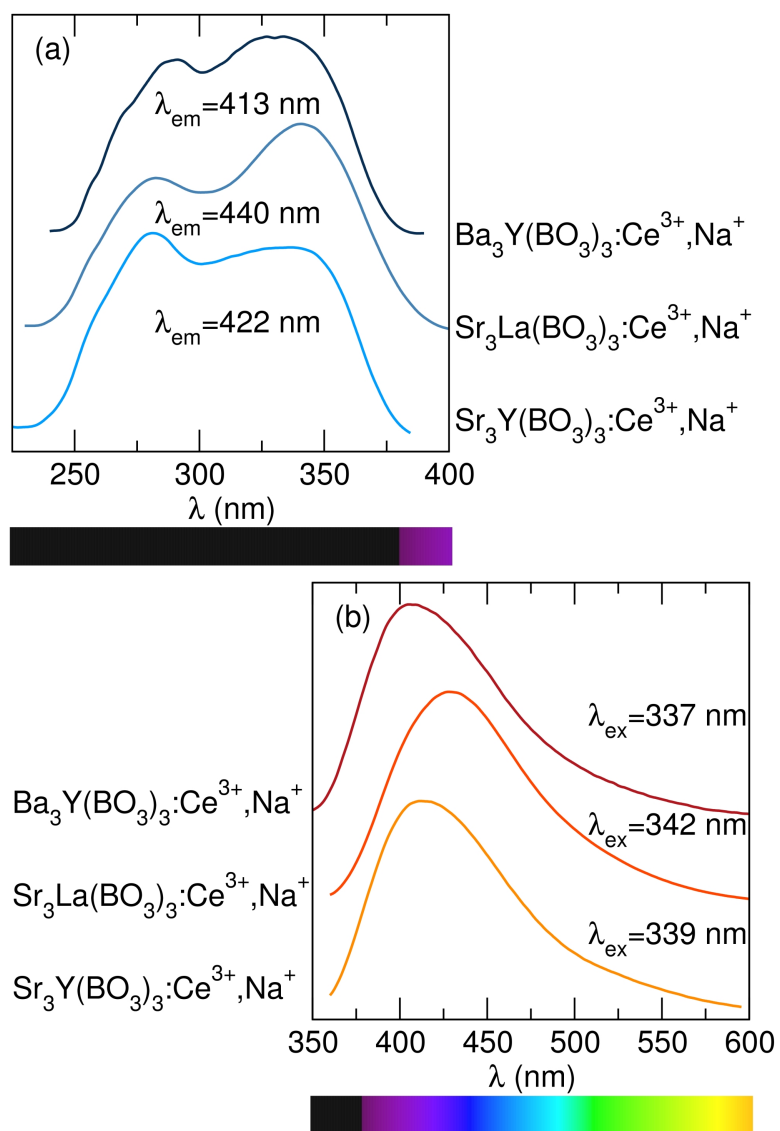
Figure 4.4: Photoluminescence (a) excitation spectra and (b) emission spectra of $Ba_{2.88}YCe_{0.06}Na_{0.06}(BO_3)_3$, $Sr_{2.88}LaCe_{0.06}Na_{0.06}(BO_3)_3$, and $Sr_{2.88}YCe_{0.06}Na_{0.06}(BO_3)_3$ collected at room temperature. Excitation/emission spectra were recorded using the maximum emission/excitation wavelength. Reproduced with permission from reference [105], ©2013 Royal Society of Chemistry.

sulting in a broad spectrum that represents more wavelengths in the blue region and may produce higher color rendition devices. The quantum yield of these materials was measured to be 16% for $Ba_3Y(BO_3)_3$:Ce^{3+},Na^+, 50% for $Sr_3La(BO_3)_3$:Ce^{3+},Na^+, and 45% for $Sr_3Y(BO_3)_3$:Ce^{3+},Na^+. The higher quantum yield for the Sr-compounds compared to the Ba-compound may be due to Ce^{3+} and Na^+ having ionic radii closer to that of Sr^{2+} than Ba^{2+}, and the increased rigidity of the lattice which may aid in reducing pathways for nonradiative emission. It should also be noted that the addition of Na^+ for charge compensation resulted in a two-fold increase in quantum yield compared to substitution of only Ce^{3+} for the divalent cation. The higher quantum yield with the addition of Na^+ can most likely be attributed to a lower defect concentration compared to samples prepared without Na^+. Due to the high preparation temperatures used, we expect Na^+ volatility to result in a lower concentration of Na^+ in the final composition compared to the initial loaded composition. With Na^+ optimization, we would expect the quantum yield to increase and be maximized at the optimal Na^+ concentration.

To understand the observed optical properties, the polyhedral environment of the potential Ce^{3+} substitution sites were analyzed based on the refined structural parameters. Emission in these compounds arises due to electronic transitions in Ce^{3+} from the $5d$ ($^2D_{3/2}$, $^2D_{5/2}$) excited state to the $4f$ ($^2F_{5/2}$, $^2F_{7/2}$)
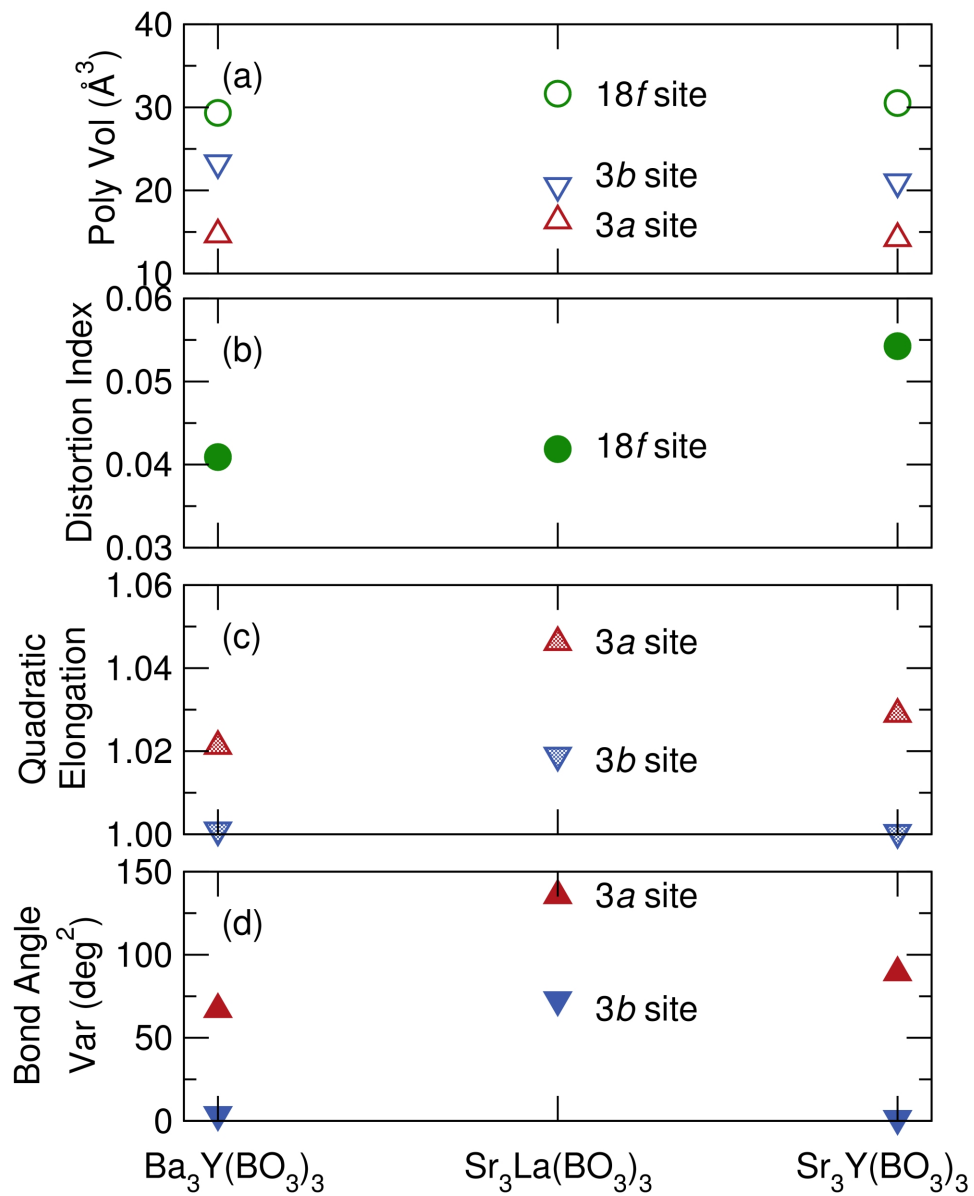
Figure 4.5: Changes in polyhedral volume and distortion of the three potential active site polyhedra between the different compounds may dictate and explain the observed optical properties. Reproduced with permission from reference [105], ©2013 Royal Society of Chemistry.

ground states.[72] The crystal field splitting of the Ce^{3+} $5d$ states is greatly affected by the local environment, including Ce–O bond lengths and the degree of distortion of the Ce^{3+} coordination polyhedra.[21, 38, 74–76] The crystal field splitting strength[24], Δ or Dq, can be modeled by

$$\Delta = Dq = \frac{Ze^2r^4}{6R^5} \tag{4.1}$$

where R is the distance between the central ion and its ligands, Z is the charge or valence of the anion, e is the charge of the electron, and r is the radius of the $5d$ wavefunctions. Based on the decrease in unit cell volume on going from $Ba_3Y(BO_3)_3$:Ce^{3+},Na^+ to $Sr_3La(BO_3)_3$:Ce^{3+},Na^+ to $Sr_3Y(BO_3)_3$:Ce^{3+},Na^+ we would expect the crystal field splitting to increase in this order, resulting in a red-shift of the emission wavelength. We must also consider the local environment of each potential Ce^{3+} substitution site. Figure 4.5a shows the changes in polyhedral volume as related to changes in bond length for the three potential Ce^{3+} substitution sites, calculated through the method outlined by Swanson and Peterson[68]. There does not appear to be a clear trend associated with changes in polyhedral volume between the different compounds. Going from $Ba_3Y(BO_3)_3$:Ce^{3+},Na^+ to $Sr_3La(BO_3)_3$:Ce^{3+},Na^+ to $Sr_3Y(BO_3)_3$:Ce^{3+},Na^+, the $18f$ and $3a$ sites both exhibit a slight increase and then decrease in polyhedral volume, while the $3b$ site exhibits a slight decrease and then increase in polyhedral volume.

Figure 4.5b, c, and d show the changes in polyhedral distortion between the different compounds. For the irregular polyhedron of the $18f$ site, we employ a previously defined polyhedral distortion index[67] D

$$D = \frac{1}{n} \sum_{i=1}^{n} \frac{| l_i - l_{av} |}{l_{av}} \tag{4.2}$$

where l_i is the distance from the central atom to the ith coordinating atom and l_{av} is the average bond length. The distortion of the octahedral $3a$ and $3b$ sites is defined by the quadratic elongation[123] $\langle \lambda \rangle$

$$\langle \lambda \rangle = \frac{1}{n} \sum_{i=1}^{n} \left(\frac{l_i}{l_0} \right)^2 \tag{4.3}$$

where l_0 is the center-to-vertex distance of a regular polyhedron of the same volume and l_i is the distance from the central atom to the ith coordinating atom, and by the bond angle variance[123] σ^2

$$\sigma^2 = \frac{1}{m-1} \sum_{i=1}^{m} (\phi_i - \phi_0)^2 \tag{4.4}$$

where m is (number of faces in the polyhedron)$\times 3/2$, or the number of bond angles, in this case 12, ϕ_i is the ith bond angle, and ϕ_0 is the ideal bond angle for a regular polyhedron, in this case $90°$. We see from Figure 4.5b that there is an increase in polyhedral distortion of the $18f$ site going from $Ba_3Y(BO_3)_3$:Ce^{3+},Na^+ to $Sr_3La(BO_3)_3$:Ce^{3+},Na^+ to $Sr_3Y(BO_3)_3$:Ce^{3+},Na^+, which would also predict a red-shift in the optical properties in agreement with the change in unit cell volume, resulting in $Sr_3Y(BO_3)_3$:Ce^{3+},Na^+ having the most red-shifted emission.

144

However, the quadratic elongation and bond angle variance of the octahedra at sites $3a$ and $3b$, shown in Figure 4.5c and d, show the highest degree of distortion in $Sr_3La(BO_3)_3$:Ce^{3+},Na^+, predicting this compound to have the most red-shifted optical properties.

We find that the photoluminescence characteristics are highly dictated by the local structure. The decrease in lattice parameters and unit cell volume do not predict the observed optical properties. We also find that the distortion of the octahedral sites largely dictates the observed optical properties. The increase in polyhedral distortion of the $18f$ site on going from $Ba_3Y(BO_3)_3$:Ce^{3+},Na^+ to $Sr_3La(BO_3)_3$:Ce^{3+},Na^+ to $Sr_3Y(BO_3)_3$:Ce^{3+},Na^+, would have predicted a red-shift in the optical properties in agreement with the change in unit cell volume, resulting in $Sr_3Y(BO_3)_3$:Ce^{3+},Na^+ having the most red-shifted emission. Instead, the quadratic elongation and bond angle variance of the octahedra, which show the highest degree of distortion in $Sr_3La(BO_3)_3$:Ce^{3+},Na^+, confirming this compound to have the most red-shifted optical properties. The increased distortion of the octahedra causes a larger crystal field splitting, illustrated by both the red-shifted excitation and emission wavelengths and the large Stokes shift for $Sr_3La(BO_3)_3$:Ce^{3+},Na^+ which possesses the most distorted octahedra. The trend associated with the FWHM of the emission spectra does not correspond with the trends seen for the Stokes shift. This trend is most likely destroyed due to the

145

Table 4.5: Maximum wavelength and integrated intensity for each of the Gaussian functions fit to the excitation spectra collected at 77 K corresponding to Ce^{3+} excitation from three distinct environments.

sample	excitation maxima		
	λ_1	λ_2	λ_3
$Ba_{2.88}YCe_{0.06}Na_{0.06}(BO_3)_3$	288 nm ($34{,}697\,cm^{-1}$)	333 nm ($29{,}989\,cm^{-1}$)	347 nm ($28{,}832\,cm^{-1}$)
$Sr_{2.88}LaCe_{0.06}Na_{0.06}(BO_3)_3$	280 nm ($35{,}691\,cm^{-1}$)	335 nm ($29{,}871\,cm^{-1}$)	350 nm ($28{,}568\,cm^{-1}$)
$Sr_{2.88}YCe_{0.06}Na_{0.06}(BO_3)_3$	282 nm ($35{,}474\,cm^{-1}$)	333 nm ($30{,}033\,cm^{-1}$)	349 nm ($28{,}687\,cm^{-1}$)

differing effects of polyhedral volume and distortion in the different compounds, in addition to Ce^{3+} on multiple crystal sites.

Analyzing the excitation spectra of these compounds at 77 K, we are able to distinguish three excitation bands corresponding to the three different environments of Ce^{3+} in the structure. Figure 4.6 shows the low temperature excitation spectra for each compound fit to three Gaussian functions, with Table 4.5 listing the maximum excitation wavelength and integrated intensity of each. Using the structural analysis of the active site polyhedra, each excitation curve can be assigned to Ce^{3+} on each site. The highest energy excitation curve, centered at ≈285 nm, can be assigned to Ce^{3+} in the $18f$ site. This is the largest polyhedron in terms of volume and should therefore give the smallest crystal field splitting. The polyhedral volume changes for the $18f$ site between the different compositions also follows the wavelength shift of this excitation peak. The poly-
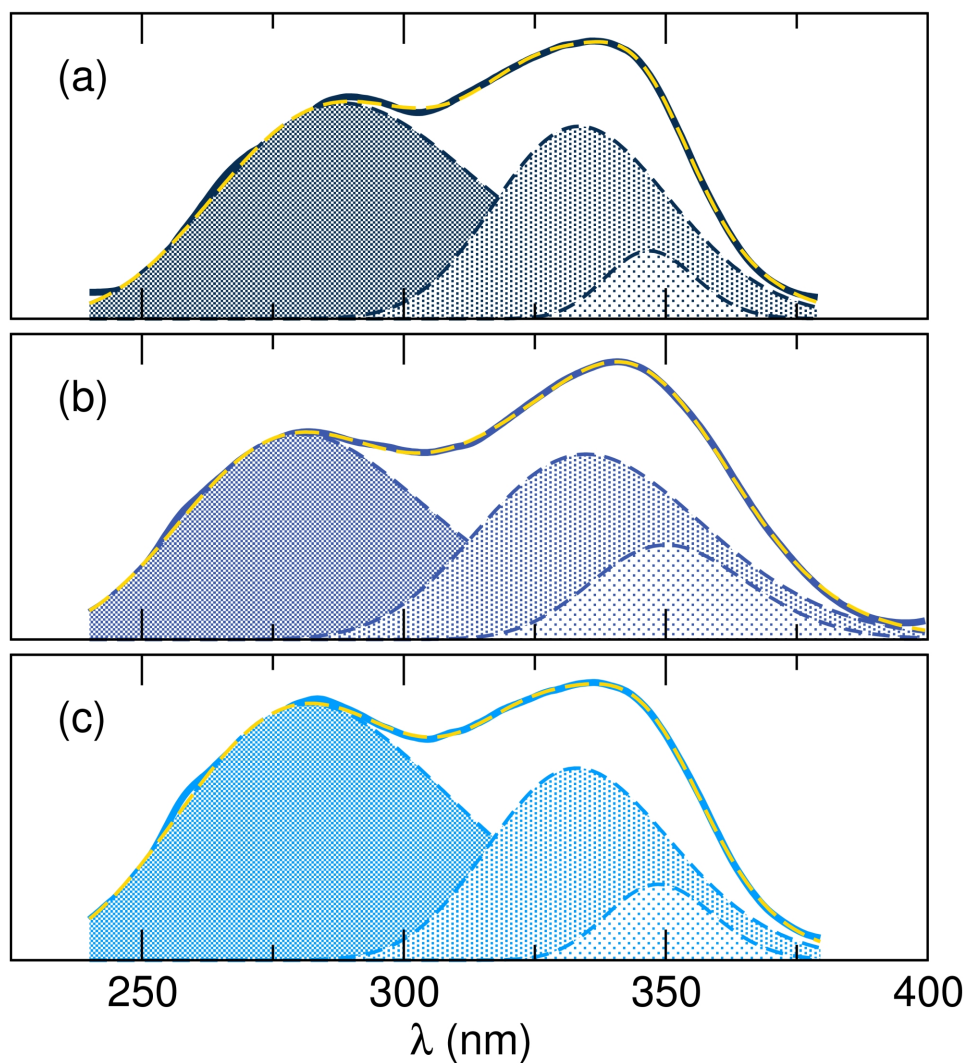
Figure 4.6: Excitation spectra of $Ba_{2.88}YCe_{0.06}Na_{0.06}(BO_3)_3$, $Sr_{2.88}LaCe_{0.06}Na_{0.06}(BO_3)_3$, and $Sr_{2.88}YCe_{0.06}Na_{0.06}(BO_3)_3$ collected at 77 K fit to three Gaussian functions representing Ce^{3+} in three distinct environments in the crystal structure. Reproduced with permission from reference [105], ©2013 Royal Society of Chemistry.

hedral volume of the $18f$ site is smallest for $Ba_3Y(BO_3)_3$:Ce^{3+},Na^+ which has the most red-shifted excitation peak at 288 nm, with the largest polyhedral volume for $Sr_3La(BO_3)_3$:Ce^{3+},Na^+ which has the most blue-shifted excitation peak at 280 nm. The distortion of this active site does not seem to affect the trend of crystal field splitting in this case.

The next excitation peak centered at $\approx$335 nm can be assigned to Ce^{3+} in the $3b$ site. This site has the largest volume of the two octahedra, but is smaller that the $18f$ site. The $3b$ site is also less distorted than the $3a$ site, pointing to less crystal field splitting and a higher excitation energy for Ce^{3+} on the $3b$ site compared to the $3a$ site. The distortion trends of the $3b$ site polyhedron in the different compounds also follows the shift in excitation wavelength. The quadratic elongation and bond angle variance are about same for $Ba_3Y(BO_3)_3$:Ce^{3+},Na^+ and $Sr_3Y(BO_3)_3$:Ce^{3+},Na^+ which both have the excitation peak centered at 333 nm. The octahedron is most distorted for $Sr_3La(BO_3)_3$:Ce^{3+},Na^+, shown by the larger quadratic elongation and bond angle variance, leading to a larger crystal field splitting in this compound and a more red-shifted excitation centered at 335 nm. The volume changes of the $3b$ site between compounds does not seem to correlate strongly with the optical trends seen, although the most red-shifted compound does possess the smallest polyhedral volume.

The final and most red shifted excitation peak centered at $\approx$350 nm can

then be assigned to Ce^{3+} in the $3a$ site. This site should possess the largest crystal field splitting due to the smallest polyhedral volume and the most distorted octahedron. The distortion trends of the $3a$ site polyhedron in the different compounds somewhat follows the shift in excitation wavelength with the $Sr_3La(BO_3)_3$:Ce^{3+},Na^+ having the most distorted octahedron the most red-shifted excitation wavelength. The small integrated intensity for this excitation curve is likely due to both the small number of $3a$ sites in the unit cell and also the small polyhedral volume of the site, which may lead to less Ce^{3+} incorporation.

4.4 Conclusions

The relationships between structure, composition, and optical properties of the family of cerium-substituted borates $A_3RE(BO_3)_3$:Ce^{3+},Na^+ (A = Ba, Sr; RE = Y, La) have been studied through an examination of the coordination environment around the active site polyhedra in relation to their photoluminescence properties. These compounds are efficiently excited by UV light of $\approx$340 nm with blue emission at a maximum wavelength of 413 nm for $Ba_3Y(BO_3)_3$:Ce^{3+},Na^+, 422 nm for $Sr_3Y(BO_3)_3$:Ce^{3+},Na^+, and 440 nm for $Sr_3La(BO_3)_3$:Ce^{3+},Na^+, with respective quantum yields of 16%, 45% and 50%. Excitation spectra recorded at

77 K revealed three distinct excitation bands corresponding to Ce^{3+} located on the three independent crystallographic sites. Comparing the positions of these excitation bands with crystal field splitting effects due to changes in polyhedral volumes and distortions led to the assignment of the highest energy excitation band at $\approx$285 nm corresponding to Ce^{3+} on the $18f$ site, the excitation band at $\approx$335 nm corresponding to Ce^{3+} on the $3b$ site, and the excitation band at $\approx$350 nm corresponding to Ce^{3+} on the $3a$ site.

Chapter 5

Data-driven discovery of energy materials: Efficient BaM_2Si$_3$O$_{10}$:Eu^{2+} (M = Sc, Lu) phosphors for application in solid-state white lighting

---

[1]The contents of this chapter have substantially appeared in reference [124]: J. Brgoch, K. Hasz, K. A. Denault, C. K. H. Borg, A. A. Mikhailovsky, and R. Seshadri, Data-driven discovery of energy materials: Efficient BaM_2Si$_3$O$_{10}$:Eu^{2+} (M = Sc, Lu) phosphors for application in solid state white lighting, *Faraday Discuss.* **176** 333–347 (2014) ©2014 Royal Society of Chemistry.

In developing phosphors for application in solid state lighting, it is advantageous to target structures from databases with highly condensed polyhedral networks that produce rigid host compounds. Rigidity limits channels for non-radiative decay that will decrease luminescent quantum yield. $BaM_2Si_3O_{10}$ (M = Sc, Lu) follows this design criteria and is studied here as an efficient Eu^{2+}-based phosphor. M = Sc^{3+} and Lu^{3+} compounds with Eu^{2+} substitution were prepared and characterized using synchrotron X-ray powder diffraction and photoluminescence spectroscopy. Substituting Eu^{2+} according to $Ba_{1-x}Eu_xSc_2Si_3O_{10}$ and $Ba_{1-x}Eu_xLu_2Si_3O_{10}$ results in UV-to-blue and UV-to-blue-green phosphors, respectively. Interestingly, substituting Eu^{2+} in the Lu^{3+} containing material produces two emission peaks, at low temperature and with 365 nm excitation, as allowed by two substitution sites. The photoluminescence of the Sc^{3+} compound is robust at high temperature, decreasing by only 25% of its room temperature intensity at 503 K while the Lu-analogue has a large drop (75%) of its room temperature intensity. The decrease in emission intensity is explained as stemming from charge transfer quenching due to the short distances separating the luminescent centers on the Lu^{3+} substitution site. The correlation between structure and optical response in these two compounds indicates that even though the structures are three-dimensionally connected, high symmetry is required to prevent structural distortions that could impact photoluminescence.

152

5.1 Introduction

The current search for novel phosphors has recently centered on identifying compounds that contain highly rigid bonding networks.[35, 125, 126] This concept is classically employed to understand photoluminescence efficiency in molecular chemistry[127] as well as in inorganic-organic frameworks.[128] Extending this principle to bulk inorganic compounds should aid in the identification of new, highly efficient phosphors. Structures with the most rigid bonding networks tend to emerge in high symmetry structures with dense polyhedral packing.[35] Thus, preparing materials that have a large degree of connectivity makes it possible to limit non-radiative relaxation by suppressing phonons. Additionally, the photoluminescent quantum yield (Φ) can be influenced by the symmetry of a structure. Crystal structures with higher symmetry are not prone to structural relaxation (or distortion) due to chemical substitution or electronic excitation, which can produce soft-phonon modes ultimately affecting Φ. Previous research has successfully applied this approach to understand the exceptional efficiency of two phosphors, YAG:Ce^{3+} [125] and $La_3Si_6N_{11}$:Ce^{3+}.[126] These compounds contain high symmetry and dense polyhedral networks that yield a rigid structure and drive their excellent Φ. This concept also provides an interpretation

of the unique temperature-dependent photoluminescence in the orthosilicate solid solution, $(Sr_xBa_{2-x})SiO_4:Eu^{2+}$.[36] Moreover, a number of novel phosphors have been identified based on the principle of structural rigidity, including $A_3RE(BO_3)_3:Ce^{3+}$ (A = Ba, Sr; RE = Y, La),[105] $NaY_9Si_6O_{26}:Ce^{3+}$ and $Na_3YSi_2O_7:Ce^{3+}$,[129] and $(Ba_{1-x}Sr_x)Al_2Si_2O_8:Eu^{2+}$.[130]

Continuing the search for structure-types with a dense packing of polyhedra has revealed $BaM_2Si_3O_{10}$ (M = Sc, Lu, Y, Gd)[131, 132], which contains fully connected SiO_4 and MO_6 polyhedral units. Although a variety of M atoms have been identified in this structure-type, the optical properties of only the yttrium analogue have been reported. Substituting a variety of luminescent centers in $BaY_2Si_3O_{10}$ has resulted in emission in the blue (Ce^{3+}), green (Tb^{3+}), and red (Eu^{3+}) regions of the visible spectrum.[133] Moreover, this phosphor host can be co-doped with Ce^{3+} and Tb^{3+} to tune the emission color between blue and green.[134] Preparing the M = Sc or Lu analogues as phosphors, with the smaller ionic radii of the M atom, is ideal for maintaining the highly connected crystal structure while enhancing structural rigidity following Coulomb's law for ionic bonding. Moreover, decreasing the unit cell volume should enhance crystal field splitting of the Eu^{2+} $5d$ orbitals providing a desired red-shift of the emission spectrum.

Thus, we present two new Eu^{2+}-substituted silicate phosphors,

154

$Ba_{1-x}Eu_xM_2Si_3O_{10}$ (M = Sc, Lu), that are capable of efficiently down-converting a UV-LED emission into the blue and blue-green region, respectively, of the visible spectrum. Their preparation was achieved using high temperature solid state methods and the products characterized using synchrotron X-ray powder diffraction and optical property measurements. The Φ of these two compounds is reported as a function of Eu^{2+} concentration along with their temperature and time-dependent optical properties. From the in-depth property analysis of these two compounds, we are able to further our understanding of the structure-property relationship in inorganic phosphors that are necessary for the next generation of solid state white lighting.

5.2   Experimental

Polycrystalline samples of $Ba_{1-x}Eu_xM_2Si_3O_{10}$ (M = Sc, Lu; x = 0.005, 0.01, 0.02, 0.03, 0.04, 0.05, 0.06) were prepared using traditional high tempera-ture solid state methods. Starting materials ($BaCO_3$, Cerac, 99.9%; Eu_2O_3, Aldrich, 99.9%; Lu_2O_3, Materion, 99.9%; Sc_2O_3, Stanford Materials, 99.99%; SiO_2, Johnson-Matthey, 99.9%) were weighed out in desired stoichiometric ra-tios and thoroughly ground with an agate mortar and pestle. The molar ratio of Ba^{2+} to Eu^{2+} was systematically varied to explore the effect of Eu^{2+} concen-

tration on the optical properties. The mixtures were pressed into pellets and placed in alumina crucibles (3 mm; AdValue Technology) with sacrificial powder of the same composition to prevent contamination between the pellet and the crucible. The pellets were fired in a tube furnace under reducing conditions (5% H_2/95% Ar). $Ba_{1-x}Eu_xSc_2Si_3O_{10}$ ($x = 0.005$, 0.01, 0.02, 0.03, 0.04, 0.05, 0.06) was fired at 1375 °C for 10 hrs whereas $Ba_{1-x}Eu_xLu_2Si_3O_{10}$ ($x = 0.005$, 0.01, 0.02, 0.03, 0.04, 0.05, 0.06) was fired at 1475 °C for 5 hrs. Both reactions employed heating and cooling rates of 3 °C/min. The resulting compounds were ground with an agate mortar and pestle for characterization.

Structural properties were probed using synchrotron X-ray powder diffraction (XRD) collected at beamline 11-BM at the Advanced Photon Source, Argonne National Laboratory[135] using a calibrated wavelength of 0.413837 Å. The room temperature diffraction data were analyzed using the Rietveld method within the General Structure Analysis System (GSAS).[95, 96] The background was handled using a 9-term shifted-Chebyshev function, while the peak shapes were handled using a pseudo-Voigt function, with Finger-Cox-Jephcoat asymmetry to correct for axial divergence at low angle.

Room temperature photoluminescence spectra and quantum yield were measured with a Horiba Fluoromax-4 fluorometer using a 150 W xenon arc lamp for excitation and a 150 mm Spectralon™-coated Quantum-Φ integrating sphere

attachment. Each of the samples were thoroughly mixed with silicon resin (GE Silicones, RTV615) and applied to a quartz substrate (Chemglass) for measurement. The Φ was calculated based on the method of de Mello *et al.*[136]

Temperature and time dependent measurements of the photoluminescence were collected at 77 K, 295 K, and 503 K using a home-built fluorimeter incorporating a cryostat for low temperature measurements and a heating stage for high temperature data collection. Lifetime measurements were carried out using the Time-Correlated Single Photon Counting (TCSPC) technique[137] as described previously[36]. Here, 200 fs excitation pulses with a wavelength of 365 nm were generated by doubling the fundamental frequency of femtosecond Ti:Sapphire laser (Coherent Mira 900) pulses in a commercial optical harmonic generator (Inrad). The laser repetition rate was reduced to 200 kHz by a home-made acousto-optical pulse picker to avoid saturation of the phosphor. The TCSPC system is equipped with an ultrafast microchannel plate photomultiplier tube detector (Hamamatsu R3809U-51) and electronics board (Becker & Hickl SPC-630), and has an instrument response time of about 65 ps. The triggering signal for the TCSPC board was generated by sending a small fraction of the laser beam onto a fast (400 MHz bandwidth) Si photodiode (Thorlabs Inc.). Fluorescence signals were dispersed using an Acton Research SPC-500 monochromator after passing through a pump blocking, long-wavelength, autofluorescence-free, in-

terference filter (Omega Filters, ALP series). The monochromator was equipped with a CCD camera (Roper Scientific PIXIS-400), allowing for monitoring of the time-averaged fluorescence spectrum. Luminescence transients were not deconvolved with the instrument response function since their characteristic time constants were much longer than the width of the system response to the excitation pulse.

All calculations were carried out using the Vienna *ab initio* Simulation Package (VASP; version 5.2)[50, 52, 53] which employs the projector augmented wave method (PAW) of Blöchl[54] as adapted by Kresse and Joubert.[55] Initial relaxation of the atomic positions were performed to insure the compounds are in their electronic ground state. The elastic tensors were then determined from the stress-strain relationship of six finite distortions of the crystal[138] using displacements of $\pm0.015\,$Å. Exchange and correlation were described by Perdew-Burke-Ernzerhof generalized gradient approximation (PBE).[56] The energy cut-off of the plane wave basis set was $650\,$eV and approximately $100\,\mathbf{k}$-points (determined using a Gamma grid) were used. The energy convergence criteria was set to $1\times10^{-6}\,$eV per formula unit to ensure accurate electronic convergence. The Debye temperature (Θ_{D}) was estimated from the VASP-calculated elastic constants (C_{ij}) as described previously.[35]

5.3   Results and Discussion

Materials with a high Θ_D are ideal phosphor hosts due to the presence of high-energy phonon modes that limit non-radiative recombination. The highest Θ_D values arise in with connected polyhedral units that produce rigidly bound structural units. As a result, Θ_D for the three-dimensionally connected $BaM_2Si_3O_{10}$ (M = Sc, Lu) host was calculated prior to synthesis ensuring the potential of this compound. The resulting Debye temperatures of 543 K and 500 K for M = Sc and Lu, respectively, surpass related compounds by nearly 100 K. For example, $Ba_9Y_2Si_6O_{24}$, which crystallizes with two-dimensional layers of YO_6 octahedra corner shared with SiO_4 tetrahedra, has a Θ_D of 409 K.[85] Thus, based on the higher Θ_D and more rigid bonding network, $BaM_2Si_3O_{10}$ (M = Sc, Lu) is expected to have improved optical properties compared to such related systems.

$Ba_{1-x}Eu_xM_2Si_3O_{10}$ (M = Sc, Lu) was prepared using high temperature solid state methods and the structure refined against synchrotron X-ray powder diffraction data. The compounds both crystallize in space group $P2_1/m$ (No. 11) with the $BaGd_2Si_3O_{10}$ structure-type, illustrated in Figure 5.1a. As shown in Figure 5.1b and 5.1c, the compounds are nearly phase pure with the small unidentified impurity peaks likely corresponding alternate silicate phases. Using the known Gd-based structure type as an initial structural model, the lattice pa-

Table 5.1: Crystal structure refinement data for the isostructural $Ba_{0.99}Eu_{0.01}Sc_2Si_3O_{10}$ and $Ba_{0.97}Eu_{0.03}Lu_2Si_3O_{10}$ determined using the Rietveld method against synchrotron X-ray powder diffraction data.

	$M = Sc$	$M = Lu$
radiation type,	synchrotron X-ray (11-BM)	
λ (Å)	0.413837	
2θ range (degree)	2.5 to 50	
temperature (K)	295	
crystal system	monoclinic	
space group; Z	$P2_1/m$ (No. 11); 2	
lattice parameters	$a = 5.27359(1)$ Å	$a = 5.35430(1)$ Å
	$b = 11.92596(4)$ Å	$b = 12.1205(1)$ Å
	$c = 6.59206(2)$ Å	$c = 6.78250(1)$ Å
	$\beta = 107.0428(2)°$	$\beta = 106.6045(3)°$
volume (Å^3)	396.386(1)	421.820(1)
R_p (%)	11.38	13.37
R_{wp} (%)	16.35	20.21

rameters and atomic positions were refined using the Rietveld method and are presented in Table 5.1 and Table 5.2.

This structure contains Ba^{2+} cations on a mirror plane that are coordinated by 10 neighboring oxygen atoms with an average Ba–O bond length of 2.9(2) Å for both compounds, in agreement with related silicates.[85, 129] The structure also contains distorted SiO_4 tetrahedra that form corner-sharing zig-zag trimers. There are two crystallographically independent Si^{4+} cations with average Si–O bond lengths of 1.57(9) Å (Si1) and 1.62(8) Å (Si2) in the Lu^{3+} structure. These SiO_4 trimers are connected *via* two highly distorted, edge-sharing MO_6 octahedra. When $M = Sc^{3+}$, the average Sc–O bond length is 2.16(8) Å whereas the
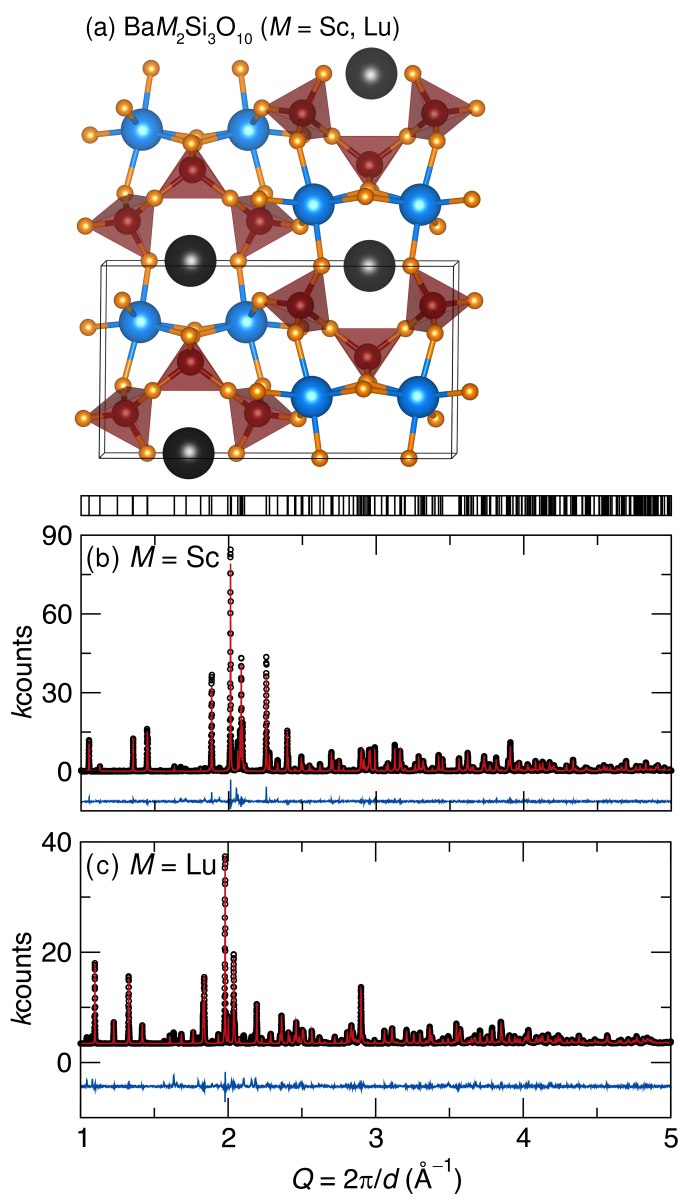
Figure 5.1: (a) The crystal structure of $Ba_{1-x}M_2Si_3O_{10}$ illustrated near the [100] direction with the SiO_4 tetrahedra (red) and MO_6 distorted octahedra (blue) highlighted, the Ba is illustrated in black. The synchrotron X-ray powder diffraction data (black circles) were refined using the Rietveld method (fit in red) for (b) $Ba_{0.99}Eu_{0.01}Sc_2Si_3O_{10}$ and (c) $Ba_{0.97}Eu_{0.03}Lu_2Si_3O_{10}$. The difference between the data and the Rietveld fit is shown in blue. Reproduced with permission from reference [124], ©2014 Royal Society of Chemistry.

Table 5.2: Refined atomic coordinates and equivalent isotropic displacement parameters of (a) $Ba_{0.99}Eu_{0.01}Sc_2Si_3O_{10}$ and (b) $Ba_{0.97}Eu_{0.03}Lu_2Si_3O_{10}$ determined by Rietveld refinement of powder synchrotron X-ray diffraction data collected at room temperature. The concentration of Eu^{2+} (x) was excluded from the refinement due to its low substitution level.

atom	site	x	y	z	U_{eq} ($\times 10^2$ Å^2)
			$Ba_{0.99}Eu_{0.01}Sc_2Si_3O_{10}$		
Ba1	$2e$	0.7599(1)	$\frac{1}{4}$	0.02665(8)	0.72(1)
Sc1	$4f$	0.1526(2)	0.10197(9)	0.6753(1)	0.67(3)
Si1	$2e$	0.5741(5)	$\frac{1}{4}$	0.4907(4)	0.50(5)
Si2	$4f$	0.2996(3)	0.0541(1)	0.2089(2)	0.05(4)
O1	$2e$	0.3412(9)	$\frac{1}{4}$	0.6011(7)	1.1(1)
O2	$2e$	0.8680(9)	$\frac{1}{4}$	0.6286(7)	0.2(1)
O3	$4f$	0.5418(6)	0.1429(2)	0.3310(5)	1.0(1)
O4	$4f$	0.4500(7)	0.9419(2)	0.2025(5)	0.7(1)
O5	$4f$	0.1490(6)	0.1119(2)	0.9899(5)	1.0(1)
O6	$4f$	0.1044(7)	0.0422(2)	0.3499(5)	0.8(1)
			$Ba_{0.97}Eu_{0.03}Lu_2Si_3O_{10}$		
Ba1	$2e$	0.7606(2)	$\frac{1}{4}$	0.0202(2)	0.94(3)
Lu1	$4f$	0.1542(1)	0.10006(5)	0.68249(9)	0.14(1)
Si1	$2e$	0.584(1)	$\frac{1}{4}$	0.4923(8)	0.9(1)
Si2	$4f$	0.3043(8)	0.0578(3)	0.2115(6)	0.3(1)
O1	$2e$	0.378(2)	$\frac{1}{4}$	0.599(1)	0.6(3)
O2	$2e$	0.858(2)	$\frac{1}{4}$	0.619(1)	0.8(3)
O3	$4f$	0.547(1)	0.1445(6)	0.332(1)	0.7(2)
O4	$4f$	0.442(1)	0.9420(6)	0.195(1)	0.6(2)
O5	$4f$	0.153(1)	0.1271(7)	0.003(1)	0.7(2)
O6	$4f$	0.106(1)	0.0564(6)	0.340(1)	0.5(2)

Lu–O bond length is 0.12 Å longer. The M–M bond length separating the dimers is 3.531(1) Å and 3.635(1) Å for Sc^{3+} and Lu^{3+}, respectively. Due to the connectivity of the MO_6 dimers and SiO_4 trimers, the structure bears the desirable three-dimensional bonding network which gives rise to its high calculated Θ_D.

Incorporating Sc^{3+} or Lu^{3+} as M in the compound leads to moderate changes in the refined crystal structure due to their respective ionic radii. For example, the MO_6 polyhedral volume increases from 12.42 Å^3 to 14.84 Å^3 going from the smaller 6-coordinate Sc^{3+} (r_{eff} = 0.745 Å) to the larger Lu^{3+} (r_{eff} = 0.861 Å) cation.[63] The increase in polyhedral volume is directly proportional to the observed 6% increase in unit cell volume. Additional structural modifications also occur that may not be anticipated.

For example, the MO_6 octahedra are more distorted when M = Sc^{3+} relative to M = Lu^{3+}, as highlighted by their respective quadratic elongation ($\langle \lambda \rangle$), Equation 5.1.[123] Here, $\langle \lambda \rangle$ is defined by l_0, the center-to-vertex distance of a regular polyhedron of the same volume and l_i, the distance from the central atom to the ith coordinating atom.

$$\langle \lambda \rangle = \frac{1}{n} \sum_{i=1}^{n} \left(\frac{l_i}{l_0} \right)^2 \tag{5.1}$$

From the calculation of these polyhedron parameters, provided in Table 5.3,

Table 5.3: Changes in polyhedral volume and distortion of the cation sites for $Ba_{0.99}Eu_{0.01}Sc_2Si_3O_{10}$ and $Ba_{0.97}Eu_{0.03}Lu_2Si_3O_{10}$.

	M = Sc	M = Lu
MO_6 poly. vol. ($Å^3$)	12.42	14.84
$\langle\lambda\rangle$	1.005	1.048
σ^2 (deg.^{2})	177.68	151.88
BaO_{10} poly. vol. ($Å^3$)	49.54	50.05
BaO_{10} distortion index	0.0699	0.0668

the ScO_6 octahedron is nearly ideal with a $\langle\lambda\rangle$ approaching 1 whereas the structure with the LuO_6 shows a large distortion of the octahedron with $\langle\lambda\rangle$ increasing dramatically. These changes surely stem from the ionic size of the M atom. Because the crystal structure is three-dimensionally connected, the substitution of Lu^{3+} can not be solely accommodated by an increase in the unit cell volume. A distortion of the local environment must also occur. Regardless, M does not affect BaO_{10} with the polyhedral volume of changing by only $0.11\,Å^3$ between the two compounds. This is further illustrated by the small change of the Ba^{2+} polyhedral distortion index (D)[67], defined by Equation 7.4 where l_i is the distance from the central atom to the ith coordinating atom and l_{av} is the average bond length

$$D = \frac{1}{n}\sum_{i=1}^{n}\frac{\mid l_i - l_{av}\mid}{l_{av}} \tag{5.2}$$

Substituting Eu^{2+} for Ba^{2+} site following $Ba_{1-x}Eu_xM_2Si_3O_{10}$ (M = Sc, Lu) is
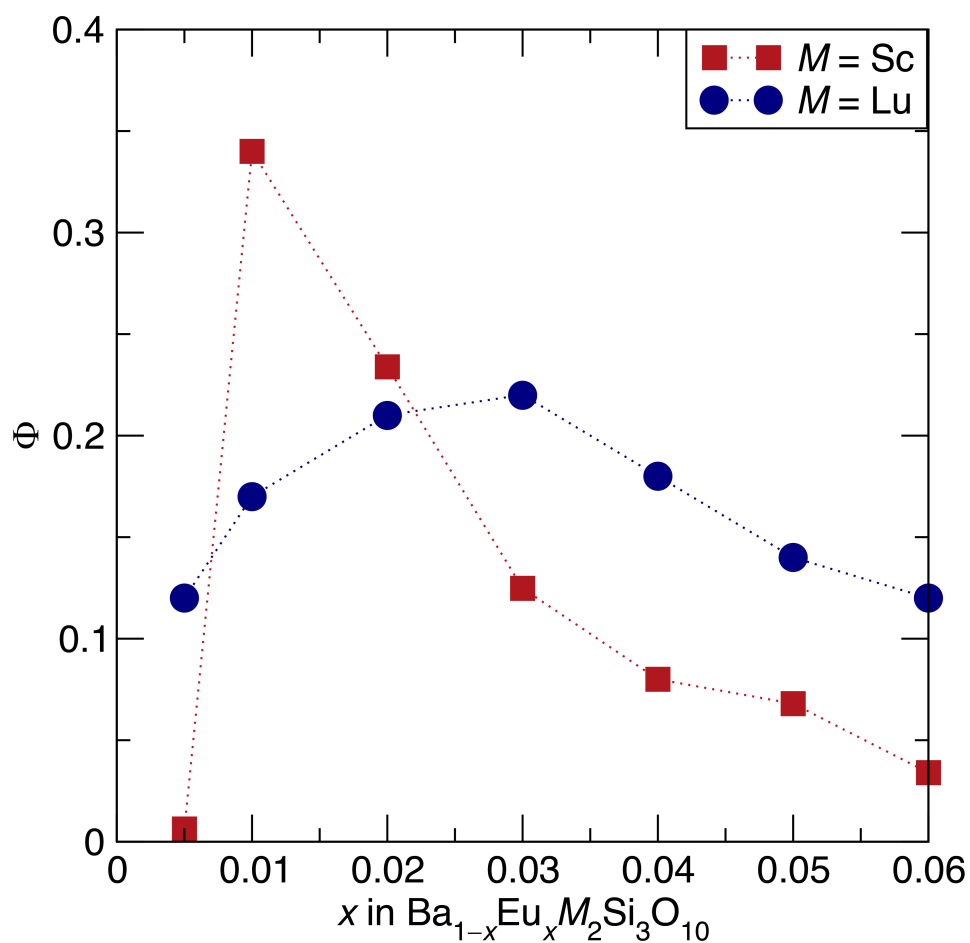
Figure 5.2: The Eu^{2+} concentration (x) that yields the highest photoluminescent quantum yield (Φ) for $Ba_{1-x}Eu_xM_2Si_3O_{10}$ $(M = Sc, Lu)$ using a $\lambda_{ex} = 365\,nm$. Additional measurements with $\lambda_{ex} = 330\,nm$ produced comparable results. Reproduced with permission from reference [124], ©2014 Royal Society of Chemistry.

ideal due to their isovalency. By varying the concentration of Eu^{2+} ($x = 0.005$, 0.01, 0.02, 0.03, 0.04, 0.05, 0.06) the optimal quantum yield was identified for both compositions. As shown in Figure 5.2, the Φ for $M = $ Sc is negligible at 0.5% Eu^{2+} substitution but dramatically increase to $\approx$35% at 1% followed by a decrease with the further addition rare-earth ions. Lu^{3+} achieves a maximum Φ of 24% at 3% Eu^{2+}. The moderate quantum yields reported here could likely be improved through the inclusion of a flux during preparation or additional post processing to control particle size and morphology. Nevertheless, the Φ measured for these compounds are lower than expected based on their high Debye temperatures.

The room temperature excitation and emission spectra for $Ba_{1-x}Eu_xM_2Si_3O_{10}$ ($M = $ Sc, Lu) with the optimal Eu^{2+} concentration are presented in Figure 5.3. Both compounds have a broad excitation spectra ($\lambda_{em} = 430\,\text{nm}$) extending from $<250\,\text{nm}$ to $400\,\text{nm}$ with a λ_{max} $\approx$315 nm. Additionally, there is a shoulder present in both of the excitation spectra at $\approx$360 nm. In both compounds, the emission peaks are broad (FWHM $>$ 75 nm) arising from the Eu^{2+} $5d \rightarrow 4f$ ($^8H_j \rightarrow {}^8S_{7/2}$) transitions. Specifically, exciting $Ba_{0.99}Eu_{0.01}Sc_2Si_3O_{10}$ at 260 nm or 315 nm produces a single emission peak as fit by a Gaussian function centered at approximately 440 nm. The emission spectrum of $Ba_{0.97}Eu_{0.03}Lu_2Si_3O_{10}$ ($\lambda_{ex} = 260\,\text{nm}$ and 315 nm) can
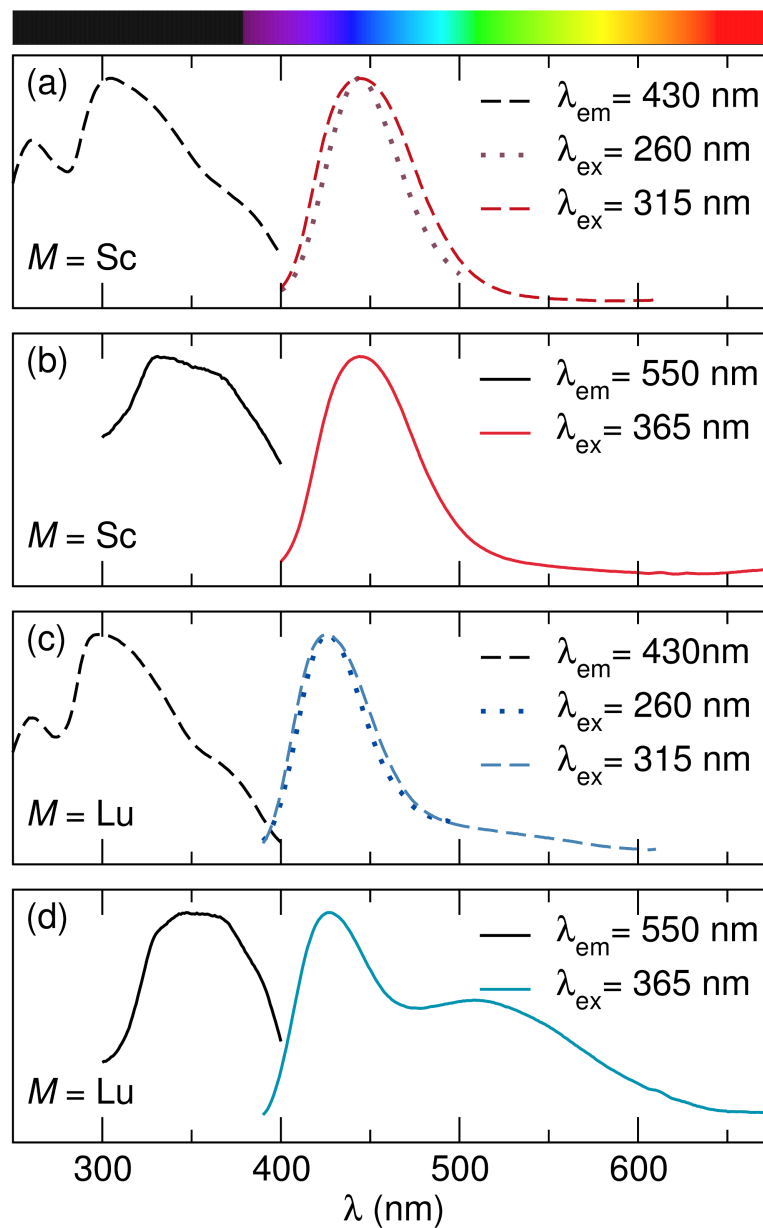
Figure 5.3: The florescence spectra for (a,b) $Ba_{0.99}Eu_{0.01}Sc_2Si_3O_{10}$ and (c,d) $Ba_{0.97}Eu_{0.03}Lu_2Si_3O_{10}$ using a variety of excitation wavelengths, including $\lambda_{ex} = $ 260 nm, 315 nm, and 365 nm with emission monitored at $\lambda_{em} = $ 430 nm and 550 nm. Reproduced with permission from reference [124], ©2014 Royal Society of Chemistry.
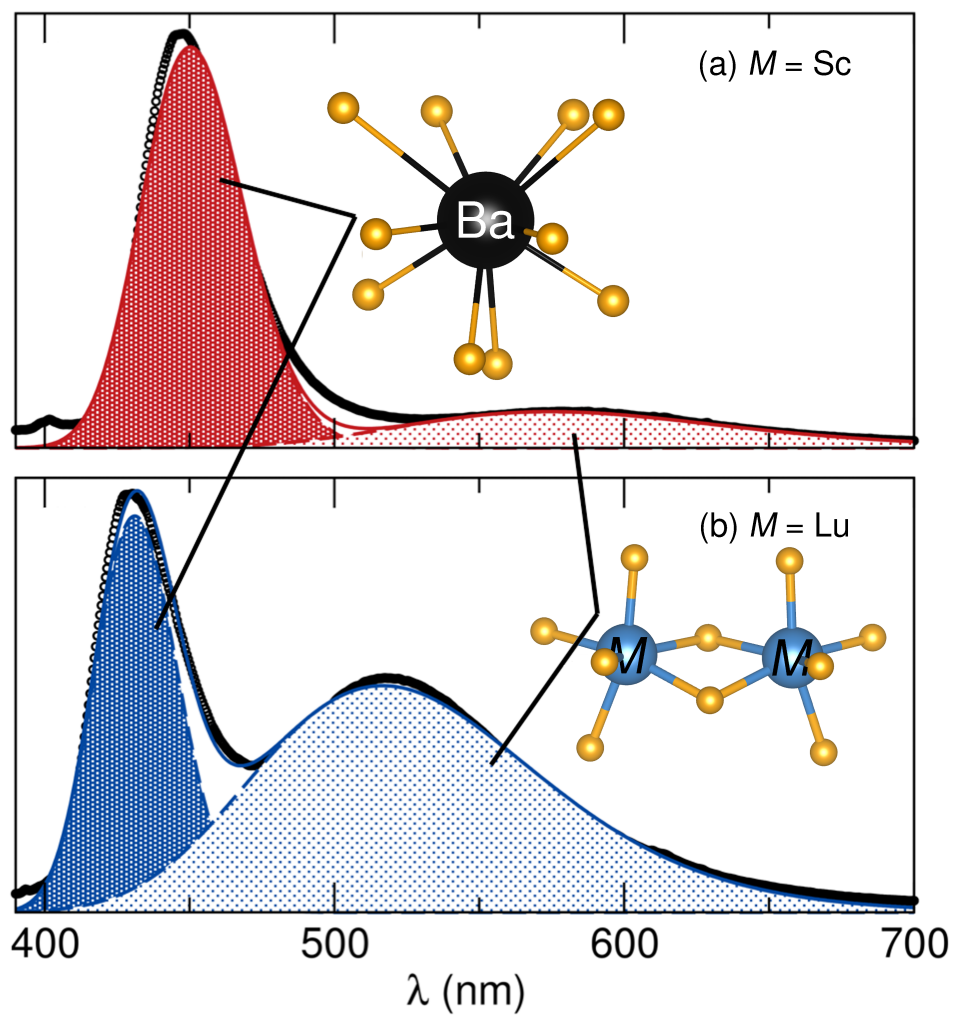
Figure 5.4: The emission spectrum (λ_{ex} = 365 nm) at 77 K for (a) $Ba_{0.99}Eu_{0.01}Sc_2Si_3O_{10}$ and (b) the $Ba_{0.97}Eu_{0.03}Lu_2Si_3O_{10}$ can be fit with two Gaussian curves indicating presence of two independent luminescent centers. Reproduced with permission from reference [124], ©2014 Royal Society of Chemistry.

also be fit by a single Gaussian and is slightly blue shifted compared to the scandium analogue with a center at 427 nm. This is consistent with a decrease in crystal field splitting due the a larger unit cell and polyhedral volume (see Table 5.1). In both compounds, there is a small Stokes shift of $\approx$50 nm due to the substitution of Eu^{2+} on the slightly large Ba^{2+} site. This gives rise to a large degree of "self-absorption" that is one of the potential causes of the lower than expected Φ.

Surprisingly, when $Ba_{0.97}Eu_{0.03}Lu_2Si_3O_{10}$ is excited at 365 nm the emission spectrum is remarkably different with the addition of second, broad emission peak at longer wavelength. The appearance of this second emission peak requires the addition of a second Gaussian function centered at 527 nm to fit the data. Cooling $Ba_{0.99}Eu_{0.01}Sc_2Si_3O_{10}$ to 77 K and exciting at 365 nm also yields an additional longer wavelength peak, as shown in Figure 5.4a. The enhanced emission at longer wavelength peak (at 77 K) requires two Gaussian functions to fully described the emission data. Measuring the emission of $Ba_{0.97}Eu_{0.03}Lu_2Si_3O_{10}$ at 77 K (Figure 5.4b) further enhances the magnitude of the two emission peaks confirming the need for two Gaussian functions to describe the optical data.

The two emission peaks in these compounds are rather surprising considering the crystal structure contains a single substitution site (Ba1) for the lumines-

169

cent center. Thus, the longer wavelength emission must arise from a local distortion in the crystal structure that allows additional Eu^{2+} occupation. Because this emission is dramatically red-shifted compared to the main emission peak ($\approx$120 nm) and extremely broad (FWHM $\approx$100 nm at 77 K), it is most likely to arise from the presence of a second, highly-distorted Eu^{2+} site. In this crystal structure, the potential second substitution site is the MO_6 dimer. Because the ionic radius of Eu^{2+} is much larger (1.17 Å; 6-coordinate) than Sc^{3+} (0.745 Å; 6-coordinate) or Lu^{2+} (0.861 Å; 6-coordinate) the substitution at this crystallographic site will require a large local distortion to accommodate the change. The local symmetry of the M-atom site is a general (Wyckoff $4f$) position allowing this site to readily distort without constraint. Nevertheless, the concentration of Eu^{2+} on the M site is will be small but it is clearly consequential to the optical properties. In fact, the presence of two luminescent sites increases the probability of charge-transfer between excited states that is known to quench luminescence.

Understanding optical properties of a phosphor as a function of temperature is critical when considering potential device integration. Two primary requirements for a new phosphor are a stable emission intensity (*i.e.*, constant Φ) and robust emission color across a range of temperatures. As shown in Figure 5.5a, the emission intensity of $Ba_{0.99}Eu_{0.01}Sc_2Si_3O_{10}$ decreases by 25% from room tem-
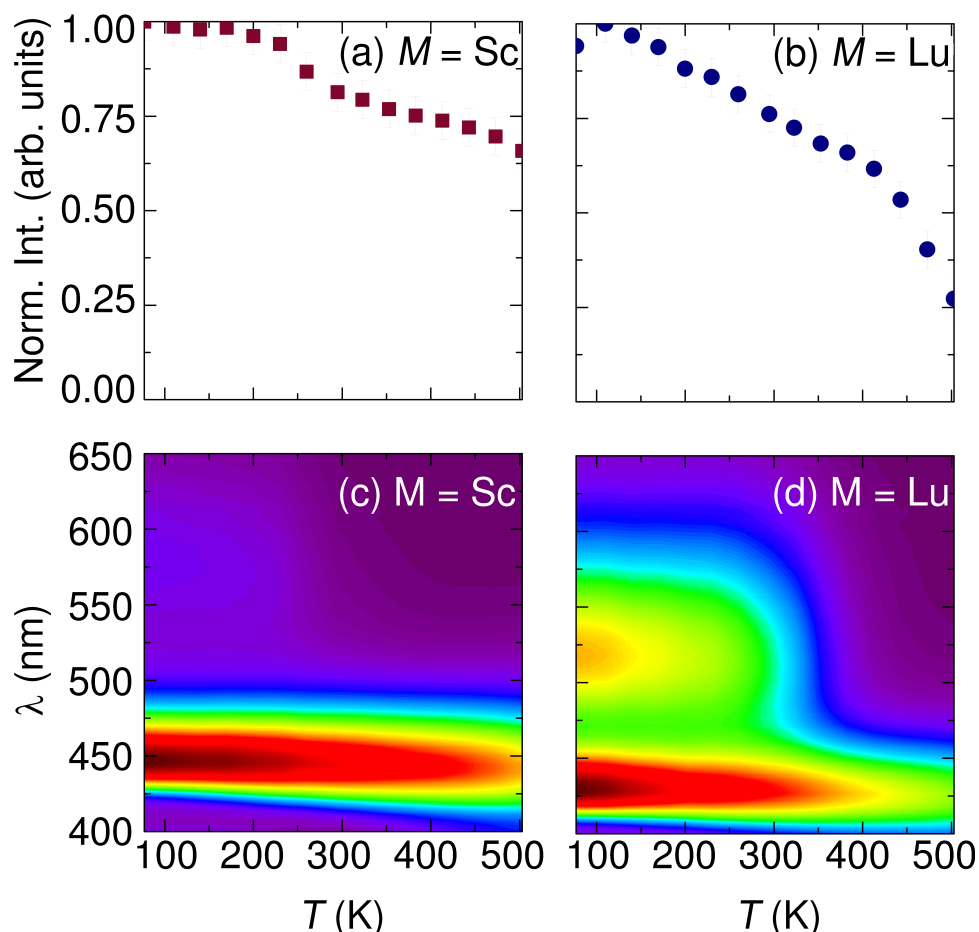
Figure 5.5: The relative integrated emission intensity for (a) $Ba_{0.99}Eu_{0.01}Sc_2Si_3O_{10}$ shows a decrease of only 25% of room temperature intensity at 503 K compared to (b) $Ba_{0.97}Eu_{0.03}Lu_2Si_3O_{10}$ which decreases by 75% over the same range. (c) A minimal shift in $\lambda_{em,max}$ is observed in $Ba_{0.99}Eu_{0.01}Sc_2Si_3O_{10}$ along with an enhancement of the longer wavelength peak <200 K. (d) A small red-shift in $\lambda_{em,max}$ is observed in $Ba_{0.97}Eu_{0.03}Lu_2Si_3O_{10}$ along with a large increase in the intensity of the peak at 510 nm below 300 K. Reproduced with permission from reference [124], ©2014 Royal Society of Chemistry.

perature to 503 K. This decrease in intensity is comparable with other thermally robust phosphors such as YAG:Ce^{3+}[125] which decreases by a similar amount over the same temperature range. The related phosphor, $Ba_9Y_2Si_6O_{24}$:Ce^{3+}, also shows a decrease of around 20% by 503 K.[85] Both of these compounds contain highly connected polyhedra that yield an exceptional quantum yield as certainly impact the high temperature properties of these phosphors. However, the emission intensity of $Ba_{0.97}Eu_{0.03}Lu_2Si_3O_{10}$, Figure 5.5b, is quite different with a decrease of nearly 75% of its emission intensity at high temperature.

The effect of Eu^{2+} in the two crystallographic sites becomes more apparent as a function of temperature. As the temperature decreases, the emission from both compounds red-shifts due to crystal field effects. When M = Sc, the main emission peak sharpens at low temperature while the intensity of the second emission peak at longer wavelength ($\approx$575 nm) increases slightly below 200 K. The optical properties of M = Lu changes considerably below room temperature. The position and intensity of the main emission peak is fairly stable below 400 K; however, the intensity of the second emission peak increases dramatically below 325 K, as observed in Figure 5.5d. The unique appearance of the second emission peak as a function of temperature arises by shutting down quenching due to charge transfer. At low temperature, charge transfer between the short distances separating the octahedral dimer sites (3.531(1) Å for Sc^{3+} and

3.635(1) Å for Lu^{3+}) is limited, allowing emission from these substitution sites to emerge. Therefore, to maintain emission intensity as a function of temperature the substitution of Eu^{3+} on the Lu^{3+} site needs to be inhibited.

The temperature dependent photoluminescence lifetimes provide additional information about the optical properties of these materials, Figure 5.6. Under 365 nm excitation with emission monitored at 433 nm and 550 nm the luminescence decay requires a bi-exponential function for a correct fit at λ_{em} = 433 nm and λ_{em} = 550 nm. Two separate lifetimes, a slow component ($\approx$500 ns) (Figure 5.6) and a fast component ($<$25 ns), compose the signal. The silicone epoxy used to encapsulate the samples was checked for photoluminescence due to the UV excitation wavelength employed. Here, only a fast, mono-exponential photoluminescent lifetime of $<$2 ns was present when excited at 365 nm. Interestingly, a sample prepared without rare-earth substitution, *e.g.,* $BaLu_2Si_3O_{10}$, showed luminescence (λ_{ex} = 365 nm) that required a bi-exponential decay to fit the data. In the unsubstituted compound, the lifetimes were $\approx$2 ns and 5 ns, respectively. The faster ($\approx$2 ns) component in the unsubstituted compound is certainly from the silicone epoxy. The 5 ns component in these experiments is most likely present due to defect states present the crystal structure giving rise to different recombination rate, which is known to arise in silicates.[139, 140] The existence of defect states identified in the host structure from these mea-
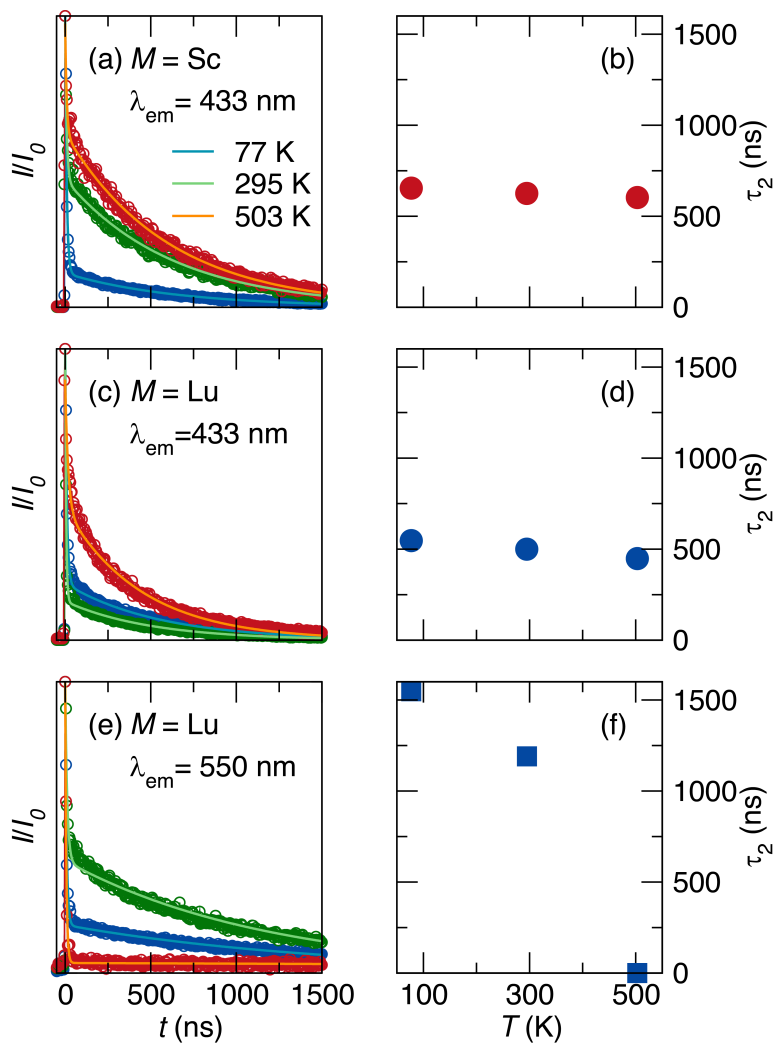
Figure 5.6: The luminescence decay as fit to a bi-exponential function for (a) $Ba_{0.99}Eu_{0.01}Sc_2Si_3O_{10}$ with the extracted lifetimes shown in (b) while the data in (c) are for $Ba_{0.97}Eu_{0.03}Lu_2Si_3O_{10}$ with the corresponding lifetime in (d) while excited at 365 nm and monitored at 433 nm. The lifetime was also monitored at 550 nm for $Ba_{0.97}Eu_{0.03}Lu_2Si_3O_{10}$ as shown in (e) with the extracted lifetimes in (f). Reproduced with permission from reference [124], ©2014 Royal Society of Chemistry.

surements also act as a quenching mechanism further limiting Φ. Focusing on the slower component (τ_2), the lifetime measurements were from the fit data and are plotted on the right side of Figure 5.6. The slower component, on the time scale of 500 ns to 1000 ns, is inline with previous lifetime measurements of Eu^{2+}. This further confirms the signal arises from the allowed $5d$ to $4f$ transition. Increasing the temperature from 77 K to 503 K accelerates the slower decay time nearly linearly due the increase in the rate of recombination at elevated temperatures.

5.4 Conclusions

The interest in photoluminescence from the $Ba_{1-x}Eu_xM_2Si_3O_{10}$ (M = Sc, Lu) phosphor was derived based on its highly connected SiO_4–MO_6 polyhedral network and reasonably high Θ_D. The compounds can be prepared from stoichiometric ratios of starting materials using high temperature ceramic methods. Characterization of these materials using synchrotron X-ray powder diffraction indicate the materials are nearly pure phase while optical measurements show Eu^{2+} substitutes on the Ba^{2+} site as expected and surprisingly on the M^{3+} site. Although the atomic radii of Eu^{2+} and M^{3+} are different, the low symmetry of the structure allows it adapt and incorporate the M atom. The presence

175

of this second site is detrimental to the Φ due to charge-transfer quenching. The temperature dependent photoluminescence highlights the thermally robust emission that arises in highly connected compounds. In fact, the emission intensity of $Ba_{0.99}Eu_{0.01}Sc_2Si_3O_{10}$ drops by only 25% of the room temperature value, which is comparable to industry standard phosphors. The emission intensity of $Ba_{0.97}Eu_{0.03}Lu_2Si_3O_{10}$ decreases by 75% also because of quenching associated with the second Eu^{2+} site. The temperature dependent lifetime measurements require a bi-exponential function to fit the luminescence decay with a slow relaxation process between $450\,ns$ and $650\,ns$ corresponding to Eu^{2+} radiative relaxation. From the optical properties identified in these compounds, it is clear that even in highly connected structures, high symmetry is also required to prevent structural distortions that can limit the efficiency of new phosphors.

Chapter 6

Consequences of optimal bond valence on structural rigidity and improved luminescence properties in $Sr_xBa_{2-x}SiO_4$:Eu^{2+} orthosilicate phosphors

The orthosilicate phosphors $Sr_xBa_{2-x}SiO_4$:Eu^{2+} have now been known for over four decades and have found extensive recent use in solid-state white lighting. It is well-recognized in the literature and in practice that intermediate compositions in the solid-solutions between the orthosilicates Sr_2SiO_4 and Ba_2SiO_4 yield the best phosphor hosts when the thermal stability of luminescence is considered. We employ a combination of synchrotron X-ray diffraction, total scattering measurements, density functional theory calculations, and low-temperature heat capacity measurements, in conjunction with detailed temperature- and time-resolved studies of luminescence properties to understand the origins of the improved luminescence properties. We observe that in the intermediate compositions, the two cation sites in the crystal structure are optimally bonded as determined from bond valence sum calculations. Optimal bonding results in a more rigid lattice, as established by the intermediate compositions possessing the highest Debye temperature, which are determined experimentally from low-temperature heat capacity measurements. Greater rigidity in turn results in the highest luminescence efficiency for intermediate compositions at elevated temperatures.

6.1 Introduction

As the temperature of an LED increases during operation, thermal quenching of phosphor photoluminescence can lead to decreased efficiency and color instability. The emergence of high-power LEDs and laser-based white lighting for high brightness applications has led to increased research in understanding and optimizing the thermal stability of phosphor luminescence.[15] The widely used phosphor for solid state white lighting, YAG:Ce^{3+}, is not ideal as it suffers from thermal quenching at elevated temperatures.[34] Consequently, understanding the mechanisms of thermal quenching in phosphors and designing new compositions that maintain luminescence at high temperatures is an important goal in phosphor research.

Another widely used class of phosphors with interesting thermal quenching behavior is orthosilicates with the general composition A_2SiO_4 (A = Sr, Ba) substituted with Eu^{2+} on the (Sr/Ba) site. These compounds exhibit efficient excitation under both near-UV (λ_{max} = 405 nm) and blue (λ_{max} = 450 nm) light, with the emission ranging from green for Ba$_2$SiO$_4$:Eu^{2+} to yellow for Sr$_2$SiO$_4$:Eu^{2+}.[101, 141, 142] The Sr and Ba end-member compositions show strong thermal quenching of the photoluminescence, while intermediate compositions of the solid-solution Sr$_x$Ba$_{2-x}$SiO$_4$:Eu^{2+} exhibit improved thermal

179

performance.[27, 143] No explanation for this improved behavior has been previously noted in the literature.

In this work, we correlate the chemical bonding of the host crystal structure to the luminescent properties of the orthosilicate solid-solution phosphor $Sr_xBa_{2-x}SiO_4$:Eu^{2+}, identifying the origin of thermal stability in these compounds. Temperature and time dependent photoluminescence measurements are coupled with high resolution synchrotron X-ray diffraction and total scattering, low temperature heat capacity, and density functional theory calculations to discern changes in the average and local structure on the observed optical properties.

6.2   Experimental

Samples were prepared through traditional solid state routes. The end member compositions, $Sr_{1.90}Eu_{0.10}SiO_4$ and $Ba_{1.90}Eu_{0.10}SiO_4$, were prepared through a conventional high temperature solid-state reaction using starting materials of $BaCO_3$ (Materion, 99.9%), $SrCO_3$ (Materion, 99.5%), SiO_2 (Johnson-Matthey, 99.9%), and Eu_2O_3 (Aldrich, 99.99%), with $2\,wt\%$ NH_4Cl (Aldrich, 99.99%) as a flux. Powders were intimately mixed using an agate mortar and pestle for approximately $30\,minutes$, then pressed into pellets and placed in alumina

crucibles (CoorsTek) on a bed of sacrificial powder to prevent contact with the crucible. Samples were heated at $1300\,^\circ$C for 3 h in a reducing atmosphere of 5%H$_2$/95%N$_2$ with heating and cooling ramps of $2\,^\circ$C/min. Intermediate compositions include $Sr_{0.86}Ba_{1.06}Eu_{0.08}SiO_4$ (43% Sr), $Sr_{0.92}Ba_{0.98}Eu_{0.10}SiO_4$ (46% Sr), $Sr_{1.24}Ba_{0.64}Eu_{0.12}SiO_4$ (62% Sr), and $Sr_{1.46}Ba_{0.39}Eu_{0.15}SiO_4$ (73% Sr).

Room temperature photoluminescence spectra were obtained on a Perkin Elmer LS55 spectrophotometer equipped with a xenon lamp. Photoluminescence quantum yield (PLQY) was measured using phosphor powders encapsulated in silicone resin (GE Silicones, RTV-615) and deposited on transparent quartz substrates (Chemglass). The samples were placed inside a Spectralon™-coated integrating sphere (6 inch diameter, Labsphere) and excited using 405 nm light generated by a solid-state laser (Crystalaser DL-405-40-S) operated at a power between 1 mW and 2 mW. The light was collected by a quartz lens and directed onto a calibrated Si photodiode (Newport 818-UV), using filters (Omega Filters) to collect respective wavelengths. Data collection and processing procedures were conducted similar to those described by Greenham *et al.*[59] Temperature dependence of the photoluminescence was measured in the temperature range from 77 K to 503 K using a home-built fluorimeter incorporating a cryostat for low temperature measurements and a heating stage for high temperature data collection.

Decay time measurements were collected in the temperature range from 77 K to 503 K using the Time-Correlated Single Photon Counting (TCSPC) technique[137]. Approximately 200 fs excitation pulses with a wavelength 440 nm were generated by doubling the fundamental frequency of femtosecond Ti:Sapphire laser (Coherent Mira 900) pulses in a commercial optical harmonic generator (Inrad). The laser repetition rate was reduced to 200 kHz by a home-made acousto-optical pulse picker in order to avoid saturation of the phosphor. The TCSPC system is equipped with an ultrafast microchannel plate photomultiplier tube detector (Hamamatsu R3809U-51) and electronics board (Becker & Hickl SPC-630), and has instrument response time of about 60-65 ps. The triggering signal for the TCSPC board was generated by sending a small fraction of the laser beam onto a fast (400 MHz bandwidth) Si photodiode (Thorlabs Inc.). Fluorescence signal was dispersed using an Acton Research SPC-500 monochromator after passing through a pump blocking, long-wavelength pass, autofluorescence-free, interference filter (Omega Filters, ALP series). The monochromator is equipped with a CCD camera (Roper Scientific PIXIS-400), allowing for monitoring of the time-averaged fluorescence spectrum. Luminescence transients were not deconvolved with the instrument response function since their characteristic time constants were much longer than the width of the system response to the excitation pulse.

Synchrotron X-ray powder diffraction data were collected at room temperature and 100 K on the 11-BM instrument at the Advanced Photon Source (APS), Argonne National Laboratory using an average wavelength of $\lambda = 0.413523$ Å. Rietveld analysis was carried out using the General Structure Analysis System (GSAS)[95, 96]. The background was handled using a shifted Chebyshev function, while the peak shapes were handled using a pseudo-Voigt function with Finger-Cox-Jephcoat asymmetry to correct for axial divergence at low angles. X-ray total scattering data were collected at room temperature on the 11-ID-B instrument at the APS, Argonne National Laboratory using an energy of 90 keV and an average wavelength of 0.13702 Å. The data were extracted using PDFgetX3[144] with $Q_{max} = 30$ Å. Least-squares refinement was performed on the pair-distribution function (PDF) to obtain average structure information using PDFgui.[145]

Low-temperature heat capacity was measured using a Quantum Design Physical Properties Measurement System. Heat capacity measurements from 1.9 K to 20 K were collected on pellets with a mass of approximately 15 mg and analyzed using thermal relaxation calorimetry. A thin layer of Apiezon N grease ensured thermal contact between the platform and the sample. The heat capacity of the Apiezon N grease was collected separately and subtracted from the measured sample heat capacity. Samples of Sr_2SiO_4, Ba_2SiO_4, and $Sr_{0.9}Ba_{1.1}SiO_4$ ($\approx46\%$

Sr) without Eu^{2+} substitution were measured to avoid any magnetic contributions to the heat capacity.

Density Functional Theory (DFT) calculations were performed using the Vienna *ab initio* Simulation Package (VASP).[50–53] Unit cells were constructed for Sr_2SiO_4, Ba_2SiO_4, and $SrBaSiO_4$. The bulk modulus and Poisson's ratio were calculated using the Voigt-Reuss-Hill (VRH) approximations[146] based on the elastic constants (C_{ij}) determined using VASP and the arithmetic relations outlined by Wu *et al.*[147]. The elastic moduli were then used to estimate the Debye temperature (Θ_D) using the quasi-harmonic Debye model.[148–150] All VASP (version 5.2) calculations were performed using the projector augmented wave method (PAW).[54, 55] Initial relaxation of the atomic positions were performed to ensure the compounds are in their electronic ground state. The elastic tensors were then determined from the stress-strain relationship of six finite distortions of the crystal using displacements of ± 0.015 Å.[138] Exchange and correlation were described by the 1996 version of the Perdew-Burke-Ernzerhof generalized gradient approximation (GGA-PBE).[56, 57] The energy cutoff of the plane wave basis set was 600 eV and 100 **k**-points (determined using a Monkhorst-Pack grid) was used. The energy convergence criteria was set to 1×10^{-6} eV per formula unit to ensure accurate electronic convergence.
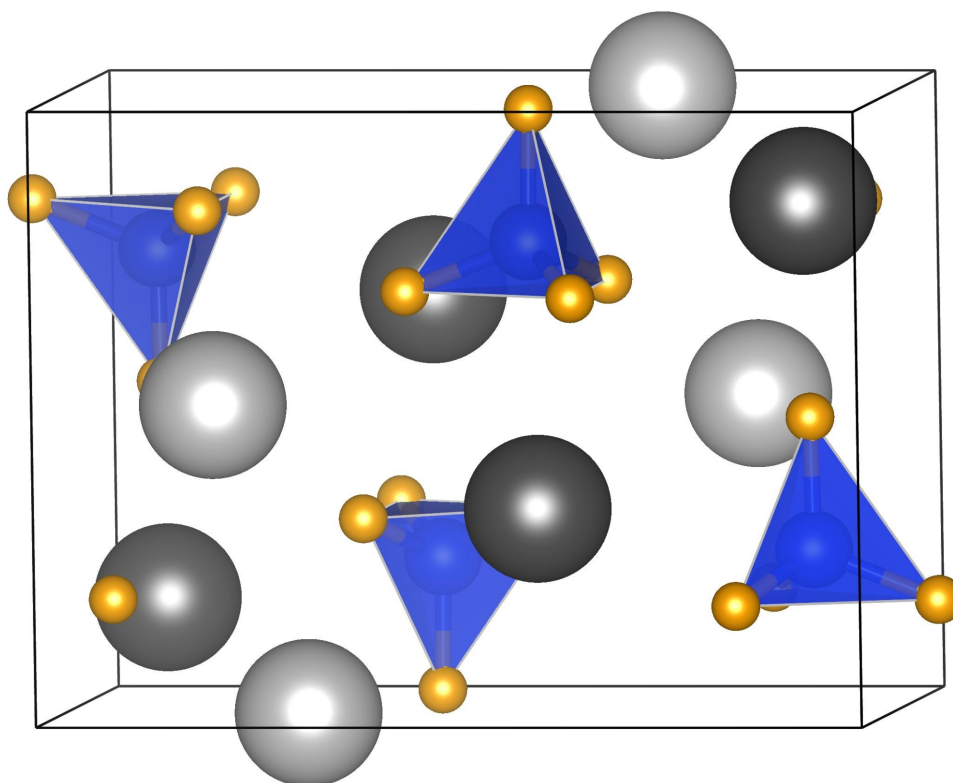
Figure 6.1: Crystal structure of $Sr_xBa_{2-x}SiO_4$ in the orthorhombic space group $Pmcn$ (No. 62) with SiO_4 polyhedra shown as blue, O^{2-} shown as orange, the Sr/Ba1 10-coordinate site shown as dark gray, and the Sr/Ba2 9-coordinate site shown as light gray. Reproduced with permission from reference [36], ©2014 American Chemical Society.

6.3 Results and Discussion

Barium orthosilicate crystallizes in the orthorhombic space group $Pmcn$ (No. 62) with the β-K_2SO_4 structure type. Strontium orthosilicate exists in two polymorphs: the orthorhombic α phase is the same structure type as Ba_2SiO_4, while the monoclinic β phase crystallizes in space group $P2_1/n$ (No. 14) with the

Table 6.1: Comparison of effective ionic radii indicates potential site mixing between Sr^{2+} and Ba^{2+} in intermediate compounds and potential Eu^{2+} substitution in both crystallographic sites.

| site | CN | effective ionic radii (Å) | | |
		Sr^{2+}	Ba^{2+}	Eu^{2+}
Sr/Ba1 $4c$	10	1.36	1.52	1.35
Sr/Ba2 $4c$	9	1.31	1.47	1.30

Ca_2SiO_4 structure type. The addition of Ba^{2+} or Eu^{2+} in Sr_2SiO_4 stabilizes the α phase at room temperature. Due to the presence of β-Sr_2SiO_4 at lower temperatures, only room temperature photoluminescence of the Sr_2SiO_4:Eu^{2+} and Ba_2SiO_4:Eu^{2+} end members are discussed here. The intermediate compositions of the $Sr_xBa_{2-x}SiO_4$:Eu^{2+} solid-solution phosphor maintain the orthorhombic β-K_2SO_4 structure for all Sr^{2+} concentrations and temperatures explored here. The unit cell, shown in Figure 6.1, can accommodate Eu^{2+} in two distinct sites, the 10-coordinate Wyckoff site $4c$ (Sr/Ba1) with a larger polyhedral volume and the 9-coordinate Wyckoff site $4c$ (Sr/Ba2) with a smaller polyhedral volume. A comparison of ionic radii for Sr^{2+}, Ba^{2+}, and Eu^{2+}, shown in Table 6.1, indicate possible site mixing of Sr^{2+} and Ba^{2+} in the intermediate compositions and that Eu^{2+} substitution can occur on both sites.

Excitation and emission spectra, collected at room temperature, are shown in Figure 6.2 for all compositions and Table 6.2 lists all relevant photoluminescent properties. All samples can be efficiently excited with both blue (λ_{max} =
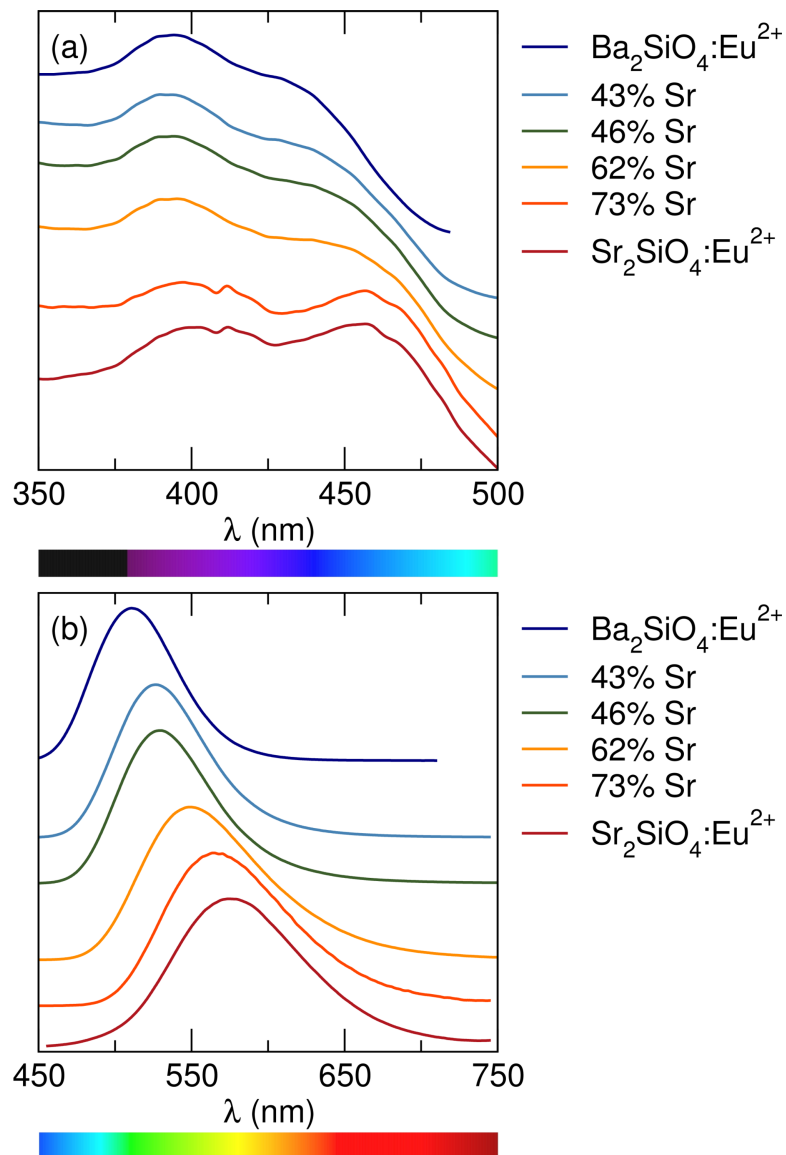
Figure 6.2: (a) Excitation and (b) emission spectra collected at room temperature using the maximum emission/excitation wavelength for each sample show excitation across the near-UV to blue region with broad emission across the green to yellow region of the visible spectrum. Reproduced with permission from reference [36], ©2014 American Chemical Society.
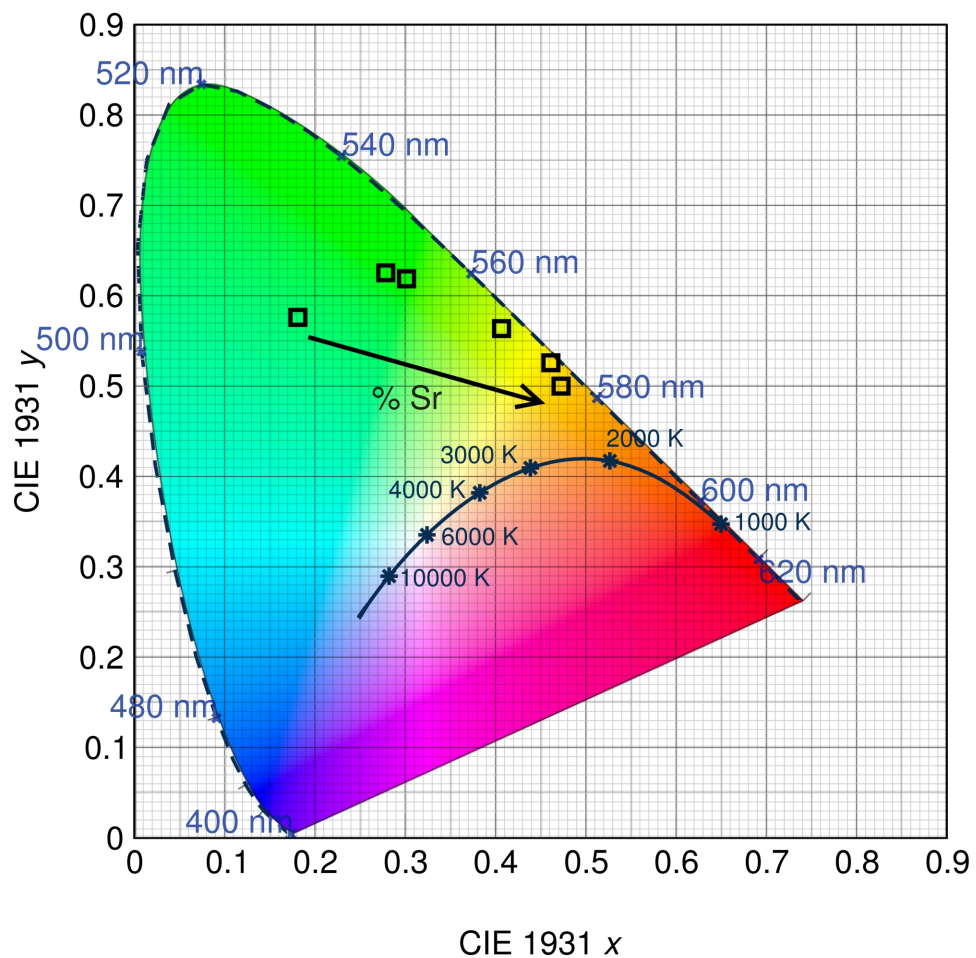
Figure 6.3: Increasing Sr^{2+} content results in a shift in emission color from green to yellow, shown on the CIE diagram, capturing the effects of the broadening emission spectrum as well. Reproduced with permission from reference [36], ©2014 American Chemical Society.
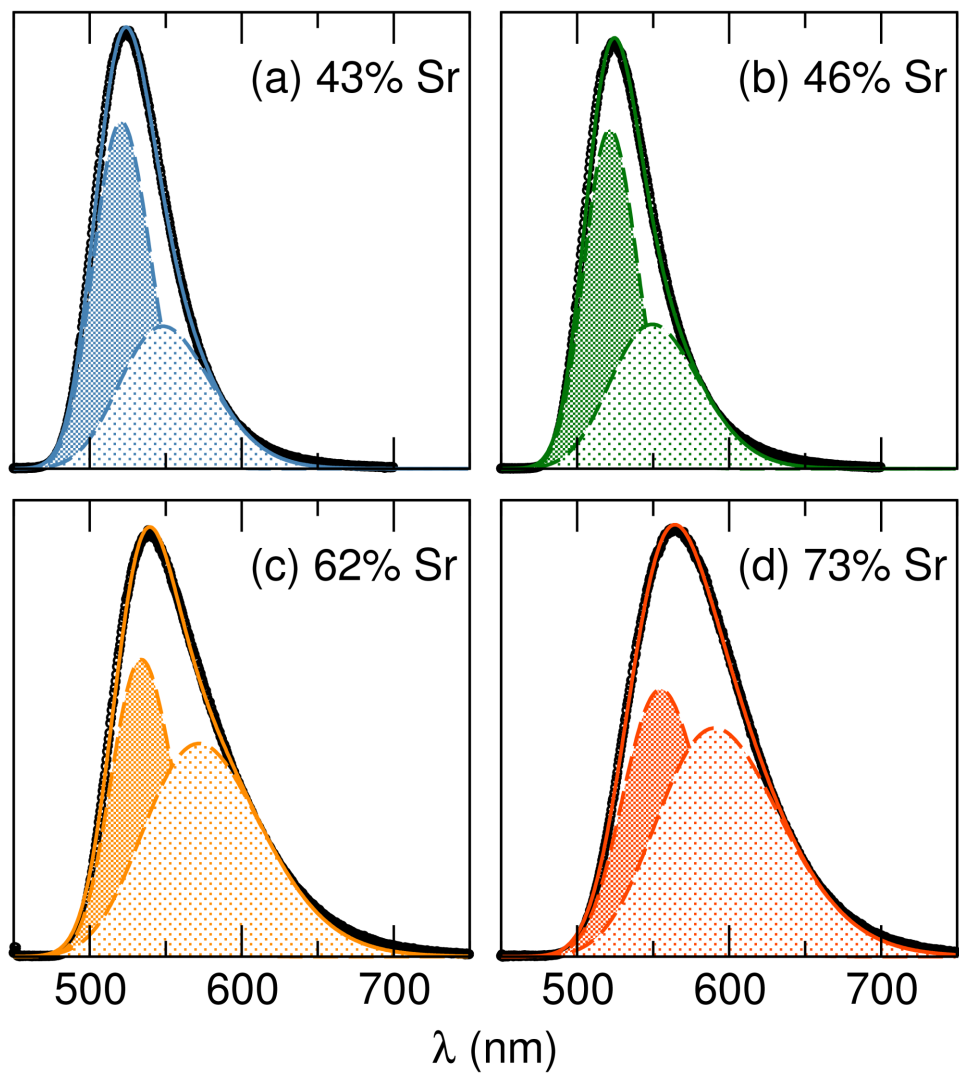
Figure 6.4: Emission spectra at 77 K fit to two Gaussian functions for (a) 43% Sr, (b) 46% Sr, (c) 62% Sr, and (d) 73% Sr show the contribution to the emission spectra from Eu^{2+} in two distinct crystallographic sites. Dashed lines represent the individual Gaussian functions and the solid line represents the total fit. Reproduced with permission from reference [36], ©2014 American Chemical Society.

Table 6.2: Photoluminescent properties measured at room temperature, including the maximum excitation and emission wavelength, FWHM of the emission spectrum, the difference between the maximum emission wavelength and the maximum excitation wavelength ($\Delta\lambda$), and photoluminescent quantum yield ($\pm 5\%$).

sample	λ_{ex} (nm)	λ_{em} (nm)	FWHM (nm)	$\Delta\lambda$ (nm)	PLQY (%)
Ba_2SiO_4:Eu^{2+}	395	511	64	116	–
43% Sr	390	527	69	137	89
46% Sr	394	530	72	136	90
62% Sr	396	549	92	153	89
73% Sr	397	565	96	168	88
Sr_2SiO_4:Eu^{2+}	405	574	100	169	–

450 nm) and near-UV ($\lambda_{max} = 405$ nm) light and emit in the green to yellow region, making these materials ideal for white lighting applications. The excitation spectrum exhibits a slight red-shift with increasing Sr^{2+} content, while the emission spectrum shows a large red-shift of about 65 nm, increasing the difference between the maximum emission wavelength and the maximum excitation wavelength ($\Delta\lambda$). The maximum emission wavelength (λ_{em}) shifts from 511 nm for Ba_2SiO_4:Eu^{2+} to 574 nm for Sr_2SiO_4:Eu^{2+}, and the FWHM increases from 64 nm to 100 nm with increasing Sr^{2+} content. The effects of varying the Sr/Ba ratio on the emission color is clearly illustrated on the Commission Internationale de l'Eclairage (CIE) diagram, in Figure 6.3, with the emission color shifting from green to yellow-orange as Sr^{2+} content increases. In addition, the two emission bands arising from Eu^{2+} on two distinct crystallographic sites can be resolved at 77 K, shown in Figure 6.4. The photoluminescent quantum yield

Table 6.3: Thermal properties extracted from temperature dependent lifetimes for intermediate samples including the maximum temperature up to which photoluminescence is stable, T_{max}, and the activation energy for thermal quenching, ΔE.

sample	T_{max} (K)	ΔE (eV)
43% Sr	383	0.59(4)
46% Sr	413	0.67(5)
62% Sr	323	0.58(1)
73% Sr	294	0.54(3)

is about 90±5% for all intermediate compositions.

To explore the mechanisms of thermal quenching, temperature dependent photoluminescence lifetimes were collected from 77 K to 503 K under 440 nm excitation monitored at the respective maximum emission wavelength for all intermediate compositions. Single- and bi-exponential functions were used to fit the decrease in intensity as a function of time at 77 K. A bi-exponential fit was required to achieve suitable agreement with the data, indicating Eu^{2+} is present in two distinct coordination environments, in agreement with the consideration of the ionic radii, the crystal structure, and the low temperature emission spectra (see above). Figure 6.5 shows the extracted lifetimes from the bi-exponential fit and a weighted average lifetime (determined from the pre-exponential factors) as a function of temperature; the maximum temperature up to which photoluminescence is stable is highlighted by the dashed line for each sample. There is a fast and a slow component of the lifetime, and a resulting weighted average
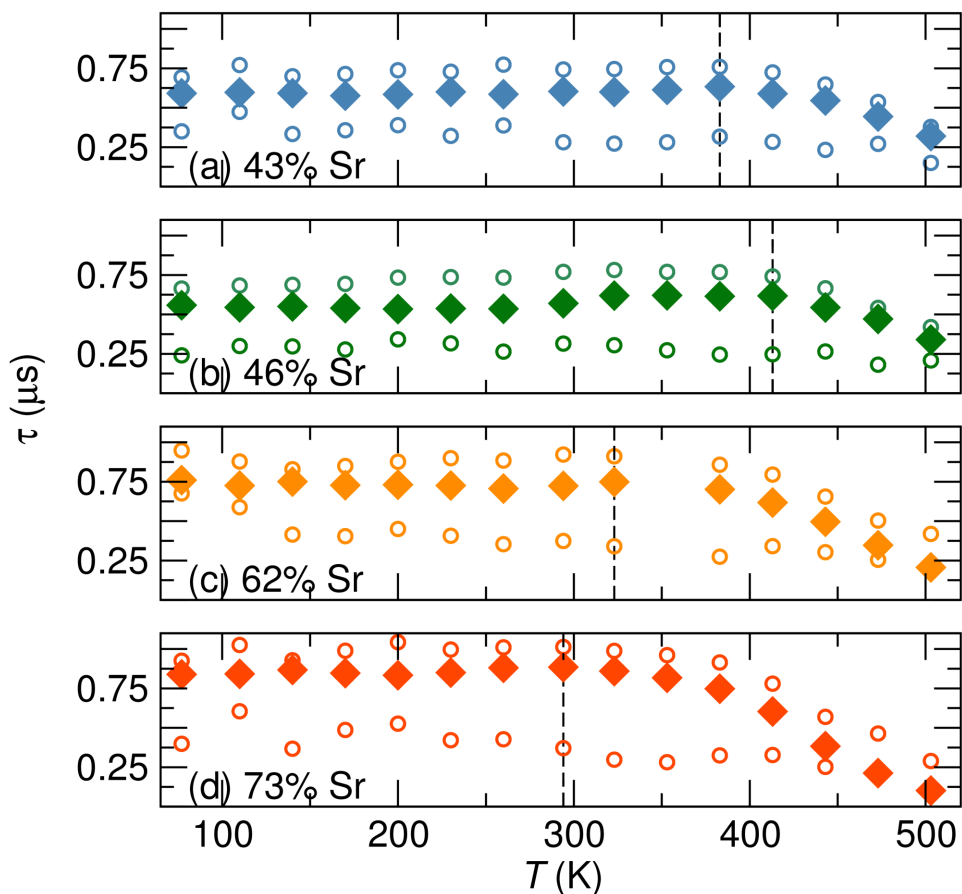
Figure 6.5: Lifetimes extracted from bi-exponential fits to the intensity decay for (a) 43% Sr, (b) 46% Sr, (c) 62% Sr, and (d) 73% Sr show the composition with 46% Sr is thermally stable up to a higher temperature compared to the other samples. Open circles represent the two measured lifetimes and closed diamonds represent the weighted average lifetime. Dashed vertical lines indicate the maximum temperature before the lifetime begins to decrease due to thermal quenching. Reproduced with permission from reference [36], ©2014 American Chemical Society.
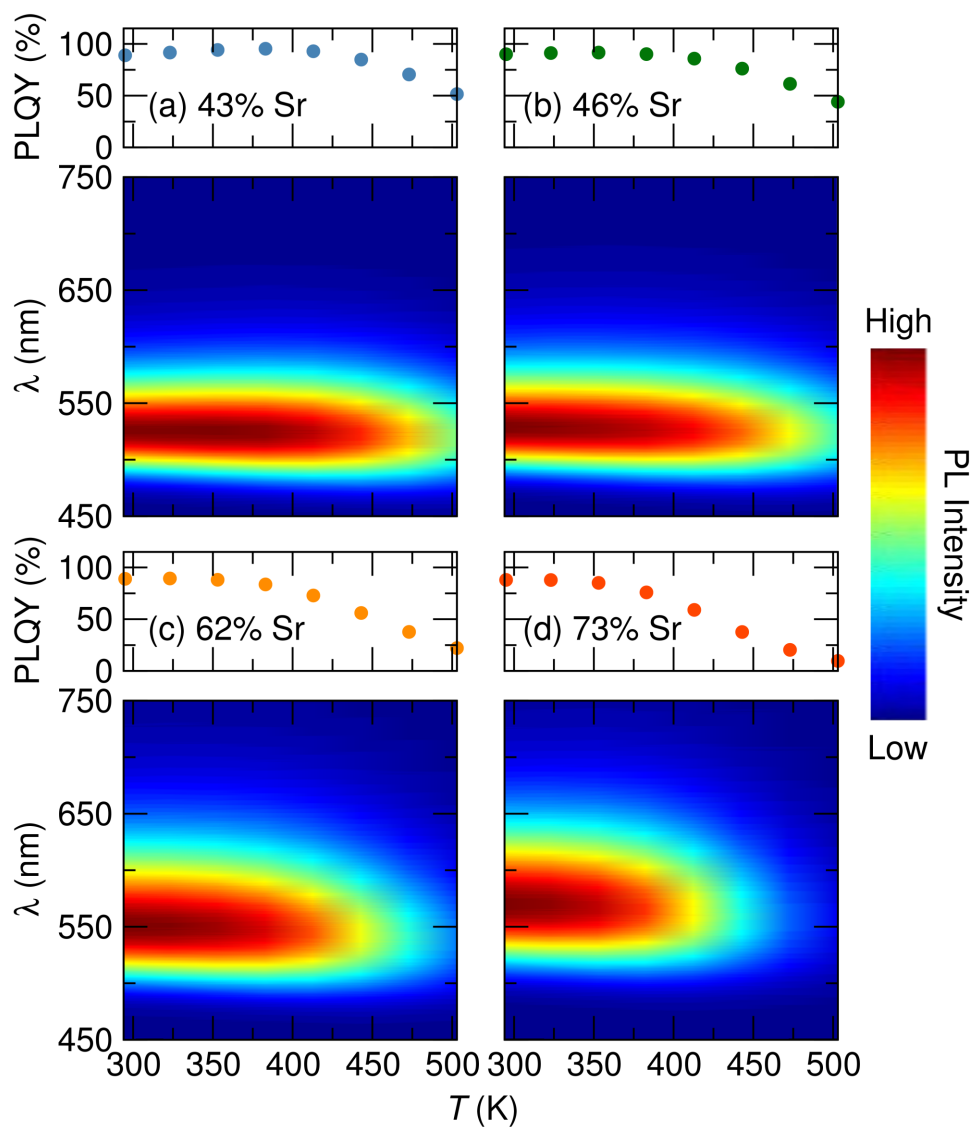
Figure 6.6: Maximum emission wavelength and FWHM of the emission spectra stay relatively constant from room temperature to 500 K with a slight decrease in photoluminescent quantum yield (based on integrated intensity) for intermediate compositions (a) 43% Sr, (b) 46% Sr, (c) 62% Sr, and (d) 73% Sr. Reproduced with permission from reference [36], ©2014 American Chemical Society.

lifetime. The longer lifetime dominates for all intermediate compositions, with a relative percentage of approximately 75%. The longer lifetime value of $\approx 0.7\,\mu s$ for Ba-rich compositions and $\approx 0.9\,\mu s$ for Sr-rich compositions agrees well with previous reports.[86] The shorter lifetime value of $\approx 0.3\,\mu s$ is shorter by a factor of two compared to previous reports, most likely arising from concentration quenching due to the high Eu^{2+} concentration. The two lifetimes are most likely due to the two Eu^{2+} environments. In this case, lifetimes cannot be assigned to the corresponding Eu^{2+} site because emission from both sites are being monitored simultaneously (based on the fits to the low temperature emission spectra) due to the choice of monitoring wavelength.

There is a trend of increasing lifetime as Sr^{2+} content increases, which also corresponds to increasing Eu^{2+} concentration. This may be caused by increased reabsorption of the emission as Eu^{2+} concentration increases, as was shown previously by Bachmann *et. al.* in YAG:Ce^{3+}.[34] The decrease in photoluminescent lifetime can be attributed to the onset of thermal quenching. It should also be considered that the Eu^{2+} concentration may play a role in the onset of thermal quenching, but we do not see a clear trend here from the changes in concentration. From this lifetime information, the activation energy for thermal

quenching, ΔE, can be extracted using[27]

$$\Gamma(T) = \Gamma_\nu + \Gamma_0 \exp\left(\frac{-\Delta E}{k_\mathrm{B}T}\right) \qquad (6.1)$$

where Γ_ν is the radiative decay rate of the $5d$ state of Eu^{2+}, Γ_0 is the attempt rate for thermal quenching, k_B is the Boltzmann constant, and T is temperature. The extracted activation energies for thermal quenching are listed in Table 6.3. The intermediate compositions with 46% Sr shows the highest thermal stability and activation energy for quenching. The intermediate compositions also show relatively stable color properties with increasing temperature. The emission maximum and FWHM remain relatively constant up to 500 K, with only a slight increase in the FWHM (Figure 6.6). The effective emission efficiency at elevated temperatures was determined by relating the integrated emission intensity at each temperature to the room temperature PLQY value. It should be noted that this is not a true quantum efficiency for elevated temperatures because this does not take into account any changes in sample absorption. At 413 K, the approximate operating temperature of a current LED, the 43% Sr composition maintains a PLQY of 85±5% and the 46% Sr composition maintains a PLQY of 75±5%.

To understand the origins of the high photoluminescence thermal stability for the intermediate compositions with 46% Sr, we explore the average and
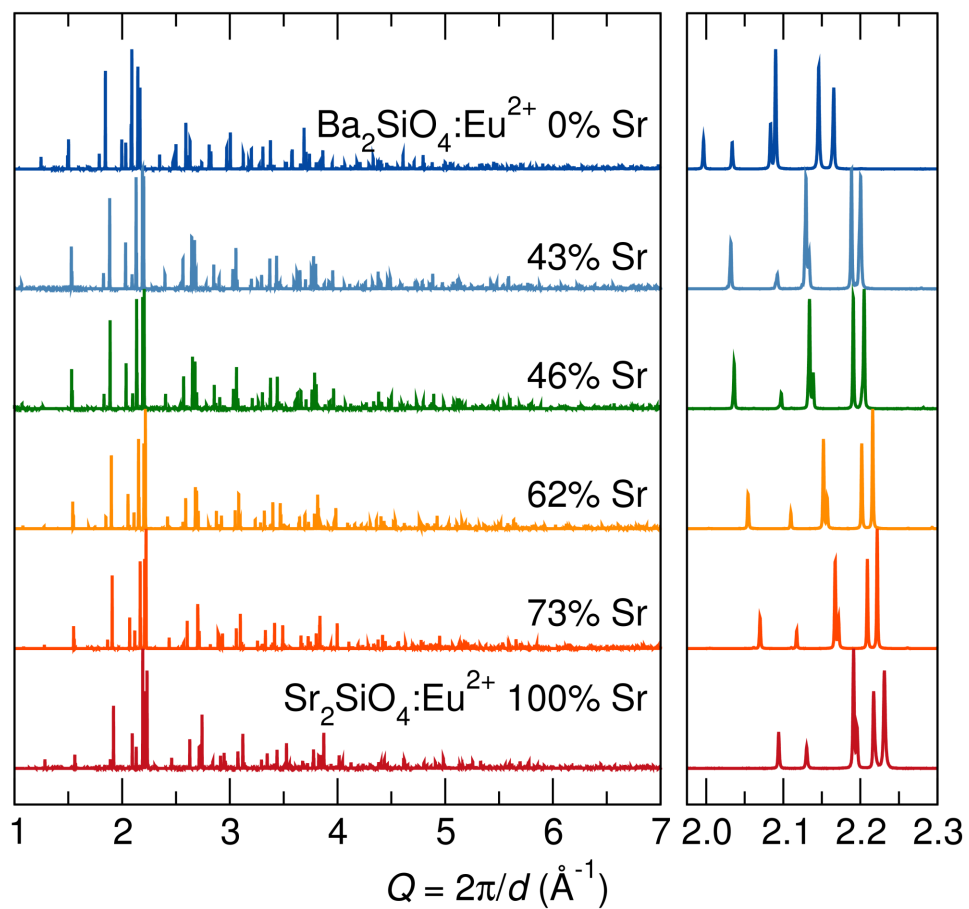
Figure 6.7: High resolution synchrotron X-ray diffraction patterns indicate changes in the average structure as Sr^{2+} content increases, highlighted by shifts in the main diffraction peaks (shown on right). Reproduced with permission from reference [36], ©2014 American Chemical Society.
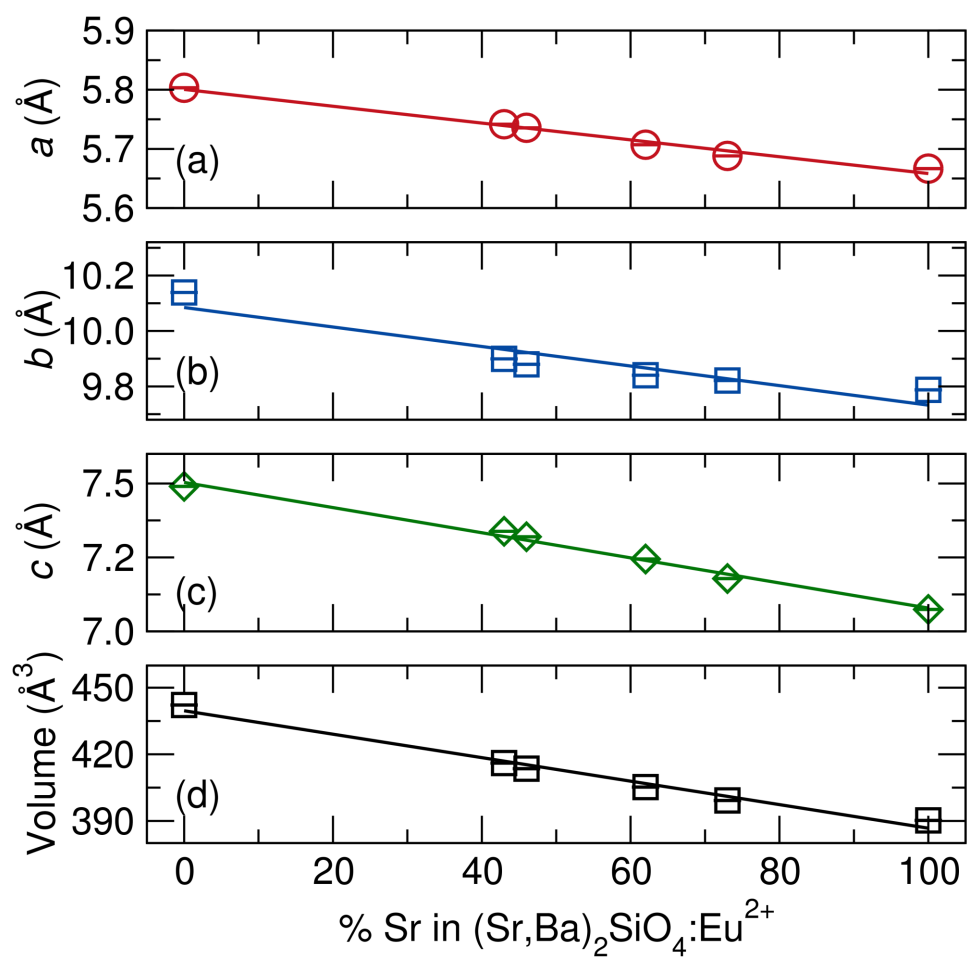
Figure 6.8: Refined (a) a lattice parameter, (b) b lattice parameter, (c) c lattice parameter, and (d) unit cell volume show a linear decrease following Végard's law as the smaller Sr^{2+} replaces the larger Ba^{2+} with increasing Sr^{2+} content. Error bars are shown and are smaller than the data point symbols. Reproduced with permission from reference [36], ©2014 American Chemical Society.
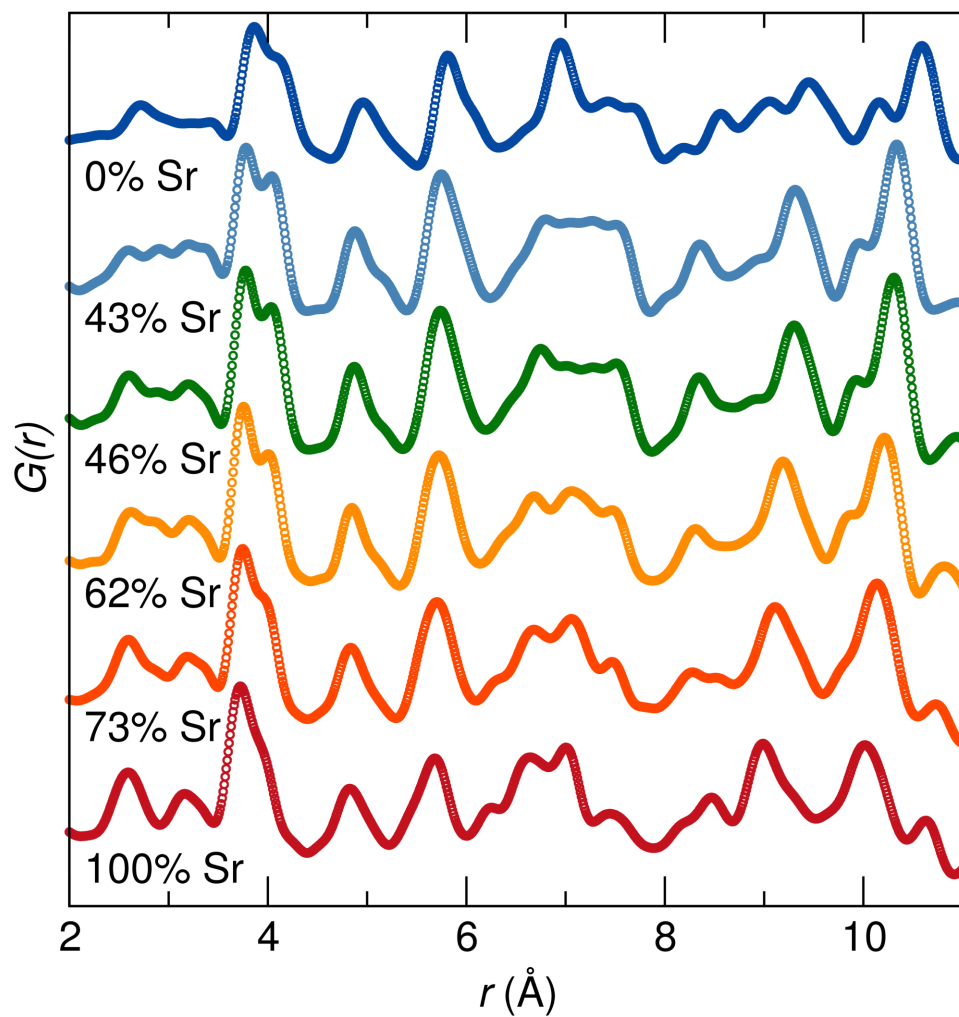
Figure 6.9: Analysis of the X-ray pair distribution function collected at room temperature shows changes in peak intensity and position in the low-r region indicating changes in the local structure as Sr^{2+} content increases. Reproduced with permission from reference [36], ©2014 American Chemical Society.

local crystal structure of these materials. High resolution synchrotron X-ray diffraction data collected at room temperature for all compositions are shown in Figure 6.7. Rietveld refinements indicate all samples are nearly pure phase and in good agreement with the structural models. Lattice parameters and unit cell volume, shown in Figure 6.8, show a linear decrease following Végard's law as expected with the smaller Sr^{2+} replacing the larger Ba^{2+}. X-ray pair distribution function (PDF) analysis, shown in Figure 6.9, indicates a change in the local structure as the Sr^{2+} content increases. The low-r region of the PDF shows changes in the local structure corresponding to the Sr/Ba (and Eu) to oxygen distances in the first coordination shell relating directly to the changes observed in the optical properties.

The polyhedral volume of the Sr/Ba1 and Sr/Ba2 sites were calculated using the method outlined by Swanson and Peterson[68]. A polyhedral distortion index, D, can be calculated following[67]

$$D = \frac{1}{n} \sum_{i=1}^{n} \frac{\mid l_i - l_{av} \mid}{l_{av}} \tag{6.2}$$

where l_i is the distance from the central atom to the ith coordinating atom and l_{av} is the average bond length. Figure 6.10 reveals a decrease in the polyhedral volume and an increase in the distortion of both of the Eu^{2+} active site polyhedra as Sr^{2+} content increases. Referring to crystal field splitting theory,
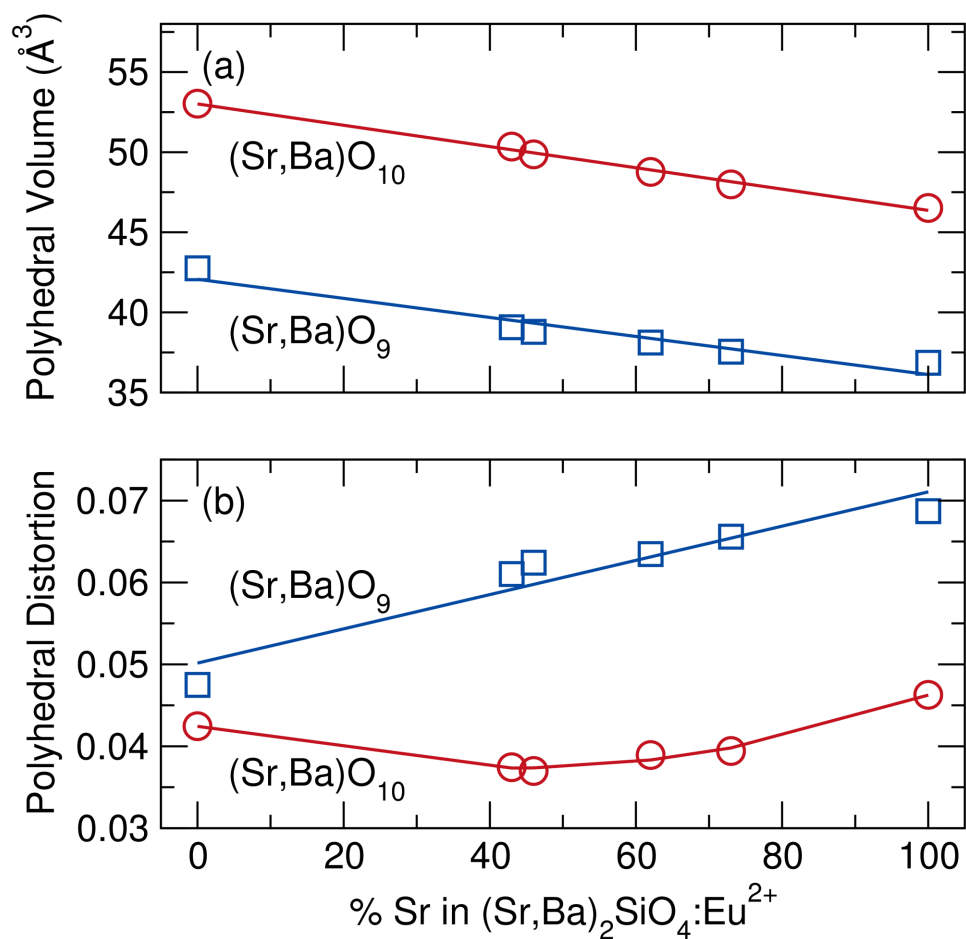
Figure 6.10: (a) Both activator ion sites experience a decrease in polyhedral volume as Sr^{2+} content increases and (b) an increase in the polyhedral distortion, both effects leading to the red-shifted optical properties observed. Reproduced with permission from reference [36], ©2014 American Chemical Society.

Dorenbos has described the crystal field splitting of the $5d$ levels in Ce^{3+} to be related to the Ce–anion distance by an R^{-2} relationship.[81] Previous work has shown that increasing polyhedral distortion may also increase the crystal field splitting.[38] Therefore, the observed decrease in polyhedral volume and increased distortion cause strong crystal field splitting and the resulting red-shift in the optical properties as Sr^{2+} content increases.

In the structural models for the intermediate compositions, site mixing between Sr^{2+} and Ba^{2+} was considered and occupancies were refined. Substitution of Eu^{2+} was not considered in the models due to the low concentrations. The refined compositions match the loaded stoichiometries. Refined occupancies are illustrated in Figure 6.11a, and show that the smaller Sr^{2+} prefers the smaller 9-coordinate Sr/Ba2 site, while the larger Ba^{2+} prefers the larger 10-coordinate Sr/Ba1 site. This is also observed by considering bond valence sums (BVS)[69], shown in Figure 6.11b. Ba^{2+} is highly overbonded with a BVS greater than +2 ($\approx$ +2.25) in the small Sr/Ba2 site, while Sr^{2+} is highly underbonded ($\approx$ +1.75) in the large Sr/Ba1 site. Taking into account the refined occupancies, the adjusted BVSs for each site are shown in Figure 6.11c. The end member compositions cause one site to be overbonded and one site to be underbonded, while the intermediate compositions with varying Sr/Ba ratios are able to balance this and achieve an optimized bonding network with a BVS close to +2 for
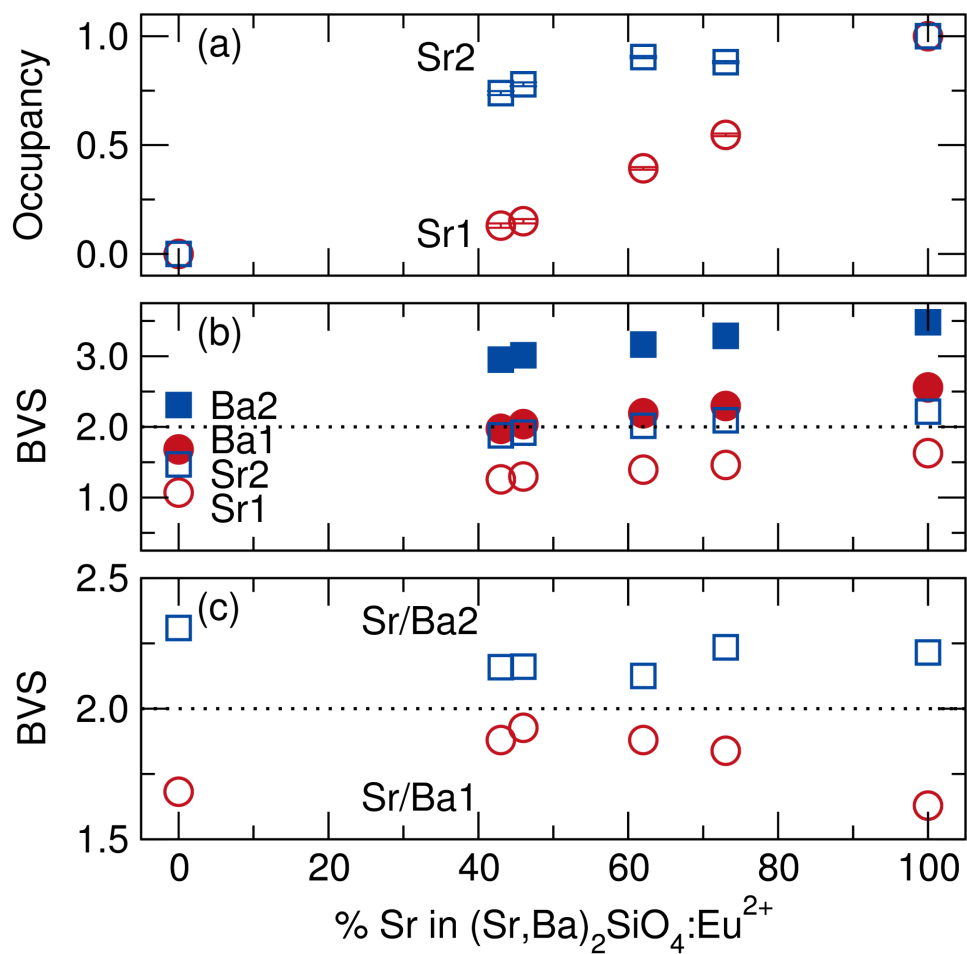
Figure 6.11: (a) Refined occupancies, (b) bond valence sums, and (c) occupancy-corrected bond valence sums indicate an optimal bonding environment for intermediate compositions compared to end member compositions. Reproduced with permission from reference [36], ©2014 American Chemical Society.

Table 6.4: Debye temperature, Θ_D, measured using low temperature heat capacity and calculated using density functional theory.

sample	Θ_D measured (K)	Θ_D calculated (K)
α-Sr_2SiO_4	–	360
β-Sr_2SiO_4	368	428
$Sr_{0.9}Ba_{1.1}SiO_4{}^a$ ($\approx$46% Sr)	390	328
Ba_2SiO_4	336	307

^{a} Composition $SrBaSiO_4$ was used for calculated Θ_D.

both sites. This indicates that the intermediate compositions form a highly rigid crystal structure, which will have an influence on the thermal stability of the photoluminescence.

Further exploring the structural rigidity of these compounds by measuring low temperature heat capacity, the specific heat (C_P) of Sr_2SiO_4, Ba_2SiO_4, and $Sr_{0.9}Ba_{1.1}SiO_4$ ($\approx$46% Sr) without Eu^{2+} substitution are shown in Figure 6.12. The Debye temperature, Θ_D, used as a measure of structural rigidity, can be extracted from the data by fitting the specific heat below 5 K to the Debye model in the low-temperature limit[148–150]

$$C_p \sim \frac{12 N k_B \pi^4}{5} \left(\frac{T}{\Theta_D} \right)^3 \tag{6.3}$$

where N is the number of atoms per formula unit multiplied by Avogadro's number, k_B is the Boltzmann constant, and T is the temperature. Fits to the data are shown in Figure 6.12 and the extracted Θ_D are listed in Table 6.4. The Θ_D of α-Sr_2SiO_4 cannot be determined using the low temperature heat capacity method
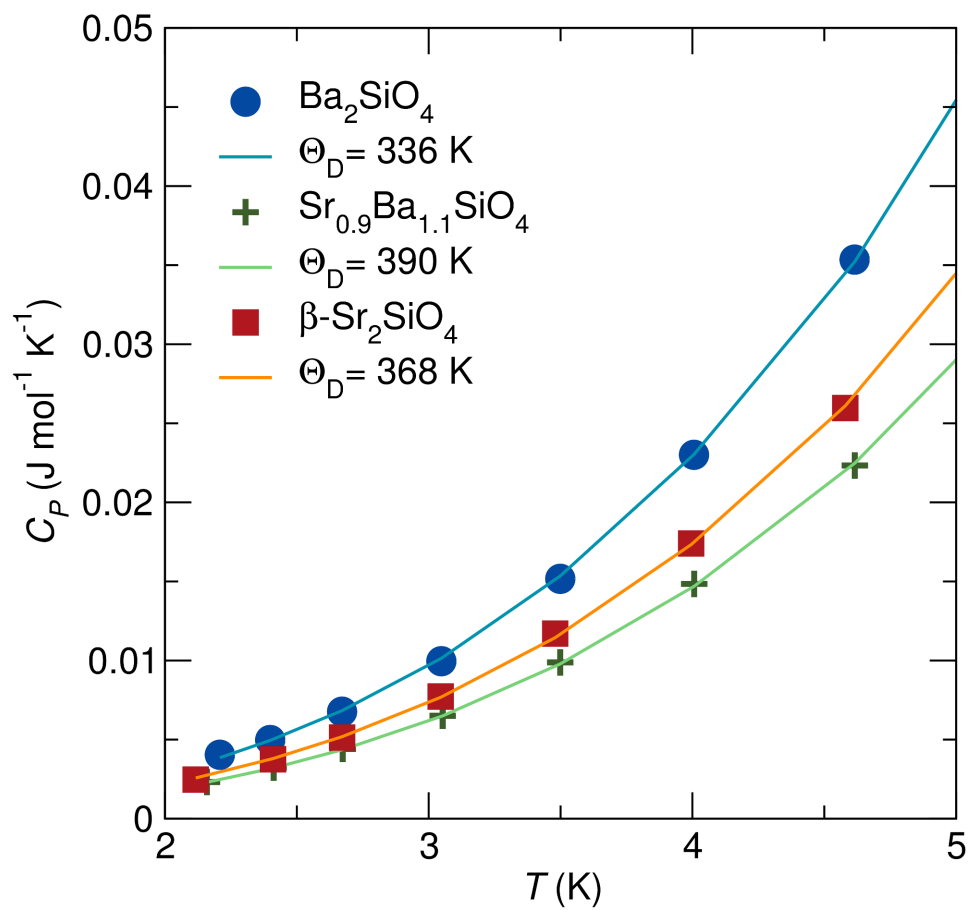
Figure 6.12: Low temperature heat capacity and extracted Debye temperatures indicate that the intermediate compound $Sr_{0.9}Ba_{1.1}SiO_4$ has the highest Debye temperature, and thus the most rigid crystal structure compared to either end member composition. Reproduced with permission from reference [36], ©2014 American Chemical Society.

due to the formation of β-Sr_2SiO_4. We instead measured the heat capacity of the β phase to compare the measured Θ_D to the calculated value. The measured Debye temperature is highest for the intermediate composition $Sr_{0.9}Ba_{1.1}SiO_4$, indicating a more rigid crystal structure compared to the Ba_2SiO_4 end member and the β-Sr_2SiO_4 composition. Based on atomic mass considerations, a higher Debye temperature is expected as the Sr^{2+} content increases due to the lighter Sr^{2+} atom replacing the heavier Ba^{2+} atom. Therefore, the higher Debye temperature for the intermediate compound is directly linked to the local structure and the optimized bonding in the intermediate composition, giving rise to the improved thermal stability of the photoluminescence.

Density functional theory has recently been explored as a method for predicting the Debye temperature and structural rigidity of phosphor hosts[35]. Applying this method, the calculated Debye temperatures are listed in Table 6.4 along with the experimentally measured values. Using DFT we are able to determine the theoretical Θ_D of both the α- and β-Sr_2SiO_4 structures. For the intermediate composition, a unit cell of $SrBaSiO_4$ was used with Sr^{2+} fully occupying the Sr/Ba2 site and Ba^{2+} fully occupying the Sr/Ba1 site. The calculated Θ_D follows the trend expected based on atomic mass considerations for the solid-solution, with Ba_2SiO_4 having the lowest Θ_D (307 K), the intermediate compound a slightly higher Θ_D (328 K), and α-Sr_2SiO_4 the highest Θ_D (360 K).

Surprisingly, DFT is unable to capture the local structure of the intermediate compound that leads to the optimized bonding and high Θ_D. Additionally, the measured and calculated Θ_D for β-Sr_2SiO_4 are not in good agreement, and is predicted to have the highest Θ_D which is not evidenced in the measured heat capacity, and requires further investigation.

6.4 Conclusions

Using a combination of optical and structural characterization techniques, the origins the thermal stability of luminescence are revealed in the orthosilicate solid-solution phosphor $Sr_xBa_{2-x}SiO_4$:Eu^{2+}. The intermediate composition with 46% Sr has the highest resistance to thermal quenching of luminescence, remaining stable up to 413 K, and maintaining an emission efficiency of 75% (based on integrated intensity). The activation energy for thermal quenching is 0.57 eV for this composition. Structural studies using high resolution X-ray diffraction and total scattering show that the intermediate compositions possess optimal bonding that creates a more rigid crystal structure compared to the end-member compositions. An indicator of the increased structural rigidity is obtained from low temperature heat capacity to determine the Debye temperature, and suggests the intermediate composition of $Sr_{0.9}Ba_{1.1}SiO_4$ indeed

does possess the highest Debye temperature. The high Debye temperature limits access to phonon modes which may contribute to thermal quenching of the luminescence. This result provides an impetus for the search for new, efficient phosphor hosts that possess highly connected structures and optimized bonding interactions.

6.5   Appendix
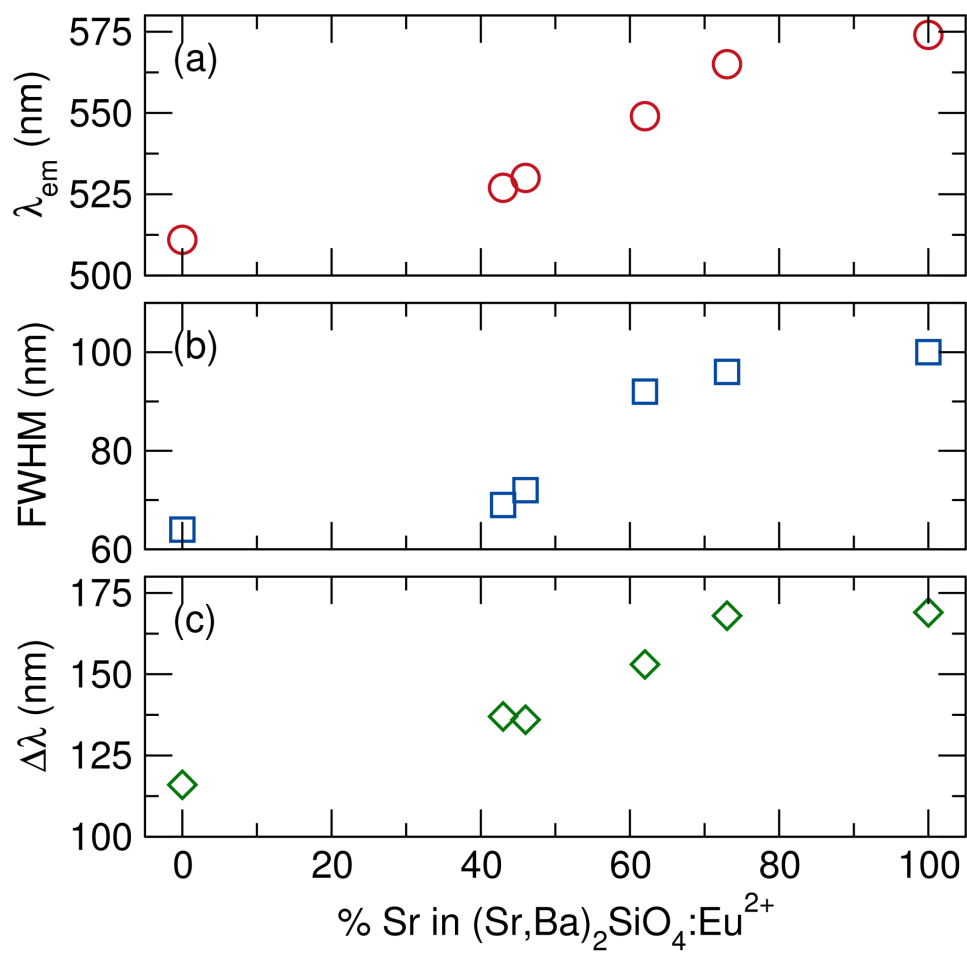
Figure 6.13: Changes in the photoluminescent properties with increasing Sr^{2+} content show (a) a large red-shift in the maximum emission wavelength, (b) an increase in the FWHM of the emission spectrum, and (c) an increase in the difference between the maximum emission wavelength and the maximum excitation wavelength ($\Delta\lambda$). Reproduced with permission from reference [36], ©2014 American Chemical Society.
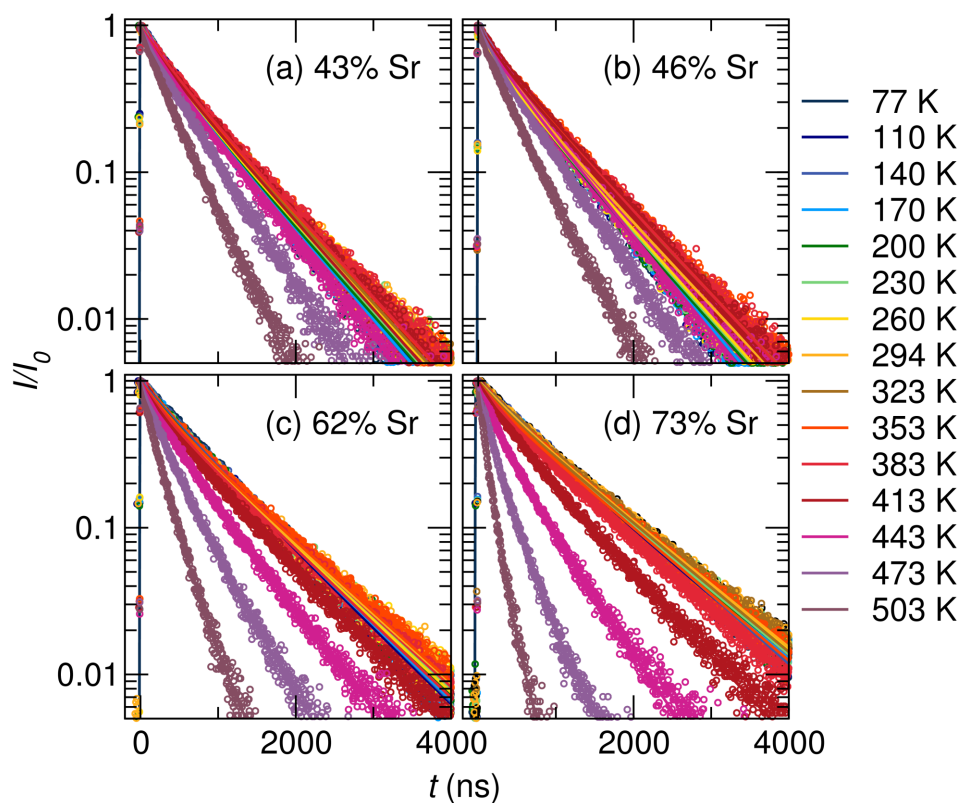
Figure 6.14: Intensity decay as function of time measured from 77 K to 503 K under 440 nm excitation for (a) 43% Sr, (b) 46% Sr, (c) 62% Sr, and (d) 73% Sr is used to analyze thermal quenching of photoluminescence. Reproduced with permission from reference [36], ©2014 American Chemical Society.
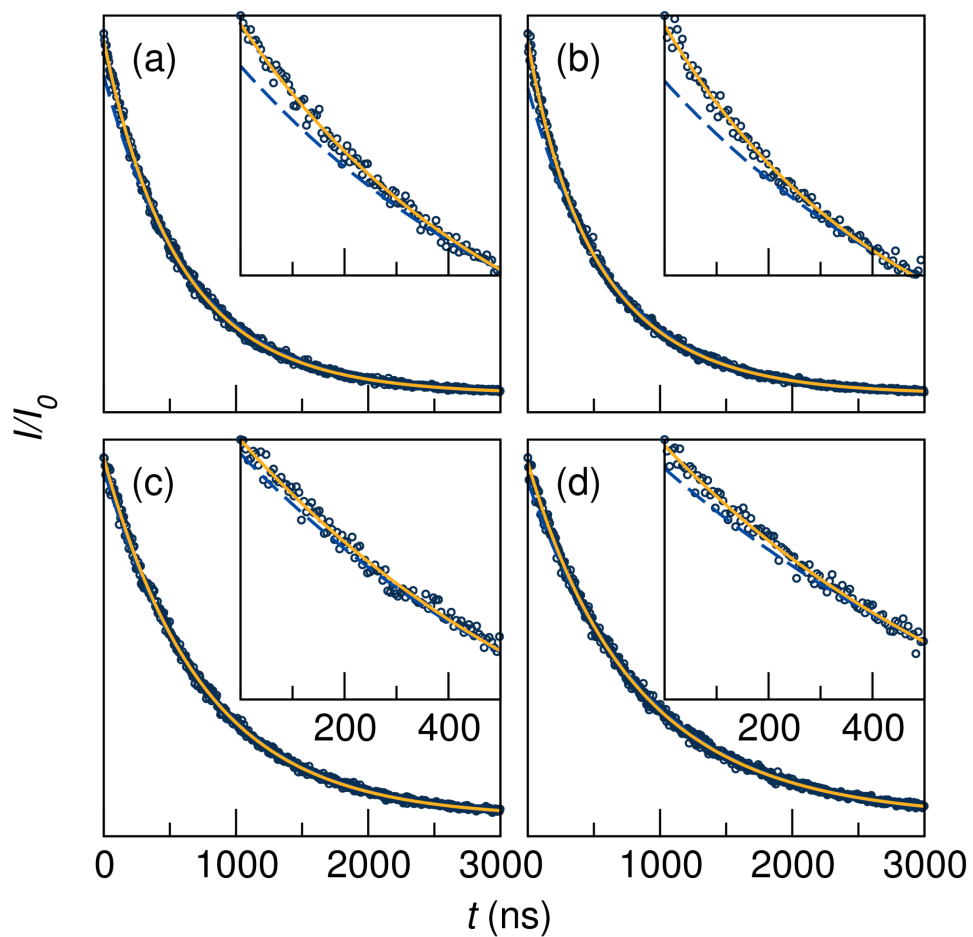
Figure 6.15: Intensity decay as a function of time collected at 77 K for (a) 43% Sr, (b) 46% Sr, (c) 62% Sr, and (d) 73% Sr. A bi-exponential fit (solid yellow line) leads to better agreement with the data than a single exponential fit (blue dashed line), suggesting Eu^{2+} exists in two distinct environments within the host. Reproduced with permission from reference [36], ©2014 American Chemical Society.
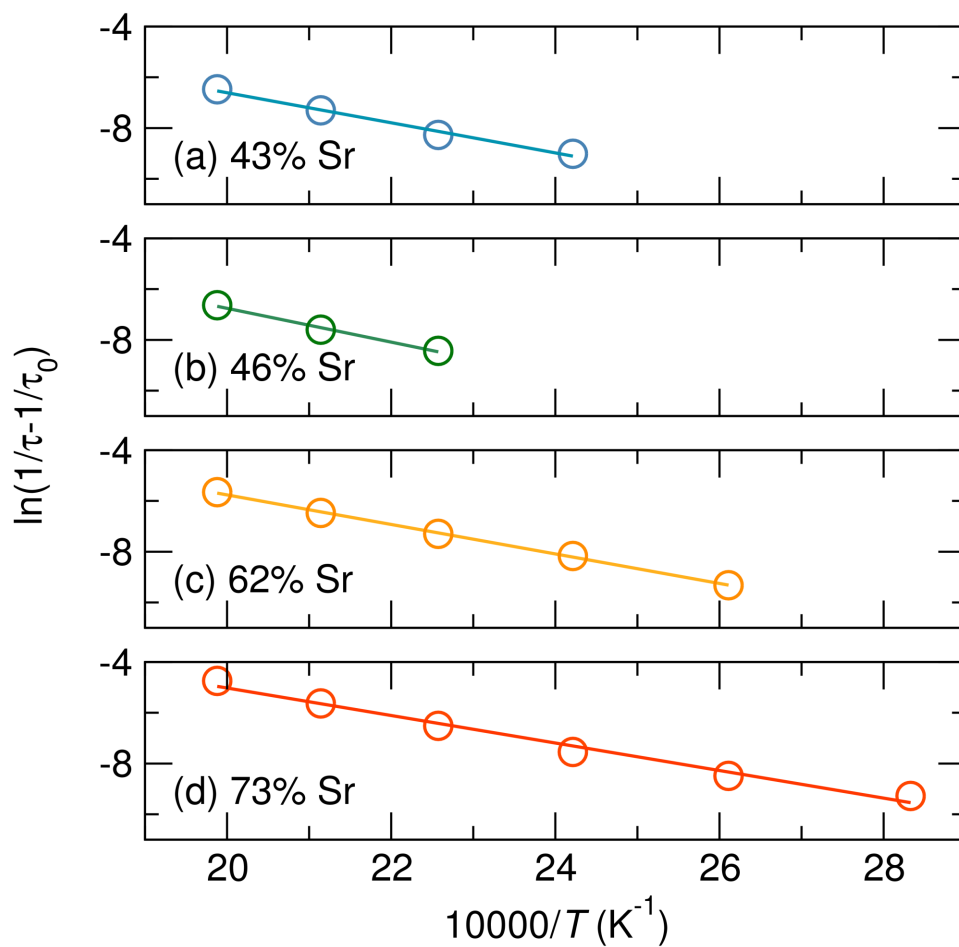
Figure 6.16: Fits to the Arrhenius equation relating the activation energy for thermal quenching to temperature dependent lifetimes are shown for (a) 43% Sr, (b) 46% Sr, (c) 62% Sr, and (d) 73% Sr. The highest high activation energy is required for the composition with 46% Sr. Reproduced with permission from reference [36], ©2014 American Chemical Society.
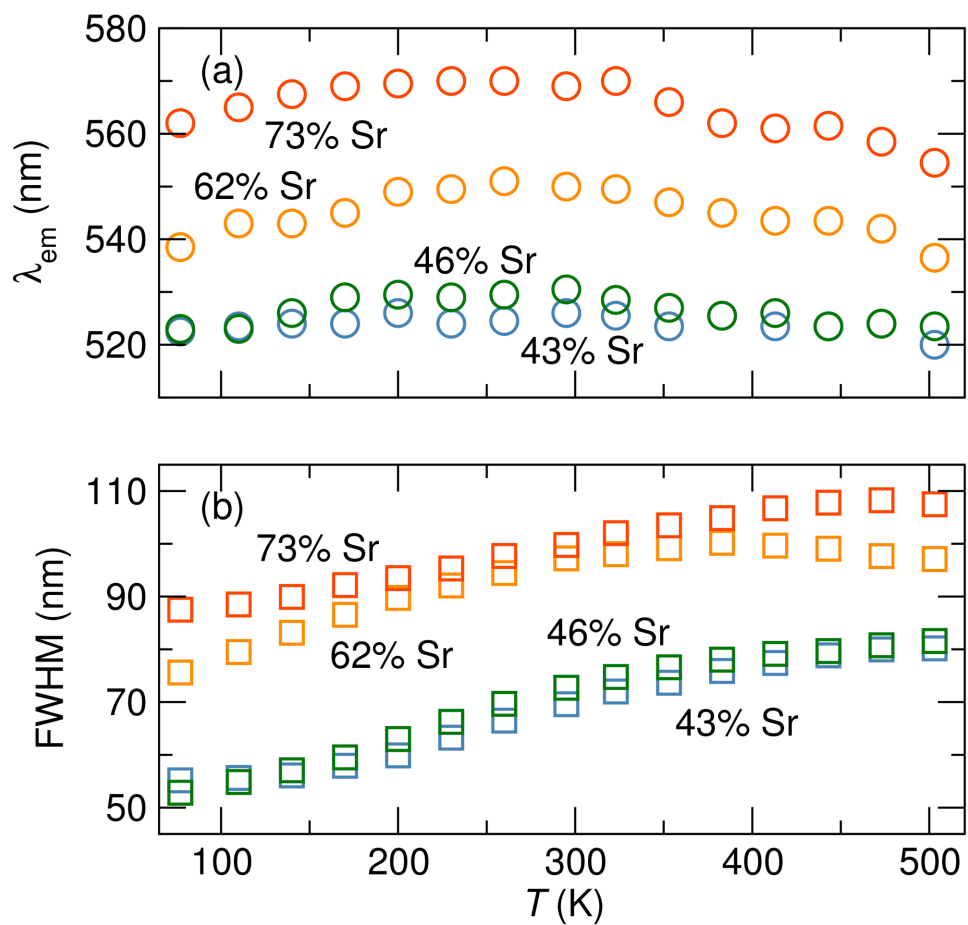
Figure 6.17: Intermediate compounds exhibit (a) relatively stable maximum emission wavelength and (b) slight increase in the FWHM of the emission spectrum with increasing temperature up to 500 K. Reproduced with permission from reference [36], ©2014 American Chemical Society.
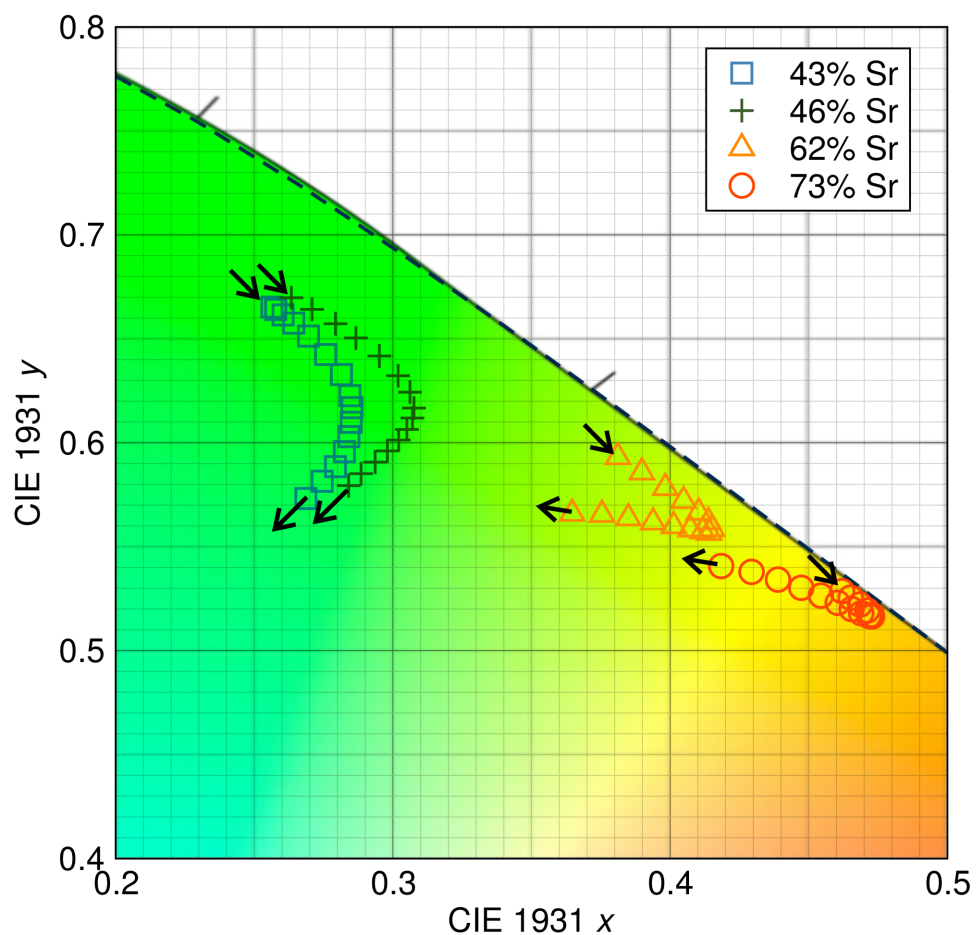
Figure 6.18: Tracking the changes in emission color for intermediate samples as temperature increases from 77 K to 503 K (indicated by arrows) shows that the samples are relatively stable with small changes in emission color. Reproduced with permission from reference [36], ©2014 American Chemical Society.
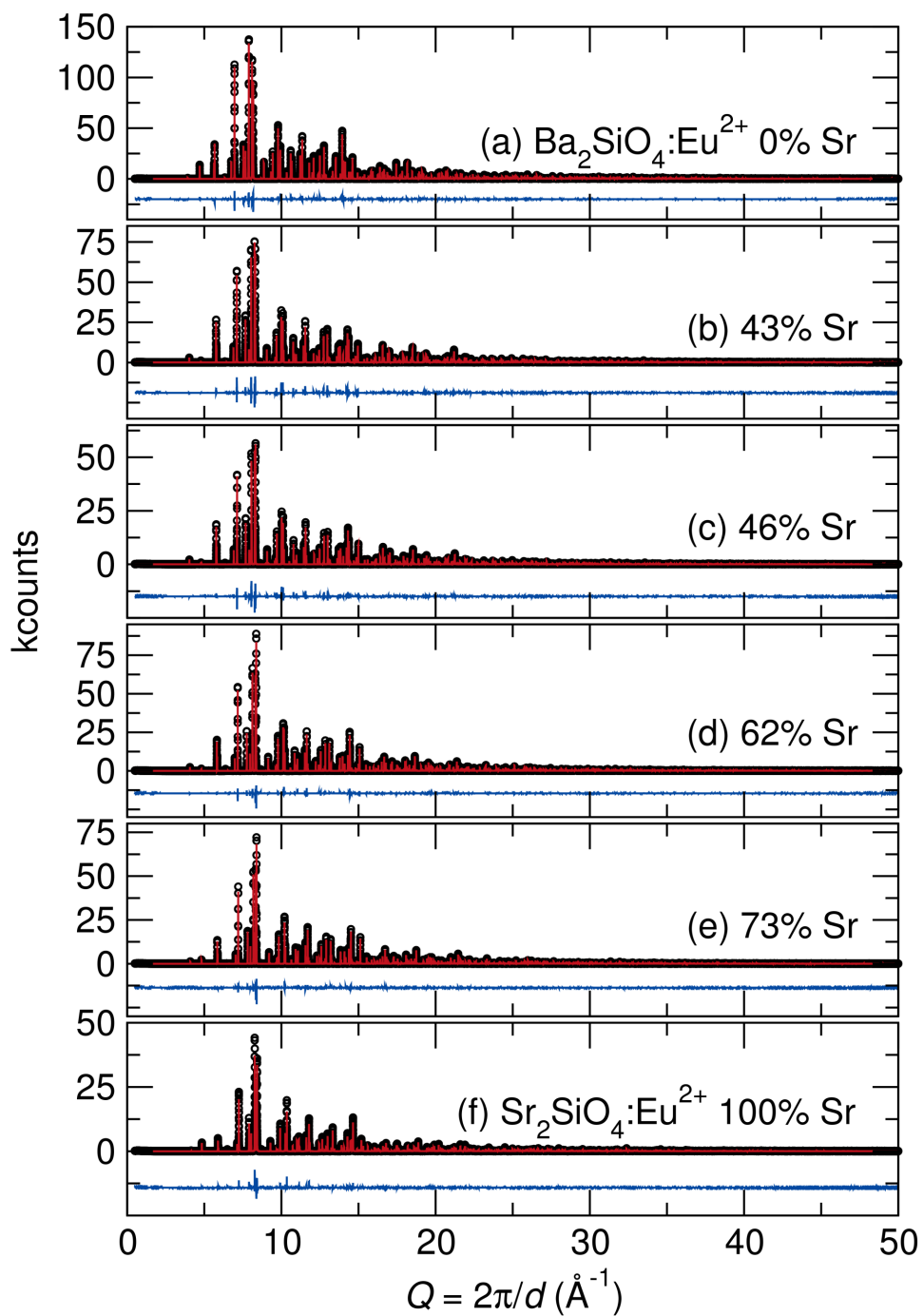
Figure 6.19: Rietveld refinements of synchrotron X-ray diffraction data collected at room temperature for all samples show nearly pure phase materials in good agreement with the structural model. Reproduced with permission from reference [36], ©2014 American Chemical Society.

Chapter 7

Average and local structure, Debye temperature, and structural rigidity in some oxide compounds related to phosphor hosts

The average and local structure of the oxides Ba_2SiO_4, $BaAl_2O_4$, $SrAl_2O_4$, and Y_2SiO_5 are examined in order to evaluate crystal rigidity in light of recent stud-

---

[1]The contents of this chapter have been accepted and will substantially appear in reference [151]: K. A. Denault, J. Brgoch, S. D. Kloß, M. W. Gaultois, J. Siewenie, K. Page, and R. Seshadri, Average and local structure, Debye temperature, and structural rigidity in some oxide compounds related to phosphor hosts, *ACS Appl. Mater. Interfaces* **accepted** (2015) ©2015 American Chemical Society.

ies suggesting that highly connected and rigid structures yield the best phosphor hosts. Simultaneous momentum-space refinements of synchrotron X-ray and neutron scattering yield accurate average crystal structures, with reliable atomic displacement parameters. The Debye temperature Θ_D, which has proven to be a useful proxy for structural rigidity, is extracted from the experimental atomic displacement parameters and compared with predictions from density functional theory calculations and experimental low-temperature heat capacity measurements. The role of static disorder on the measured displacement parameters, and the resulting Debye temperatures are also analyzed using pair distribution function of total neutron scattering, as refined over varying distance ranges of the pair distribution function. The interplay between optimal bonding in the structure, structural rigidity, and correlated motion in these structures is examined, and the different contributions are delineated.

7.1 Introduction

The geometry and chemistry of the host material are critical in the selection of known phosphors and in the discovery of new phosphor materials for use in phosphor converted LED applications. Until recently, a majority of new phosphors were identified through chemical substitution in known

compounds,[1, 38, 42, 43] with occasional high throughput searches of familiar parameter space.[152, 153] An alternative, potentially more efficient method presented recently employs Density Functional Theory (DFT) to screen for new potential phosphor hosts with high photoluminescent quantum yield (PLQY).[35] It has been suggested by some of us that highly three-dimensionally connected structures, such as yttrium aluminum garnet (YAG), possesses high PLQY (>90%) — when substituted with appropriate amounts of Ce^{3+} — due to structural rigidity that limits, at measurement temperatures, accessible phonon modes that would lead to non-radiative quenching mechanisms.[35, 125] Structural rigidity, however, is not easily quantified in a solid and can be difficult to capture as a single parameter. The Debye temperature (Θ_D) was identified previously,[35] as an useful proxy for structural rigidity. Θ_D is easily calculated within the quasi-harmonic Debye model using elastic constants determined from *ab initio* calculations.[35] Within this framework, rare-earth substituted phosphor hosts are selected by searching through crystal structure databases (*e.g.*, Inorganic Crystal Structure Database (ICSD)) for compounds with a high Θ_D, in addition to certain other parameters associated with plausible chemistry. These parameters include elemental compositions that would withstand reaction conditions, dopant sites for the activator ion, and a sufficiently wide band gap.

Experimentally, Θ_D is obtained either from low temperature heat capac-

ity measurements or from atomic displacement parameters determined from careful scattering (typically neutron) studies. The latter technique is usually associated with studies of monoatomic solids, and for more complex solids, a weighted average of the displacement parameters across all atoms in the unit cell has been found to yield agreement with other techniques.[125] Θ_D measured experimentally using these two methods for a number of phosphor hosts has been shown to agree well with values calculated from DFT-derived parameters.[36, 125, 126, 154]

In this work, we explore the structural signatures of several known oxide phosphor hosts, through a careful examination of the average and local structure determined using time-of-flight neutron scattering (including total scattering) and synchrotron powder diffraction methods. The oxide hosts Ba_2SiO_4, $BaAl_2O_4$, $SrAl_2O_4$, and Y_2SiO_5 were studied using these scattering techniques and low-temperature heat capacity measurements. The Debye temperature has been obtained using parameters obtained from DFT calculations, and measured from isotropic atomic displacement parameters refined from 15 K neutron scattering data using both average and local structure techniques. Separately, Θ_D has been extracted from fitting the low temperature heat capacity measured between 1.8 K and 20 K. Pair distribution function analysis of neutron scattering data collected at 15 K has been performed to explore local *versus* long-range

rigidity, as described by the impact of correlated motion on the extracted Debye temperature. Finally, structural rigidity has been correlated with the ability of the different structure types to best optimize bonding around the countercations that provide the substitution sites for the phosphor activator ions.

7.2   Experimental

Samples of Ba_2SiO_4, $BaAl_2O_4$, $SrAl_2O_4$, and Y_2SiO_5 were prepared by conventional high temperature solid-state reaction using starting materials of $BaCO_3$ (Materion, 99.9%), $SrCO_3$ (Aldrich, 99.9%), Y_2O_3 (Materion, 99.9%), CeO_2 (99.99% purity, Alfa Aesar), SiO_2 (Johnson Matthey, 99.9%), and Al_2O_3 (Sigma-Aldrich, 99.99%). Powders were intimately mixed using an agate mortar and pestle for approximately 30 minutes, pressed into pellets, and placed in dense alumina crucibles on a bed of sacrificial powder to prevent contact with the crucible. Samples were heated in a reducing atmosphere of $5\% \, H_2 / 95\% \, N_2$ with heating and cooling ramps of $3 \, °C/min.$ and $4 \, °C/min$, respectively, at $1350 \, °C$ for $4 \, h$ for Ba_2SiO_4, $1600 \, °C$ for $12 \, h$ for $BaAl_2O_4$, $1400 \, °C$ for $12 \, h$ for $SrAl_2O_4$, and $1400 \, °C$ for $12 \, h$ for Y_2SiO_5.

High-resolution synchrotron X-ray powder diffraction data were collected on the 11-BM instrument at the Advanced Photon Source (APS) at Argonne Na-

219

tional Laboratory, at a temperature of 300 K using an average wavelength of λ = 0.413742 Å. Neutron powder diffraction data were collected using the NPDF instrument at the Los Alamos Neutron Science Center at Los Alamos National Laboratory. Samples were placed in vanadium containers, and time-of-flight neutron data was collected at 300 K and 15 K from four detector banks located at $\pm46°$, $\pm90°$, $\pm119°$, and $\pm148°$. Rietveld analysis was carried out using the General Structure Analysis System (GSAS)[95, 96]. Simultaneous refinements of the X-ray and neutron scattering data collected at 300 K were completed by adjusting the profile shapes and backgrounds (shifted Chebyshev function for X-ray, power series for neutron), refining neutron absorption coefficients, and adjusting the instrument parameters. These parameters were then kept static, and the X-ray data only was used to refine the unit cell parameters. Both X-ray and neutron data were then used to refine the atomic positions. Then only neutron data was used to refine the atomic displacement parameters. Refinements of low temperature data were completed using only neutron powder diffraction data collected at 15 K. Crystal structures were visualized using the software VESTA.[155]

Density Functional Theory (DFT) calculations were performed using the Vienna *ab initio* Simulation Package (VASP 5.3)[50–53] within the projector augmented wave method (PAW).[54, 55] Initial relaxation of the atomic positions

were performed until the residual forces were $<1 \times 10^{-2}$ eV/Å. Exchange and correlation were described by Perdew-Burke-Ernzerhof using the generalized gradient approximation (GGA-PBE).[56] The energy cutoff of the plane wave basis set and the number of **k**-points used for each calculation are detailed in the Appendix. The bulk modulus and Poisson ratio were calculated as described previously[35] using the Voigt-Reuss-Hill (VRH) approximation[146] from the stress-strain relationship driven by ± 0.015 Å displacements.[138] The elastic moduli were then used to estimate the Debye temperature (Θ_D) using the quasi-harmonic Debye model.[35, 148–150]

Debye temperatures for crystallographically distinct atoms, $\Theta_{\mathrm{D},i}$ were calculated from isotropic atomic displacement parameters using the low-temperature approximation:[156]

$$\Theta_{\mathrm{D},i} = \frac{3\hbar^2 N_A}{4k_\mathrm{B} M U_{\mathrm{iso},i}} \tag{7.1}$$

where i represents the atomic species Ba, Sr, Y, Si, Al, or O, M is the atomic weight of the atom, and $U_{\mathrm{iso},i}$ the isotropic atomic displacement parameter of the individual atomic species in the unit cell. The overall Debye temperature, Θ_D, was found by taking the weighted average of $\Theta_{\mathrm{D},i}$ from each atomic species, according to their Wyckoff multiplicities in the unit cell:

$$\Theta_{\mathrm{D}} = \frac{\sum m_i \Theta_{\mathrm{D},i}}{\sum m_i} \tag{7.2}$$

where m_i is the Wyckoff multiplicity of the individual atomic species.

Low-temperature heat capacity was measured using a Quantum Design Physical Properties Measurement System. Heat capacity measurements from 1.8 K to 20 K were collected on pellets with a mass of approximately 15 mg and analyzed using thermal relaxation calorimetry. A thin layer of Apiezon-N grease was used to ensure thermal contact between the platform and the sample. The heat capacity of the Apiezon-N grease was collected separately and subtracted from the measured sample heat capacity. The Θ_{D} was then extracted by fitting the heat capacity to the Debye model in the low-temperature limit:

$$C_p \approx \frac{12 N k_{\mathrm{B}} \pi^4}{5} \left(\frac{T}{\Theta_{\mathrm{D}}} \right)^3 \tag{7.3}$$

where N is the number of atoms per formula unit multiplied by the Avogadro number, k_{B} is the Boltzmann constant, and T is the temperature.

Pair distribution function (PDF) analysis was performed on the neutron powder diffraction data collected at 15 K. The data were extracted using PDFgetN[157] with $Q_{max} = 25\,\text{Å}$, $Q_{max} = 40\,\text{Å}$, $Q_{max} = 25\,\text{Å}$, and $Q_{max} = 40\,\text{Å}$ for Ba_2SiO_4, $BaAl_2O_4$, $SrAl_2O_4$, and Y_2SiO_5, respectively, based on data qual-

ity and collection time. Least-squares refinements were performed on the PDF to obtain local structure information using PDFgui.[145] The real-space instrument parameters Q_{damp} and Q_{broad} were determined from a crystalline material calibration standard and fixed at $0.00623\,\text{Å}^{-1}$ and $0.0021\,\text{Å}^{-1}$, respectively. Refinement ranges of $1\,\text{Å}$ to r_{max}, with $r_{max} = 5\,\text{Å}$, $10\,\text{Å}$, $15\,\text{Å}$, $20\,\text{Å}$, and $50\,\text{Å}$, were chosen to explore the effects of diffuse thermal scattering and correlated motion on the local structure and the average structure. Crystal structure depcitions and calculations of distance and distortion parameters were carried out using the VESTA suite of programs.[155]

7.3   Results and Discussion

The host structures Ba_2SiO_4, $BaAl_2O_4$, $SrAl_2O_4$, and Y_2SiO_5 were chosen for this study to explore the effects of various connectivity, coordination, and composition on structural rigidity. Upon Ce^{3+} substitution, these structures all exhibit photoluminescence from two crystallographically distinct sites in the host structure, occurring in the near-UV to visible spectrum, although their luminescent properties are not the focus of this study. Simultaneous co-refinements of high resolution synchrotron X-ray and neutron power diffraction data collected at $300\,\text{K}$ were conducted using the undoped host materials in order to describe
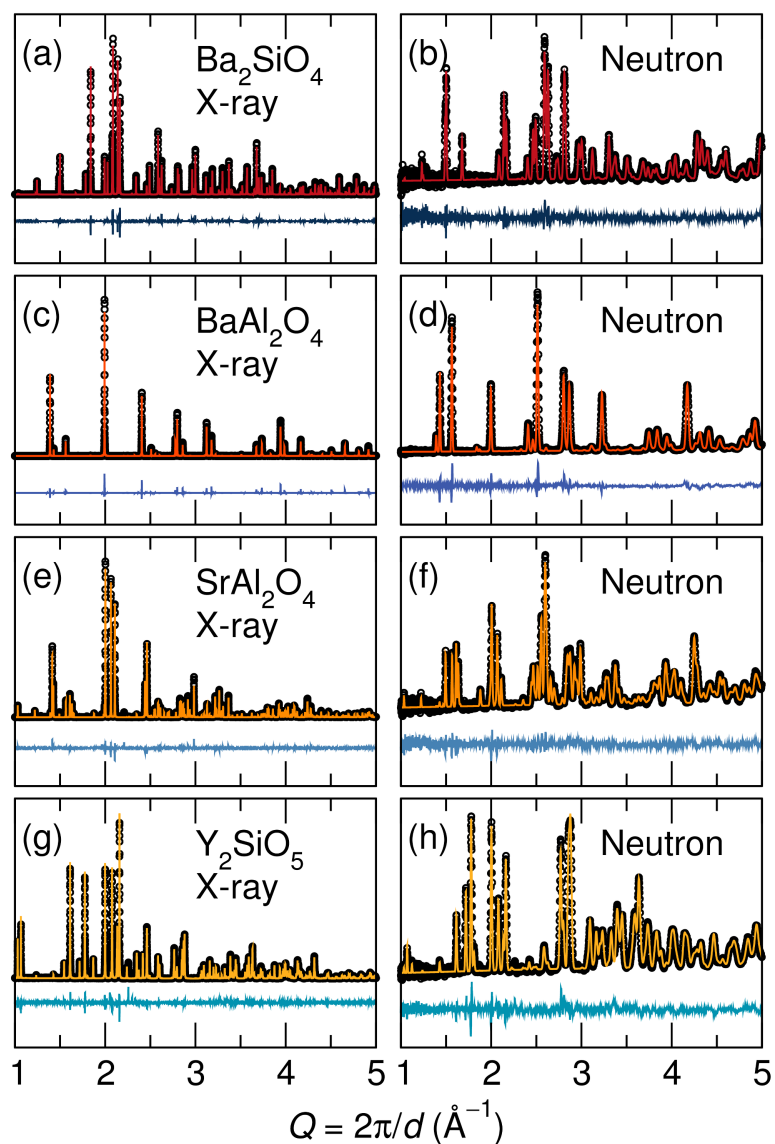
Figure 7.1: Rietveld co-refinements of combined high resolution synchrotron X-ray diffraction from beam line 11-BM (left) and neutron powder diffraction from the NPDF instrument (right) collected at 300 K for (a,b) Ba_2SiO_4, (c,d) $BaAl_2O_4$, (e,f) $SrAl_2O_4$, and (g,h) Y_2SiO_5. The small circles are measured data and solid lines the fit, with the differences displayed beneath. Neutron data presented here is from from bank 1. Reproduced with permission from reference [151], ©2015 American Chemical Society.
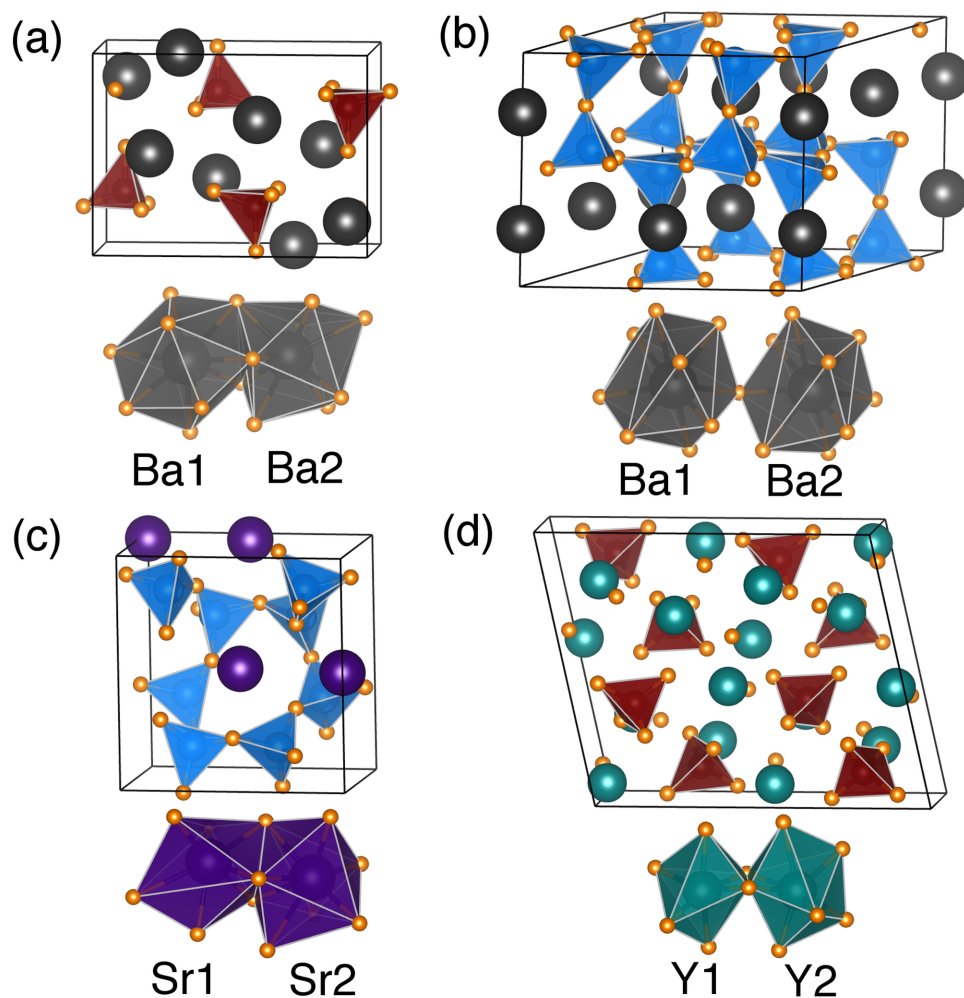
Figure 7.2: Crystal structure and polyhedral coordination environment for (a) Ba_2SiO_4, (b) $BaAl_2O_4$, (c) $SrAl_2O_4$, and (d) Y_2SiO_5 refined from combined high resolution synchrotron X-ray and neutron powder diffraction data collected at 300 K. The alkaline-earth and rare-earth cations are depicted as large spheres, while Si and Al are situated in the centers of the rendered SiO_4 and AlO_4 polyhedra (tetrahedra). Reproduced with permission from reference [151], ©2015 American Chemical Society.

the average structure of these compounds at room temperature. Figure 7.1 shows the fits against both the X-ray data and the neutron data with good agreement between the data and the structural model. The crystallographic refinement data for all compounds are listed in the Appendix. The crystal structures are illustrated in Figure 7.2.

Ba$_2$SiO$_4$ crystallizes in the orthorhombic space group $Pmcn$ (No. 62) with the β-K$_2$SO$_4$ structure type, containing isolated SiO$_4$ tetrahedra.[158] BaAl$_2$O$_4$ and SrAl$_2$O$_4$ are derivatives of the tridymite structure in space group $P6_3/mmc$ (No. 194), where the Ba^{2+} and Sr^{2+} ions are situated in the channels created by the tridymite-related AlO$_4$ tetrahedral corner connected network. BaAl$_2$O$_4$ was first reported in 1937 in the hexagonal space group $P6_322$ (No. 182), but since that time the observation of satellite reflections in X-ray diffraction data have suggested a superstructure doubling of the a and b lattice parameters, resulting in space group $P6_3$ (No. 173).[159] There has been some discussion around whether this description is only an average structure description, and the local structure may instead more closely resemble the monoclinic $P2_12_12_1$ (No. 19) or the monoclinic $P2_1$ (No. 4) structure in which SrAl$_2$O$_4$ crystallizes.[160, 161] In this study, we have found the hexagonal space group $P6_3$ (No. 173) structural model, with the KNa$_3$Al$_4$Si$_4$O$_{16}$ structure type, to fit both the high and low temperature average and local structure. This model has been used for all

226

Table 7.1: Comparison of effective ionic radii indicates potential substitution sites for Ce^{3+} in different coordination geometries.

CN	atom	effective ionic radii (Å)	Ce^{3+} effective ionic radii (Å)
9	Ba^{2+}	1.47	1.196
10	Ba^{2+}	1.52	1.25
7	Sr^{2+}	1.21	1.07
8	Sr^{2+}	1.26	1.143
6	Y^{3+}	0.90	1.01
7	Y^{3+}	0.96	1.07

subsequent refinements of $BaAl_2O_4$. $BaAl_2O_4$ contains AlO_4 dimers while the AlO_4 units in $SrAl_2O_4$ are fully connected in three dimensions.

Y_2SiO_5 crystallizes in the low temperature X_1 structure in the monoclinic space group $P2_1/c$ (No.14) and the high temperature X_2 structure in the monoclinic space group $I2/a$ (No. 15). The high temperature X_2 structure has been reported to have stronger luminescence compared to the X_1 structure type.[162] In this study, we have refined the X_2 structural model with the $(Mn,Fe)_2PO_4F$ structure type, containing isolated SiO_4 tetrahedra, and thus have used this model for all subsequent refinements of Y_2SiO_5.

Table 7.1 compares the effective ionic radii of the potential activator ion Ce^{3+} in different coordination environments with the effective ionic radii of cations in the host structure that represent possible substitution sites.[63] Comparison of effective ionic radii indicates that all of the structures contain two potential substitution sites for Ce^{3+}, Table 7.2 lists the characteristics of the coordina-

Table 7.2: Structural information of the potential sites for Ce^{3+} substitution from Rietveld co-refinements of combined high resolution synchrotron X-ray and neutron powder diffraction data collected at 300 K including site, coordination number (CN), average bond length, polyhedral volume, polyhedral distortion index (D), and bond valence sum (BVS).

sample	site	CN	ave. bond length (Å)	poly. vol. (Å^3)	D	BVS
Ba_2SiO_4	Ba1 $4c$	10	2.984	53.214	0.0445	1.675
	Ba2 $4c$	9	2.828	43.210	0.0466	2.254
$BaAl_2O_4$	Ba1 $2a$	9	2.921	43.000	0.0388	1.706
	Ba2 $6c$	9	2.955	44.783	0.0575	1.682
$SrAl_2O_4$	Sr1 $2a$	7	2.680	26.240	0.0465	1.684
	Sr2 $2a$	8	2.749	33.296	0.0734	1.743
Y_2SiO_5	Y1 $8f$	6	2.272	14.536	0.0078	3.039
	Y2 $8f$	7	2.361	18.782	0.0330	2.902

tion environments. Since the bonding environment of these cation sites will influence the activator ion energy levels and in turn the optical properties, we have focused on an analysis of these coordination environments. The polyhedral volume of the sites were calculated using the method outlined by Swanson and Peterson[68]. A polyhedral distortion index, D, can also be calculated following[67]

$$D = \frac{1}{n} \sum_{i=1}^{n} \frac{\mid l_i - l_{av} \mid}{l_{av}} \tag{7.4}$$

where l_i is the distance from the central atom to the ith coordinating atom and l_{av} is the average bond length. The polyhedra of each of the two cation sites in each structure is illustrated in Figure 7.2 with the refined crystal structures.

The two Ba–O polyhedra in Ba_2SiO_4 have strikingly different coordination

Table 7.3: Debye temperature calculated using density functional theory, measured using atomic displacement parameters from Rietveld refinement of neutron scattering data collected at 15 K, low temperature heat capacity collected at 1.8 K, and atomic displacement parameters from PDF analysis of neutron scattering data collected at 15 K refined from 1 Å to 50 Å.

sample	Θ_D (K)			
technique	DFT	Rietveld U_{iso}	C_p	PDF U_{iso}
Ba_2SiO_4	305	311	305	294
$BaAl_2O_4$	354	377	316	387
$SrAl_2O_4$	475	352	455	430
Y_2SiO_5	513	500	419	350

environments. There exists a larger, under-bonded 10-coordinated Ba1 site and a smaller, over-bonded and structurally distorted 9-coordinated Ba2 site. In the $BaAl_2O_4$ structure, both Ba^{2+} sites are 9-coordinated and under-bonded, with the volume of the Ba2 site slightly larger but more distorted compared to Ba1. $SrAl_2O_4$ exhibits two Sr sites that are both under-bonded, with the Sr2 site having a slightly larger volume, but also more distorted coordination than the Sr1 site. In Y_2SiO_5, there exists a smaller, over-bonded, but less distorted 6-coordinated Y1 site and a larger, under-bonded 7-coordinated Y2 site.

Density functional theory (DFT) provides a method for predicting Θ_D, which is indicative of structural rigidity in phosphor hosts.[35] This method was used to calculate Θ_D for each compound using the structure determined from room temperature co-refinements. Θ_D results are listed in Table 7.3. Based on Pauling's rules for ionic crystal structures,[163] we would expect that structures

Table 7.4: Polyhedral information of the potential sites for Ce^{3+} substitution from Rietveld refinements of neutron powder diffraction data collected at 15 K including site, coordination number (CN), average bond length, polyhedral volume, polyhedral distortion index (D), and bond valence sum (BVS).

sample	site	CN	bond length (Å)	poly. vol. (Å^3)	D	BVS
Ba_2SiO_4	Ba1 $4c$	10	2.973	52.585	0.0462	1.735
	Ba2 $4c$	9	2.816	42.753	0.0456	2.313
$BaAl_2O_4$	Ba1 $2a$	9	2.897	41.837	0.0289	1.773
	Ba2 $6c$	9	2.954	44.569	0.0660	1.788
$SrAl_2O_4$	Sr1 $2a$	7	2.670	26.005	0.0472	1.728
	Sr2 $2a$	8	2.732	32.994	0.0707	1.800
Y_2SiO_5	Y1 $8f$	6	2.268	14.458	0.0080	3.072
	Y2 $8f$	7	2.355	18.645	0.0316	2.944

containing polyhedra of lower charge cations (Al^{3+} instead of Si^{4+}) and oxygen would be better connected and therefore more rigid, and this is indeed borne out by the DFT calculations.

Ba_2SiO_4 contains isolated SiO_4 tetrahedra and a divalent cation with the largest coordination numbers for this series of compounds explored, producing the lowest Θ_D. $BaAl_2O_4$ and $SrAl_2O_4$ contain similar elements but different AlO_4 connectivity. $BaAl_2O_4$ contains corner-connected AlO_4 dimers, while in $SrAl_2O_4$ AlO_4 tetrahedra are fully three-dimensionally connected. The higher degree of connectivity in $SrAl_2O_4$ leads to the higher Θ_D, as observed. Finally, Y_2SiO_5 contains isolated SiO_4 tetrahedra; however the higher cation charge of yttrium compared to barium or strontium leads to stronger bonding and a higher Θ_D.

Refinements of low temperature neutron power diffraction data collected at
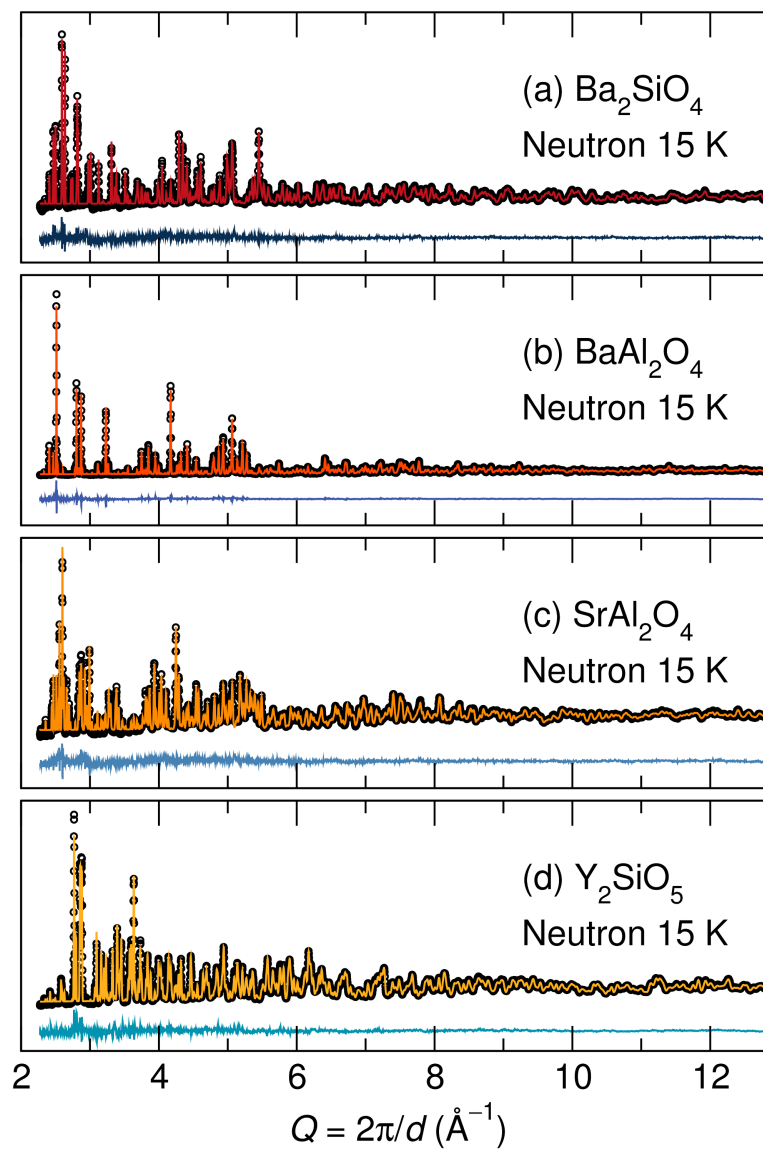
Figure 7.3: Rietveld refinements of low temperature neutron powder diffraction data collected at 15 K and normalized for (a) Ba_2SiO_4, (b) $BaAl_2O_4$, (c) $SrAl_2O_4$, and (d) Y_2SiO_5. Circles represent the data and solid lines the fit, with the difference beneath. Reproduced with permission from reference [151], ©2015 American Chemical Society.
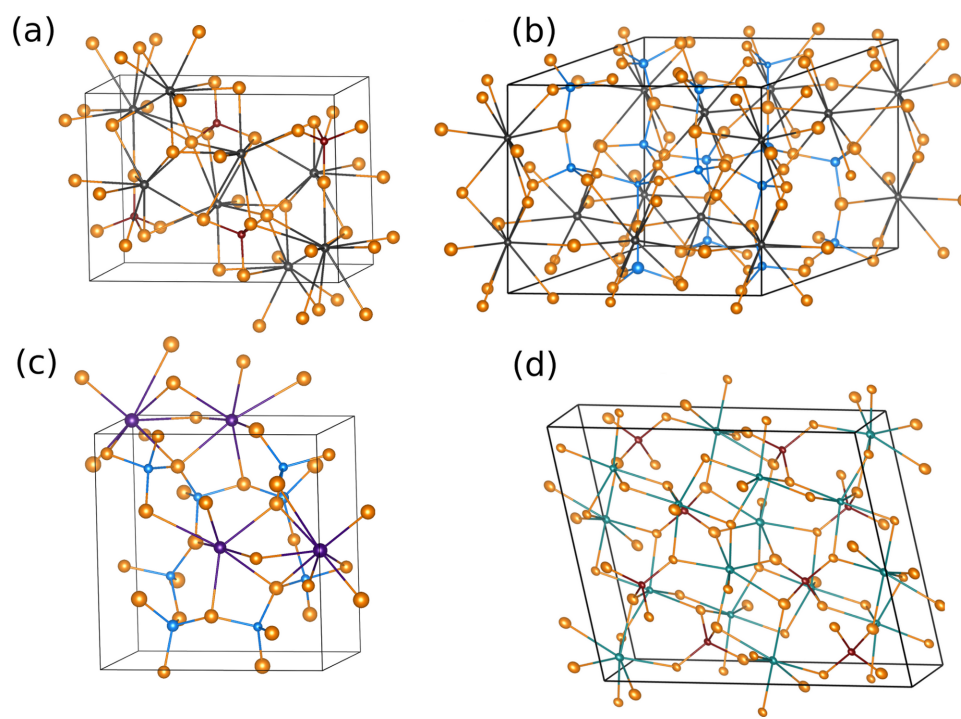
Figure 7.4: Crystal structures showing 99% probability atomic displacement parameters for (a) Ba_2SiO_4, (b) $BaAl_2O_4$, (c) $SrAl_2O_4$, and (d) Y_2SiO_5 refined using low temperature neutron powder diffraction data collected at 15 K. Drawings produced by VESTA.[155] Reproduced with permission from reference [151], ©2015 American Chemical Society.

15 K were conducted to extract atomic displacement parameters (U_{iso}) to experimentally determine Θ_{D}. Figure 7.3 shows excellent agreement between the structural models and the data. The crystal data and refinement information are listed in the Appendix.

The coordination environment of each potential site for Ce^{3+} substitution are listed in Table 7.4 for the low temperature structural refinements. The crystal structures, illustrated in Figure 7.4, show 99% probability U_{iso} ellipsoids.

The Θ_{D} is then determined from U_{iso} for each structure using the equations described previously, with results listed in Table 7.3. The experimentally determined Θ_{D} agrees well (± 25 K) for all compounds except $SrAl_2O_4$. For $SrAl_2O_4$, the experimentally determined Θ_{D} from U_{iso} is lower than predicted by the DFT calculations. This disagreement could result from static disorder in the average $SrAl_2O_4$ crystal structure, contributing to larger than expected atomic displacements and a low Θ_{D}. Based on the pair distribution (PDF) analysis presented in what follows, Θ_{D} from PDF U_{iso} fit over the range of 1 Å to 50 Å, also representing the average structure, is determined to be 430 K. This result is higher than estimated from the average structure Rietveld analysis and supports static disorder as a cause for the lower than expected Θ_{D}.

Low-temperature heat capacity measurements were also performed to exper-

233
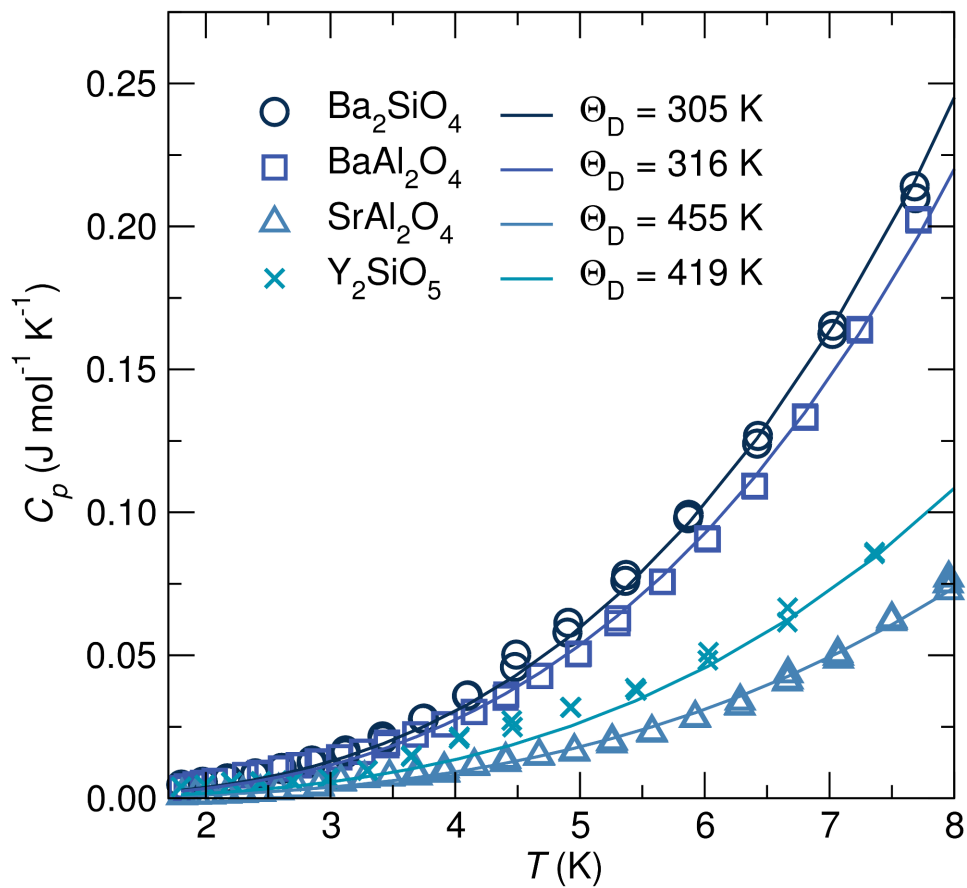
Figure 7.5: Low temperature heat capacity with extracted Debye temperatures for Ba_2SiO_4, $BaAl_2O_4$, $SrAl_2O_4$, and Y_2SiO_5. Reproduced with permission from reference [151], ©2015 American Chemical Society.

imentally determine Θ_D. The heat capacities (C_p) of Ba_2SiO_4, $BaAl_2O_4$, $SrAl_2O_4$, and Y_2SiO_5 were collected at temperatures as low as 1.8 K and are shown in Figure 7.5. The data were fit to the Debye model, in the linear region of the log-log plot, and the extracted Θ_D are listed in Table 7.3. While the Debye model was fit very well to the heat capacity of other compounds from 3 K to 8 K, an anomaly in the heat capacity of Y_2SiO_5 prevents appropriate use of the simple Debye model below 5 K, and makes the measured value for this compound somewhat less than reliable. A plot of C_p/T^3 *vs.* T for Y_2SiO_5 reveals a peak ranging from 3 K to 6 K, well within the low temperature fitting range, pointing towards the presence of localized, optic-like modes. One possibility for the anomaly at low temperatures in Y_2SiO_5 are Van Hove singularities arising from the vibrational density of states (VDOS) crossing the Debye density of states, leading to a flat phonon dispersion curve.[164, 165] Since the T^3 Debye model only accounts for low-frequency phonon contributions to the specific heat, and breaks down when temperatures exceed between *e.g.*, $T > \Theta_D/50$ to $\Theta_D/100$,[166, 167] the use of the higher-temperature data leads to a lower-than-expected Θ_D determined for Y_2SiO_5.

Understanding the local structure of phosphor hosts is crucially important to understanding their resultant optical properties. In addition, understanding long-range and short-range structural rigidity may provide further insights into
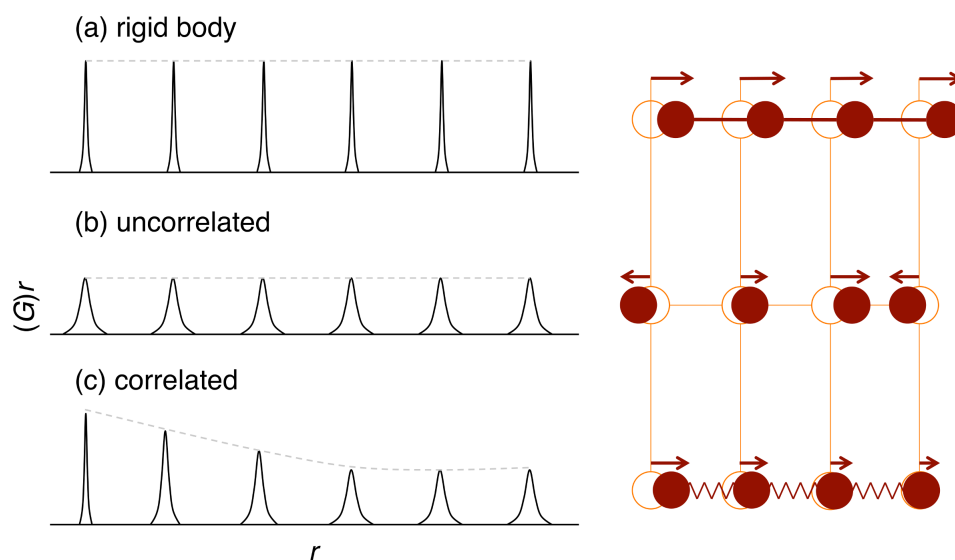
Figure 7.6: A visualization of the impact of correlated atomic motion on the pair distribution function. (a) Rigid body motion as depicted using a chain of atoms can be expected to give δ-function peaks in the PDF of the infinite crystal. (b) Completely uncorrelated motion as associated with Einstein modes should yield PDF peaks whose widths do not vary with increasing distance. (c) Correlated motion combines the features of (a) and (b). Adapted with permission from Jeong *et al.*[168], ©2003 American Physical Society. Reproduced with permission from reference [151], ©2015 American Chemical Society.

the role of structural rigidity in phosphors. Pair distribution function (PDF) analysis is one method that can be used to study the local structure of phosphor hosts. In this study, we have analyzed the PDF of the low temperature neutron powder diffraction data collected at 15 K, and determined Θ_D from refined U_{iso}. The PDFs were fit over different real-space r_{max}-ranges to evaluate the effects of thermal diffuse scattering and static disorder on the measured Θ_D and to evaluate the role of correlated motion.

The correlated motion of atoms and its impact on the PDF is depicted in Figure 7.6. Rigid-body thermal motion contains atoms moving the same distance and in the same direction as the atom being observed, which is represented in a PDF as a series of sharp peaks for all distances from the atom or ranges of r. In uncorrelated atomic motion, all atoms move independently of the atom being observed, which is represented as a series of broad peaks for all ranges of r. Correlated atomic motion in the PDF is a combination of the observations where the local structure may not translate into the average, long-range structure. This is represented in a PDF as sharp peaks at low-r, similar to rigid-body thermal motion, and broad peaks at high-r, similar to uncorrelated atomic motion. This correlated motion is captured in the PDF by the empirical parameters δ_1 and δ_2, often used for high temperature and low temperature behavior, respectively. The final PDF peak width is given by[168, 169]

$$\sigma_{ij} = \sigma'_{ij}\sqrt{1 - \frac{\delta_1}{r_{ij}} - \frac{\delta_2}{r_{ij}^2} + Q_{broad}^2 r_{ij}^2} \qquad (7.5)$$

where σ'_{ij} is the peak width without correlation, computed from U_{iso}. The degree of correlated motion within a material is dictated by both interatomic interactions and atomic geometry based on crystal structure.

The PDFs were first fit over the range of $1\,\text{Å}$ to $50\,\text{Å}$ to refine the low temperature δ_2 correlated motion parameter. This fit range represents the long-range, average structure. Then, δ_2 was fixed and the data were fit over subsequently lower ranges of r_{max}, including $1\,\text{Å}$ to $20\,\text{Å}$, $1\,\text{Å}$ to $15\,\text{Å}$, $1\,\text{Å}$ to $10\,\text{Å}$, and $1\,\text{Å}$ to $5\,\text{Å}$. Refinements of the PDFs fit over the range of $1\,\text{Å}$ to $20\,\text{Å}$ are illustrated in Figure 7.7 for all host structures with good agreement between the structural model and the data. Fits to the PDF for all r_{max}-ranges are shown in the Supporting Information.

The correlated motion parameter, δ_2, is refined to be $2.35\,\text{Å}^2$, $2.78\,\text{Å}^2$, $2.79\,\text{Å}^2$, and $2.52\,\text{Å}^2$ for Ba_2SiO_4, $BaAl_2O_4$, and $SrAl_2O_4$, and Y_2SiO_5, respectively. The correlated motion parameter should be representative of the degree of structural rigidity in a material and thus associated with the Θ_D. We find that the degree of correlated motion follows closely the degree of structural connectivity, as discussed earlier. Ba_2SiO_4 and Y_2SiO_5 contain isolated SiO_4 tetrahedra
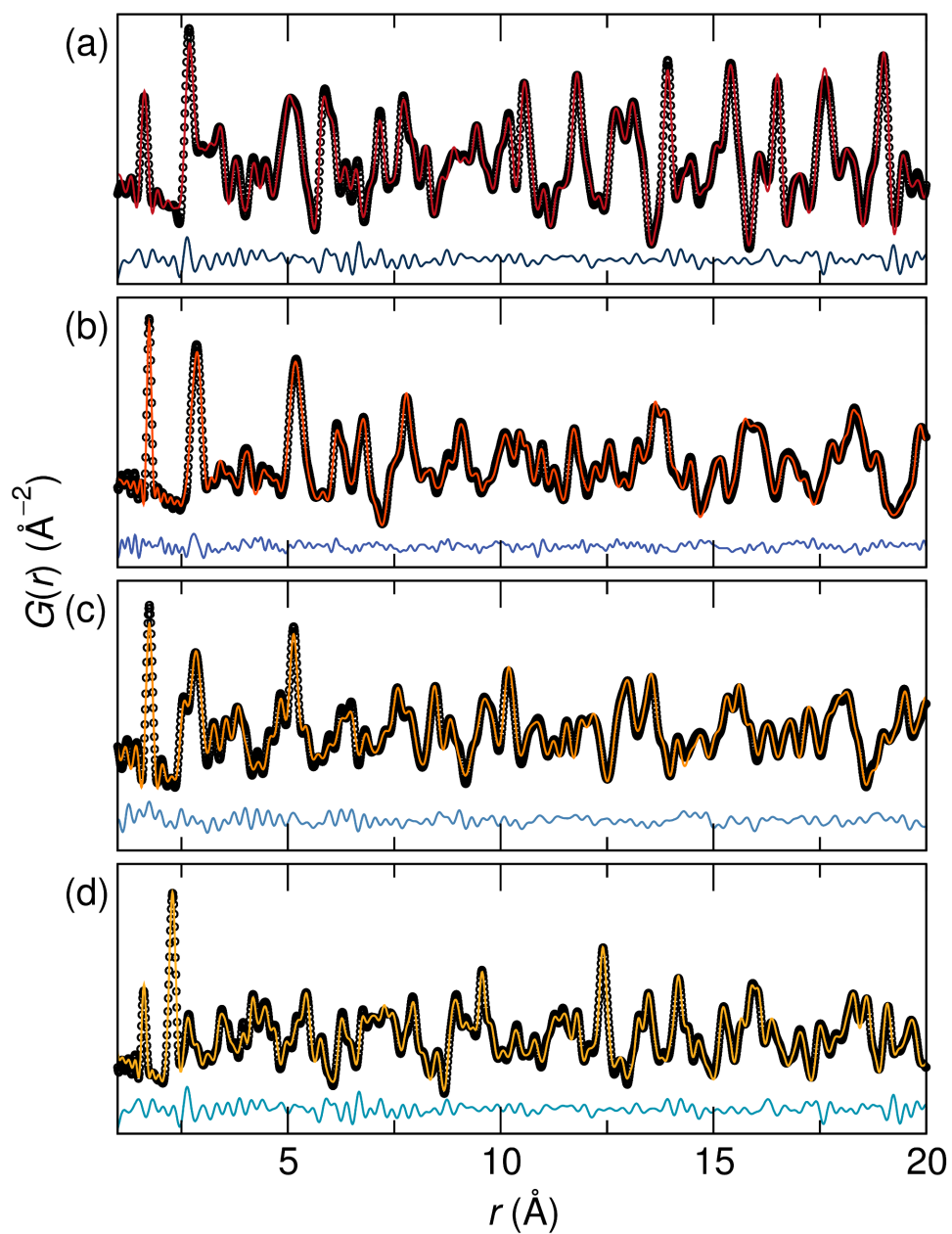
Figure 7.7: Least squares refinements of the pair distribution function of (a) Ba_2SiO_4, (b) $BaAl_2O_4$, (c) $SrAl_2O_4$, and (d) Y_2SiO_5 from low temperature neutron powder diffraction data collected at 15 K and fit from 1 Å to 20 Å. Circles represent the data and solid lines the fit, with the differences beneath. Reproduced with permission from reference [151], ©2015 American Chemical Society.
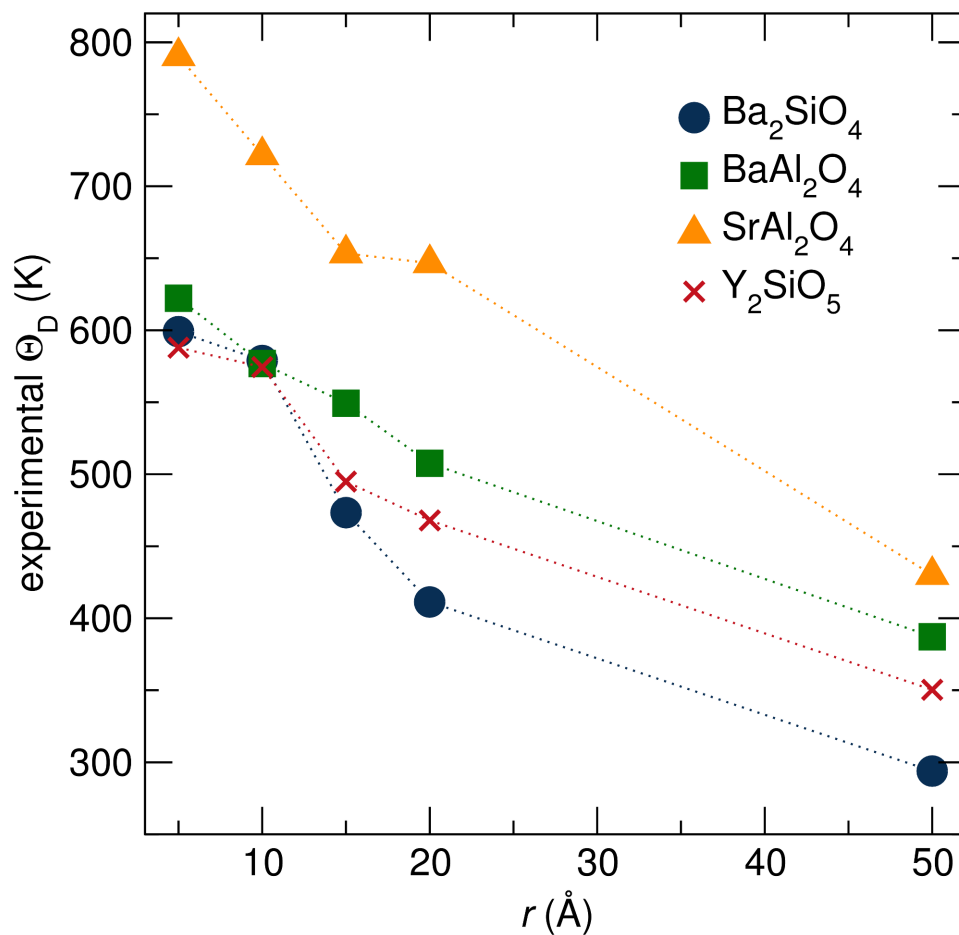
Figure 7.8: Θ_D as a function of fitting range r_{max} determined from atomic displacement parameters refined using the pair distribution function of the neutron diffraction data collected at 15 K. Reproduced with permission from reference [151], ©2015 American Chemical Society.

and a lower correlated motion parameter compared to the AlO_4 dimers and three-dimensionally connected AlO_4 tetrahedra in $BaAl_2O_4$ and $SrAl_2O_4$, respectively.

The PDF peak width modeled using U_{iso} contains information on both the thermal diffuse scattering and static disorder. Fitting the PDF over varying r_{max}-ranges can be used to evaluate the effects of thermal diffuse scattering. It will be manifested as significantly smaller U_{iso} for short-range modeling (lower r) where the effects of the averaged thermal diffuse scattering are minimized.[170] Θ_D for each r_{max}-range determined using U_{iso} from PDF refinements are shown in Figure 7.8. The Θ_D determined from refined U_{iso} from the PDF is higher in the low-r region, corresponding to the local structure, decreasing with increasing r_{max}-range, as r approaches the average structure description.

In the low-r region for $r_{max} = 5$ Å, it is the local structure of the first coordination shell of the polyhedra being observed. This is a useful range for observing the local rigidity that may influence optical properties pertaining to specific crystallographic sites and activator ion substitution. For example, we would expect this local rigidity to affect expansion or contraction, and distortion, of the lattice that may or may not occur with activator ion substitution. This could have implications as to why specific activator ions have optimal performance in certain structures and how this affects optical properties like quantum yield and Stokes

shift.

As r_{max} increases, Θ_D decreases, gaining contributions from the long-range thermal diffuse scattering and interactions from the lattice as a whole. In the high-r region of $r_{max} = 50$ Å, corresponding to the long-range average structure, Θ_D agrees well (± 45 K) with values determined using other average structure techniques, and are listed in Table 7.3. The Θ_D for Y_2SiO_5 is somewhat lower than expected, which may be influenced by the lower than expected correlated motion parameter included in the refinement.

Figure 7.9 shows the Θ_D determined from the four methods used: DFT calculated, experimentally measured from Rietveld refined U_{iso} from 15 K neutron powder diffraction data, from low temperature heat capacity measurements, and from PDF U_{iso} refined from 15 K neutron powder diffraction data fit over varying ranges of r_{max}. Also included as a reference are the Θ_D for silver and alumina measured using the low temperature heat capacity method discussed here.

For those materials where the local structure Θ_D decreases drastically to the average structure Θ_D, there is a large amount of thermal diffuse scattering present. Figure 7.10a shows the difference in measured Θ_D from the local structure 1 Å to 5 Å PDF fit range to the DFT calculated Θ_D as a percentage of
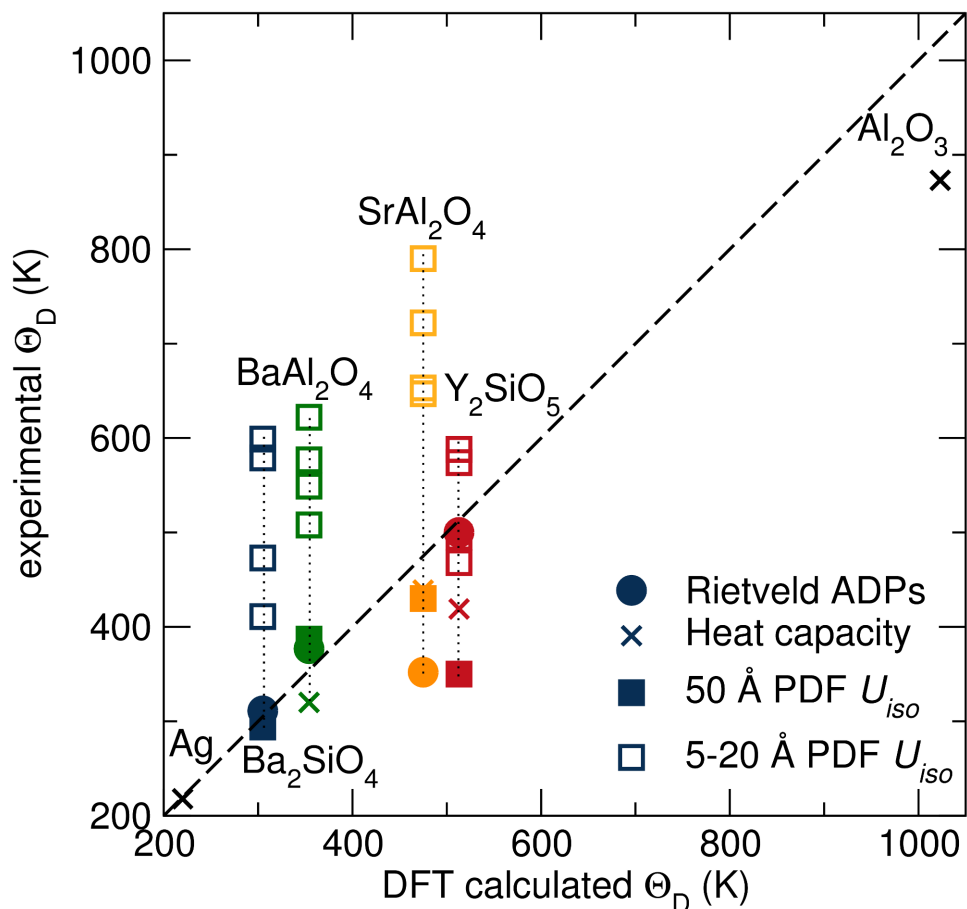
Figure 7.9: Calculated Θ_D from DFT and experimental Θ_D determined using atomic displacement parameters from Rietveld and PDF refinements of low temperature neutron powder diffraction data collected at 15 K, and extracted from low temperature heat capacity collected at 1.8 K for all compositions. The different datapoints for the PDF refinements indicate increasing values of r_{max}, with the trend that the PDF-calculated Debye temperature for sample decreases with increasing r_{max}. Also included as a reference are the Θ_D for silver and alumina measured using the low temperature heat capacity method. Reproduced with permission from reference [151], ©2015 American Chemical Society.
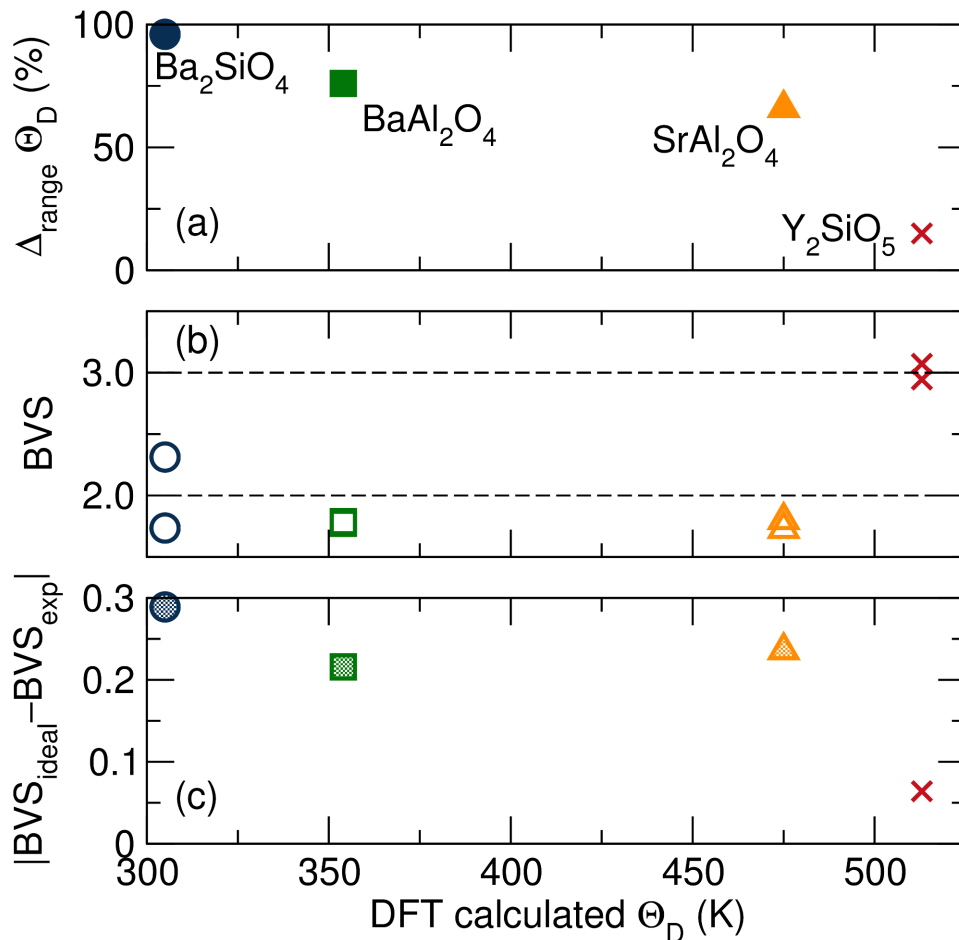
Figure 7.10: (a) The difference in measured Θ_D from the local structure $1\,\text{Å}$ to $5\,\text{Å}$ PDF fitting range and the average structure DFT calculated Θ_D as a percentage of the expected DFT calculated Θ_D, (b) the bond valence sums (BVS) for each cation site in each composition determined from Rietveld refinement of neutron diffraction data collected at $15\,\text{K}$ showing the deviation from ideal $+2$ for Ba^{2+} and Sr^{2+} and ideal $+3$ for Y^{3+}, and (c) the average deviation from ideal bond valence sums weighted by site multiplicity shows that for more optimized structures the changes in measured Θ_D as a function of PDF fitting range and the difference in bond valence sum from ideal is smaller, coinciding with higher Θ_D materials. Reproduced with permission from reference [151], ©2015 American Chemical Society.

the expected DFT calculated Θ_D. We find that, for the compounds studied here, this large change from local to average Θ_D corresponds with a low Θ_D.

We also find that the thermal diffuse scattering measured through PDF analysis and resulting Θ_D can be related to the structural parameters refined using average structure techniques as an indication of average structural rigidity. Figure 7.10b shows the bond valence sum (BVS) determined for each of the two cation sites in each structure compared to the predicted BVS of $+2$ for Ba^{2+} and Sr^{2+} and $+3$ for Y^{3+}. Figure 7.10c shows the average difference between the ideal BVS and experimental BVS for each site, based on multiplicity. We find that for materials that are optimally bonded, the distance from the ideal BVS is small and the difference in measured Θ_D as a function of PDF fit range is also small, representing a material with high structural rigidity and a high Θ_D. The Θ_D can therefore be considered a measure of rigidity for the average structural description, whereas local structures techniques like PDF can be used to determine the rigidity of the local structure using a description of correlated motion or a local structure Θ_D, which may provide future insights as to the role of local structural rigidity in phosphor compounds.

7.4 Conclusions

The results presented here explore the role of structural rigidity in several oxide structures as host materials for phosphors used in solid-state lighting. The average structures of Ba_2SiO_4, $BaAl_2O_4$, $SrAl_2O_4$, and Y_2SiO_5 are determined through simultaneous refinements of synchrotron X-ray diffraction and neutron scattering. The Debye temperature (Θ_D) is used as a proxy to quantify structural rigidity and is predicted using Density Functional Theory (DFT) calculations in agreement with qualitative analysis of the structures based Pauling's rules for ionic crystals. The Θ_D is then measured experimentally using refined atomic displacement parameters (U_{iso}) from neutron scattering data collected at 15 K and extracted from low temperature heat capacity measurements. The rigidity of the local structure *versus* the average structure is then explored by analyzing the effects of correlated motion and diffuse thermal scattering on the pair distribution function (PDF) obtained from 15 K neutron scattering. Correlated motion in the PDF appears stronger for structures with a higher degree of connectivity and the difference in Θ_D corresponding to the local structure compared to the average structure varies based on the degree of diffuse thermal motion present. For highly rigid structures, the difference in Θ_D from the local to the average structure is small, indicating little thermal motion, and coinciding with

high calculated Θ_D and ideal bond valence sums determined from analysis of the average structure. Additionally, rigidity of the local structure may present an avenue for understanding the effects of activator ion substitution on the host structure and its impacts on the optical properties.

7.5   Appendix

Table 7.5: Details necessary to reproduce the density functional theory calculations including the kinetic energy cutoffs (E_{cut}) and the number of k-points of the un-perturbed crystal structures generated using the Monkhorst-Pack (MP) or the Γ k-mesh scheme as noted.

compound	E_{cut} (eV)	**k**-mesh (scheme; No. of **k**-points)
Ba_2SiO_4	600	6×4×6 (Γ; 84)
$BaAl_2O_4$	650	10×10×10 (Γ; 108)
$SrAl_2O_4$	650	6×6×8 (Γ; 112)
Y_2SiO_5	650	6×4×6 (MP; 112)

Table 7.6: Crystal data from Rietveld co-refinements of combined high resolution synchrotron X-ray and neutron powder diffraction data collected at 300 K.

refined formula	Ba_2SiO_4	$BaAl_2O_4$	$SrAl_2O_4$	Y_2SiO_5
radiation type	synchrotron X-ray (11-BM) and time-of-flight neutron (NPDF)			
X-ray λ (Å)	0.413742			
X-ray 2θ range (°)	0.5 to 49.995			
neutron bank angle θ (°)	bank 1: ±46; bank 2: ±90; bank 3: ±119; bank 4: ±148			
neutron Q range (Å^{-1})	bank 1: 0.89 to 5.42; bank 2: 1.67 to 9.41;			
	bank 3: 2.04 to 11.47; bank 4: 2.27 to 12.80			
temperature (K)	300			
crystal system	orthorhombic	hexagonal	monoclinic	monoclinic
space group; Z	$Pmcn$; 4	$P6_3$; 8	$P2_1$; 4	$I2/a$; 8
unit cell (Å)	$a = 5.810117(7)$	$a = 10.44920(2)$	$a = 8.43904(1)$	$a = 10.42072(3)$
	$b = 10.21694(1)$	$b = 10.44920$	$b = 8.81425(2)$	$b = 6.72810(2)$
	$c = 7.505903(8)$	$c = 8.79196(3)$	$c = 5.156355(9)$	$c = 12.49657(3)$
	$\alpha = 90°$	$\alpha = 90°$	$\alpha = 90°$	$\alpha = 90°$
	$\beta = 90°$	$\beta = 90°$	$\beta = 93.4094(1)°$	$\beta = 102.6905(2)°$
	$\gamma = 90°$	$\gamma = 120°$	$\gamma = 90°$	$\gamma = 90°$
volume (Å^3)	445.562(1)	831.347(3)	382.870(1)	854.751(3)

Table 7.7: Fitting statistics from Rietveld co-refinements of combined high resolution synchrotron X-ray and neutron powder diffraction data collected at 300 K.

refined formula	Ba_2SiO_4	$BaAl_2O_4$	$SrAl_2O_4$	Y_2SiO_5
R_p (%) synchrotron X-ray	11	15	9.1	13
R_p (%) neutron bank 1	3.5	6.1	3.5	4.3
R_p (%) neutron bank 2	3.1	5.8	3.0	3.2
R_p (%) neutron bank 3	1.8	3.9	1.7	2.0
R_p (%) neutron bank 4	1.8	3.9	1.7	2.2
total R_p (%)	7.6	11	6.0	5.4
R_{wp} (%) synchrotron X-ray	14	20	12	18
R_{wp} (%) neutron bank 1	4.7	8.1	4.8	5.9
R_{wp} (%) neutron bank 2	4.6	7.9	4.3	4.9
R_{wp} (%) neutron bank 3	2.6	5.4	2.5	3.0
R_{wp} (%) neutron bank 4	2.7	5.4	2.5	3.1
total R_{wp} (%)	6.2	9.7	4.8	5.2
R_f^2 (%) synchrotron X-ray	8.2	17	12	13
R_f^2 (%) neutron bank 1	6.8	7.4	6.3	6.3
R_f^2 (%) neutron bank 2	9.1	10	6.5	5.2
R_f^2 (%) neutron bank 3	7.0	9.2	4.7	4.0
R_f^2 (%) neutron bank 4	9.2	10	6.7	5.3
χ^2	5.7	36	4.2	6.4

Table 7.8: Refined atomic parameters as determined by Rietveld co-refinement of combined high resolution synchrotron X-ray and neutron powder diffraction data collected at 300 K for Ba_2SiO_4. U_{iso} is defined as one-third of the trace of the orthogonalized U^{ij} tensor.

atom	site	x	y	z	occupancy	U_{iso} ($\times 10^2$ Å^2)
Ba1	$4c$	$\frac{1}{4}$	0.08627(3)	0.16092(5)	1	0.69(2)
Ba2	$4c$	$\frac{1}{4}$	0.69427(3)	$-0.00842(4)$	1	0.57(2)
Si1	$4c$	$\frac{1}{4}$	0.4199(1)	0.2278(1)	1	0.10(2)
O1	$4c$	$\frac{1}{4}$	0.4169(1)	0.0109(2)	1	1.05(2)
O2	$4c$	$\frac{1}{4}$	0.5704(1)	0.3073(2)	1	1.01(3)
O3	$8d$	0.0191(2)	0.34885(9)	0.3069(1)	1	1.19(2)

Table 7.9: Refined atomic parameters as determined by Rietveld co-refinement of combined high resolution synchrotron X-ray and neutron powder diffraction data collected at 300 K for $BaAl_2O_4$. U_{iso} is defined as one-third of the trace of the orthogonalized U^{ij} tensor.

atom	site	x	y	z	occupancy	U_{iso} ($\times 10^2$ Å^2)
Ba1	$2a$	0	0	0.2451(2)	1	1.2(1)
Ba2	$6c$	0.50439(7)	0.00360(7)	0.2555(2)	1	0.61(4)
Al1	$6c$	0.1616(4)	0.3367(4)	0.0550(3)	1	0.40(7)
Al2	$6c$	0.1556(4)	0.3294(4)	0.4449(3)	1	0.04(6)
Al3	$2b$	$\frac{1}{3}$	$\frac{2}{3}$	0.9409(6)	1	0.4(1)
Al4	$2b$	$\frac{1}{3}$	$\frac{2}{3}$	0.5496(6)	1	1.1(1)
O1	$6c$	0.1799(3)	$-0.0007(4)$	0.9730(3)	1	1.19(6)
O2	$6c$	0.6869(3)	0.0035(4)	0.0294(3)	1	1.23(5)
O3	$6c$	0.4944(4)	0.1764(3)	0.9824(3)	1	0.71(5)
O4	$6c$	0.1818(3)	0.5032(5)	0.9994(3)	1	0.79(5)
O5	$6c$	0.1209(2)	0.3238(3)	0.2480(3)	1	2.03(5)
O6	$2b$	$\frac{1}{3}$	$\frac{2}{3}$	0.7424(6)	1	1.81(7)

Table 7.10: Refined atomic parameters as determined by Rietveld co-refinement of combined high resolution synchrotron X-ray and neutron powder diffraction data collected at 300 K for $SrAl_2O_4$. U_{iso} is defined as one-third of the trace of the orthogonalized U^{ij} tensor.

atom	site	x	y	z	occupancy	U_{iso} ($\times 10^2$ Å^2)
Sr1	$2a$	0.49148(6)	$-0.0008(1)$	0.2501(1)	1	0.87(3)
Sr2	$2a$	0.02909(6)	0.9932(1)	0.2027(1)	1	1.25(3)
Al1	$2a$	0.1890(2)	0.8305(2)	0.7152(3)	1	0.88(7)
Al2	$2a$	0.7993(2)	0.8393(2)	0.7315(3)	1	0.48(6)
Al3	$2a$	0.7087(2)	0.6682(2)	0.2211(3)	1	0.30(5)
Al4	$2a$	0.6806(2)	0.1709(2)	0.7959(3)	1	0.15(5)
O1	$2a$	0.2653(2)	0.1739(2)	0.4364(4)	1	0.96(4)
O2	$2a$	0.7305(2)	0.3165(2)	0.5871(4)	1	0.88(4)
O3	$2a$	0.3258(2)	0.4911(3)	0.3495(3)	1	1.34(4)
O4	$2a$	0.2670(2)	0.9838(2)	0.8987(3)	1	0.61(3)
O5	$2a$	0.1758(2)	0.2977(2)	0.9366(4)	1	0.89(4)
O6	$2a$	0.2059(2)	0.6661(2)	0.9086(4)	1	0.95(4)
O7	$2a$	0.4890(2)	0.2164(2)	0.8818(3)	1	0.87(4)
O8	$2a$	0.9937(2)	0.8854(2)	0.6513(3)	1	1.06(4)

Table 7.11: Refined atomic parameters as determined by Rietveld co-refinement of combined high resolution synchrotron X-ray and neutron powder diffraction data collected at 300 K for Y_2SiO_5. U_{iso} is defined as one-third of the trace of the orthogonalized U^{ij} tensor.

atom	site	x	y	z	occupancy	U_{iso} ($\times 10^2$ Å^2)
Y1	$8f$	0.30654(5)	0.37691(7)	0.14220(4)	1	0.38(2)
Y2	$8f$	0.42813(5)	−0.25508(8)	−0.03700(4)	1	0.45(2)
Si1	$8f$	0.3744(1)	−0.0913(2)	0.18172(8)	1	0.32(2)
O1	$8f$	0.29855(9)	−0.2859(1)	0.11982(8)	1	0.76(3)
O2	$8f$	0.4493(1)	−0.0019(2)	0.09000(9)	1	0.88(2)
O3	$8f$	0.47152(9)	−0.1446(1)	0.29639(7)	1	0.51(2)
O4	$8f$	0.2635(1)	0.0677(2)	0.20023(8)	1	0.76(2)
O5	$8f$	0.38000(9)	0.4052(1)	−0.01723(8)	1	0.45(2)

Table 7.12: Crystal data from Rietveld refinement of low temperature neutron powder diffraction data collected at 15 K.

refined formula	Ba_2SiO_4	$BaAl_2O_4$	$SrAl_2O_4$	Y_2SiO_5
radiation type	time-of-flight neutron (NPDF)			
neutron bank angle θ (°)	bank 1: ±46; bank 2: ±90; bank 3: ±119; bank 4: ±148			
neutron Q range (Å^{-1})	bank 1: 0.89 to 5.42; bank 2: 1.67 to 9.41;			
	bank 3: 2.04 to 11.47; bank 4: 2.27 to 12.80			
temperature (K)	15			
crystal system	orthorhombic	hexagonal	monoclinic	monoclinic
space group; Z	$Pmcn$; 4	$P6_3$; 8	$P2_1$; 4	$I2/a$; 8
unit cell (Å)	a = 5.78160(5)	a = 10.43048(3)	a = 8.41634(8)	a = 10.39605(9)
	b = 10.18585(9)	b = 10.43048	b = 8.78882(8)	b = 6.71397(6)
	c = 7.48624(6)	c = 8.75080(4)	c = 5.15165(5)	c = 12.4723(1)
	α = 90°	α = 90°	α = 90°	α = 90°
	β = 90°	β = 90°	β = 93.5079(9)°	β = 102.6136(7)°
	γ = 90°	γ = 120°	γ = 90°	γ = 90°
volume (Å^3)	440.869(5)	824.492(4)	380.352(4)	849.543(9)

Table 7.13: Fitting statistics from Rietveld refinement of low temperature neutron powder diffraction data collected at 15 K.

refined formula	Ba_2SiO_4	$BaAl_2O_4$	$SrAl_2O_4$	Y_2SiO_5
R_p (%) neutron bank 1	3.4	4.7	3.9	3.8
R_p (%) neutron bank 2	2.9	2.7	3.2	2.4
R_p (%) neutron bank 3	1.5	1.8	1.5	1.7
R_p (%) neutron bank 4	1.6	2.4	1.7	2.0
total R_p (%)	1.7	2.2	1.8	1.9
R_{wp} (%) neutron bank 1	4.9	6.3	5.5	5.3
R_{wp} (%) neutron bank 2	4.1	4.1	4.5	3.9
R_{wp} (%) neutron bank 3	2.2	2.9	2.3	2.7
R_{wp} (%) neutron bank 4	2.5	4.0	2.6	3.1
total R_{wp} (%)	2.7	3.7	2.9	3.1
$R_f{}^2$ (%) neutron bank 1	4.5	5.0	6.0	5.8
$R_f{}^2$ (%) neutron bank 2	6.0	3.3	5.1	3.4
$R_f{}^2$ (%) neutron bank 3	3.9	2.4	2.6	2.3
$R_f{}^2$ (%) neutron bank 4	4.4	3.9	3.9	3.5
χ^2	2.2	17	2.7	6.4

Table 7.14: Refined atomic parameters as determined by Rietveld refinement of low temperature neutron powder diffraction data collected at 15 K for Ba_2SiO_4. U_{iso} is defined as one-third of the trace of the orthogonalized U^{ij} tensor.

atom	site	x	y	z	occupancy	U_{iso} ($\times 10^2$ Å^2)
Ba1	$4c$	$\frac{1}{4}$	0.0856(1)	0.1600(1)	1	0.30(2)
Ba2	$4c$	$\frac{1}{4}$	0.6934(1)	$-0.0096(2)$	1	0.31(2)
Si1	$4c$	$\frac{1}{4}$	0.4203(12)	0.2285(1)	1	0.24(2)
O1	$4c$	$\frac{1}{4}$	0.4159(1)	0.0102(1)	1	0.62(2)
O2	$4c$	$\frac{1}{4}$	0.5715(1)	0.3072(1)	1	0.64(2)
O3	$8d$	0.0184(1)	0.34953(7)	0.30760(9)	1	0.61(1)

Table 7.15: Refined atomic parameters as determined by Rietveld refinement of low temperature neutron powder diffraction data collected at $15\,\mathrm{K}$ for $BaAl_2O_4$. U_{iso} is defined as one-third of the trace of the orthogonalized U^{ij} tensor.

atom	site	x	y	z	occupancy	U_{iso} ($\times\,10^2$ Å^2)
Ba1	$2a$	0	0	0.2449(3)	1	0.22(4)
Ba2	$6c$	0.5061(1)	0.0082(1)	0.2582(2)	1	0.28(2)
Al1	$6c$	0.1550(3)	0.3312(3)	0.0641(2)	1	0.31(4)
Al2	$6c$	0.1542(3)	0.3278(3)	0.4511(2)	1	0.37(4)
Al3	$2b$	$\frac{1}{3}$	$\frac{2}{3}$	0.9507(4)	1	0.17(6)
Al4	$2b$	$\frac{1}{3}$	$\frac{2}{3}$	0.5497(5)	1	0.59(7)
O1	$6c$	0.1767(2)	$-0.0035(2)$	0.9795(2)	1	0.54(2)
O2	$6c$	0.6867(2)	0.0006(2)	0.0479(2)	1	0.60(2)
O3	$6c$	0.4970(2)	0.1806(2)	0.9900(2)	1	0.51(3)
O4	$6c$	0.1786(2)	0.5010(3)	1.0045(2)	1	0.41(3)
O5	$6c$	0.1104(1)	0.3206(1)	0.2578(2)	1	0.69(2)
O6	$2b$	$\frac{1}{3}$	$\frac{2}{3}$	0.7472(3)	1	0.68(3)

Table 7.16: Refined atomic parameters as determined by Rietveld refinement of low temperature neutron powder diffraction data collected at $15\,\mathrm{K}$ for $SrAl_2O_4$. U_{iso} is defined as one-third of the trace of the orthogonalized U^{ij} tensor.

atom	site	x	y	z	occupancy	U_{iso} ($\times\,10^2$ Å^2)
Sr1	$2a$	0.4906(2)	0.0004(2)	0.2510(3)	1	0.49(3)
Sr2	$2a$	0.0313(2)	0.9938(3)	0.2005(3)	1	0.63(3)
Al1	$2a$	0.1894(4)	0.8309(3)	0.7133(6)	1	0.27(5)
Al2	$2a$	0.8003(4)	0.8407(4)	0.7307(6)	1	0.26(5)
Al3	$2a$	0.7074(4)	0.6701(4)	0.2222(6)	1	0.43(5)
Al4	$2a$	0.6797(4)	0.1692(4)	0.8018(6)	1	0.26(5)
O1	$2a$	0.2639(3)	0.1723(3)	0.4370(5)	1	0.65(4)
O2	$2a$	0.7307(3)	0.3166(3)	0.5909(4)	1	0.63(4)
O3	$2a$	0.3294(2)	0.4912(3)	0.3442(4)	1	0.75(3)
O4	$2a$	0.2680(2)	0.9830(3)	0.8967(3)	1	0.50(3)
O5	$2a$	0.1716(3)	0.2955(2)	0.9358(5)	1	0.80(4)
O6	$2a$	0.2066(3)	0.6660(3)	0.9039(4)	1	0.67(3)
O7	$2a$	0.4858(3)	0.2194(2)	0.8835(4)	1	0.61(4)
O8	$2a$	0.9928(2)	0.8880(2)	0.6474(4)	1	0.50(4)

Table 7.17: Refined atomic parameters as determined by Rietveld refinement of low temperature neutron powder diffraction data collected at $15\,\mathrm{K}$ for Y_2SiO_5. U_{iso} is defined as one-third of the trace of the orthogonalized U^{ij} tensor.

atom	site	x	y	z	occupancy	U_{iso} ($\times 10^2$ Å^2)
Y1	$8f$	0.30674(8)	0.3762(1)	0.14183(7)	1	0.19(2)
Y2	$8f$	0.42795(8)	−0.2556(1)	−0.03695(6)	1	0.25(2)
Si1	$8f$	0.3742(1)	−0.0916(2)	0.1823(1)	1	0.19(2)
O1	$8f$	0.2992(1)	−0.2856(2)	0.11914(8)	1	0.48(2)
O2	$8f$	0.4487(1)	−0.0008(2)	0.08975(9)	1	0.48(2)
O3	$8f$	0.4716(1)	−0.1451(2)	0.29626(8)	1	0.28(2)
O4	$8f$	0.2627(1)	0.0678(2)	0.20039(9)	1	0.35(2)
O5	$8f$	0.3802(1)	0.4050(2)	−0.01764(9)	1	0.30(2)
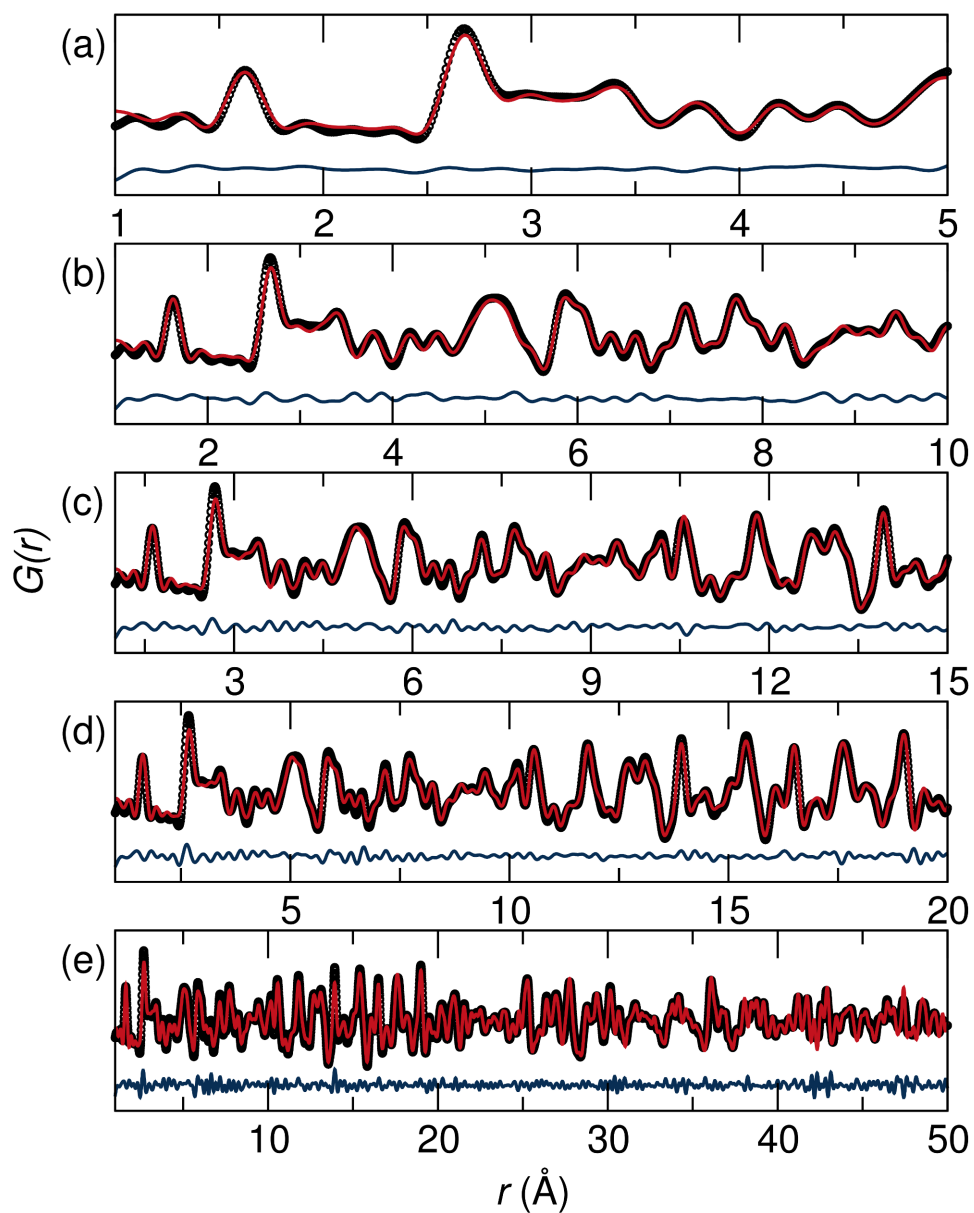
Figure 7.11: Least squares refinements of the pair distribution function of Ba_2SiO_4 from low temperature neutron powder diffraction data collected at $15\,K$ fit from (a) $1\,Å$ to $5\,Å$, (b) $1\,Å$ to $10\,Å$, (c) $1\,Å$ to $15\,Å$, (d) $1\,Å$ to $20\,Å$, and (e) $1\,Å$ to $50\,Å$. Black circles represent the data and solid lines the fit, with the difference below. Reproduced with permission from reference [151], ©2015 American Chemical Society.
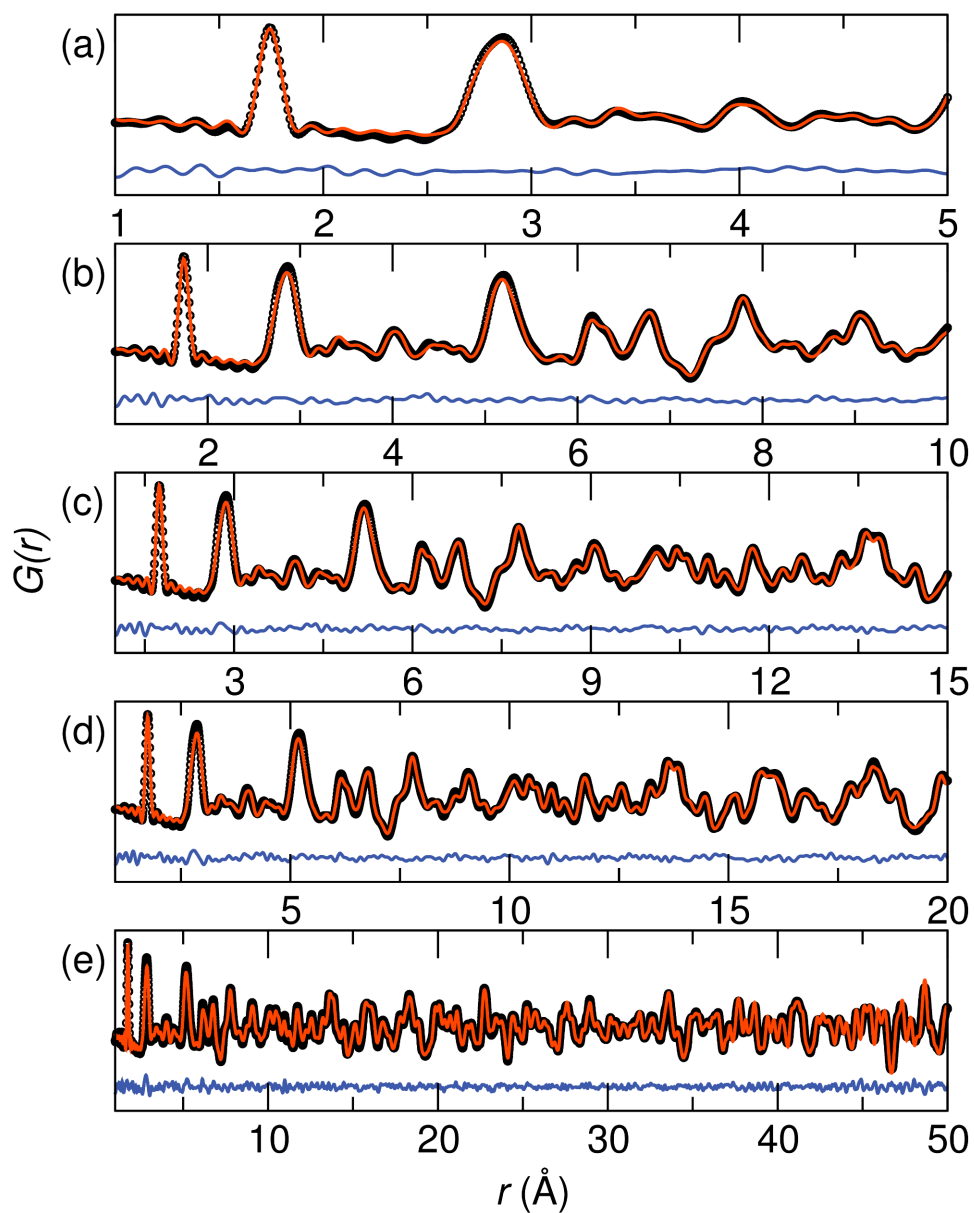
Figure 7.12: Least squares refinements of the pair distribution function of $BaAl_2O_4$ from low temperature neutron powder diffraction data collected at 15 K fit from (a) 1 Å to 5 Å, (b) 1 Å to 10 Å, (c) 1 Å to 15 Å, (d) 1 Å to 20 Å, and (e) 1 Å to 50 Å. Black circles represent the data and solid lines the fit, with the difference below. Reproduced with permission from reference [151], ©2015 American Chemical Society.
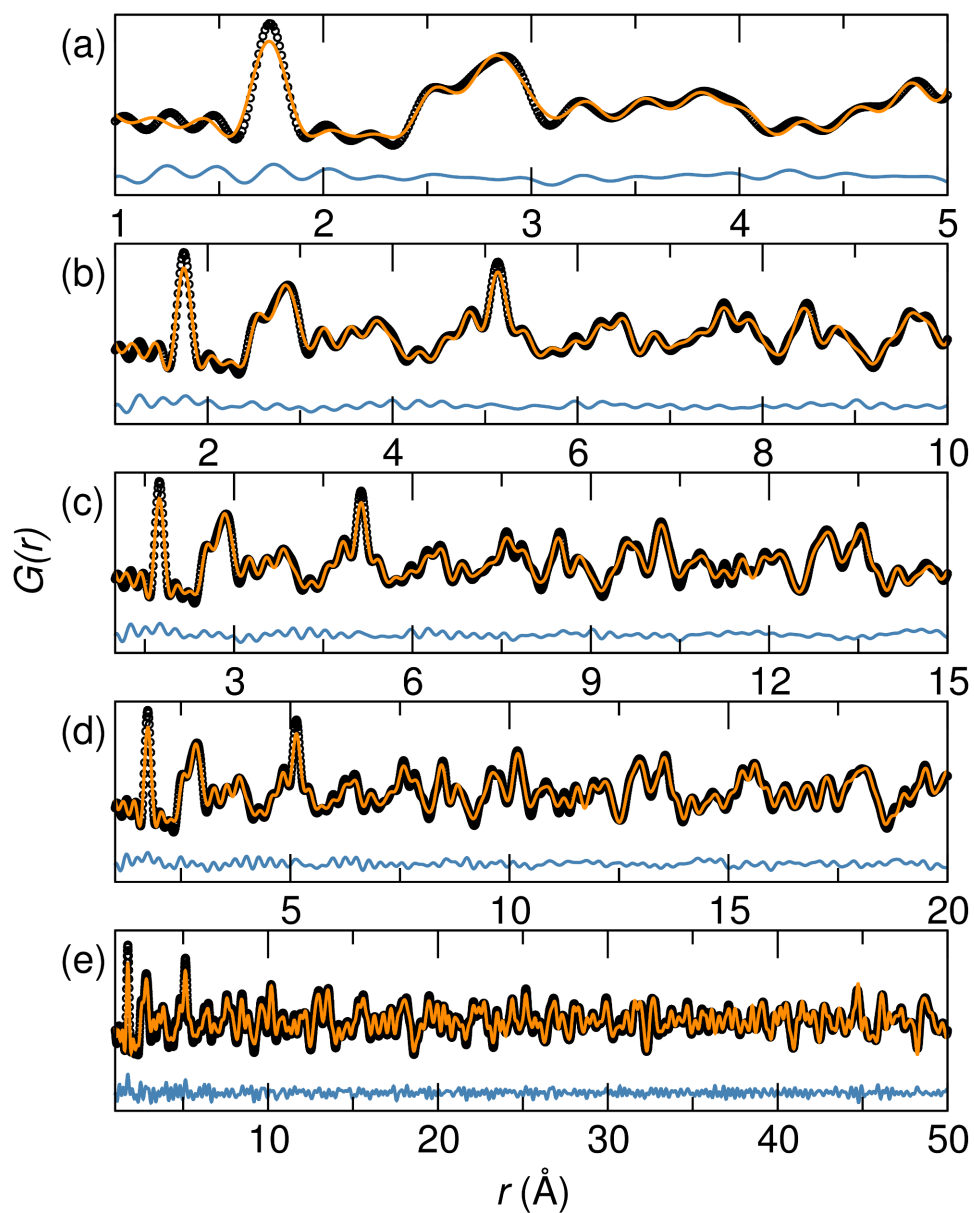
Figure 7.13: Least squares refinements of the pair distribution function of $SrAl_2O_4$ from low temperature neutron powder diffraction data collected at 15 K fit from (a) 1 Å to 5 Å, (b) 1 Å to 10 Å, (c) 1 Å to 15 Å, (d) 1 Å to 20 Å, and (e) 1 Å to 50 Å. Black circles represent the data and solid lines the fit, with the difference below. Reproduced with permission from reference [151], ©2015 American Chemical Society.
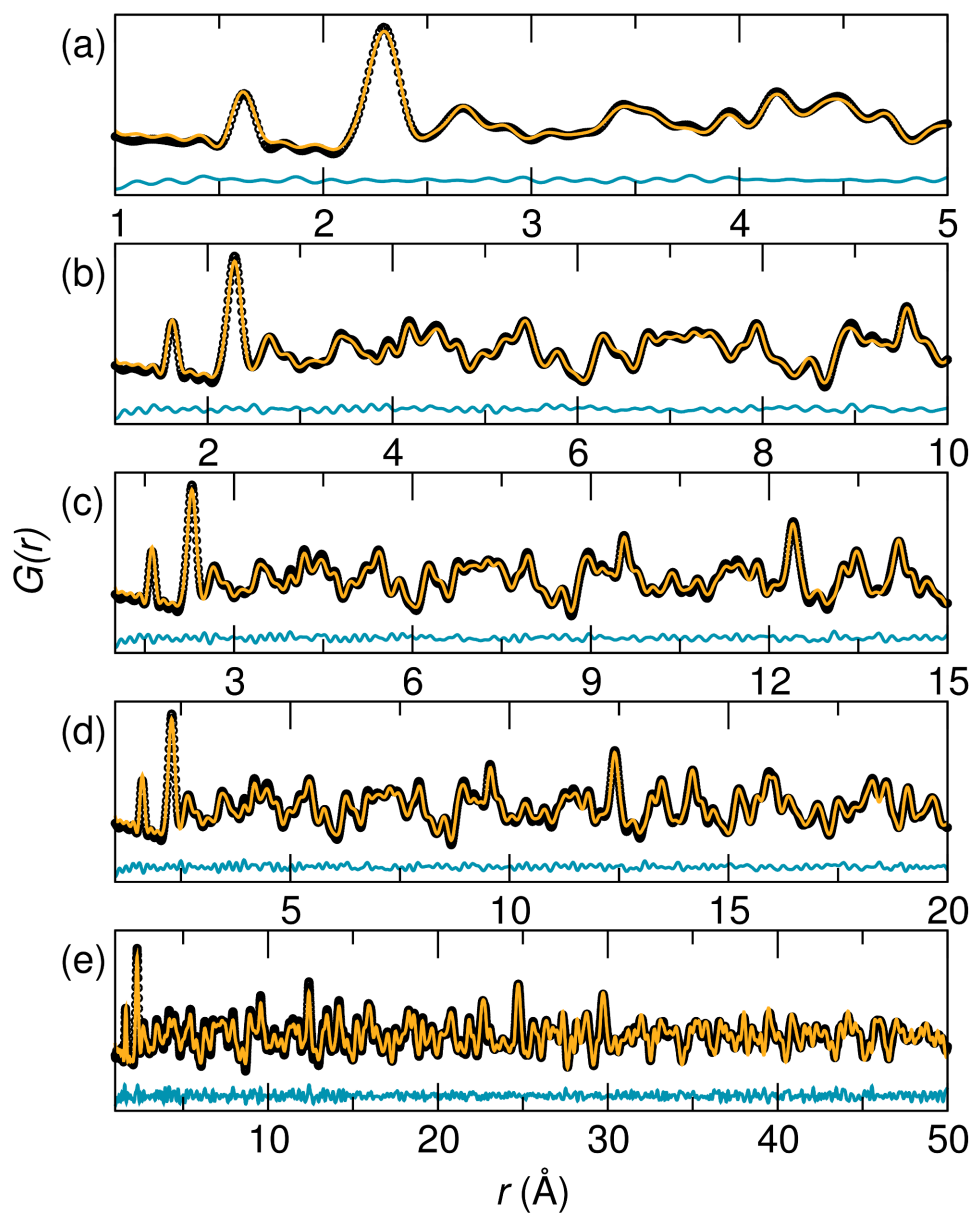
Figure 7.14: Least squares refinements of the pair distribution function of Y_2SiO_5 from low temperature neutron powder diffraction data collected at 15 K fit from (a) 1 Å to 5 Å, (b) 1 Å to 10 Å, (c) 1 Å to 15 Å, (d) 1 Å to 20 Å, and (e) 1 Å to 50 Å. Black circles represent the data and solid lines the fit, with the difference below. Reproduced with permission from reference [151], ©2015 American Chemical Society.

Chapter 8

Summary and Future Directions

We have explored in depth and presented an understanding of the structure–composition–property relationships in newly developed and well-known phosphor materials for high-performance solid-state white lighting. We began by presenting the development of of a green-yellow emitting oxyfluoride solid-solution phosphor $Sr_2Ba(AlO_4F)_{1-x}(SiO_5)_x$:$Ce^{3+}$ for thermally stable, high color rendition solid state white lighting. An examination of the host lattice, and the local structure around the Ce^{3+} activator ions through a combination of density functional theory, synchrotron X-ray and neutron powder diffraction and total scattering, and electron paramagnetic resonance, points to how chemical substitutions play a crucial role in tuning the optical properties of the phosphor. The

maximum emission wavelength can be tuned from green (λ_{em} = 523 nm) to yellow (λ_{em} = 552 nm) by tuning the composition, x. Photoluminescent quantum yield is determined to be 70±5% for some of the examples in the series. Excellent thermal properties were found for the $x = 0.5$ sample, with the photoluminescence intensity at 160 °C only decreased to 82% of its room temperature value. Phosphor-converted LED devices fabricated using an InGaN LED (λ_{max} = 400 nm) exhibit high color rendering white light with $R_a = 70$ and a correlated color temperature near 7000 K. The value of R_a could be raised to 90 by the addition of a red component, and the correlated color temperature lowered to near 4000 K.

Next, we identified two new phosphor solid-solution systems, $(Ba_{1-x}Sr_x)_9Sc_2Si_6O_{24}$:$Ce^{3+}$,$Li^+$ and $Ba_9(Y_{1-y}Sc_y)_{1.94}Ce_{0.06}Si_6O_{24}$, and analyzed the tuning of luminescent properties through composition. The structures were characterized using synchrotron X-ray powder diffraction, show the solid-solution closely follows Végard's law. The substitution of Sr for Ba in $(Ba_{1-x}Sr_x)_9Sc_2Si_6O_{24}$:$Ce^{3+}$,$Li^+$ results in decrease of the alkaline earth-oxygen bond distances by more than 0.1 Å at all three crystallographic sites, leading to changes in optical properties. The room temperature photoluminescent measurements show the structure has three excitation peaks corresponding to Ce^{3+} occupying the three independent alkaline earth sites. The emission

of $(Ba_{1-x}Sr_x)_9Sc_2Si_6O_{24}$:$Ce^{3+}$, Li^+ is red-shifted from the near-UV ($\lambda_{max} = 384$ nm) for $x = 0$ to blue ($\lambda_{max} = 402$ nm) for $x = 1$. The red-shifted photoluminescent quantum yield also increases when Sr is substituted for Ba in these compounds. The end member $Ba_9Y_2Si_6O_{24}$:Ce^{3+} was identified as an efficient blue-green phosphor for application in solid-state lighting. The photoluminescent characterization identified a major peak at 394 nm in the excitation spectrum making this material viable for near-UV LED excitation. An efficient emission, with a quantum yield of ≈60%, covers a broad portion (430 nm to 675 nm) of the visible spectrum leading to the blue-green color. Concentration quenching occurs when the Ce^{3+} content exceeds ≈3 mole% while high temperature photoluminescent measurements show a 25% drop of the room temperature efficiency at 500 K. The emission of this compound can be red-shifted via the solid-solution, $Ba_9(Y_{1-y}Sc_y)_{1.94}Ce_{0.06}Si_6O_{24}$ ($x = 0.1$, 0.2) allowing for tunable color properties when device integration is considered.

We then explored the structure–composition relationships and optical properties in the newly developed cerium-substituted $(Sr,Ba)_3(Y,La)(BO_3)_3$ borate phosphors through a combination of high resolution synchrotron X-ray powder diffraction and photoluminescence. Examination of the coordination environment of the Ce^{3+} active site polyhedra coupled with photoluminescence at 77 K reveal three distinct excitation bands corresponding to Ce^{3+} located

on three distinct crystallographic sites. Comparing the position of these excitation bands with crystal field splitting effects due to changes in polyhedral volumes and distortions suggest an assignment of the three excitation bands. These compounds are efficiently excited by UV light ($\approx$340 nm) with blue emission at a maximum wavelength of 413 nm for $Ba_3Y(BO_3)_3$:Ce^{3+},Na^+, 422 nm for $Sr_3Y(BO_3)_3$:Ce^{3+},Na^+, and 440 nm for $Sr_3La(BO_3)_3$:Ce^{3+},Na^+. The most efficient compound was determined to be $Sr_3La(BO_3)_3$:Ce^{3+},Na^+ with a quantum yield of 50%.

A data-driven discovery of energy materials then revealed the efficient $BaM_2Si_3O_{10}$:Eu^{2+} (M = Sc, Lu) phosphors. M = Sc^{3+} and Lu^{3+} compounds with Eu^{2+} substitution were prepared and characterized using synchrotron X-ray powder diffraction and photoluminescence spectroscopy. Substituting Eu^{2+} according to $Ba_{1-x}Eu_xSc_2Si_3O_{10}$ and $Ba_{1-x}Eu_xLu_2Si_3O_{10}$ results in UV-to-blue and UV-to-blue-green phosphors, respectively. Interestingly, substituting Eu^{2+} in the Lu^{3+} containing material produces two emission peaks, at low temperature and with 365 nm excitation, as allowed by two substitution sites. The photoluminescence of the Sc^{3+} compound is robust at high temperature, decreasing by only 25% of its room temperature intensity at 503 K while the Lu-analogue has a large drop (75%) of its room temperature intensity. The decrease in emission intensity is explained as stemming from charge transfer quenching due to the

short distances separating the luminescent centers on the Lu^{3+} substitution site. The correlation between structure and optical response in these two compounds indicates that even though the structures are three-dimensionally connected, high symmetry is required to prevent structural distortions that could impact photoluminescence.

Next, the consequences of optimal bond valence on structural rigidity were explored and linked to the improved luminescence properties in $Sr_xBa_{2-x}SiO_4$:Eu^{2+} orthosilicate phosphors. We employed a combination of synchrotron X-ray diffraction, total scattering measurements, density functional theory calculations, and low-temperature heat capacity measurements, in conjunction with detailed temperature- and time-resolved studies of luminescence properties to understand the origins of the improved luminescence properties. We observe that in the intermediate compositions, the two cation sites in the crystal structure are optimally bonded as determined from bond valence sum calculations. Optimal bonding results in a more rigid lattice, as established by the intermediate compositions possessing the highest Debye temperature, which are determined experimentally from low-temperature heat capacity measurements. Greater rigidity in turn results in the highest luminescence efficiency for intermediate compositions at elevated temperatures.

We then conducted an in-depth analysis of the average and local structure,

Debye temperature, and structural rigidity in oxide phosphor host materials. The average and local structure of the oxide phosphor hosts Ba_2SiO_4, $BaAl_2O_2$, $SrAl_2O_4$, and Y_2SiO_5 were explored to evaluate the degree of structural rigidity and the underlying structural signatures that lead to efficient photoluminescence. Simultaneous refinements of synchrotron X-ray diffraction and neutron scattering reveal the average crystal structure allowing an analysis of the bonding environment around substituted Ce^{3+} activator ions relating to the observed optical properties of these phosphors. The Debye temperature (Θ_D) is then used as a proxy for structural rigidity and is predicted using Density Functional Theory (DFT) calculations, measured experimentally using refined atomic displacement parameters (U_{iso}) from neutron scattering data collected at 15 K using both average and local structure techniques, and extracted from low temperature heat capacity measurements collected at 1.8 K. The effects of thermal scattering and static disorder on the measured U_{iso} and resulting Θ_D are analyzed using pair distribution function (PDF) analysis of 15 K neutron scattering data. Varying the fit range in the PDF analysis, capturing the average and the local structure, reveals the degree of thermal diffuse scattering within a material, and shows the correlations between thermal diffuse scattering, Θ_D, and bond valence sums.

Finally, new light generation strategies including quantum dots and laser-

based lighting have been explored. Quantum dots have the potential to be used in solid state white lighting applications as an additional down-converting component to better represent wavelengths in the red spectral region, leading to higher quality white light with improved color rendering. In this contribution, we report on color characteristics of phosphor-converted white light-emitting diodes that utilize inorganic garnet-based phosphors, with quantum dots incorporated appropriately. Devices were fabricated using red-emitting CdSe/ZnS core/shell quantum dots (λ_{em} = 560 nm or λ_{em} = 590 nm) in conjunction with yellow-emitting $Y_3Al_5O_{12}$:Ce^{3+} or green-emitting $Lu_3Al_5O_{12}$:Ce^{3+} and a blue-emitting InGaN LED (λ_{em} = 450 nm). Several phosphor/quantum dot geometries were examined, including encapsulating the phosphor powder and quantum dots together in silicone resin, or in two separate layers of silicone resin, with either the quantum dots closest to the LED or the phosphor particles closest to the LED. The quantum dots were most efficient when encapsulated with the phosphor particles in the resin. Devices with $Y_3Al_5O_{12}$:Ce^{3+} and quantum dots (λ_{em} = 590 nm) achieved a correlated color temperature of 4000 K, color rendering index of 81, and luminous efficacy of 57 lm/W, while devices with $Lu_3Al_5O_{12}$:Ce^{3+} and quantum dots (λ_{em} = 590 nm) achieved a correlated color temperature of 5700 K, a color rendering index of 90, and luminous efficacy of 22 lm/W. The results obtained suggest that the use of quantum dots may allow

266

for solid state white lighting devices with high color rendition.

Laser-based white lighting offers a viable option as an efficient and color-stable high-power solid-state white light source. We show that white light generation is possible using blue or near-UV laser diodes in combination with yellow-emitting cerium-substituted yttrium aluminum garnet (YAG:Ce) or a mixture of red-, green-, and blue-emitting phosphors. A variety of correlated color temperatures (CCT) are achieved, ranging from cool white light with a CCT of $4400\,K$ using a blue laser diode to a warm white light with a CCT of $2700\,K$ using a near-UV laser diode, with respective color rendering indices of 57 and 95. The luminous flux of these devices are measured to be $252\,lm$ and $53\,lm$ with luminous efficacies of $76\,lm/W$ and $19\,lm/W$, respectively. An estimation of the maximum efficacy of a device comprising a blue laser diode in combination with YAG:Ce is calculated and the results are used to optimize the device.

With solid-state lighting devices moving into the high-power regime with high-power LEDs and laser-based lighting, the thermal and flux stability of phosphor luminescence will become of paramount importance. Much attention has thus far been focused on understanding the structural effects that tune optical properties like excitation and emission spectra to optimal wavelengths. This work has gained an in-depth understanding of these mechanisms, along with beginning the exploration into how the rigidity of phosphor host structures plays

a role in affecting the optical properties. We have found that highly rigid structures promote high photoluminescent quantum yield and high thermal stability of the photoluminescence. Further exploration into the role of structural rigidity and its effect on optical properties may reveal how different the activator ions are affected in different structures, in terms of photoluminescent quantum yield and thermal quenching of the luminescence. Moving forward, understanding the role of flux saturation quenching in phosphor materials under intense high-power excitation sources may be needed for next generation technologies. Using this information in practice and as new screening methods for developing high performing phosphors may now be implemented.

Bibliography

[1] N. C. George, K. A. Denault, and R. Seshadri. Phosphors for solid-state white lighting. *Annu. Rev. Mater. Res.*, 43(1):481–501, 2013.

[2] S. Nakamura, T. Mukai, and M. Senoh. Candela-class high-brightness InGaN/AlGaN double-heterostructure blue-light-emitting diodes. *Appl. Phys. Lett.*, 64(13):1687–1689, 1994.

[3] E. F. Schubert and J. K. Kim. Solid-state light sources getting smart. *Science*, 308(5726):1274–1278, 2005.

[4] T. Jüstel, H. Nikol, and C. Ronda. New developments in the field of luminescent materials for lighting and displays. *Angew. Chem. Int. Ed.*, 37(22):3084–3103, 1998.

[5] S. Ye, F. Xiao, Y. X. Pan, Y. Y. Ma, and Q. Y. Zhang. Phosphors in phosphor-converted white light-emitting diodes: Recent advances in materials, techniques and properties. *Mater. Sci. Eng. R*, 71:1–34, 2010.

[6] C. Feldmann, T. Jüstel, C. R. Ronda, and P. J. Schmidt. Inorganic luminescent materials: 100 years of research and application. *Adv. Funct. Mater.*, 13(7):511–516, 2003.

[7] E. F. Schubert. *Light-Emitting Diodes*. Cambridge University Press, 2006.

[8] M. R Krames, O. B Shchekin, R. Müller-Mach, G. O Müller, Ling Zhou, G. Harbers, and M. G Craford. Status and future of high-power light-emitting diodes for solid-state lighting. *J. Disp. Technol.*, 3(2):160–175, 2007.

[9] P. F. Smet, A. B. Parmentier, and D. Poelman. Selecting conversion phosphors for white light-emitting diodes. *J. Electrochem. Soc.*, 158:R37, 2011.

[10] R. Müller-Mach, G. Mueller, M. R. Krames, H. A. Höppe, F. Stadler, W. Schnick, T. Jüstel, and P. Schmidt. Highly efficient all-nitride phosphor-converted white light emitting diode. *Phys. Status Solidi A*, 202(9):1727–1732, 2005.

[11] G. Blasse and A. Bril. A new phosphor for flying-spot cathode-ray tubes for color television: Yellow-emitting $Y_3Al_5O_{12}$:Ce^{3+}. *Appl. Phys. Lett.*, 11:53–55, 1967.

[12] G. Blasse and A. Bril. Investigation of some Ce^{3+}-activated phosphors. *J. Chem. Phys.*, 47:5139, 1967.

[13] R.-J. Xie and N. Hirosaki. Silicon-based oxynitride and nitride phosphors for white LEDs – a review. *Sci. Tech. Adv. Mater.*, 8:588–600, 2007.

[14] A. Birkel, K. A. Denault, N. C. George, C. E. Doll, B. Héry, A. A. Mikhailovsky, C. S. Birkel, B.-C. Hong, and R. Seshadri. Rapid microwave preparation of highly efficient Ce^{3+}-substituted garnet phosphors for solid state white lighting. *Chem. Mater.*, 24:1198–1204, 2012.

[15] K. A. Denault, M. Cantore, S. Nakamura, S. P. DenBaars, and R. Seshadri. Efficient and stable laser-driven white lighting. *AIP Advances*, 3(7):072107, 2013.

[16] M. D. Chambers and D. R. Clarke. Doped oxides for high-temperature luminescence and lifetime thermometry. *Annu. Rev. Mater. Res.*, 39(1):325–359, 2009.

[17] C. K. Jørgensen. Electron transfer spectra of lanthanide complexes. *Molec. Phys.*, 5(3):271–277, 1962.

[18] R. J. Lang. The spectrum of trebly ionized cerium. *Can. J. Res.*, 14a(7):127–130, 1936.

[19] P. Dorenbos, J. Andriessen, and C. W. E. van Eijk. $4f^{n-1}5d$ centroid shift in lanthanides and relation with anion polarizability, covalency, and cation electronegativity. *J. Solid State Chem.*, 171(1–2):133–136, 2003.

[20] P. Dorenbos. Relating the energy of the $[Xe]5d^1$ configuration of Ce^{3+} in inorganic compounds with anion polarizability and cation electronegativity. *Phys. Rev. B*, 65(23):1–6, 2002.

[21] J. L. Wu, G. Gundiah, and A. K. Cheetham. Structure–property correlations in Ce-doped garnet phosphors for use in solid state lighting. *Chem. Phys. Lett.*, 441(4–6):250–254, 2007.

[22] T. Hoshina and S. Kuboniwa. $4f$-$5d$ transition of Tb^{3+} and Ce^{3+} in MPO_4(M=Sc, y and lu). *J. Phys. Soc. Jpn.*, 31(3):828–840, 1971.

[23] C. K. Jörgensen. *Modern Aspects of Ligand Field Theory*. North-Holland, Amsterdam, 1971.

[24] P. D. Rack and P. H. Holloway. The structure, device physics, and material properties of thin film electroluminescent displays. *Mater. Sci. Eng., R*, 21(4):171–219, 1998.

[25] P. Dorenbos. Crystal field splitting of lanthanide $4f^{n-1}5d$-levels in inorganic compounds. *J. Alloys Compd.*, 341(1–2):156–159, 2002.

[26] G. Blasse, W. Schipper, and J. J. Hamelink. On the quenching of the luminescence of the trivalent cerium ion. *Inorg. Chim. Acta*, 189(1):77–80, 1991.

[27] P. Dorenbos. Thermal quenching of Eu^{2+} 5d–4f luminescence in inorganic compounds. *J. Phys-Condens. Matt.*, 17(50):8103–8111, 2005.

[28] K. C. Bleijenberg and G. Blasse. QMSCC calculations on thermal quenching of model phosphor systems. *J. Solid State Chem.*, 28(3):303–307, 1979.

[29] P. Dorenbos. Absolute location of lanthanide energy levels and the performance of phosphors. *J. Lumin.*, 122-123:315–317, 2007.

[30] W. M. Yen, S. Shionoya, and H. Yamamoto. *Phosphor Handbook*. Taylor & Francis Group, 2nd edition, 2007.

[31] P. Dorenbos. The $4f^n \leftrightarrow 4f^{n-1}5d$ transitions of the trivalent lanthanides in halogenides and chalcogenides. *J. Lumin.*, 91(1–2):91–106, 2000.

[32] M. J. Weber. Nonradiative decay from 5d states of rare earths in crystals. *Solid State Comm.*, 12(7):741–744, 1973.

[33] Teruhiko Hoshina. $5d \leftrightarrow 4f$ radiative transition probabilities of Ce^{3+} and Eu^{2+} in crystals. *J. Phys. Soc. Jpn.*, 48(4):1261–1268, 1980.

[34] V. Bachmann, C. Ronda, and A. Meijerink. Temperature quenching of yellow Ce^{3+} luminescence in YAG:Ce. *Chem. Mater.*, 21(10):2077–2084, 2009.

[35] J. Brgoch, S. P. DenBaars, and R. Seshadri. Proxies from ab initio calculations for screening efficient Ce^{3+} phosphor hosts. *J. Phys. Chem. C*, 117(35):17955–17959, 2013.

[36] K. A. Denault, J. Brgoch, M. W. Gaultois, A. Mikhailovsky, R. Petry, H. Winkler, S. P. DenBaars, and R. Seshadri. Consequences of optimal bond valence on structural rigidity and improved luminescence properties in $Sr_xBa_{2-x}SiO_4$:Eu^{2+} orthosilicate phosphors. *Chem. Mater.*, 26(7):2275–2282, 2014.

[37] M. W. Gaultois, T. D. Sparks, C. K. H. Borg, R. Seshadri, W. D. Bonificio, and D. R. Clarke. Data-driven review of thermoelectric materials: Performance and resource considerations. *Chemistry of Materials*, 25(15):2911–2920, 2013.

[38] K. A. Denault, N. C. George, S. R. Paden, S. Brinkley, A. A. Mikhailovsky, J. Neuefeind, S. P. DenBaars, and R. Seshadri. A green-yellow emitting oxyfluoride solid solution phosphor $Sr_2Ba(AlO_4F)_{1-x}(SiO_5)_x$:$Ce^{3+}$ for thermally stable, high color rendition solid state white lighting. *J. Mater. Chem.*, 22:18204–18213, 2012.

272

[39] W. B. Im, Y. Kim, N. N. Fellows, H. Masui, G. A. Hirata, S. P. DenBaars, and R. Seshadri. A yellow-emitting Ce^{3+} phosphor, $La_{1-x}Ce_xSr_2AlO_5$, for white light-emitting diodes. *Appl. Phys. Lett.*, 93(9):091905, 2008.

[40] W. B. Im, N. N. Fellows, S. P. DenBaars, and R. Seshadri. $La_{1-x-0.025}Ce_{0.025}Sr_{2+x}Al_{1-x}Si_xO_5$ solid solutions as tunable yellow phosphors for solid state white lighting. *J. Mater. Chem.*, 19:1325–1330, 2009.

[41] W. B. Im, Y. Fourré, S. Brinkley, J. Sonoda, S. Nakamura, S. P. DenBaars, and R. Seshadri. Substitution of oxygen by fluorine in the $GdSr_2AlO_5$:Ce^{3+} phosphors: $Gd_{1-x}Sr_{2+x}AlO_{5-x}F_x$ solid solutions for solid state white lighting. *Opt. Express*, 17:22673–22679, 2009.

[42] W. B. Im, S. Brinkley, J. Hu, A. Mikhailovsky, S. P. DenBaars, and R. Seshadri. $Sr_{2.975-x}Ba_xCe_{0.025}AlO_4F$: A highly efficient green-emitting oxyfluoride phosphor for solid state white lighting. *Chem. Mater.*, 22(9):2842–2849, 2010.

[43] W. B. Im, N. George, J. Kurzman, S. Brinkley, A. Mikhailovsky, J. Hu, B. F. Chmelka, S. P. DenBaars, and R. Seshadri. Efficient and color-tunable oxyfluoride solid solution phosphors for solid-state white lighting. *Adv. Mater.*, 23(20):2300–2305, 2011.

[44] K. Uheda. Application of nitride and oxynitride compounds to various phosphors for white led. *Key Eng. Mater.*, 403:15–18, 2009.

[45] Y. Q. Li, A. C. A. Delsing, G. de With, and H. T. Hintzen. Luminescence properties of Eu^{2+}-activated alkaline-earth silicon-oxynitride $MSi_2O_{2-\delta}N_{2+2/3\delta}$ (M = Ca, Sr, Ba): A promising class of novel LED conversion phosphors. *Chem. Mater.*, 17(12):3242–3248, 2005.

[46] A. A. Setlur, W. J. Heward, M. E. Hannah, and U. Happek. Incorporation of Si^{4+}-N^3 into Ce^{3+}-doped garnets for warm white LED phosphors. *Chem. Mater.*, 20(19):6277–6283, 2008.

[47] J. A. Kechele, O. Oeckler, F. Stadler, and W. Schnick. Structure elucidation of $BaSi_2O_2N_2$ – A host lattice for rare-earth doped luminescent materials in phosphor-converted (pc)-LEDs. *Solid State Sci.*, 11(2):537–543, 2009.

[48] C. Hecht, F. Stadler, P. J. Schmidt, V. Baumann, and W. Schnick. $SrAlSi_4N_7:Eu^{2+}$ – a nitridoalumosilicate phosphor for warm white light (pc) LEDs with edge-sharing tetrahedra. *Chem. Mater.*, 21(8):1595–1601, 2009.

[49] H. A. Höppe, H. Lutz, P. Morys, W. Schnick, and A. Seilmeier. Luminescence in Eu^{2+}-doped $Ba_2Si_5N_8$: Fluorescence, thermoluminescence, and upconversion. *J. Phys. Chem. Solids*, 61(12):2001–2006, 2000.

[50] G. Kresse and J. Hafner. Ab initio molecular dynamics for liquid metals. *Phys. Rev. B*, 47(1):558–561, 1993.

[51] G. Kresse and J. Hafner. Ab initio molecular-dynamics simulation of the liquid-metal-amorphous-semiconductor transition in germanium. *Phys. Rev. B*, 49:14251, 1994.

[52] G. Kresse and J. Furthmüller. Efficiency of ab-initio total energy calculations for metals and semiconductors using a plane-wave basis set. *Comput. Mat. Sci.*, 6:15, 1996.

[53] G. Kresse and J. Furthmüller. Efficient iterative schemes for ab initio total-energy calculations using a plane-wave basis set. *Phys. Rev. B*, 54:11169, 1996.

[54] P. E. Blöchl. Projector augmented-wave method. *Phys. Rev. B*, 50(24):17953–17979, 1994.

[55] G. Kresse and D. Joubert. From ultrasoft pseudopotentials to the projector augmented-wave method. *Phys. Rev. B*, 59(3):1758–1775, 1999.

[56] J. P. Perdew, K. Burke, and M. Ernzerhof. Generalized gradient approximation made simple. *Phys. Rev. Lett.*, 77(18):3865–3868, 1996.

[57] J. P. Perdew, K. Burke, and M. Ernzerhof. Erratum: Generalized gradient approximation made simple. *Phys. Rev. Lett.*, 78:1396, 1997.

[58] G. Baldinozzi, J.-F. Bérar, and G. Calvarin. Segregation and site selectivity in Zr-doped Y_2O_3. *J. Phys.: Condens. Matter*, 9(45):9731–9744, 1997.

[59] N. C. Greenham, I. D. W. Samuel, G. R. Hayes, R. T. Phillips, Y. A. R. R. Kessener, S. C. Moratti, A. B. Holmes, and R. H. Friend. Measurement of absolute photoluminescence quantum efficiencies in conjugated polymers. *Chem. Phys. Lett.*, 241(1-2):89 – 96, 1995.

[60] S. E. Brinkley, N. Pfaff, K. A. Denault, Z. Zhang, H. T. Hintzen, R. Seshadri, S. Nakamura, and S. P. DenBaars. Robust thermal performance of $Sr_2Si_5N_8$:Eu^{2+}: An efficient red emitting phosphor for light emitting diode based white lighting. *Appl. Phys. Lett.*, 99(24):241106, 2011.

[61] T. Vogt, P. M. Woodward, B. A. Hunter, A. K. Prodjosantoso, and B. J. Kennedy. Sr_3mo_4f (m = al, ga)–A new family of ordered oxyfluorides. *J. Solid State Chem.*, 144(1):228–231, 1999.

[62] J. K. Park, C. H. Kim, S. H. Park, H. D. Park, and S. Y. Choi. Application of strontium silicate yellow phosphor for white light-emitting diodes. *Appl. Phys. Lett.*, 84(10):1647–1649, 2004.

[63] R. D. Shannon. Revised effective ionic radii and systematic studies of interatomic distances in halides and chalcogenides. *Acta Crystallogr. A*, 32:751–767, 1976.

[64] Y. Q. Jia. Radii and effective ionic radii of the rare earth ions. *J. Solid State Chem.*, 187(1):184–187, 1991.

[65] P. V. Kelsey and J. J. Brown. Ce^{3+}-activated photoluminescence in the BaO–SrO–SiO_2 system: I. Crystalline phases. *J. Electrochem. Soc.*, 123(9):1384–1388, 1976.

[66] A. K. Prodjosantoso, B. J. Kennedy, T. Vogt, and P. M. Woodward. Cation and anion ordering in the layered oxyfluorides $Sr_{3-x}A_xAlO_4F$ (A = Ba, Ca). *J. Solid State Chem.*, 172(1):89–94, 2003.

[67] W. H. Baur. The geometry of polyhedral distortions. predictive relationships for the phosphate group. *Acta Crystallogr. B*, 30:1195–1215, 1974.

[68] D. K. Swanson and R. C. Peterson. Polyhedral volume calculations. *Can. Mineral.*, 18(2):153–156, 1980.

[69] N. E. Brese and M. O'Keeffe. Bond-valence parameters for solids. *Acta Crystallogr. B*, 47(2):192–197, 1991.

[70] L. Pidol, O. Guillot-Noël, A. Kahn-Harari, B. Viana, D. Pelenc, and D. Gourier. EPR study of Ce^{3+} ions in lutetium silicate scintillators $Lu_2Si_2O_7$ and Lu_2SiO_5. *J. Phys. Chem. Solids*, 67:643–650, 2006.

[71] M. Brustolon and E. Giamello, editors. *Electron Paramagnetic Resonance: A Practitioner's Toolkit*. Wiley, 2008.

[72] G. Blasse and B. C. Grabmaier. *Luminescent Materials*. Springer-Verlag, Berlin, 1994.

[73] S. Shionoya and W. M. Yen. *Phosphor Handbook*. CRC Press, New York, 1998.

[74] W. W. Holloway, Jr. and M Kestigian. On the fluorescence of cerium-activated garnet crystals. *Phys. Lett.*, 25(8):614–615, 1967.

[75] W. W. Holloway, Jr. and M. Kestigian. Optical properties of cerium-activated garnet crystals. *J. Opt. Soc. Am.*, 59:60, 1969.

[76] J. M. Robertson, M. W. van Tol, W. H. Smits, and J. P. H. Heynen. Colorshift of the Ce^{3+} emission in monocrystalline epitaxially grown garnet layers. *Philips J. Res.*, 36(1):15–30, 1981.

[77] T. Egami and S. J. L. Billinge. *Underneath the Bragg peaks: Structural Analysis of Complex Materials*. Pergamon, Amsterdam, 2003.

[78] T. Egami. Local structure of ferroelectric materials. *Annu. Rev. Mater. Res*, 37:297–315, 2007.

[79] I. K. Jeong, F. Mohiuddin-Jacobs, V. Petkov, S. J. L. Billinge, and S. Kycia. Local structure of $In_xGa_{1-x}As$ semiconductor alloys by high-energy synchrotron x-ray diffraction. *Phys. Rev. B*, 63:205202, 2001.

[80] P Dorenbos. $5d$-level energies of Ce^{3+} and the crystalline environment. I. Fluoride compounds. *Phys. Rev. B*, 62:15640–15649, 2000.

[81] P Dorenbos. $5d$-level energies of Ce^{3+} and the crystalline environment. III. Oxides containing ionic complexes. *Phys. Rev. B*, 64:125117, 2001.

[82] S. Bhushan and M. V. Chukichev. Temperature dependent studies of cathodoluminescence of green band of ZnO crystals. *J. Mater. Sci. Lett.*, 7:319–321, 1988.

[83] Y. Chen, B. Liu, C. Shi, G. Ren, and G. Zimmerer. The temperature effect of Lu_2SiO_5:Ce^{3+} luminescence. *Nucl. Instrum. Methods Phys. Res., Sect. A*, 537(1–2):31–35, 2005.

[84] J. Brgoch, C. K. H. Borg, K. A. Denault, S. P. DenBaars, and R. Seshadri. Tuning luminescent properties through solid-solution in $(Ba_{1x}Sr_x)_9Sc_2Si_6O_{24}$:$Ce^{3+}$,$Li^+$. *Solid State Sci.*, 18:149 – 154, 2013.

[85] J. Brgoch, C. K. H. Borg, K. A. Denault, A. Mikhailovsky, S. P. DenBaars, and R. Seshadri. An efficient, thermally stable cerium-based silicate phosphor for solid state white lighting. *Inorg. Chem.*, 52(14):8010–8016, 2013.

[86] S. H. M. Poort, A. Meyerink, and G. Blasse. Lifetime measurements in Eu^{2+}-doped host lattices. *J. Phys. Chem. Solids*, 58(9):1451–1456, 1997.

[87] J. S. Kim, P. E. Jeon, J. C. Choi, and H. L. Park. Emission color variation of M_2SiO_4:Eu^{2+} (M=Ba, Sr, Ca) phosphors for light-emitting diode. *Solid State Comm.*, 133(3):187–190, 2005.

[88] J. S. Kim, Y. H. Park, S. M. Kim, J. C. Choi, and H. L. Park. Temperature-dependent emission spectra of M_2SiO_4:Eu^{2+} (M = Ca, Sr, Ba) phosphors for green and greenish white LEDs. *Solid State Comm.*, 133(7):445–448, 2005.

[89] Z. Cui, G. Jia, D. Deng, Y. Hua, S. Zhao, L. Huang, H. Wang, H. Ma, and S. Xu. Synthesis and luminescence properties of glass ceramics containing $MSiO_3$:Eu^{2+} (M=Ca, Sr, Ba) phosphors for white LED. *J. Lumin.*, 132(1):153–160, 2012.

[90] J. S. Kim, K. T. Lim, Y. S. Jeong, P. E. Jeon, J. C. Choi, and H. L. Park. Full-color $Ba_3MgSi_2O_8$:Eu^{2+},Mn^{2+} phosphors for white-light-emitting diodes. *Solid State Comm.*, 135(1-2):21–24, 2005.

[91] Q. Fei, C. K. Chang, and D. L. Mao. Luminescent properties of $Sr_2MgSi_2O_7$ and $Ca_2MgSi_2O_7$ long lasting phosphors activated by Eu^{2+}, Dy^{3+}. *J. Alloy Compd.*, 390(1-2):133–137, 2005.

[92] L. H. Wang, L. F. Schneemeyer, R. J. Cava, and T. Siegrist. A new barium scandium silicate: $Ba_9Sc_2(SiO_4)_6$. *J. Solid State Chem.*, 113(1):211–214, 1994.

[93] T. Nakano, Y. Kawakami, K. Uematsu, Ta. Ishigaki, K. Toda, and M. Sato. Novel Ba–Sc–Si-oxide and oxynitride phosphors for white LED. *J. Lumin.*, 129(12):1654–1657, 2009.

[94] L. Bian, T. L. Zhou, J. J. Yang, Z. Song, and Q. L. Liu. Crystal structure and photoluminescence of $(Ba_{1-x-y}Sr_yEu_x)_9Sc_2Si_6O_24$. *J. Lumin.*, 132(10):2541–2545, 2012.

[95] A. C. Larson and R. B. Von Dreele. General Structure Analysis System (GSAS). *Los Alamos National Laboratory Report LAUR*, pages 86–748, 2000.

[96] B. H. Toby. EXPGUI, a grahical user interface for GSAS. *J. Appl. Cryst.*, 34(2):210–213, 2001.

[97] J. Tauc, R. Grigorov, and A. Vancu. Optical properties and electronic structure of amorphous germanium. *Physica Status Solidi*, 15(2):627, 1966.

[98] G. Blasse and N. Sabbatini. The quenching of rare-earth ion luminescence in molecular and non-molecular solids. *Mater. Chem. Phys.*, 16(3–4):237–252, 1987.

[99] D. Van der Voort and G. Blasse. Luminescence of the europium(3+) ion in zirconium(4+) compounds. *Chem. Mater.*, 3(6):1041–1045, 1991.

[100] D. Van der Voort and G. Blasse. The luminescence of europium(III) and cerium(III) in calcium sulfate: Activators with an effective charge. *J. Solid State Chem.*, 87(2):350–359, 1990.

[101] G. Blasse, W. L. Wanmaker, J. W. ter Vrugt, and A. Bril. Fluorescence of Eu^{2+}-activated silicates. *Philips Res. Rep.*, 23(2):189–200, 1968.

[102] W. B. Im, Y.-I. Kim, J. H. Kang, D. Y. Jeon, H. K. Jung, and K. Y. Jung. Neutron Rietveld analysis for optimized $CaMgSi_2O_6$:Eu^{2+} and its luminescent properties. *J. Mater. Res.*, 20(8):2061–2066, 2005.

[103] S. S. Yao, L. H. Xue, Y. Y. Li, Y. You, and Y. W. Yan. Concentration quenching of Eu^{2+} in a novel blue-green emitting phosphor: $Ba_2ZnSi_2O_7$:Eu^{2+}. *Appl. Phys. B-Lasers O*, 96(1):39–42, 2009.

[104] C. J. da Silva, M. T. de Araujo, E. A. Gouveia, and A. S. Gouveia-Neto. Thermal effect on multiphonon-assisted anti-Stokes excited upconversion fluorescence emission in Yb^{3+}-sensitized Er^{3+}-doped optical fiber. *Appl. Phys. B-Lasers O*, 70:185–188, 2000.

[105] K. A. Denault, Z. Cheng, J. Brgoch, S. P. DenBaars, and R. Seshadri. Structure-composition relationships and optical properties in cerium-substituted $(Sr,Ba)_3(Y,La)(BO_3)_3$ borate phosphors. *J. Mater. Chem. C*, 1:7339–7345, 2013.

[106] D. Zhao and G. Wang. Growth and spectroscopic characterization of Er^{3+}:$Sr_3Y(BO_3)_3$ crystal. *J. Lumin.*, 130(3):424–428, 2010.

[107] P.-H. Haumesser, R. Gaumé, B. Viana, E. Antic-Fidancev, and D. Vivien. Spectroscopic and crystal-field analysis of new Yb-doped laser materials. *J. Phys.: Condens. Matter*, 13(23):5427, 2001.

[108] P.-H. Haumesser, R. Gaumé, B. Viana, and D. Vivien. Determination of laser parameters of ytterbium-doped oxide crystalline materials. *J. Opt. Soc. Am. B*, 19(10):2365–2375, 2002.

[109] S. Pan, Z. Hu, Z. Lin, and G. Wang. Growth and optical properties of Yb^{3+}-doped α-$Ba_3Y(BO_3)_3$ crystal. *J. Cryst. Growth*, 263(1–4):214–217, 2004.

[110] R. Gaumé, P.-H. Haumesser, E. Antic-Fidancev, P. Porcher, B. Viana, and D. Vivien. Crystal field calculations of Yb^{3+}-doped double borate crystals for laser applications. *J. Alloy Compd.*, 341(1–2):160–164, 2002.

[111] R. Gaumé, B. Viana, D. Vivien, J. P. Roger, D. Fournier, J. P. Souron, G. Wallez, S. Chénais, F. Balembois, and P. Georges. Mechanical, thermal and laser properties of Yb:$(Sr_{1x}Ca_x)_3Y(BO_3)_3$ (Yb:CaBOYS) for 1 μm laser applications. *Opt. Mater.*, 24(1–2):385–392, 2003.

[112] D. Zhao, Z. Hu, Z. Lin, and G. Wang. Growth and spectral properties of Er^{3+}/Yb^{3+}-codoped $Sr_3Y(BO_3)_3$ crystal. *J. Cryst. Growth*, 277(1–4):401–405, 2005.

[113] J. Pan, Z. Hu, Z. Lin, and G. Wang. Growth and spectral properties of Nd^{3+}-doped $Sr_3Y(BO_3)_3$ crystal. *J. Cryst. Growth*, 260(3–4):456–459, 2004.

[114] Y. Fujimoto, Y. Yokota, T. Yanagida, J. Pejchal, H. Konno, K. Sugiyama, M. Nikl, and A. Yoshikawa. Crystal growth and characterization of $Sr_3Y(BO_3)_3$. *IEEE T. Nucl. Sci.*, 57(3):1264–1267, 2010.

[115] X. Meng, L. Zhang, and G. Wang. Growth and spectral properties of Tm^{3+}-doped $Sr_3Y(BO_3)_3$ crystal. *J. Alloy Compd.*, 481(1–2):354–357, 2009.

[116] D.-Y. Wang, T.-M. Chen, and B.-M. Cheng. Host sensitization of Tb^{3+} ions in tribarium lanthanide borates $Ba_3Ln(BO_3)_3$ (Ln = Lu and Gd). *Inorg. Chem.*, 51(5):2961–2965, 2012.

[117] R. Simura, S. Kawai, K. Sugiyama, T. Yanagida, T. Sugawara, T. Shishido, and A. Yoshikawa. Valence state of dopant and scintillation properties of Ce-doped $Sr_3Y(BO_3)_3$ crystal. *J. Cryst. Growth*, 362(0):296–299, 2013.

[118] X. Z. Li, X. L. Chen, J. K. Jian, L. Wu, Y. P. Xu, and Y. G. Cao. Phase relations in the Y_2O_3–BaO–B_2O_3 system. *J. Alloy Compd.*, 365(1–2):277–280, 2004.

[119] S. K. Pan, G. F. Wang, and Z. X. Huang. Synthesis and structure of $Ba_3La_2(BO_3)_4$ crystal. *Chinese J. Struc. Chem.*, 21(4):382–384, 2002.

[120] X. Z. Li, X. L. Chen, L. Wu, Y. G. Cao, T. Zhou, and Y. P. Xu. $Ba_3YB_3O_9$: phase transition and crystal structure. *J. Alloy Compd.*, 370(1–2):53–58, 2004.

[121] X. Z. Li, X. L. Chen, J. K. Jian, L. Wu, Y. P. Xu, and Y. G. Cao. Thermal stability and crystal structure of β-$Ba_3YB_3O_9$. *J. Solid State Chem.*, 177(1):216–220, 2004.

[122] M. Mączka, A. Waśkowska, A. Majchrowski, J. Kisielewski, W. Szyrski, and J. Hanuza. Crystal structure and lattice dynamics of $Sr_3Y(BO_3)_3$. *J. Solid State Chem.*, 181(12):3211–3216, 2008.

[123] K. Robinson, G. V. Gibbs, and P. H. Ribbe. Quadratic elongation: A quantitative measure of distortion in coordination polyhedra. *Science*, 172(3983):567–570, 1971.

[124] J. Brgoch, K. Hasz, K. A. Denault, C. K. H. Borg, A. A. Mikhailovsky, and R. Seshadri. Data-driven discovery of energy materials: Efficient $BaM_2Si_3O_{10}$:Eu^{2+} (M = Sc, Lu) phosphors for application in solid state white lighting. *Faraday Discuss.*, 176:333–347, 2014.

[125] N. C. George, A. J. Pell, G. Dantelle, K. Page, A. Llobet, M. Balasubramanian, G. Pintacuda, B. F. Chmelka, and R. Seshadri. Local environments of dilute activator ions in the solid-state lighting phosphor $Y_{3-x}Ce_xAl_5O_{12}$. *Chem. Mater.*, 25(20):3979–3995, 2013.

[126] N. C. George, A. Birkel, J. Brgoch, B.-C. Hong, A. A. Mikhailovsky, K. Page, A. Llobet, and R. Seshadri. Average and local structural origins of the optical properties of the nitride phosphor $La_{3-x}Ce_xSi_6N_{11}$ ($0 < x \leq 3$). *Inorg. Chem.*, 52(23):13730–13741, 2013.

[127] A. F. Pozharskii, A. Soldatenkov, and A. R. Katritzky. *Heterocycles in Life and Society: An Introduction to Heterocyclic Chemistry, Biochemistry and Applications*. Wiley, 2011.

[128] J. D. Furman, B. C. Melot, S. J. Teat, A. A. Mikhailovsky, and A. K. Cheetham. Towards enhanced ligand-centred photoluminescence in

inorganic-organic frameworks for solid state lighting. *Phys. Chem. Chem. Phys.*, 13:7622–7629, 2011.

[129] J. Brgoch, C. K. H. Borg, K. A. Denault, J. R. Douglas, T. A. Strom, S. P. DenBaars, and R. Seshadri. Rapid microwave preparation of cerium-substituted sodium yttrium silicate phosphors for solid state white lighting. *Solid State Sci.*, 26:115 – 120, 2013.

[130] J. Brgoch, S. D. Kloß, K. A. Denault, and R. Seshadri. Accessing $(Ba_{1-x}Sr_x)Al_2Si_2O_8$:$Eu^{2+}$ phosphors for solid state white lighting via microwave assisted preparation: Tuning emission color through coordination environment. *Z. Anorg. Allg. Chem.*, 640(6):1182–1189, 2014.

[131] U. Kolitsch, M. Wierzbicka, and E. Tillmanns. $BaY_2Si_3O_{10}$: A new flux-grown trisilicate. *Acta Cryst. C*, 62(12):i97–i99, 2006.

[132] M. Wierzbicka-Wieczorek, U. Kolitsch, and E. Tillmanns. Synthesis and structural study of five new trisilicates, $BaREE_2Si_3O_{10}$ (REE = Gd, Er, Yb, Sc) and $SrY_2Si_3O_{10}$, including a review on the geometry of the Si_3O_{10} unit. *Eur. J. Mineral.*, 22:245–258, 2010.

[133] W.-R. Liu, C. C. Lin, Y.-C. Chiu, Y.-T. Yeh, S.-M. Jang, R.-S. Liu, and B.-M. Cheng. Versatile phosphors $BaY_2Si_3O_{10}$:RE (RE = Ce^{3+}, Tb^{3+}, Eu^{3+}) for light-emitting diodes. *Opt. Express*, 17(20):18103–18109, 2009.

[134] Z. Xia, Y. Liang, D. Yu, M. Zhang, W. Huang, M. Tong, J. Wu, and J. Zhao. Photoluminescence properties and energy transfer in color tunable $BaY_2Si_3O_{10}$:Ce,Tb phosphors. *Opt. Laser Technol.*, 56:387 – 392, 2014.

[135] J. Wang, B. H. Toby, P. L. Lee, L. Ribaud, S. M. Antao, C. Kurtz, M. Ramanathan, R. B. Von Dreele, and M. A. Beno. A dedicated powder diffraction beamline at the Advanced Photon Source: Commissioning and early operational results. *Rev. Sci. Instrum.*, 79(8):085105–085105–7, 2008.

[136] J. C. de Mello, H. F. Wittmann, and R. H. Friend. An improved experimental determination of external photoluminescence quantum efficiency. *Adv. Mater.*, 9(3):230–232, 1997.

[137] W. Becker. *Advanced Time-Correlated Single Photon Counting Techniques*, volume 81 of *Springer Series in Chemical Physics*. Springer, Berlin, Heidelberg, New York, 2005.

[138] Y. Le Page and P. Saxe. Elastic constants in vasp. *Phys. Rev. B*, 65:104104, 2002.

[139] G.-L. Davies, J. E. McCarthy, A. Rakovich, and Y. K. Gun'ko. Towards white luminophores: Developing luminescent silica on the nanoscale. *J. Mater. Chem.*, 22:7358–7365, 2012.

[140] Z. Bai, M. Fujii, K. Imakita, and S. Hayashi. Strong white photoluminescence from annealed zeolites. *J.Luminescence*, 145:288 – 291, 2014.

[141] J. K. Park, M. A. Lim, C. H. Kim, H. D. Park, J. T. Park, and S. Y. Choi. White light-emitting diodes of GaN-based Sr_2SiO_4:Eu and the luminescent properties. *Appl. Phys. Lett.*, 82(5):683–685, 2003.

[142] J. S. Yoo, S. H. Kim, W. T. Yoo, G. Y. Hong, K. P. Kim, J. Rowland, and P. H. Holloway. Control of spectral properties of strontium-alkaline earth-silicate-europium phosphors for LED applications. *J. Electrochem. Soc.*, 152(5):G382–G385, 2005.

[143] T. L. Barry. Fluorescence of Eu^{2+}-activated phases in binary alkaline earth orthosilicate systems. *J. Electrochem. Soc.*, 115(11):1181–1184, 1968.

[144] P. Juhás, T. Davis, C. L. Farrow, and S. J. L. Billinge. PDFgetX3: A rapid and highly automatable program for processing powder diffraction data into total scattering pair distribution functions. *J. Appl. Cryst.*, 46:560–566, 2013.

[145] C. L. Farrow, P. Juhás, J. W. Liu, D. Bryndin, E. S. Božin, J. Bloch, Th. Proffen, and S. J. L. Billinge. PDFfit2 and PDFgui: computer programs for studying nanostructure in crystals. *J. Phys.-Condens. Mat.*, 19(33):335219, 2007.

[146] R. Hill. Voigt-Reuss-Hill Approx. *Phys. Soc. London*, 65:350, 1952.

[147] Z.-J. Wu, E.-J. Zhao, H.-P. Xiang, X.-F. Hao, X.-J. Liu, and J. Meng. Crystal structures and elastic properties of superhard IrN_2 and IrN_3 from first principles. *Phys. Rev. B*, 76:054115, 2007.

[148] E. Francisco, J. M. Recio, M. A. Blanco, A. Martín Pendás, and A. Costales. Quantum-mechanical study of thermodynamic and bonding properties of MgF_2. *J. Phys. Chem. A*, 102(9):1595–1601, 1998.

[149] E. Francisco, M. A. Blanco, and G. Sanjurjo. Atomistic simulation of SrF_2 polymorphs. *Phys. Rev. B*, 63:094107, 2001.

[150] J.P. Poirier. *Introduction to the Physics of the Earth's Interior*. Cambridge University Press, 2000.

[151] K. A. Denault, J. Brgoch, S. D. Kloß, M. W. Gaultois, J. Siewenie, K. Page, R. Seshadri. Average and local structure, Debye temperature, and structural rigidity in some oxide compounds related to phosphor hosts. *ACS Appl. Mater. Interfaces*, accepted, 2015.

[152] E. Danielson, J. H. Golden, E. W. McFarland, C. M. Reaves, W. H. Weinberg, and X. D. Wu. A combinatorial approach to the discovery and optimization of luminescent materials. *Nature*, 389(6654):944–948, 10 1997.

[153] K.-S. Sohn, D. H. Park, S. H. Cho, B. I. Kim, and S. I. Woo. Genetic algorithm-assisted combinatorial search for a new green phosphor for use in tricolor white LEDs. *J. Combi. Chem.*, 8(1):44–49, 2006.

[154] J. Brgoch, M. W. Gaultois, M. Balasubramanian, K. Page, B.-C. Hong, and R. Seshadri. Local structure and structural rigidity of the green phosphor β-SiAlON:Eu^{2+}. *Appl. Phys. Lett.*, 105(18):181904, 2014.

[155] K. Momma and F. Izumi. VESTA3 for three-dimensional visualization of crystal, volumetric and morphology data. *J. Appl. Crystallogr.*, 44(6):1272–1276, 2011.

[156] B. T. M. Willis and A. W. Pryor. *Thermal Vibrations in Crystallography*. Cambridge University Press, 1975.

[157] P. F. Peterson, M. Gutmann, Th. Proffen, and S. J. L. Billinge. PDFgetN: a user-friendly program to extract the total scattering structure factor and the pair distribution function from neutron powder diffraction data. *J. Appl. Crystallogr.*, 33:1192–1192, 2000.

[158] H.P. Grosse and E. Tillmanns. Bariumorthosilicate, Ba_2SiO_4. *Cryst. Struct. Commun.*, 3(599-601), 1974.

[159] A.-K. Larsson, R. L. Withers, J. M. Perez-Mato, J. D. Fitz Gerald, P. J. Saines, B. J. Kennedy, and Y. Liu. On the microstructure and symmetry of apparently hexagonal $BaAl_2O_4$. *J. Solid State Chem.*, 181(8):1816 – 1823, 2008.

[160] A.-R. Schulze and Hk. Müller Buschbaum. Zur verbindungsbildung von MeO: M_2O_3. IV. Zur struktur von monoklinem $SrAl_2O_4$. *Z. Anorg. Allg. Chem.*, 475(4):205–210, 1981.

[161] M. Avdeev, S. Yakovlev, A. A. Yaremchenko, and V. V. Kharton. Transitions between $P2_1$, $P6_3(\sqrt{A})$, and $P6_322$ modifications of $SrAl_2O_4$ by in situ high-temperature X-ray and neutron diffraction. *J. Solid State Chem.*, 180(12):3535 – 3544, 2007.

[162] J. Lin, Q. Su, H. Zhang, and S. Wang. Crystal structure dependence of the luminescence of rare earth ions (Ce^{3+}, Tb^{3+}, Sm^{3+}) in Y_2SiO_5. *Mate. Res. Bull.*, 31(2):189 – 196, 1996.

[163] L. Pauling. The principles determining the structure of complex ionic crystals. *J. Am. Chem. Soc.*, 51(4):1010–1026, 1929.

[164] D. J. Safarik, R. B. Schwarz, and M. F. Hundley. Similarities in the C_p/T^3 peaks in amorphous and crystalline metals. *Phys. Rev. Lett.*, 96:195902, 2006.

[165] B. C. Melot, R. Tackett, J. O'Brien, A. L. Hector, G. Lawes, R. Seshadri, and A. P. Ramirez. Large low-temperature specific heat in pyrochlore $Bi_2Ti_2O_7$. *Phys. Rev. B*, 79:224111, 2009.

[166] M. Blackman. The theory of the specific heat of solids. *Rep. Prog. Phys.*, 8(1):11–30, 1941.

[167] D. H. Parkinson. The specific heats of metals at low temperatures. *Rep. Prog. Phys.*, 21:226–270, 1958.

[168] I.-K. Jeong, R. H. Heffner, M. J. Graf, and S. J. L. Billinge. Lattice dynamics and correlated atomic motion from the atomic pair distribution function. *Phys. Rev. B*, 67:104301, 2003.

[169] I.-K. Jeong, Th. Proffen, F. Mohiuddin-Jacobs, and S. J. L. Billinge. Measuring correlated atomic motion using X-ray diffraction. *J. Phys. Chem. A*, 103(7):921–924, 1999.

[170] Th. Proffen, K. L. Page, S. E. McLain, B. Clausen, T. W. Darling, J. A. TenCate, S.-Yub Lee, and E. Ustundag. Atomic pair distribution function analysis of materials containing crystalline and amorphous phases. *Z. Kristallogr.*, 220(12):1002, 2005.

[171] K. A. Denault, A. A. Mikhailovsky, S. Brinkley, S. P. DenBaars, and R. Seshadri. Improving color rendition in solid state white lighting through the use of quantum dots. *J. Mater. Chem. C*, 1:1461–1466, 2013.

[172] K. T. Lee and P. B. Aswath. Synthesis of hexacelsian barium aluminosilicate by a solid-state process. *J. Am. Cer. Soc.*, 83(12):2907–2912, 2000.

[173] H.-S. Chen, C.-K. Hsu, and H.-Y. Hong. InGaN-CdSe-ZnSe quantum dots white LEDs. *IEEE Photonic Tech. L.*, 18(1):193–195, 1, 2006.

[174] H. Wang, K.-S. Lee, J.-H. Ryu, C.-H. Hong, and Y.-H. Cho. White light emitting diodes realized by using an active packaging method with CdSe/ZnS quantum dots dispersed in photosensitive epoxy resins. *Nanotechnology*, 19(14):145202, 2008.

[175] W. Chung, K. Park, H. J. Yu, J. Kim, B.-H. Chun, and S. H. Kim. White emission using mixtures of CdSe quantum dots and PMMA as a phosphor. *Opt. Mater.*, 32(4):515–521, 2010.

[176] X. Wang, W. Li, and K. Sun. Stable efficient CdSe/CdS/ZnS core/multi-shell nanophosphors fabricated through a phosphine-free route for white light-emitting-diodes with high color rendering properties. *J. Mater. Chem.*, 21:8558–8565, 2011.

[177] J. Ziegler, S. Xu, E. Kucur, F. Meister, M. Batentschuk, F. Gindele, and T. Nann. Silica-coated InP/ZnS nanocrystals as converter material in white LEDs. *Adv. Mater.*, 20(21):4068–4073, 2008.

[178] H. S. Jang, H. Yang, S. W. Kim, J. Y. Han, S.-G. Lee, and D. Y. Jeon. White light-emitting diodes with excellent color rendering based on organically capped CdSe quantum dots and Sr_3SiO_5:Ce^{3+},Li^+ phosphors. *Adv. Mater.*, 20(14):2696–2702, 2008.

[179] H. S. Jang, B.-H. Kwon, H. Yang, and D. Y. Jeon. Bright three-band white light generated from CdSe/ZnSe quantum dot-assisted Sr_3SiO_5:Ce^{3+},Li^+-based white light-emitting diode with high color rendering index. *Appl. Phys. Lett.*, 95(16):161901, 2009.

[180] S. Kim, T. Kim, M. Kang, S. K. Kwak, T. W. Yoo, L. S. Park, I. Yang, S. Hwang, J. E. Lee, S. K. Kim, and S.-W. Kim. Highly luminescent InP/GaP/ZnS nanocrystals and their application to white light-emitting diodes. *J. Am. Chem. Soc.*, 134(8):3804–3809, 2012.

[181] X. Wang, X. Yan, W. Li, and K. Sun. Doped quantum dots for white-light-emitting diodes without reabsorption of multiphase phosphors. *Adv. Mater.*, 24(20):2742–2747, 2012.

[182] C. B. Murray, D. J. Norris, and M. G. Bawendi. Synthesis and characterization of nearly monodisperse CdE (E = sulfur, selenium, tellurium) semiconductor nanocrystallites. *J. Am. Chem. Soc.*, 115(19):8706–8715, 1993.

[183] M. A. Hines and P. Guyot-Sionnest. Synthesis and characterization of strongly luminescing ZnS-capped CdSe nanocrystals. *J. Phys. Chem.*, 100(2):468–471, 1996.

[184] B. O. Dabbousi, J. Rodriguez-Viejo, F. V. Mikulec, J. R. Heine, H. Mattoussi, R. Ober, K. F. Jensen, and M. G. Bawendi. (CdSe)ZnS core-shell quantum dots:Synthesis and characterization of a size series of highly luminescent nanocrystallites. *J. Phys. Chem. B*, 101(46):9463–9475, 1997.

[185] Y. Ohno. Color rendering and luminous efficacy of white LED spectra. *Proc. of SPIE*, 5530:88–98, 2004.

[186] Z. Liu, T. Wei, E. Guo, X. Yi, L. Wang, J. Wang, G. Wang, Y. Shi, I. Ferguson, and J. Li. Efficiency droop in InGaN/GaN multiple-quantum-well blue light-emitting diodes grown on free-standing GaN substrate. *Appl. Phys. Lett.*, 99(9):091104, 2011.

[187] J. H. Son and J.-L. Lee. Strain engineering for the solution of efficiency droop in InGaN/GaN light-emitting diodes. *Opt. Express*, 18(6):5466–71, 2010.

[188] Y. Xu, L. Chen, Y. Li, G. Song, Y. Wang, W. Zhuang, and Z. Long. Phosphor-conversion white light using InGaN ultraviolet laser diode. *Appl. Phys. Lett.*, 92(2):021129, 2008.

[189] Y. Xu, H. Hu, W. Zhuang, G. Song, Y. Li, and L. Chen. White light emission from ultraviolet laser diode. *Laser Phys.*, 19(3):403–406, 2009.

[190] H.-Y. Ryu and D.-H. Kim. High-brightness phosphor-conversion white light source using InGaN blue laser diode. *J. Opt. Soc. Korea*, 14(4):415–419, 2010.

Appendix A

Improving color rendition in solid-state white lighting through the use of quantum dots

Quantum dots have the potential to be used in solid state white lighting applications as an additional down-converting component to better represent wavelengths in the red spectral region, leading to higher quality white light with improved color rendering. In this contribution, we report on color characteristics of phosphor-converted white light-emitting diodes that utilize inorganic garnet-based phosphors, with quantum dots incorporated appropriately. Devices were fabricated using red-emitting CdSe/ZnS core/shell quantum dots ($\lambda_{em} = $ 560 nm or $\lambda_{em} = $ 590 nm) in conjunction with yellow-emitting $Y_3Al_5O_{12}$:Ce^{3+} or green-emitting $Lu_3Al_5O_{12}$:Ce^{3+} and a blue-emitting InGaN LED ($\lambda_{em} = $ 450 nm). Several phosphor/quantum dot geometries were examined, including encapsulating the phosphor powder and quantum dots together in silicone resin, or in two separate layers of silicone resin, with either the quantum dots closest to the LED or the phosphor particles closest to the LED. The quantum dots were most efficient when encapsulated with the phosphor particles in the resin. Devices

---

[1]The contents of this chapter have substantially appeared in reference [171]: K. A. Denault, A. A. Mikhailovsky, S. Brinkley, S. P. DenBaars, and R. Seshadri, Improving color rendition in solid state white lighting through the use of quantum dots, *J. Mater. Chem. C* **1** 1461 (2013) ©2013 Royal Society of Chemistry.

with $Y_3Al_5O_{12}$:Ce^{3+} and quantum dots (λ_{em} = 590 nm) achieved a correlated color temperature of 4000 K, color rendering index of 81, and luminous efficacy of 57 lm/W, while devices with $Lu_3Al_5O_{12}$:Ce^{3+} and quantum dots (λ_{em} = 590 nm) achieved a correlated color temperature of 5700 K, a color rendering index of 90, and luminous efficacy of 22 lm/W. The results obtained suggest that the use of quantum dots may allow for solid state white lighting devices with high color rendition.

A.1 Introduction

YAG:Ce offers many benefits including high absorption of blue light and an extremely efficient emission process with a quantum yield around 90%. A major drawback of using YAG:Ce for solid state white lighting is the low color quality of the white light that is produced. The correlated color temperature (CCT) of such a device using exclusively YAG:Ce as the down-converting phosphor is around 4600 K, corresponding to a "cool" white light. Additionally, the color rendering index (R_a) of such as device is only about 65, resulting in poor representation of an object's true color when illuminated.

These drawbacks are principally due to the lack of emission from wavelengths in the red spectral region. Generally, this is corrected by adding a red-emitting phosphor in addition to the yellow-emitting YAG:Ce, although this can also lead to adverse effects. Adding a second down-converting component will decrease the overall efficiency of the device, especially since red-emitting phosphors tend to not be as efficient as YAG:Ce. Additionally, since the nature of the emission spectrum of a phosphor is broad, the emission from a red phosphor will trail into the near infrared, resulting in the device emitting wavelengths that are not visible to the human eye and are not contributing to the luminous output, lowering the overall efficacy of the device. One approach to obtaining efficient solid state white lighting devices with improved color properties is to use quantum dots as the red-emitting down-conversion phosphor. By changing the size of a quantum dot, the emission color can easily be tuned to emit in the red spectral region at specific wavelengths that are not present in a device using a single green- or yellow-emitting phosphor. Another advantage of using quantum dots

is that their emission spectra are narrow compared to conventional phosphors, allowing the red spectral range to be easily represented without losing energy to the near-infrared.

Previous reports of quantum dot converted devices began in 2000 with demonstrations by Bawendi and coworkers of quantum dot-polymer composites for full color white LEDs.[172] Improvements in color rendering indices and luminous efficacies for full quantum dot-converted devices have since been shown by a number of researchers. In 2006, Chen *et al.* obtained white light with an R_a of 91 and efficacy of 7.2 lm/W using a blue InGaN LED with green- and red-emitting CdSe/ZnSe quantum dots[173], Wang *et al.* in 2008 demonstrated white light with an R_a of 66 and efficacy of 6.4 lm/W using a blue InGaN LED with three sizes of CdSe/ZnS quantum dots[174], Chung *et al.* in 2009 showed white light with an R_a of 61 and efficacy of 3.8 lm/W using a blue InGaN LED with three sizes of CdSe quantum dots[175], and Wang *et al.* in 2011 achieved white light with an R_a of 88 and efficacy of 32 lm/W using a blue InGaN LED with green-, yellow-, and red-emitting CdSe/CdS/ZnS quantum dots[176].

Quantum dots have also been explored previously as an additional down-converting component in phosphor-converted LEDs. In 2008, Ziegler *et al.* obtained white light with an R_a of 86 and efficacy of 15 lm/W using a blue In-GaN LED with green-emitting $SrAl_2O_4:Eu^{2+}$, yellow-emitting YAG:Ce, and red-emitting $InP/ZnS/SiO_2$ quantum dots[177], Jang *et al.* in 2009 demonstrated white light with an R_a of 85 and efficacy of 27 lm/W using a blue InGaN LED with yellow-emitting $Sr_3SiO_5:Ce^{3+},Li^+$, and red-emitting CdSe/ZnSe quantum dots[178, 179], Kim *et al.* in 2012 showed white light with an R_a of 81 and efficacy of 55 lm/W using a blue InGaN LED with yellow-emitting YAG:Ce and red-emitting InP/GaP/ZnS quantum dots[180], and Wang *et al.* in 2012 achieved white light with an R_a of 86 and efficacy of 37 lm/W using a blue InGaN LED with yellow-emitting YAG:Ce and red-emitting CdS:Cu/ZnS quantum dots[181].

In this contribution, we have chosen to fabricate solid state white lighting devices using highly efficient yellow-emitting YAG:Ce or green-emitting LuAG:Ce ($Lu_3Al_5O_{12}:Ce^{3+}$) phosphor, red-emitting CdSe/ZnS core/shell quantum dots ($\lambda_{em} = 560$ nm or $\lambda_{em} = 590$ nm), and a blue-emitting InGaN LED ($\lambda_{em} = 450$ nm). CdSe cores were chosen for this study as they have been the sub-

ject of extensive research since reports of monodisperse nanocrystals by Murray *et al.*[182]. The addition of a ZnS shell has been shown to further improve quantum efficiencies[183, 184], allowing for the synthesis of relatively large nanocrystals with low surface defects, necessary efficient red-emitting quantum dots. We have also paid particular attention to the layering of phosphor and quantum dots to understand the impact of using multiple conversion components and to obtain devices with high color rendition while maintaining high luminous efficacies. We present results from fabrication and characterization of several devices, specifically analyzing the color properties of the white light and exploring optimal geometries.

A.2   Experimental

$Y_{2.94}Ce_{0.06}Al_5O_{12}$ and $Lu_{2.94}Ce_{0.06}Al_5O_{12}$ were prepared by intimately mixing the appropriate amounts of Y_2O_3 (99.99% purity, Materion), Lu_2O_3 (99.9% purity, Materion), Al_2O_3 (high purity, sub-micron SM8, Baikowski), and CeO_2 (99.9% purity, Materion) by grinding in an agate mortar with acetone for approximately 30 min. Powders were pressed into pellets, placed on top of sacrificial powder in alumina crucibles, and heated at $1500\,°C$ for 5 h in flowing $5\%H_2/95\%N_2$ gas with heating ramps of $2\,°min^{-1}$. The quantum dots were generously supplied by Nanoco Technologies Limited, Manchester, UK. Two sets of core/shell CdSe/ZnS quantum dots, capped with hexadecylamine (HDA), were chosen for the study with λ_{em} = 560 nm corresponding to a particle size of 3.4 nm and λ_{em} = 590 nm corresponding to a particle size of 4.0 nm. The quantum dots were received dispersed in toluene at a concentration of 5 mg/mL, with both sets rated to have a quantum yield ≥30% in solution.

Photoluminescence spectra were collected on a Perkin Elmer LS55 spectrophotometer equipped with a xenon lamp. The powder samples were measured in optically transparent silicone resin (GE Silicones, RTV-615) and the quantum dots were measured in solution with toluene.

Devices were assembled using a blue-emitting InGaN LED chip (λ_{em} = 450 nm) encapsulated in a dome of silicone resin and "caps" containing the phosphor powder and quantum dots dispersed in silicone resin. The "capping"
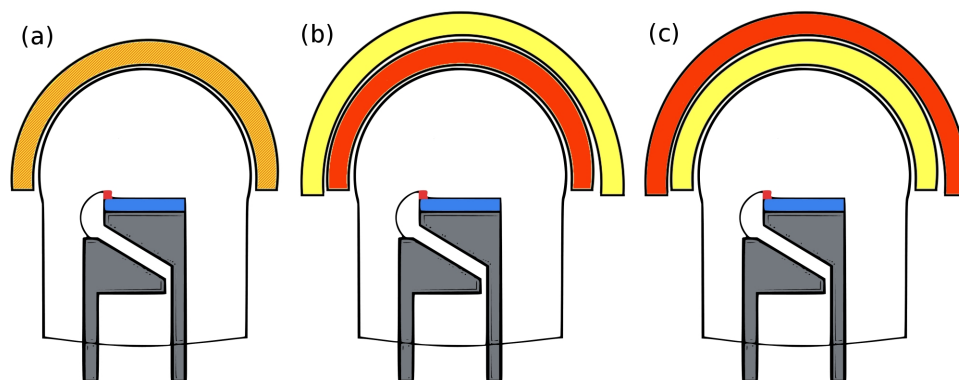
Figure A.1: Schematic illustrations of the three different cap geometries with (a) the phosphor powder and quantum dots encapsulated in a single silicone resin cap, (b) a smaller cap (of the same thickness as the single cap) containing the quantum dots, closest to the LED chip, with a larger cap (again of the same thickness) containing the phosphor powder, and (c) a smaller cap containing the phosphor powder and a larger cap containing the quantum dots. Reproduced with permission from reference [171], ©2013 Royal Society of Chemistry.

strategy, described previously,[43, 60] was employed to use the same LED for all measurements. Caps were made by adding quantum dot solution or phosphor powder into silicone resin and mixing until homogeneously dispersed. For the caps containing both phosphor and quantum dots, the quantum dot solution was first mixed into the silicone until evenly dispersed and then the phosphor powder was added and mixed until homogeneous. The silicone resin mixture was then put into molds, placed under vacuum to remove air bubbles, and cured at 150 °C for 15 min. Three different device geometries were chosen to study the interaction between the phosphor powder and the quantum dots: a single cap containing both the phosphor powder and quantum dots in an intimate mixture, a smaller cap (closest to the LED and of the same thickness as the single cap) containing the quantum dots with a larger cap (placed on top of the smaller cap and again of the same thickness as the single cap) containing the phosphor powder, and a smaller cap containing the phosphor powder with a larger cap containing the quantum dots. An air gap is present between all silicone resin interfaces. A schematic of the different device geometries is shown in Figure A.1.

Measurements were collected for YAG:Ce with CdSe/ZnS λ_{em} = 560 nm,

YAG:Ce with CdSe/ZnS λ_{em} = 590 nm, LuAG:Ce with CdSe/ZnS λ_{em} = 560 nm, and LuAG:Ce with CdSe/ZnS λ_{em} = 590 nm. For each cap, 1 g of silicone resin was used, along with 6 wt% YAG:Ce, 25 μL CdSe/ZnS (λ_{em} = 560 nm) and 25 μL CdSe/ZnS (λ_{em} = 590 nm) for YAG:Ce measurements, and 8.25 wt% LuAG:Ce, 60 μL CdSe/ZnS (λ_{em} = 560 nm) and 60 μL CdSe/ZnS (λ_{em} = 590 nm) for LuAG:Ce measurements. Electroluminescence spectra, Commission Internationale de l'Eclairage (CIE) chromaticity coordinates, and color rendering index (R_a) were collected in an integrating sphere using a forward bias current of 20 mA.

A.3   Results and Discussion

Photoluminescence excitation and emission spectra for YAG:Ce are shown in Figure A.2a and for LuAG:Ce in Figure A.2b. The overlaid absorption and emission spectra for the CdSe/ZnS λ_{em} = 560 nm quantum dots and the CdSe/ZnS λ_{em} = 590 nm quantum dots show that the first absorption edge for both sets of quantum dots occurs at wavelengths within the YAG:Ce and LuAG:Ce phosphor emission spectra. Therefore, the quantum dots will absorb light emitted from the LED as well as some of the down-converted light emitted from YAG:Ce or LuAG:Ce. The different device geometries may therefore play a role in obtaining the most efficient excitation of the quantum dots, whether it be from the LED emission or the phosphor emission.

Electroluminescence data is shown in Figure A.3 for devices composed of YAG:Ce with quantum dots and in Figure A.4 for devices composed of LuAG:Ce with quantum dots. Spectra were deconvoluted into four Gaussian curves to represent emission from the InGaN LED (λ_{em} = 450 nm), emission from the Ce^{3+} lowest lying 5d states ($^2D_{3/2}$) to the $^2F_{5/2}$ and $^2F_{7/2}$ ground states, and emission from the quantum dots. This deconvolution, as a function of the different device geometries, allows us to examine the amount of light being emitted from each component in the device, to determine the interactions that are occurring between the three components. Table A.1 summarizes the relative integrated intensities representing the percentage of light emitted from each component for the different device geometries.
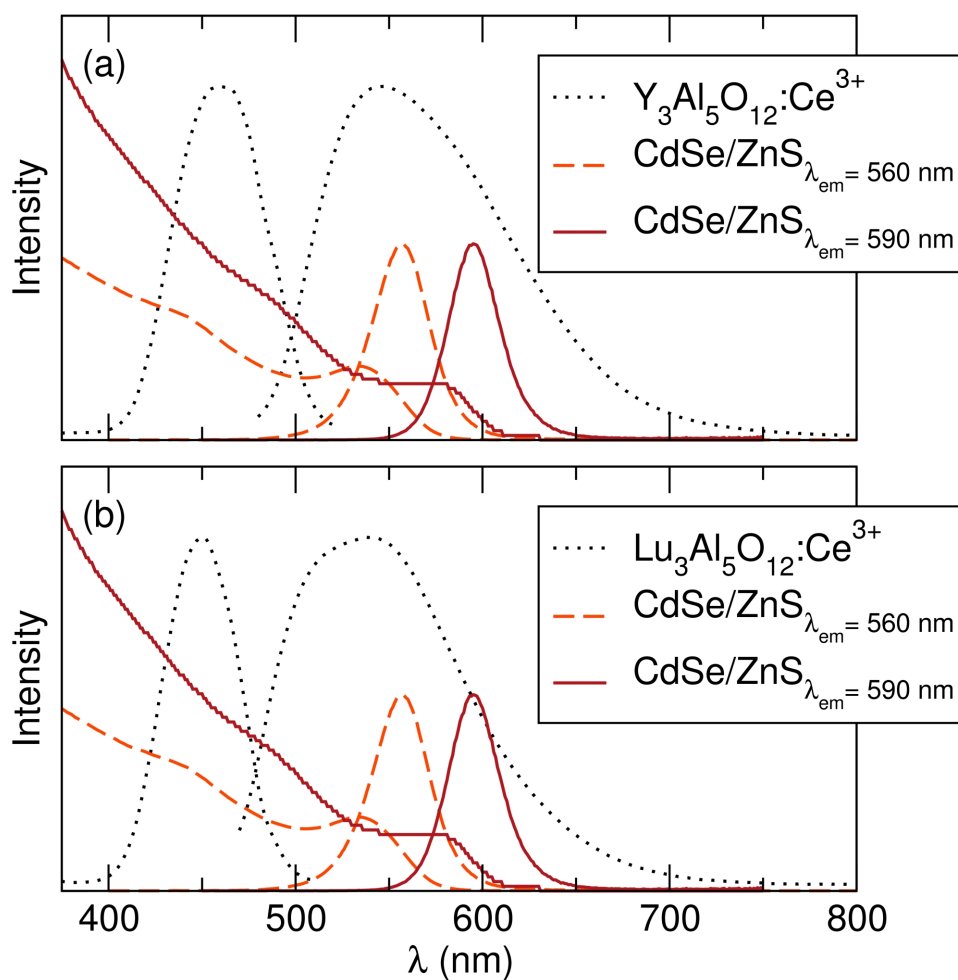
Figure A.2: Excitation and emission spectra of (a) YAG:Ce and (b) LuAG:Ce with absorption and emission spectra of CdSe/ZnS $\lambda_{em} = 560\,$nm and CdSe/ZnS $\lambda_{em} = 590\,$nm quantum dots overlaid shows the quantum dots may be excited by either the LED emission or the phosphor emission. Reproduced with permission from reference [171], ©2013 Royal Society of Chemistry.
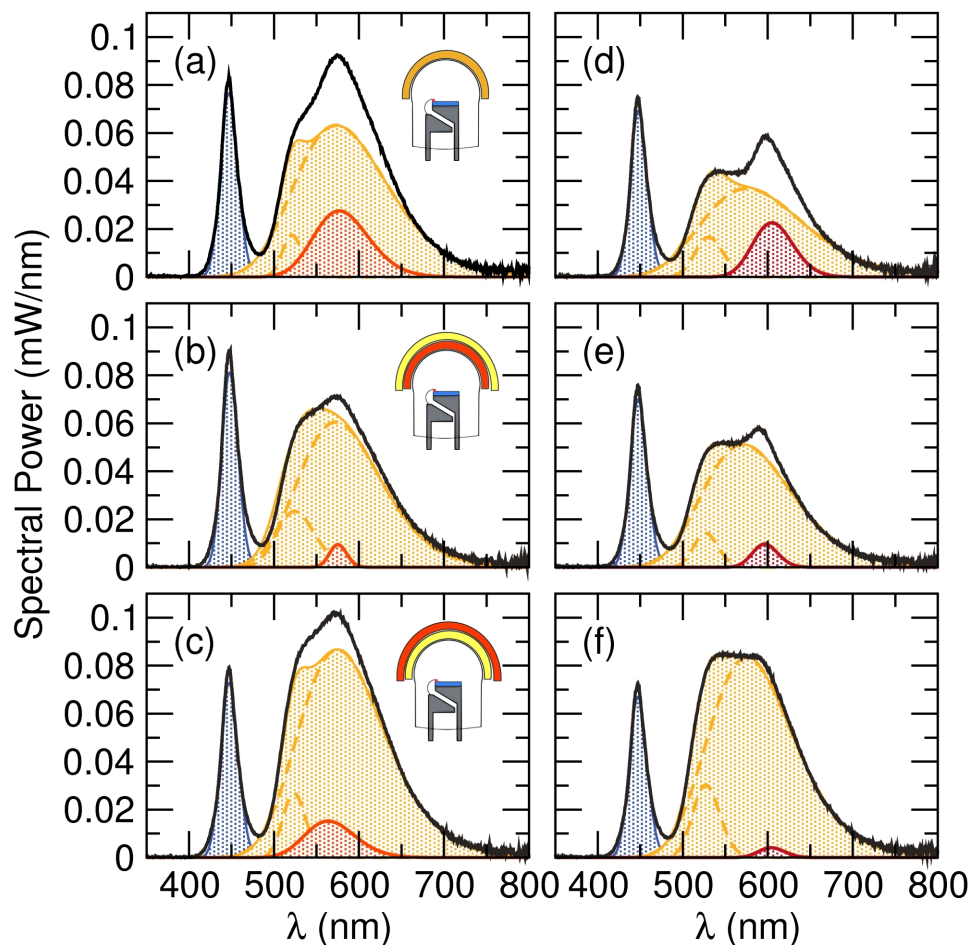
Figure A.3: The deconvolution of electroluminescence spectra for devices with YAG:Ce and quantum dots show the contributions to the spectra from each emission component for the different device geometries. Figures (a) through (c) correspond to devices containing the CdSe/ZnS $\lambda_{em} = 560$ nm quantum dots and (d) through (f) the CdSe/ZnS $\lambda_{em} = 590$ nm quantum dots. Figures (a) and (d) are devices with phosphor and quantum dots in a single cap, (b) and (e) quantum dots in the smaller cap with phosphor in the larger cap, and (c) and (f) phosphor in the smaller cap and quantum dots in the larger cap. Reproduced with permission from reference [171], ©2013 Royal Society of Chemistry.
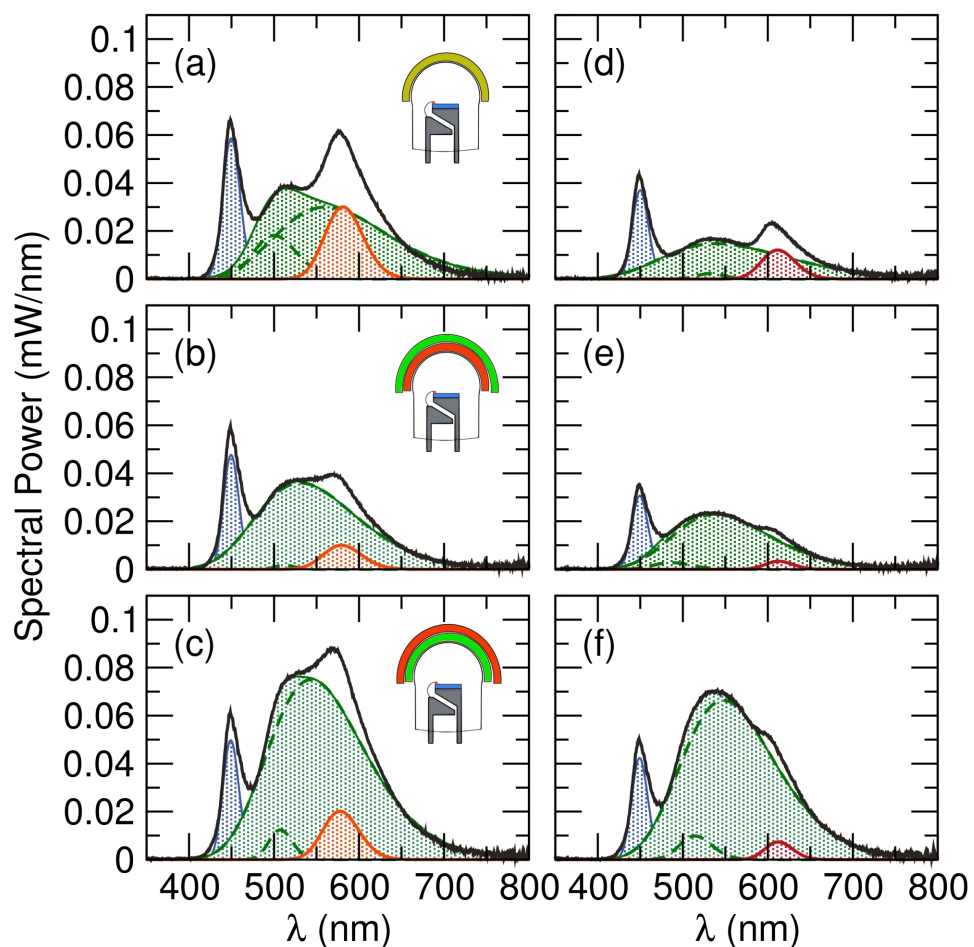
Figure A.4: The deconvolution of electroluminescence spectra for devices with LuAG:Ce and quantum dots show the contributions to the spectra from each emission component for the different device geometries. Figures (a) through (c) correspond to devices containing the CdSe/ZnS $\lambda_{em} = 560$ nm quantum dots and (d) through (f) the CdSe/ZnS $\lambda_{em} = 590$ nm quantum dots. Figures (a) and (d) are devices with phosphor and quantum dots in a single cap, (b) and (e) quantum dots in the smaller cap with phosphor in the larger cap, and (c) and (f) phosphor in the smaller cap and quantum dots in the larger cap. Reproduced with permission from reference [171], ©2013 Royal Society of Chemistry.

Table A.1: Relative integrated intensities representing the contributions from each emitting component for devices of different geometries containing both phosphor powder and quantum dots. The device geometries (a) through (f) correspond to the spectra shown in Figures A.3 and A.4.

device geometry	LED	phosphor	CdSe/ZnS
YAG:Ce (a)	15%	69%	16%
YAG:Ce (b)	18%	80%	2%
YAG:Ce (c)	13%	80%	7%
YAG:Ce (d)	18%	68%	14%
YAG:Ce (e)	19.5%	80.1%	0.4%
YAG:Ce (f)	13%	86%	1%
LuAG:Ce (a)	16%	66%	18%
LuAG:Ce (b)	15%	77%	8%
LuAG:Ce (c)	9%	83%	8%
LuAG:Ce (d)	20%	66%	14%
LuAG:Ce (e)	17%	80%	3%
LuAG:Ce (f)	9%	88%	3%

The geometry with a single cap containing both the phosphor powder and the quantum dots had the greatest percentage of quantum dot emission (14% to 18%) and less phosphor emission compared to the other two geometries. It appears that the quantum dots may therefore absorb both the LED emission and the phosphor emission. The geometry with a smaller cap containing the quantum dots and a larger cap containing the phosphor had minimal emission from the quantum dots (0.4% to 8%) and about the same amount of unconverted LED emission compared to the single cap geometry (15% to 20%). The small percentage of quantum dot emission in this geometry could be due to the emitted light being scattered and trapped within the larger phosphor powder cap before being extracted from the device. The geometry with a smaller cap containing the phosphor and a larger cap containing the quantum dots also had minimal emission from the quantum dots (3% to 8%) and less unconverted LED emission (9% to 13%) compared to the other two geometries. In this geometry, most of the LED emission is converted by the phosphor and only a small fraction of unconverted LED emission reaches the quantum dots in the outer cap. This leads to a high conversion of the LED emission by the phosphor and only a small conversion by the quantum dots. We do not see a noticeable decrease in phos-

phor emission with the phosphor encapsulated in the smaller cap, as we saw for the quantum dots encapsulated in the smaller cap. This is due to the phosphor having a higher absorption and more efficient conversion of blue light than the quantum dots, and since the phosphor is closest to the LED in this geometry the phosphor emission will be relatively high. Additionally, since the phosphor emission is the largest source of emission in these devices, losses will have a minimal effect on the overall output. Conversely, the quantum dot emission is the smallest source of emission in these devices and any losses will greatly affect the overall output.

The quantum dots are therefore not as efficiently excited by the phosphor emission when they are placed at a remote distance from the particles, compared to encapsulated within the same silicone resin. From these findings, it appears that the quantum dots are most efficiently excited when they are in close proximity to both the LED and the phosphor particles in a single silicone cap. In this geometry, the quantum dots can absorb the emission from both the LED and the phosphor particles that are in close proximity, and the emitted light can then be easily extracted from the device without encountering additional scattering losses through another layer of silicone resin.

The quality of the white light produced by the different devices was analyzed through the CIE chromaticity coordinates, as shown in Figure A.5, for each device geometry. Comparing similar two-cap geometries using either CdSe/ZnS λ_{em} = 560 nm or CdSe/ZnS λ_{em} = 590 nm quantum dots the color points do not change based on the wavelength of quantum dots used. Only in the device using a single cap do we see the effect of using different color quantum dots. This again confirms that in the single cap geometry the quantum dots are used most effectively.

The luminous efficacy and color properties of the devices are displayed in Table A.2. Devices with the single cap proved to have the warmest color temperatures and the highest color rendering indices, due to the contributions from the quantum dot emission. However, these devices suffered from a decline in the luminous efficacy, compared to devices with only YAG:Ce or LuAG:Ce. This is most likely due to self-absorption effects in the quantum dots caused by an inability to effectively disperse the quantum dots and prevent aggregation in
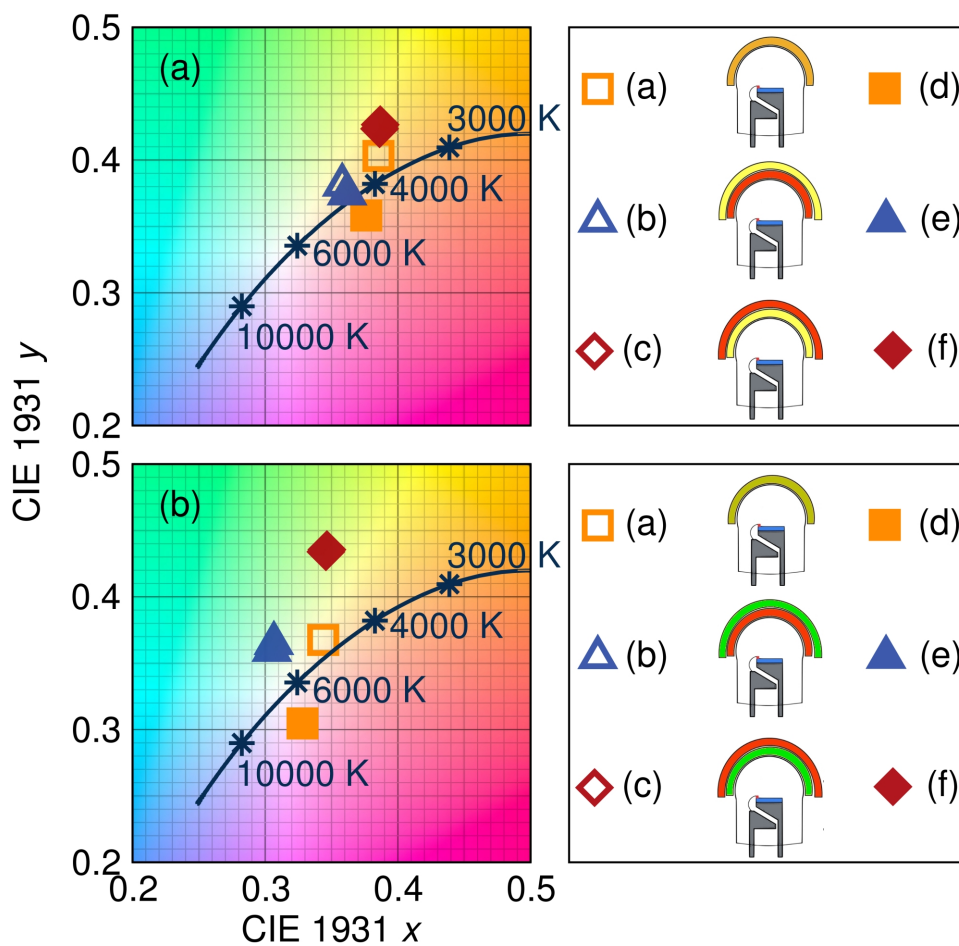
Figure A.5: CIE chromaticity coordinates show the color of the white light produced from each device containing (a) YAG:Ce with quantum dots and (b) LuAG:Ce with quantum dots. The open symbols correspond to the CdSe/ZnS $\lambda_{em} = 560\,\text{nm}$ quantum dots and the closed symbols to the CdSe/ZnS $\lambda_{em} = 590\,\text{nm}$ quantum dots, with labels (a) through (f) corresponding to the spectra shown in Figures A.3 and A.4. Reproduced with permission from reference [171], ©2013 Royal Society of Chemistry.

Table A.2: Color properties of the white light created using different device geometries containing both phosphor powder and quantum dots, compared to devices using solely YAG:Ce or LuAG:Ce. The device geometries (a) through (f) correspond to the spectra shown in Figures A.3 and A.4.

device geometry	efficacy (lm/W)	CIE (x, y)	CCT (K)	R_a
YAG:Ce	122	0.37, 0.42	4600	65
YAG:Ce (a)	93	0.39, 0.40	4100	67
YAG:Ce (b)	76	0.36, 0.38	4700	68
YAG:Ce (c)	108	0.39, 0.43	4200	65
YAG:Ce (d)	57	0.38, 0.36	4000	81
YAG:Ce (e)	62	0.36, 0.37	4500	71
YAG:Ce (f)	97	0.39, 0.42	4200	68
LuAG:Ce	125	0.31, 0.42	6100	63
LuAG:Ce (a)	59	0.34, 0.37	5100	73
LuAG:Ce (b)	45	0.31, 0.37	6600	71
LuAG:Ce (c)	96	0.35, 0.43	5200	66
LuAG:Ce (d)	22	0.33, 0.30	5700	90
LuAG:Ce (e)	27	0.30, 0.36	6700	79
LuAG:Ce (f)	78	0.35, 0.44	5200	71

the solid silicone resin matrix. Further studies will be conducted to examine the agglomeration of quantum dots in the solid state and the effects this has on the quantum yield. Homogenous dispersion of the quantum dots without agglomeration could therefore increase the color rendering of such devices, while maintaining a high luminous efficacy. Devices with the highest luminous efficacy were those with the phosphor in the smaller cap and the quantum dots in the larger cap. In this geometry, most of the light is converted by the phosphor with little contribution from the quantum dots, so the loss in efficiency is not as large. The low luminous efficacy from devices with the quantum dots in the smaller cap confirms that in this geometry the quantum dots are absorbing light from the LED, yet their emitted light is not efficiently extracted from the device, leading to decreased light output. It should also be noted that devices containing the 590 nm emitting quantum dots resulted in higher color rendering indices but lower luminous efficacies than devices containing the 560 nm emitting quantum dots. This is due to the larger Stokes shift associated with the 590 nm emitting quantum dots than for the 560 nm emitting quantum dots.

This means that more energy will be lost going from blue to 590 nm than from blue to 560 nm and so the result is a decrease in the luminous efficacy. This is always a challenge in generating high color rendering white light, as the color rendering improves with an increase in the red spectral component, the luminous efficacy suffers. Minimizing this loss is still a major goal of solid state white lighting.

A.4 Conclusions

Analysis of the color properties for solid state white lighting devices incorporating quantum dots showed the potential application for quantum dots to improve color rendering in devices. The quantum dots were used most effectively when they were in close proximity to both the LED and the phosphor particles, allowing absorption of unconverted LED emission as well as possible absorption of the phosphor emission. Using a single layer of silicone resin to encapsulate both phosphor particles and quantum dots accomplishes this, along with minimizing the losses due to scattering and re-absorption that occur when using multiple silicone resin layers.

High color rendering white light was demonstrated for devices using $Y_3Al_5O_{12}:Ce^{3+}$ and CdSe/ZnS λ_{em} = 590 nm quantum dots with a CCT of 4000 K, R_a of 81, and luminous efficacy of 57 lm/W, and for devices using $Lu_3Al_5O_{12}:Ce^{3+}$ and CdSe/ZnS λ_{em} = 590 nm quantum dots with a CCT of 5700 K, R_a of 90, and luminous efficacy of 22 lm/W. However, these devices suffered from a decrease in the luminous efficacy compared to devices using only phosphor powder. Device efficacy could be increased by effectively dispersing the quantum dots in the solid state to prevent self-absorption caused by aggregation. Therefore, the use of quantum dots with phosphor powders may allow for solid state white lighting devices with high color rendition.

Appendix B

Efficient and stable laser-driven white lighting

Laser-based white lighting offers a viable option as an efficient and color-stable high-power solid-state white light source. We show that white light generation is possible using blue or near-UV laser diodes in combination with yellow-emitting cerium-substituted yttrium aluminum garnet (YAG:Ce) or a mixture of red-, green-, and blue-emitting phosphors. A variety of correlated color temperatures (CCT) are achieved, ranging from cool white light with a CCT of 4400 K using a blue laser diode to a warm white light with a CCT of 2700 K using a near-UV laser diode, with respective color rendering indices of 57 and 95. The luminous flux of these devices are measured to be 252 lm and 53 lm with luminous efficacies of 76 lm/W and 19 lm/W, respectively. An estimation of the maximum efficacy of a device comprising a blue laser diode in combination with YAG:Ce is calculated and the results are used to optimize the device.

---

[1]The contents of this chapter have substantially appeared in reference [15]: K. A. Denault, M. Cantore, S. Nakamura, S. P. DenBaars, and R. Seshadri, Efficient and stable laser-driven white lighting, *AIP Advances* **3** 072107 (2013) published by AIP Publishing LLC, ©2013 owned by the Authors.

B.1 Introduction

Solid-state white lighting has gained interest since the development of candela-class, high brightness (In,Ga)N light emitting diodes (LEDs) by Nakamura and coworkers in 1995. [2] This development, in combination with appropriate phosphor compositions and improvements in device packaging, have led to devices that use less energy and are a viable option to replace conventional incandescent or fluorescent light sources.[7] Traditional solid-state white lighting devices comprise a blue or near-UV LED as the excitation source and one or more phosphor compositions which down-convert all or part of the LED emission to longer wavelengths.[1, 7, 185] The LEDs used in these devices currently suffer a loss in external quantum efficiency (EQE) as operating current increases, known as droop. As LED efficiency decreases with higher operating currents, the result is an increase in the temperature of the device, since this efficiency is lost as heat. The increased temperature will in turn cause more efficiency loss from the LED and may lead to a shift in the peak emission wavelength and broadening of the emission spectrum. The increased temperature of the device will also affect the phosphor, causing a decrease in efficiency and a possible shift in the peak emission wavelength of the phosphor. These changes in the spectrum of the LED and phosphor will change the ratio of light emitted by each component, resulting in a shift in the color point of the white light, and a decrease in overall device efficiency, making high-power devices difficult to achieve using single LEDs as the excitation source.[186, 187]

In contrast to LEDs, laser diodes do not exhibit this efficiency loss. The output power and EQE of laser diodes increase linearly with current, and maintains color stability of the laser emission, making laser diodes an attractive excitation source for new high-power white lighting applications.[188] Additionally, since the shift in the color coordinates of a device under increased operating current is largely due to the increased temperature of the device, a remote phosphor geometry is extremely important to eliminate thermal effects. Remote phosphors can easily employed with a laser diode, since the phosphor may be placed at a distance far from the laser source. Also, laser-based device may be operated in reflection mode, allowing for the remote phosphor to be placed on a reflective substrate that may also act as a heat sink to effectively dissipate heat away from

the phosphor.

Previous work has shown that white light emission can be achieved by exciting a phosphor with a laser diode, while maintaining color stability with increasing injection current. Xu *et al.* reported white light emission of 5.7 lm with a correlated color temperature (CCT) of 5225 K and efficacy of 13 lm/W when exciting yellow- and blue-emitting phosphors with a near-UV laser diode.[188] In 2009, the same group reported emission of white light of 3.6 lm with a CCT of 5393 K and efficacy of 8.3 lm/W using a near-UV laser diode to excite red-, green-, and blue-emitting phosphors.[189] Ryu and Kim reported emission of white light by exciting a yellow-emitting phosphor with a blue laser diode, achieving 5 lm with an efficacy of 10 lm/W.[190] The luminous flux and efficacy of such devices must reach higher values for high-power, high-brightness applications. Since these reports have been published, laser diode technologies have improved and are continuing to do so. In this letter, we demonstrate that with current commercially available laser diodes and the appropriate mix of phosphors, high-power, efficient white light generation is achievable with good color rendition and in a variety of color temperatures. The quality of the white light is analyzed for three devices, two using a near-UV (λ_{max} = 402 nm) laser diode in combination with red-, green-, and blue-emitting (RGB) phosphors of differing RGB concentrations and the third using a blue (λ_{max} = 442 nm) laser diode in combination with yellow-emitting $Y_3Al_5O_{12}$:Ce^{3+} (YAG:Ce). We also perform optimization of such a device based on an estimation of maximum efficacy.

B.2   Experimental

The proprietary RGB phosphors used in this study were obtained from Mitsubishi Chemical Corporation. They were chosen based on high absorption of near-UV (λ = 402 nm) light and a combination of emissions that represent most of the visible spectrum. Phosphor samples were prepared by mixing 50 wt% phosphor powder with silicone resin (GE Silicones, RTV-615), molded in the shape of a disk, mounted on a quartz substrate (Chemglass), and cured at 150 °C for 15 min. Photoluminescence spectra were collected using a Perkin-Elmer LS55 spectrophotometer equipped with a xenon lamp. Figure B.1 shows the ex-
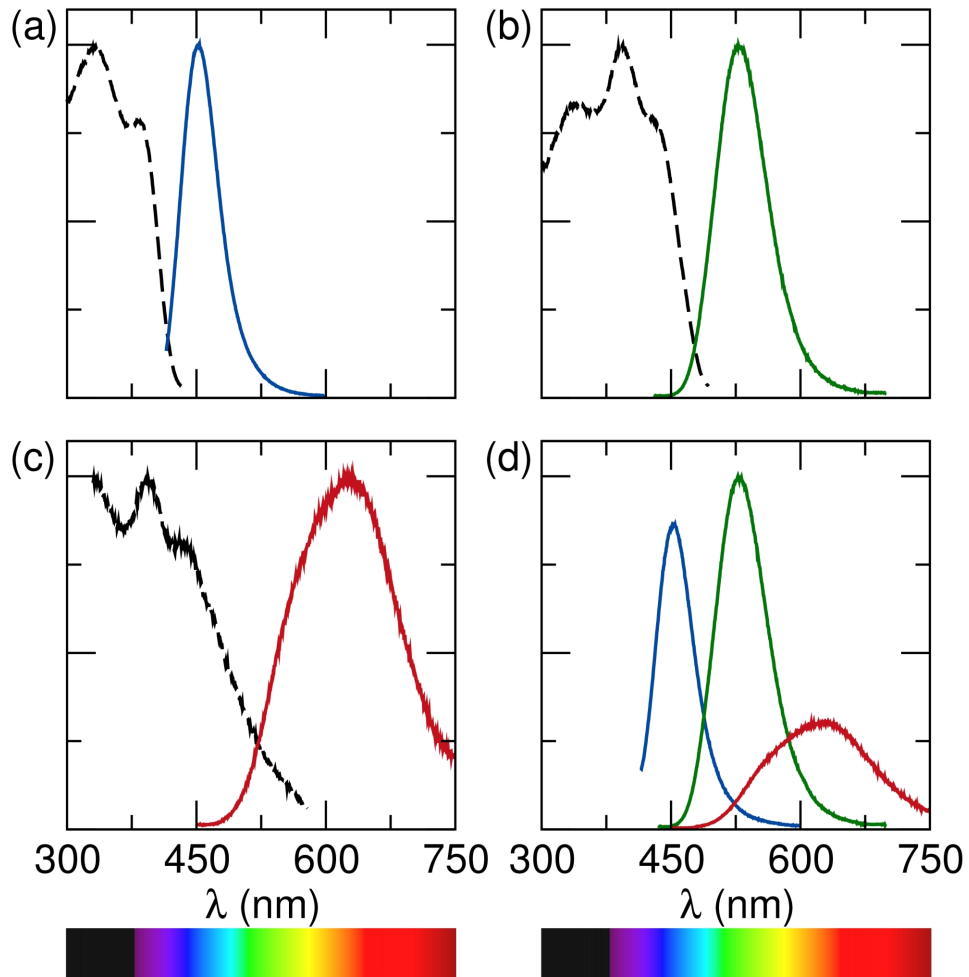
Figure B.1: Excitation and emission spectra, collected at the relative maxima of (a) the blue-emitting phosphor ($\lambda_{ex} = 335\,\text{nm}$; $\lambda_{em} = 452\,\text{nm}$), (b) the green-emitting phosphor ($\lambda_{ex} = 395\,\text{nm}$; $\lambda_{em} = 530\,\text{nm}$), (c) the red-emitting phosphor ($\lambda_{ex} = 395\,\text{nm}$; $\lambda_{em} = 630\,\text{nm}$). (d) shows the relative emission intensities collected at 402\,nm excitation. Reproduced with permission from reference [15], ⓒ2013 owned by the Authors.

Figure B.2: Schematic illustrations of the experimental setup used to measure laser excited phosphor samples in an integrating sphere. The phosphor encapsulated silicone disk, mounted on a transparent quartz substrate, is positioned with the surface at a slight angl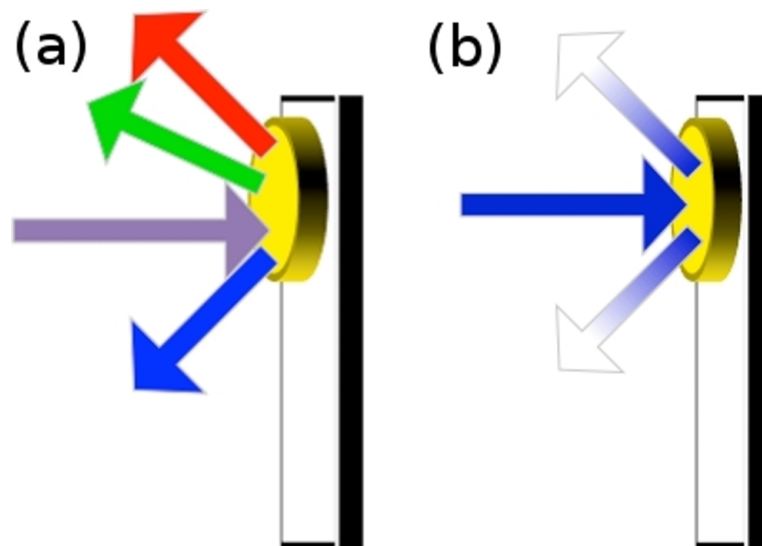e to the incoming laser beam. The resulting device operates in reflection mode due to the dense phosphor pellet, illustrated for (a) the near-UV excited RGB phosphors and (b) the blue excited YAG:Ce. Reproduced with permission from reference [15], ©2013 owned by the Authors.

citation and emission spectra for the red-, green-, and blue-emitting phosphors chosen and their relative emission intensities, used to determine the necessary concentrations of each. It should be noted that due to the broad excitation spectrum of the red-emitting phosphor, some emission from the blue-emitting phosphor is absorbed and a higher concentration of blue-emitting phosphor is needed. Two RGB ratios were chosen to demonstrate the variety of color temperatures possible using a laser-based white light source. Phosphor sample RGB_1 consists of a R : G : B weight ratio of 1.65 : 1 : 3.45 and phosphor sample RGB_2 consists of a R : G : B weight ratio of 3.3 : 1 : 2.3.

Spectral power distribution (SPD), Commission Internationale de l'Éclairage (CIE) chromaticity coordinates, and color rendering indices (R_a) were collected using an integrating sphere with the laser mounted in a side port and the phosphor sample mounted in the center of the sphere. The sample surface was

Table B.1: Measured properties including the correlated color temperature (CCT), color rendering (R_a), luminous flux (ϕ_v), and luminous efficacy (η_v) of the resulting white light using the near-UV ($\lambda_{max} = 402$ nm) laser diode in combination with phosphor samples RGB$_1$ and RGB$_2$ and using the blue ($\lambda_{max} = 442$ nm) laser diode in combination with YAG:Ce.

sample	CCT (K)	R_a	ϕ_v (lm)	η_v (lm/W)
RGB$_1$	3600	91	47	16
RGB$_2$	2700	95	53	19
YAG:Ce	4400	57	252	76

positioned at a slight angle from the incoming laser beam to prevent reflection back towards the laser port. Schematic illustrations of the experimental setup are depicted in Figure B.2. Commercially available laser diodes were used including a near-UV laser diode with $\lambda_{max} = 402$ nm, FWHM = 2.6 nm, threshold current of 30 mA, and wall plug efficiency (WPE) of 20% and a blue laser diode with $\lambda_{max} = 442$ nm, FWHM = 2.7 nm, threshold current of 150 mA, and WPE of 30%.

B.3   Results and Discussion

Operating the near-UV laser diode at 450 mA, corresponding to peak efficiency, we obtain white light with high color rendering at a variety of color temperatures by modifying the RGB phosphor ratios. The SPD and CIE chromaticity coordinates are shown in Figure B.3. The measured values are listed in Table B.1. These devices show excellent color temperature and color rendering capabilities. The luminous flux produced is comparable to current commercially available bright white LEDs of similar color temperatures. The luminous efficacies of these laser-based devices are relatively low due to the low wall plug efficiency of the laser diodes. With additional improvements in laser diode technologies, the luminous efficacy and flux of these white light sources may exceed those of commercial LED competitors. There are several advantages to using a near-UV laser diode for white lighting applications including the variety of color temperatures possible with high color rendering indices and the ability to create

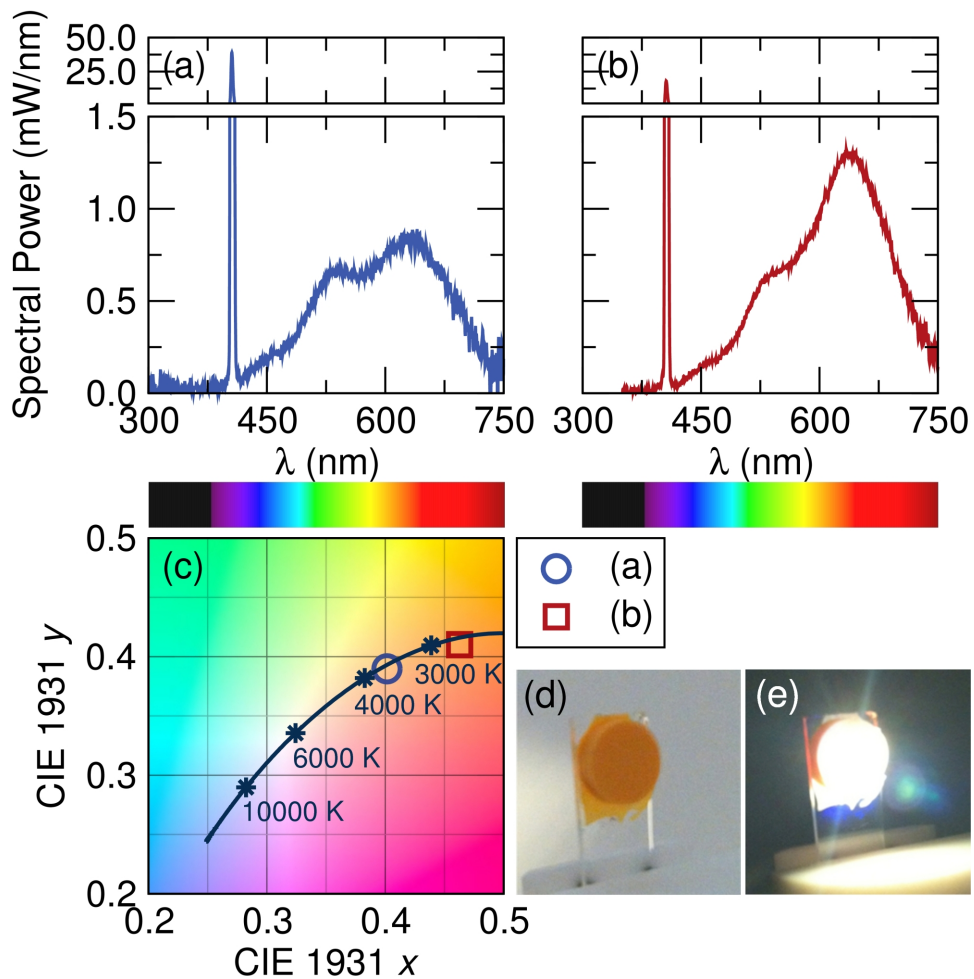Figure B.3: SPD for phosphor samples (a) RGB$_1$ and (b) RGB$_2$ excited using a near-UV ($\lambda_{max} = 402$ nm) laser diode and (c) the corresponding CIE chromaticity coordinates show white light with a variety of color temperatures is attainable. Photographs of the RGB$_2$ phosphor sample (d) without and (e) with laser excitation. Reproduced with permission from reference [15], ©2013 owned by the Authors.

eye safe devices. The unconverted near-UV laser light is not contributing to the luminous flux due to the sensitivity of the human eye. The unconverted laser light can therefore be filtered out from the resulting white light, eliminating any safety concerns due to strong laser light.

A third laser-based device was measured using the blue laser diode in combination with yellow-emitting YAG:Ce. $Y_{2.94}Ce_{0.06}Al_5O_{12}$ was prepared by intimately mixing stoichiometric amounts of Y_2O_3 (99.99% purity, Materion), Al_2O_3 (high purity, sub-micron SM8, Baikowski), and CeO_2 (99.9% purity, Materion), with 5 wt% BaF_2 (99% purity, Materion) and 0.5 wt% NH_4F (99.99% purity, Sigma-Aldrich) which act as a flux, in an agate mortar with acetone for approximately 30 min. Powder was then pressed into pellets, placed on top of sacrificial powder in alumina crucibles, and heated at 1500 °C for 5 h in flowing $5\%H_2/95\%N_2$ gas with heating ramps of $2\,°C\,min^{-1}$.

The brightness and efficacy of laser-based white lighting devices will depend on the efficiency of the multiple components used, including the laser diode and the combination of phosphors. As stated previously, the ability to produce high-brightness laser-based white lighting devices will increase as laser diode efficiencies improve. In an effort to determine the capabilities of laser-based devices, we have calculated an estimation of maximum efficacy. This calculation was performed for the blue laser diode and YAG:Ce phosphor.

A target white light was chosen with a CCT of 4555 K and R_a of 58. The ratio of laser emission to phosphor emission was varied until this target white light was reached. The resulting SPD and CIE chromaticity coordinates are shown in Figure B.4a,c. The generated SPD was deconvoluted into three Gaussian curves to represent emission from the blue laser diode and emission from the Ce^{3+} $5d$ states ($^2D_{3/2}$) to the $^2F_{5/2}$ and $^2F_{7/2}$ ground states in YAG:Ce. The resulting fraction of integrated laser emission was 0.22 and that of phosphor emission was 0.78. The luminous flux (ϕ_v) of the generated white light can be calculated using Equation B.1

$$\phi_v = K_m \int_0^\infty \frac{\mathrm{d}\phi_e(\lambda)}{\mathrm{d}\lambda} V(\lambda)\mathrm{d}\lambda \tag{B.1}$$

where K_m equals 683 lm/W for photopic vision, ϕ_e is the radiant flux, and $V(\lambda)$
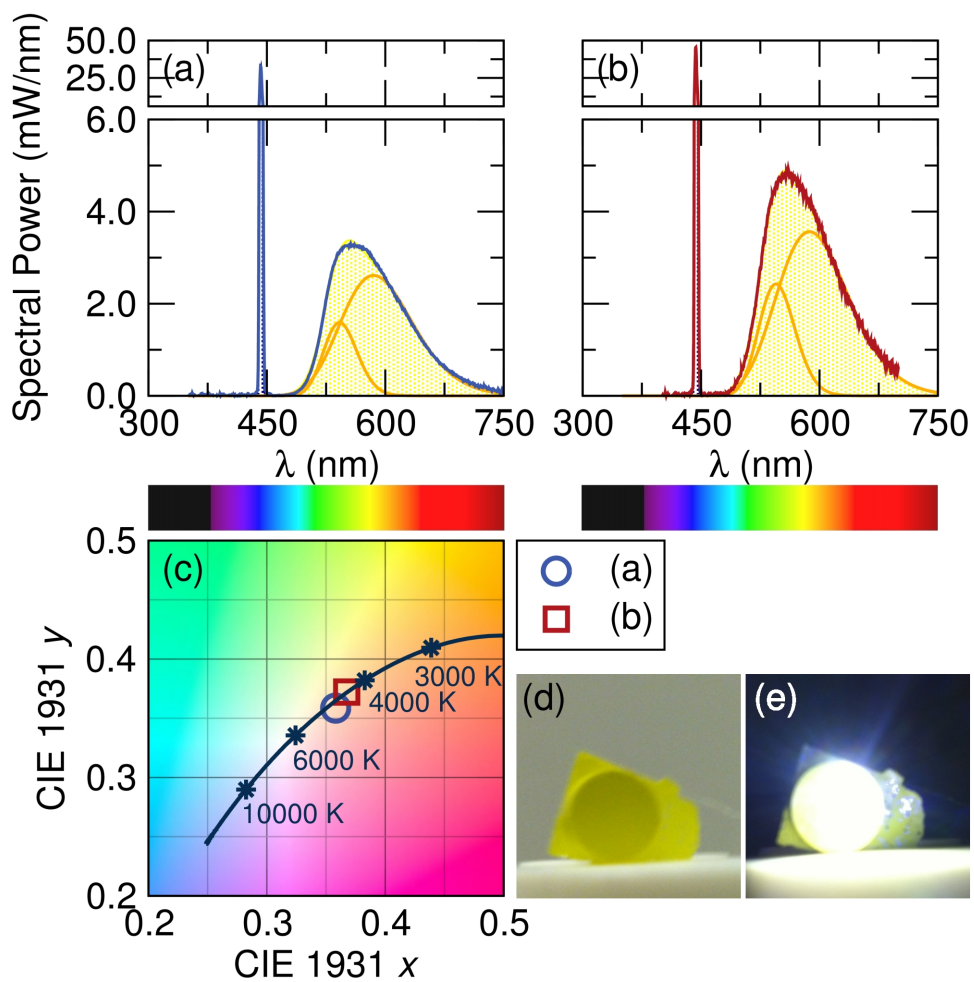
Figure B.4: (a) Calculated SPD for target white light composed of YAG:Ce and a blue laser diode, (b) experimentally measured SPD with a similar ratio of laser to phosphor emission as that of the calculated SPD, (c) the corresponding CIE chromaticity coordinates, and a photograph of the YAG:Ce phosphor sample (d) without and (e) with laser excitation. The SPDs show the fits to three Gaussian curves, representing the fraction of emitted white light from laser emission and phosphor emission. Reproduced with permission from reference [15], ©2013 owned by the Authors.

is the standard luminosity function for photopic vision. Assuming a total integrated power of 1 W for the generated white light, this results in a ϕ_v of 350 lm for the generated SPD for the target white light. The input power (P_{input}) used to generate this can be determined by Equation B.2

$$P_{input} = \frac{P_{laser}}{\eta_{wpe}} + \frac{P_{phosphor}}{\eta_s \eta_{qy} \eta_{wpe}} \tag{B.2}$$

where P_{laser} is the integrated spectral power of the laser emission in the white light SPD, $P_{phosphor}$ is the integrated spectral power of the phosphor emission, η_s is the efficiency of the Stokes loss of the phosphor, η_{qy} is the photoluminescent quantum yield of the phosphor, and η_{wpe} is the wall plug efficiency of the laser diode. Again assuming a total integrated spectral power of 1 W for the generated white light SPD, P_{laser} can be determined from the Gaussian fits to be 0.22 W and $P_{phosphor}$ to be 0.78 W. The η_s parameter may be estimated by taking the ratio of the maximum laser diode emission wavelength to the maximum phosphor emission wavelength. Using a η_s of 76% and a η_{qy} of 90% for YAG:Ce, and using a η_{wpe} of 30% for the blue laser diode, P_{input} is calculated to be 4.5 W. The luminous efficacy (η_v) of the theoretical white light is then calculated using Equation B.3

$$\eta_v = \frac{\phi_v}{P_{input}} \tag{B.3}$$

The estimated maximum efficacy for a white light with a CCT of 4555 K and R_a of 58 generated using a blue laser diode with a wall plug efficiency of 30% and YAG:Ce phosphor is then calculated to be 78 lm/W. The estimation of maximum efficacy allows us to gauge the possible capabilities of future laser-based white light devices. If the wall plug efficiency of a blue laser diode reaches 75%, we would expect the efficacy of a device using YAG:Ce to increase to almost 200 lm/W. Similar estimates may also be conducted for devices comprising multiple phosphor compositions or different laser diode wavelengths.

The blue laser diode was then operated at 750 mA, corresponding to peak efficiency, and the ratio of laser emission to phosphor emission was varied to

obtain results closest to those described in the estimated calculation. The measured SPD and CIE chromaticity coordinates are shown in Figure B.4b,c with deconvolution into three Gaussian curves to represent the emission from the laser and phosphor components. The measured fraction of integrated laser emission is 0.21 and that of phosphor emission is 0.79, similar to the calculated spectrum. The properties of the resulting white light are summarized in Table B.1. The measured luminous efficacy agrees well with the estimated luminous efficacy for such a device. We again see the luminous flux produced is comparable to current commercially available bright white LEDs of similar color temperatures. The luminous efficacy of this device is higher than that of devices using the near-UV laser diode, yet this results in a cool white light with low color rendition. This is also a common problem encountered in LED-based devices using only YAG:Ce as the conversion phosphor, due to the lack of a red component in YAG:Ce. In the case of laser excitation, the low color rendering can also be attributed to the narrow width of the laser spectrum, resulting in only a narrow range of blue wavelengths represented in the white light.

B.4 Conclusions

In conclusion, white light generation using a laser diode in combination with inorganic phosphors is a viable option for high-brightness, high-power white lighting applications. Using a near-UV laser diode in combination with RGB phosphors offers the ability to produce a wide range of color temperatures with high color rendering indices. We have achieved white light with a CCT of 3600 K, R_a of 91, luminous flux 47 lm, and luminous efficacy of 16 lm/W, along with a warm white light with a CCT of 2700 K, R_a of 95, luminous flux of 53 lm, and luminous efficacy of 19 lm/W. We have also achieved white light using a blue laser diode in combination with yellow-emitting YAG:Ce which results in a CCT of 4400 K, R_a of 57, luminous flux of 252 lm, and luminous efficacy of 76 lm/W. We have also shown that the luminous efficacy of such a device can be improved by estimating the maximum efficacy and altering the ratio of laser emission to phosphor emission in order to reach this maximum efficacy. Further improvements in these devices can be envisioned through advancements

in laser diode technologies and optimization of device packaging and phosphor properties.